OAK RIDGE NATIONAL LABORATORY LIBRARIES
3 4456 0548434 8

ARCH LIBRARY
COLLECTION

ORNL-3564
UC-20 – Controlled Thermonuclear Processes
TID-4500 (26th ed.)

THERMONUCLEAR DIVISION

SEMIANNUAL PROGRESS REPORT

FOR PERIOD ENDING OCTOBER 31, 1963

CENTRAL RESEARCH LIBRARY
DOCUMENT COLLECTION
LIBRARY LOAN COPY
DO NOT TRANSFER TO ANOTHER PERSON
If you wish someone else to see this document, send in name with document and the library will arrange a loan.

OAK RIDGE NATIONAL LABORATORY
operated by
UNION CARBIDE CORPORATION
for the
U.S. ATOMIC ENERGY COMMISSION

Printed in USA. Price: $2.25 Available from the
Office of Technical Services
U. S. Department of Commerce
Washington 25, D. C.

LEGAL NOTICE

This report was prepared as an account of Government sponsored work. Neither the United States, nor the Commission, nor any person acting on behalf of the Commission:

A. Makes any warranty or representation, expressed or implied, with respect to the accuracy, completeness, or usefulness of the information contained in this report, or that the use of any information, apparatus, method, or process disclosed in this report may not infringe privately owned rights; or

B. Assumes any liabilities with respect to the use of, or for damages resulting from the use of any information, apparatus, method, or process disclosed in this report.

As used in the above, "person acting on behalf of the Commission" includes any employee or contractor of the Commission, or employee of such contractor, to the extent that such employee or contractor of the Commission, or employee of such contractor prepares, disseminates, or provides access to, any information pursuant to his employment or contract with the Commission, or his employment with such contractor.

ORNL-3564

Contract No. W-7405-eng-26

THERMONUCLEAR DIVISION

SEMIANNUAL PROGRESS REPORT

For Period Ending October 31, 1963

DATE ISSUED

FEB 7 1964

OAK RIDGE NATIONAL LABORATORY
Oak Ridge, Tennessee
operated by
UNION CARBIDE CORPORATION
for the
U. S. ATOMIC ENERGY COMMISSION

OAK RIDGE NATIONAL LABORATORY LIBRARIES

Contents

INTRODUCTION vii

ABSTRACTING SUMMARY xi

1. DCX-1 PLASMA EXPERIMENTS 1
   - 1.1 Introduction 1
   - 1.2 Radio-Frequency Measurements 1
   - 1.3 Slow Plasma, Lithium Beam, and RF Correlations 4
   - 1.4 Electron-Cyclotron Heating 8
   - 1.5 Proton Trapping by Lorentz Dissociation of H_2^+ 10
   - 1.6 Interpretations in Terms of Instabilities 12
   - 1.7 Appendix: A Density Limit for Fast Ions in Mirror Fields 13

2. DCX-2 14
   - 2.1 Introduction 14
   - 2.2 Density and Energy of Confined Plasma 16
   - 2.3 Trapping of Molecular Beam 22
   - 2.4 Arc and Plasma Pumping 23
   - 2.5 Radio-Frequency Emission 25

3. ELECTRON-CYCLOTRON HEATING 28
   - 3.1 Electron-Cyclotron Heating Experiments in the EPA Facility 28
     - 3.1.1 Introduction 28
     - 3.1.2 EPA Experimental Facility 28
     - 3.1.3 Bremsstrahlung Measurement 33
     - 3.1.4 Flux Measurements of the Total Energy 35
     - 3.1.5 Decay Times After Power Turnoff 35
     - 3.1.6 Radial and Axial Hall-Probe Scans 36
     - 3.1.7 Pinhole-Camera X-Ray Photographs 37
     - 3.1.8 "Quantized" Instabilities 37
   - 3.2 Experiments on the Electron-Cyclotron Plasma in the Physics Test Facility (PTF) 39
     - 3.2.1 Introduction 39
     - 3.2.2 Plasma Density Measurement by Microwave Interferometry at 8 mm 39
     - 3.2.3 Instability Measurements with Small Coils 40
   - 3.3 Determination of Spatial Distribution of Energy Density of the ECP in the PTF 40
     - 3.3.1 Results 42
     - 3.3.2 Conclusions 43

4. PLASMA PHYSICS 44
   - 4.1 Stabilized Plasmas 44

4.1.1 Introduction 44
4.1.2 Stability Criterion 44
4.1.3 Cold Plasma with Ioffe Fields 46
4.1.4 Cold Plasma in Cusp Fields 47
4.1.5 Hot-Electron Plasma 51

4.2 Measurement of Plasma Decay Time and Density with a Cavity Resonator 54

4.3 Further Measurement of Ionic Sound Wave Velocity in Plasma by a Time-of-Flight Technique 55

4.4 Observations of Discharge Tube Striations Using an Image Converter 59

4.5 Positive-Ion Current Compensation for the Automatic Converter Circuit for a Langmuir Probe 62

5. VACUUM ARC RESEARCH 63

5.1 Deuterium-Arc Studies 63
5.1.1 Introduction 63
5.1.2 Direct-Current Probe Measurements 63
5.1.3 Time-Resolved Probe Measurements 63
5.1.4 Discussion 66

5.2 Lithium Arc 67

5.3 Charge-Exchange and Energy-Transfer Mechanisms for Ions in the Energetic Carbon Arcs – Atomic Q Values 67
5.3.1 Introduction 67
5.3.2 Charge-Exchange Reactions 68
5.3.3 Discussion 69

6. CROSS SECTION MEASUREMENTS 72

7. PRODUCTION, ACCELERATION, AND INJECTION OF IONIC AND ATOMIC BEAMS 73

7.1 High-Current Ion-Beam Production and Injection 73

7.2 Ion-Source Development 76

7.3 Neutral Source Development 78

8. PLASMA THEORY AND COMPUTATION 80

8.1 Stability of ORNL Plasmas 80
8.1.1 Stable Hot-Electron Plasmas 80
8.1.2 Review of DCX Instabilities 81

8.2 The Effect of Finite Ion and Electron Temperatures on the Ion-Cyclotron Resonance Instability 84

8.3 Growth Rates of Electrostatic Instabilities in Mirror Configurations 86

8.4 Plasma Diffusion by Microinstabilities 87

8.5 Impurity Radiation in Hot-Electron Plasmas 88

8.6 Stabilization of Bounded Plasmas by Electron Streams and Arcs 89

8.7 Some Effects of a Magnetic Field on Coulomb Scattering 90

8.8 Studies of Energy Enhancement in DCX-2 91

8.9 Orbit Studies in a Ioffe Magnetic Field 91

9. MAGNETICS AND SUPERCONDUCTIVITY 100
9.1 A Study on Minimum *B* Confinement Fields 100
9.1.1 Application of Ioffe Bars to DCX-2 100
9.1.2 J. Andreoletti's Field Configurations 102
9.1.3 D. A. Baker's Coil Arrangement 104
9.2 The New Magnet Laboratory 105
9.3 A Study on Models of High-Field Superconductors 107
9.3.1 Introduction 107
9.3.2 Heinz London's Model of High-Field Superconductors 108
9.3.3 C. P. Bean's Model 110
9.3.4 Model of Y. B. Kim *et al.* 112
9.3.5 Measurement Methods 116
9.3.6 Acknowledgments 118
9.4 Magnetic Moment Measurements on NbZr Wires 118
9.4.1 Introduction 118
9.4.2 Experimental 119
9.4.3 Results 120
9.4.4 Discussion 120
9.5 Schemes for Winding Coils from Tubular Conductors 121
10. VACUUM SYSTEMS, TECHNIQUES, AND MATERIAL STUDIES 126
10.1 Ionization-Gage Characteristics at Vacuum-System Base Pressures 126
10.2 Mass Spectrometric Studies 127
10.3 Physical Adsorption at Liquid-Nitrogen Temperature 129
11. DESIGN AND ENGINEERING: SERVICE REPORT 130
PUBLICATIONS, PAPERS, AND TRAVELING LECTURE PROGRAM 131

Introduction

A. H. Snell

In the activities centered around DCX-1, the past six months have been unusually revealing, and have given us an opportunity for further development of our knowledge of the basic processes that cause the spreading of the plasma – knowledge that is required if we are to develop means to prevent it. The subject has now become refined and detailed, and one can attempt only a rather shallow excerpt of Sect. 1 of this report as an indication of what has been found.

Firstly, trapping by Lorentz dissociation of H_2^+ has been made to work successfully, and it turns out to be a rather beautiful technique, yielding much more trapping for an input beam of a few tenths of a milliampere than has been obtained with gas dissociation at 10 ma. In contrast with injection of neutral atoms, the small, controlled beam presents no disposal problem.

Secondly, the increased number of trapped particles has brought us to the unpleasant realization that already at a density of 10^8 fast protons trapped per cubic centimeter, we are up against a limitation caused by the plasma spreading. When you trap more particles, they simply occupy more volume; the density does not increase. We have reached 10^8 particles/cm^3 many times in the past using gas dissociation; it has been the Lorentz dissociation, enabling us to attempt to go beyond this, that has shown that plasma spread is stopping us much sooner than we had hoped. Furthermore, the spreading that was observed a long time ago at densities of 10^9 in DCX-1 when the carbon arc was used appears now to be not necessarily attributable to the arc, except insofar as the arc accelerated the trapping rate.

Thirdly, we can now see that at containment times longer than about 10 sec, there is appreciable particle loss by some mechanism other than charge-exchange.

Fourthly, suspicion is centering around the ion clusters as causative agents of the spread, the unclustered protons perhaps scattering in the charge fields of the clusters. The electron action (spitting out along lines of force) may be secondary, as is suggested by one experiment in which electron cyclotron heating suppressed the longitudinal electron action without eliminating the proton clusters.

Fifthly, the clustering is found where the orbits of the trapped protons are most ordered, suggesting again that more mixing would be beneficial.

Sixthly, electron cyclotron heating at about 25 w is found to have some beneficial effects; for example, it decreases the plasma potential markedly, but so far it has had only a mild effect on the spreading.

Seventhly, a low-frequency signal (3 to 12 kc) has been observed for the first time, possibly connected with a slow rotation; it has not yet been studied thoroughly.

Eighthly, the clustering usually disappears promptly when the H_2^+ beam is turned off; only occasionally are isolated bursts of rf activity seen during the course of the plasma decay. It would be an exaggeration to say that we have a coherent picture that explains these observations *en masse*, but experimental leads are apparent that may contribute to understanding after further investigation.

The application of improved diagnostic methods to DCX-2 has shown that our earlier appraisal of its performance was much too pessimistic. Moveable, energy-sensitive detectors (Sect. 2.2) have yielded a map of the confined plasma (Fig. 2.8) that shows the zones occupied by the trapped proton population as the energy spreads up and down from the injected 300 kev. The bursts of escaping ions that had been seen on the gridded

probes, and which were partly the cause of our earlier evaluation, are presumably still there, but as a loss mechanism they are now known to be minor in comparison with charge-exchange. A reconciliation has still to be made with the shape of the decay curve (Sect. 2.3), but the picture given by the energy-sensitive detectors is so complete and coherent that it is hard to see how the peak particle density of 2×10^{10} fast protons per cm^3 can be wrong—this with an input H_2^+ beam of about 38 ma that is about 30% dissociated on a lithium arc.

There is some interest in comparing the peak density of 2×10^{10} in DCX-2 with old results in DCX-1. In the past, when the carbon arc was used in DCX-1, mean densities in the range 10^9 to 10^{10} cm^{-3} were repeatedly reported,[1] with H_2^+ injection currents of about 5 ma and containment times of a few milliseconds. Thus, the DCX-2 densities with the lithium arc are somewhat higher, although per milliampere of injected beam they are no greater than DCX-1 with the carbon arc. This probably means only that DCX-2 has not yet reached its full potentialities.

In the electron cyclotron heating studies, a major advance has been a tenfold scale-up in both volume and power (Sect. 3.1). This was accomplished for economy's sake in an existing vacuum-magnetic apparatus called EPA. The main answers sought by the experiment have already been obtained; they are: (1) for the same microwave power input per unit volume one obtains the same energy density as was obtained in the smaller PTF apparatus, (2) the larger plasma is more stable than the smaller one, in the sense that the proper combination of operating parameters is far less tricky to attain. Refined bremsstrahlung measurements give a hot-electron density of about 5×10^{11} e/cm^3 in EPA, and an electron temperature of 120 kev; combined, these yield a steady-state beta of 0.4. This is approximately corroborated by the flux change upon turnoff registered in a coil that encircles the plasma, which indicates a beta of 0.3. Plasma decay times are consistent with these density and temperature figures on the basis of electron-electron collisions. The energy stored in the plasma is some hundreds of joules.

An odd observation on EPA concerns the x-ray bursts that occur when the gas feed is reduced below the rate required for stability. The bursts are rather uniform in size, small bursts not being seen. In this mode of operation, the x-ray emission from EPA can be quite dangerous despite the lead shield.

Meanwhile, a few experiments have been continued on the smaller hot-electron plasma in PTF. As noted earlier, measurements of density by means of microwave interferometry have disagreed with everything else; it is now found that this is true for 8 mm microwaves as well as 4 mm microwaves, the interferometer yielding density values 3 to 10 times lower than the other measurements (Sect. 3.2). Another experiment involved the dropping of a ball through the plasma while simultaneously observing x rays axially and in the midplane, and $d\phi/dt$ in a surrounding coil. The result confirmed that high-energy electrons occupy space around the plasma, but showed that these electrons do not hold the main energy content of the plasma (Sect. 3.2.4).

One of the important events of the last six months was the emergence of the "magnetic dimples" as a promising confinement concept; the public awakening occurred at the Fontenay-aux-Roses Study Group on Magnetic Mirror Confinement in July, but, taking a cue from Russian work, we had already started some small experiments to test the confinement capabilities of such arrangements in comparison, for example, with conventional mirrors. The results of some of this work are presented in Sect. 4.1. The indications are that the multipole fields can reduce noise and improve confinement, that hot electrons also help, and that the quadrupole configuration of our "Elmo," variously called a "folded" or "split cusp" (or in the hinterland a "caulked picket fence"), looked as good if not better in these rather limited tests. We had also been considering the application of Ioffe bars to DCX-2 before its real performance was realized; examples of equal-$|B|$ surfaces and orbits for quadrupole Ioffe bars on DCX-2 are given in Sects. 8.9 and 9.1.1. The equal-$|B|$ surfaces for two other magnetic dimple configurations were also worked out using existing codes; the results are given in Sects. 9.1.2 and 9.1.3.

[1]See, for example, ORNL-2693, p. 8, Jan. 1959; ORNL-2926, p. 22, Jan. 1960; *Proc. Fourth Intern. Conf. Ionization Phenomena in Gases, Uppsala, 1959*, p. 997 (North-Holland, Amsterdam, 1960); *Nucl. Fusion* 1, 266 (1961).

Developments in plasma physics include a reconciliation of plasma sweeper and resonant cavity measurements of plasma density (Sect. 4.2), the discovery of moving striations in the positive column of rare-gas discharges and their tentative identification with ionic sound (Sect. 4.4), and the measurement of ion sound wave velocities by time of flight (Sect. 4.3). A noteworthy development was the recognition and characterization of flutes on the deuterium arc (Sect. 5.1); these flutes apparently solve a long-standing mystery as to the mechanism of the escape of deuterium from the arc, but more importantly, their presence in such a convenient apparatus as the Gas Arc Facility gives us a means of study that may be most instructive inasmuch as there is a good body of theory available for comparison and guidance. If the flutes can be controlled, hope might revive in the deuterium arc as a rather ideal dissociator or ionizer for use in high-energy injection.

Among the activities of the theoretical group, there have been calculations of general interest, such as those that deal with growth rates of instabilities (Sect. 8.3), diffusion across magnetic fields (Sects. 8.4 and 8.7), and energy loss by radiation from plasma impurities (Sect. 8.5). Subjects more particularly directed with local experimentation include a continuing examination of the DCX instabilities (Sects. 8.1, 8.2) and the stabilizing effects of electron streams and arcs (Sect. 8.6).

The new Magnet Laboratory has been placed in service with two dc solenoids that yield 60 and 90 kilogauss respectively in volumes 6 in. in diameter (Sect. 9.2). Some of the first experiments consisted of magnetization measurements on superconducting cylinders in longitudinal magnetic fields. With a soft superconductor, a rectangular loop approaching the ideal (Fig. 9.8) was obtained when end effects were properly cared for. With a hard superconductor, satisfactory loops were obtained up to 60 kilogauss (Fig. 9.11), and values of two parameters of the theory were obtained from them. Since the experiment used 25 strands of NbZr wire in parallel, it was less sensitive to wire imperfections than would be an experiment that uses a single strand.

Such is a summary of an active half-year. Some aspects of the immediate future course are clear; DCX-2, for example, requires time for further experience. The hot-electron plasmas should be probed with energetic beams of neutral atoms, Elmo should be reactivated both with electron cyclotron heating and with neutral atom injection, the electron cyclotron heating should be forced toward higher magnetic fields, magnetic dimples should continue to be scrutinized in various ways, and the increasing interplay between DCX-1 and DCX-2 should be encouraged – all of this with a continuance of the basic physics in theory, plasma physics, superconductivity, and cross section measurements. In DCX-1, immediate requirements call for an identification of the new particle-loss mechanism that is seen when containment times are long, and the role of the clusters needs to be more quantitatively understood. In any high-energy injection scheme with organized orbits, growth of clusters would seem to be inevitable once dissociation of H_2^+ upon trapped H^+ starts, because any small lump will feed itself preferentially from the molecular ion beam. Accordingly, one would either have to avoid the lumps by using mixed-up orbits, or impose a confinement strong enough to hold even a lumpy plasma. It may be that long-range thinking will suggest a rather drastic modification of DCX-1.

Abstracting Summary

1. DCX-1 PLASMA EXPERIMENTS

The mechanical configuration of the DCX-1 facility was changed in only minor respects during this report period. As a function of operating pressure, three characteristic rf modes are defined: (1) the high-pressure mode; (2) the intermediate or flare mode; and (3) the low-pressure or burst mode. In mode (1), median-plane magnetic probes show only B_z signals that are appropriate for the motion of proton clusters. In modes (2) and (3), B_θ signals are also observed, and these are found to be correlated with the pulse-like ejections of electrons out of the mirrors and with sudden increases in the plasma potential. The first observed low-frequency rotational phenomenon is reported. This is an intermittent modulation of the electron current out of the mirrors at frequencies of about 3 kc, 10 kc, or mixtures of the two. The initiating disturbance appears to be rotating in the direction of ion rotation at about 3 kc. There is also evidence for a modulation of plasma potential at these same frequencies.

The effects of adding electron-cyclotron heating at microwave power levels up to 20 w are described. Heating in a resonant zone that includes the proton stable orbit results in a partial suppression of low-pressure rf B_θ signals and of the associated electron ejections, and in a significant reduction in plasma potential. The z scattering of the protons is decreased only slightly; the effect is to increase the central proton density by about 10%. Experiments with Lorentz-force trapping were extended to higher injection currents and longer containment times. They indicate a limiting central proton density of about 10^8 cm^{-3}, and suggest that the collective interactions limit the total number of stored protons as well. It is believed that the scattering of the plasma under some conditions in these experiments was enough to cause significant loss due to collisions against the radial walls.

2. DCX-2

Improvements in diagnostic procedures have shown that the trapped plasma in DCX-2 is more dense than had previously been thought, and that there is little loss other than by charge exchange. Typical figures, using a lithium arc as dissociator, are: 2×10^{15} particles trapped, peak density of fast particles 2×10^{10} cm^{-3}; input beam 30 ma, which is 30% dissociated in the arc; base pressure 10^{-7} torr, seriously modified by arc and plasma pumping. The decay times are about 14 ms – a provisional figure because the shape of the decay curve is not yet understood. There is no slow rotation. Details are given of diagnostic procedures, analysis, plasma pumping, and radio-frequency signals observed under various operating conditions. A hydrogen arc has also been used as dissociator.

3. ELECTRON-CYCLOTRON HEATING

The scale-up of the electron-cyclotron plasma has been completed and operated in the EPA facility. The plasma is created in a 3:1 magnetic mirror field by a 10.6-Gc microwave power source capable of delivering 50 kw CW. Preliminary results show that the plasma volume is $\sim$40 liters and contains several hundred joules of stored energy with 25 kw CW microwave power. Other interesting properties of the plasma relevant to the scale-up are described.

An experiment involving the measurement of the radial energy density distribution of the ECP has been performed in the Physics Test Facility. Also, further microwave interferometry measurements have been performed, and some interesting measurements on the plasma instabilities have been performed with small coils.

4. PLASMA PHYSICS

Several combinations of magnetic cusps and mirrors were evaluated for their ability to contain cold plasma. Plasma noise and density were measured. The plasma was considered stable if its loss rate was not greater than that permitted by ion-ion multiple scattering. Cusps were found to be stable and their loss rates could be reduced by bending the cusp annulus with added axially parallel uniform field. A plasma containing electrons at 25 to 100 kev temperature was found to be stable in a simple magnetic mirror configuration.

The discrepancy previously observed in measurements of plasma density using a resonant cavity as compared with measurements using a "plasma sweeper" is now apparently understood.

Further experiments concerning the time-of-flight technique of measuring ionic-sound-wave velocity support our earlier work as well as reveal interesting new phenomena, such as reflections.

Extensive use has been made of a modified Snooperscope (a fast stroboscopic, image-converting device) to study moving striations of light in the inert gases in cylindrical discharge tubes. Present evidence suggests that the striations are produced by ion waves propagating down the tube.

A simple addition has been made to the original converter circuit which allows correction to be made for the collection of positive ions (automatic converter circuit).

5. VACUUM ARC RESEARCH

The magnetically constrained, high-density deuterium arc plasma has been shown previously to be highly ionized and relatively quiescent. It appeared to be a good plasma for the study of plasma diffusion across a magnetic field in the regime where only charged-particle collisions were important. However, Langmuir probe measurements of the region outside the main arc plasma indicate that the particle transport across the magnetic field is dominated by flutes generated by the main arc plasma. The flutes, with a cross-sectional area of about 0.2 cm^2, apparently extend the full length of the arc through a 2:1 magnetic mirror. The flutes have both radial and azimuthal velocities of 1 to 5×10^5 cm/sec across the magnetic field which are dependent on the magnetic field strength, the arc current, and the radius at which the measurement is made.

The heating and energy mixing of ionic species of energetic carbon arcs are discussed qualitatively in terms of ion-ion charge-exchange reactions and other contributing mechanisms.

Improvements in the electrode configurations of the lithium arc are described.

6. CROSS-SECTION MEASUREMENTS

Improvements in apparatus and the revision of the "σ CTR" compilation have occupied this report period.

7. PRODUCTION, ACCELERATION, AND INJECTION OF IONIC AND ATOMIC BEAMS

The 600-kv high-intensity beam test stand has delivered up to 95 ma of H_2^+ ion current through a 4-cm aperture located 350 cm from the ion source. The previously observed current limitation of 60 ma proved to be a decreased relative production of H_2^+ ions in the duoplasmatron ion source. This limitation was improved by small changes in the geometry of the source. The DCX-2 injector system, which has several operating requirements not included in the 600-kv test stand, may be limited to an injected H_2^+ current of only 40 ma. Since the calorimetric beam accountability is only 80% of the drain on the supply, it is not certain that the injected current is really this low. Modifications in the epoxy "skirts" have continued to improve the voltage holding capacity of the 600-kv accelerating column on the atmospheric side.

A hollow-cathode arc ion source has been satisfactorily operated at 30 kv in an assembly which will permit comparison of neutral beam production from either a gas cell or another hollow-cathode discharge. A total hydrogen ion beam of 35 ma has been attained with a divergence angle of 10°.

8. PLASMA THEORY AND COMPUTATION

The correspondence between hot-electron and hot-ion plasmas generated in our experiments and the predictions of stability theory is summarized. Stability of hot-electron plasmas generated by cyclotron heating is attributed to conductivity to end walls by cold plasma, and possibly to other stabilizing effects of the low-energy component of the plasma continually replenished by ionization of the large neutral gas background found to be

necessary for stable operation. In the DCX experiments, enhanced energy and spatial diffusion (in DCX-1) are attributed to charge-bunching, for example, by ion-electron microinstabilities as suggested by Harris. The development of Harris's theory is reviewed. It is argued that flutes and other macroinstabilities are ruled out by finite orbit effects.

In another section, the values of density and magnetic field such that a two-temperature ion distribution is stable against the Harris instability are mapped for various ratios of temperature parallel and perpendicular to the magnetic field.

A previously developed technique for obtaining exact upper bounds on growth rates of instabilities has been applied to configurations confined in mirror machines. The fastest growth is that of Harris's electrostatic streaming instabilities.

The same technique is used in obtaining bounds on growth rates which are then employed in setting a lower bound on the diffusion time across a magnetic field. It is found that, for practical purposes, confinement of quite dense plasmas, if they are several (e.g., 10) ion gyro-radii across, is not limited by cross-field diffusion, even if microinstabilities are present. The implication is that closed containers designed for macrostability, such as the toroidal multipole, should be stable in practice.

Effects on hot-electron plasmas of energy loss by radiation following collisional excitation of impurities have been calculated. Qualitative agreement is obtained with experiments in which xenon was introduced into the PTF hot-electron plasma.

A new approach to stabilization of bounded plasmas by electron streams has been undertaken. Shortcomings of an infinite plasma theory applied to this problem necessitated the new approach – that of considering the system as a finite, bounded plasma. Results for various boundary conditions are being investigated.

In electron-electron and electron-ion collisions, the presence of a strong magnetic field theoretically is shown to impede the transfer of energy from the direction parallel to the field to the perpendicular directions.

Preliminary phenomenological fits to data for energy diffusion in DCX-2 by microinstabilities give diffusion times a factor 10^7 to 10^8 shorter than Coulomb diffusion, but $\sim 10^4$ longer than the microinstability growth time.

A study of H_2^+ and H^+ orbits in a four-pole, infinite Ioffe bar field added to the standard DCX-2 field has begun. Particles initially near a bar are found to be lost in a few microseconds.

9. MAGNETICS AND SUPERCONDUCTIVITY

Theoretical and experimental work seems to demonstrate the merits of so-called "absolute *B* minimum field configurations" for plasma containment. Various analytical solutions have been presented recently; however, very few numerical data of the field quantities concerned have been published to date. We studied, in detail, the following special cases: The magnetic field resulting from the superposition of a quadrupole field ("Ioffe bars") and the regular magnetic field of DCX-2; three cases of field configurations produced by an axisymmetric coil arrangement suggested by J. Andreoletti; and finally, we made a numerical analysis of a field configuration due to two infinitely long current loops as described by D. A. Baker. Only the Ioffe bar arrangement produces a relatively large increase of the magnitude of *B* around the field axis in the zone of interest.

During several years, an appreciable number of magnet coils have been built in this division for producing a great variety of magnetic field shapes. The standard design of such magnet coils consists of "pancakes" of hollow, water-cooled copper conductors. Since the rated currents of the available dc generators are large (5000 to 8600 amp), the cross sections of the copper conductors must also be large, and therefore the surface of coils made up of such pancakes consists of cylindrical parts with radii and axial lengths varying in relatively large steps. For special purposes, much smoother surfaces are very desirable. A new method is described which permits the building of magnet coils with considerably improved surfaces without disadvantages with respect to simplicity and reliability of the design.

During the last report period the new magnet laboratory went into full operation. This laboratory serves for developmental work on conventional and superconducting magnet coils and consists presently of one magnet coil for 60 and another for 90 kilogauss (3 and 6 Mw dc, respectively), both with a working diameter of $6\frac{1}{2}$ in. Furthermore, a 50-kilogauss superconducting magnet coil is available. Necessary regulated current sources

and ample instrumentation for experiments with high-field and soft superconducting materials are provided. This magnet laboratory, which is one of the largest of its kind, could be built with relatively low costs, since the large dc power supplies of the Thermonuclear Division were available.

An extensive systematic study was made on models of high-field superconductors proposed by H. London, by C. P. Bean, and by Y. B. Kim *et al.* Sets of equations for tube magnetization and magnetic moment curves have been derived which are more comprehensive than those previously published. Furthermore, a measurement method for simultaneous investigations on tube magnetization and magnetic moment of high-field superconductors is described. Finally, magnetic moment measurements of bundles of NbZr wires are reported which gave well-reproducible results for complete magnetization cycles. These results are compared with calculated curves based on the model of Kim *et al.*, and the connection with the flux-creep theory applied to a comparable case is discussed.

10. VACUUM SYSTEMS, TECHNIQUES, AND MATERIALS

Results from a study of ionization gage sensitivity as a function of emission current has led to a method of determining the presence of gage contributions of gas or of pumping. Low-energy (30 v) electron ionization of organic compounds has been found to simplify significantly the mass spectra of hydrocarbon components of a vacuum system.

1. DCX-1 Plasma Experiments

J. L. Dunlap
R. S. Edwards
G. R. Haste
L. A. Massengill
C. E. Nielsen[1]
Herman Postma[2]
L. H. Reber
R. G. Reinhardt
W. J. Schill
E. R. Wells

1.1 INTRODUCTION

The mechanical configuration of the DCX-1 facility was changed in only two minor respects during this report period. A new high-vacuum liner with a circular cross section (radius = 11 in.) was installed. With the usual assortment of probes and titanium evaporators in position, this change has increased the allowable radial extent of the plasma in the median plane from 7 to 9 in. In addition, the injection system was slightly altered, and this change is described in Sect. 1.5.

Recent experiments have defined three characteristic modes of rf activity and have yielded more information about the correlations between several plasma parameters and this activity. The investigations of the effects of adding electron cyclotron heating were resumed. Studies of the properties of plasmas established by Lorentz-force dissociation of H_2^+ were continued and extended to larger injection rates and longer containment times than those previously reported for such plasmas. The details of these experiments and summarizing interpretations in terms of the collective behavior are given in the following sections.

1.2 RADIO-FREQUENCY MEASUREMENTS

For several years these reports have described the continuing development of probes and techniques for separating plasma rf signals into the various electric- and magnetic-field components. In this section we describe the equipment with which our more recent data have been obtained and illustrate the characteristic rf modes that have been found.

Figure 1.1 shows the "crown" probe employed. The two loops are at right angles and the grounded conductor goes to the center of the loops. At the proton cyclotron frequency (14 Mc) the impedance to ground through this conductor is several ohms inductive; this reactance is small enough to reduce the electric pickup to a level comparable with the magnetic. The probe is usually mounted so that the plane of one loop (the "0° loop") is parallel to the median plane. This loop is then sensitive to changes in B_z, and the other (the "90° loop") is sensitive to changes in B_θ. Both loops respond to changes in all electric fields, but most strongly to changes in E_r.

The separation of electric and magnetic responses and the required amplification are provided by the equipment shown in Fig. 1.2. In the plus mode, in-phase signals at the two ends of a probe loop are added while out-of-phase signals are subtracted, so that in this mode the system responds to electric field. In the minus mode, out-of-phase signals are added and in-phase ones subtracted, so the system then responds to magnetic field.[3] The degree to which the system separates electric and magnetic signals is frequency dependent. At 14 Mc the ratio of the desired signal component to the undesired is

[1]Consultant from Ohio State University.

[2]Presently on leave at FOM Institute voor Plasma Fysica, Rijnhuizen, Jutphaas, Netherlands.

[3]We are grateful to R. A. Dandl and H. O. Eason for pointing out to us the phase-inverting characteristics of the 460 B amplifier.

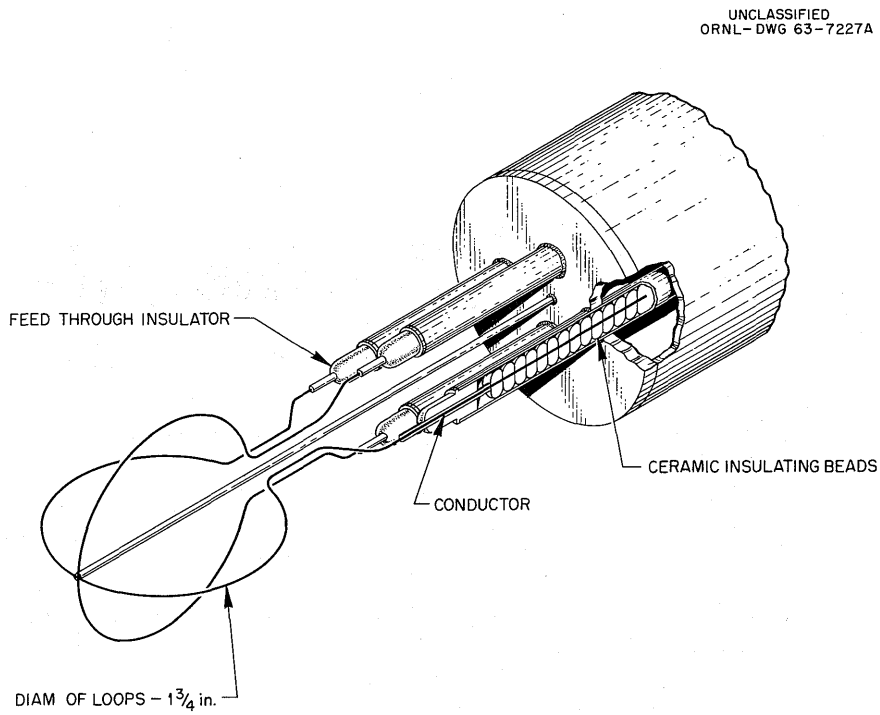

Fig. 1.1. Schematic Diagram of RF Probe.

enhanced by a factor of about 50; at 28 Mc the factor is from 5 to 10. Oscilloscopes with adequate response up to 80 Mc have occasionally been used to examine the output wave form and have shown relatively little activity above 28 Mc. The data presented here were obtained with oscilloscopes whose responses fall off rapidly above 30 Mc.

Our most thorough studies of the rf mode changes have been made by varying the background pressure when operating with gas dissociation of modest H_2^+ beam currents. There are substantially less complete observations of the effects of changing the injected current, of shifting the H_2^+ beam away from the usual median plane trajectory, of applying large dc bias potentials to end walls, etc., but these effects are not considered here.

There are three rf modes which we classify as (1) the high-pressure mode, (2) the transition or flare mode, and (3) the low-pressure or burst mode. As a function of pressure, at least, the transitions between modes are gradual.

The high-pressure mode, which is illustrated in Fig. 1.3, has been described in detail in a previous report.[4] In this mode both electric and magnetic probes indicate azimuthal clustering of circulating protons. During the initial portion of the rf build-up which follows injection of the H_2^+ beam, the

[4] *Thermonuclear Div. Semiann. Progr. Rept. Oct. 31, 1962*, ORNL-3392, p. 9.

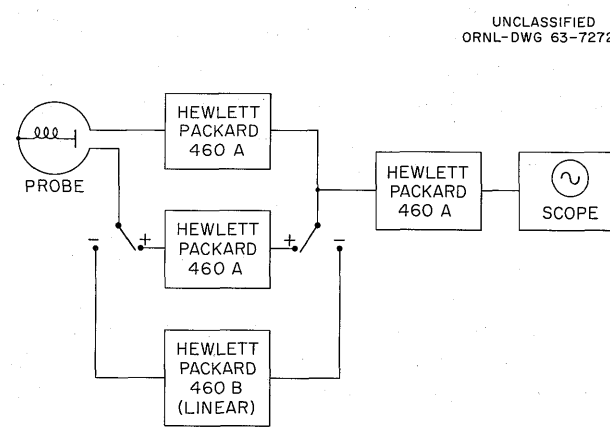

Fig. 1.2. Block Diagram of RF Equipment Used in DCX-1 Experiments.

UNCLASSIFIED
ORNL-LR-DWG 73359

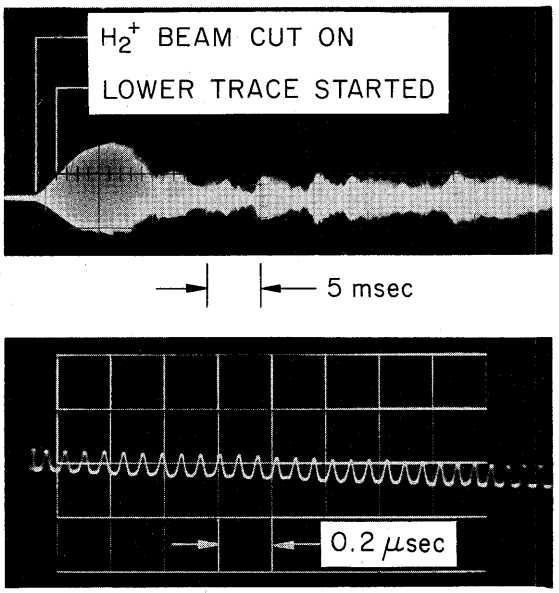

6 ma H_2^+, 4×10^{-7} torr, PROBE I IN A+B

Fig. 1.3. Signals from a Probe System Sensitive to Changes in the Radial Component of E.

UNCLASSIFIED
PHOTO 63464A

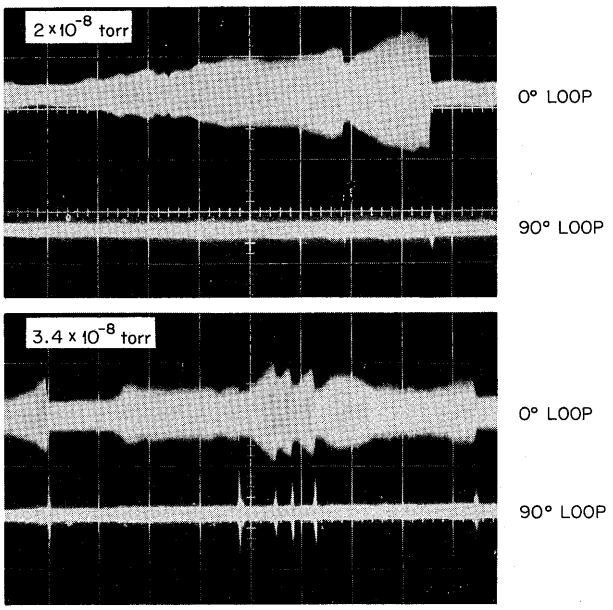

20 msec/cm

Fig. 1.4. Pressure Transition for Flare Mode RF Activity as Observed with Median-Plane Magnetic Probes. 1.5 ma H_2^+.

wave form is appropriate for the rotation of a single charge clump. The time scale for this rf buildup is such that the buildup cannot be regarded as an instability growth that could be calculated in a linear theory. At about the peak of the rf buildup, additional harmonic content appears as additional clusters are formed. In the steady state, beat frequencies in the order of 100 kc arise due to the presence of clusters with slightly different rotational frequencies. No magnetic signals are received by 90° loops in the median plane; when displaced, the 90° loops respond to changes in the B_θ component of the proton clusters. An example of the beating patterns is given in Fig. 1.6.

Figure 1.4 shows examples of the flare mode, which is restricted to a narrow pressure region. We believe that the 0° loop patterns are still those for simple proton clumping as in the high-pressure mode, but this belief has not been adequately confirmed. The frequency composition of the spikes in the 90° loop signal was determined several times in one run. They were about 25 Mc – not commensurate with the proton cyclotron frequency.

Low operating pressures yield the burst mode illustrated in Fig. 1.5. Fast sweeps of the 0° loop

UNCLASSIFIED
PHOTO 63463A

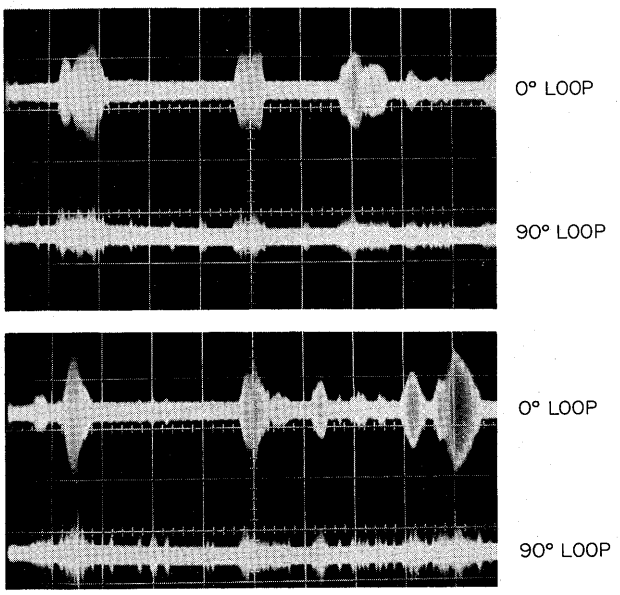

0.1 sec/cm

Fig. 1.5. Slow Sweep Median-Plane Magnetic Probe Signals with Burst Mode RF Activity. 2 ma H_2^+, 3.9×10^{-9} torr.

signals show them to be the proton cyclotron frequency, but the frequency of the 90° loop signals has not been measured. Figure 1.5 indicates a time correlation between the general levels of the signals from the two loops, and this correlation has been a consistent feature of data obtained during the present report period. However, some earlier measurements[5] have yielded 0° and 90° signals similar to these but uncorrelated in time.

Radio-frequency observations have been made at low pressures while operating with Lorentz-force trapping. While these investigations have not been as thorough as those employing gas dissociation described above, the data now available indicate that the basic features of the rf mode are independent of the trapping mechanism.

1.3 SLOW PLASMA, LITHIUM BEAM, AND RF CORRELATIONS

An earlier report[6] described a number of experiments which at low operating pressures showed time correlations between rf signals, fluctuations in the slow plasma currents out of the mirrors, and fluctuations in the plasma potential. It appeared that the unstable activity that produced the rf signals increased the electron heating rate, and that this resulted in the ejection of electrons from the plasma, thereby causing a momentary increase in the plasma potential.

In later investigations of these same phenomena, we have used the rf probe techniques that allow a more complete separation of polarizations, and have used cathode follower couplings that permit a faster time resolution of the fluctuating slow plasma and lithium-ion-beam[7] currents. The slow plasma was collected by a 12-in.-diam plate which was divided into 60° sectors that could be individually biased. This collector was centered at one mirror with the plane of the collector parallel to the median plane. The other end wall was at ground potential. The lithium beam trajectory passed through the median plane at the stable orbit radius and terminated at one of the collecting sectors.

In the high-pressure rf mode an integrating slow plasma detector shows end-plate potential variations that are correlated with beat frequency patterns in the 0° loop signal (Fig. 1.6). At the sweep rates required to display this correlation, the present equipment does not permit distinction between charge collection and capacitive coupling to a fluctuating plasma field. Fast time sweeps of the potential trace show that the line breadth (particularly evident in the lower oscillogram of Fig. 1.6) is due to 14 Mc modulation.

At lower pressures rapid ejections of electrons were again observed. Simultaneous displays of slow plasma currents and signals from a median-plane magnetic probe show these electron pulses to be most closely associated with the signal from the 90° loop. Figure 1.7 illustrates this association for flare mode activity and Fig. 1.8 for burst mode activity. On faster sweeps, the most rapid increases in electron current can be observed to occur with a time constant of a few microseconds. Comparisons of current traces to sectors operated at different bias (Figs. 1.9 and 1.10) indicate that

UNCLASSIFIED
PHOTO 63469A

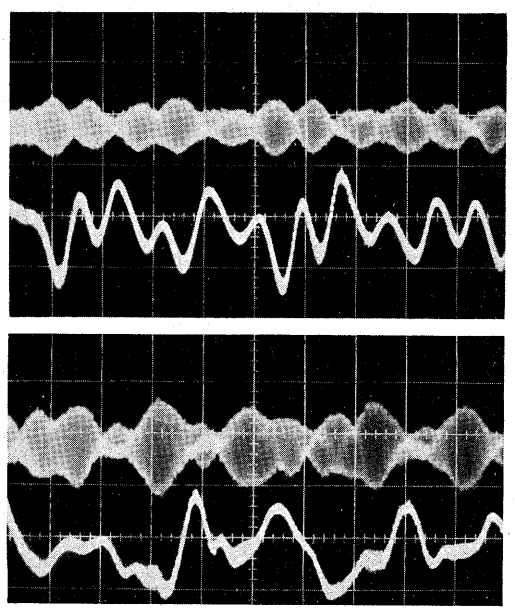

Fig. 1.6. End Wall Potential and High-Pressure RF Beating Pattern of Median-Plane Electrical Probe. 1.75 ma H_2^+, 2.2×10^{-6} torr.

[5] *Thermonuclear Div. Semiann. Progr. Rept. Oct. 31, 1962,* ORNL-3392, p. 9, Fig. 1.12.

[6] *Thermonuclear Div. Semiann. Progr. Rept. Oct. 31, 1962,* ORNL-3392, p. 3.

[7] The use of a lithium-ion beam for plasma potential measurements was first discussed in *Thermonuclear Div. Progr. Rept. Oct. 31, 1961,* ORNL-3239, p. 6.

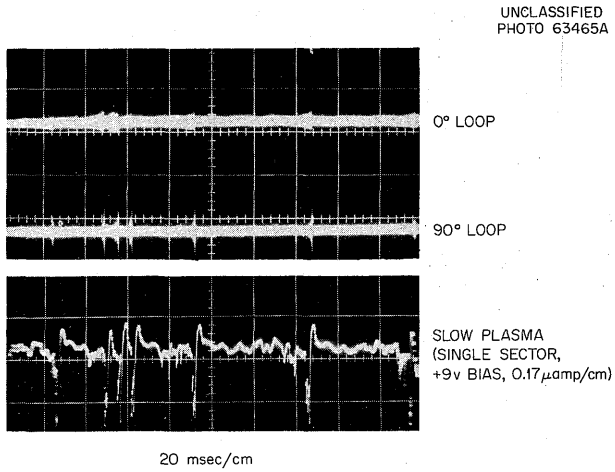

Fig. 1.7. Steady-State Response of Median-Plane Magnetic Probes and Slow Plasma Current with Flare Mode RF Activity. 1.6 ma H_2^+, 7×10^{-9} torr.

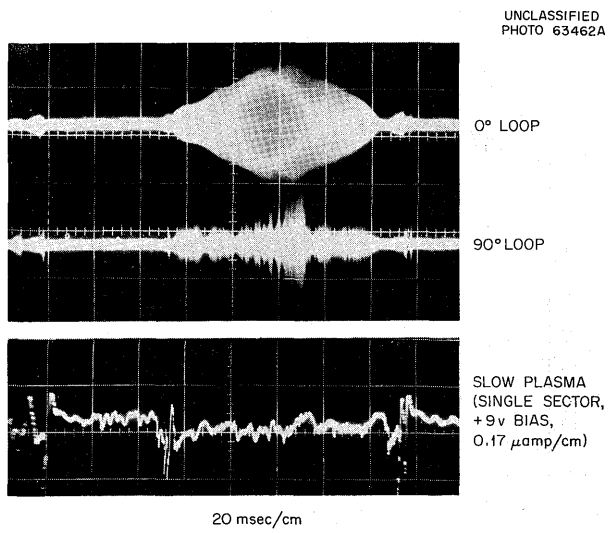

Fig. 1.8. RF Signals from Median-Plane Magnetic Probes and Slow Plasma Current for Burst Mode RF Activity. 1.6 ma H_2^+, 7×10^{-9} torr.

the electron current ejected in short pulses is relatively sensitive to a range of variation of a few volts about zero bias. From these observations it appears that these electron pulses consist almost entirely of electrons arriving at the collector with less than 27 ev energy. Nevertheless, at least under some conditions of operation, the average slow plasma current to a 27 v negatively biased plate also is correlated with the occurrence

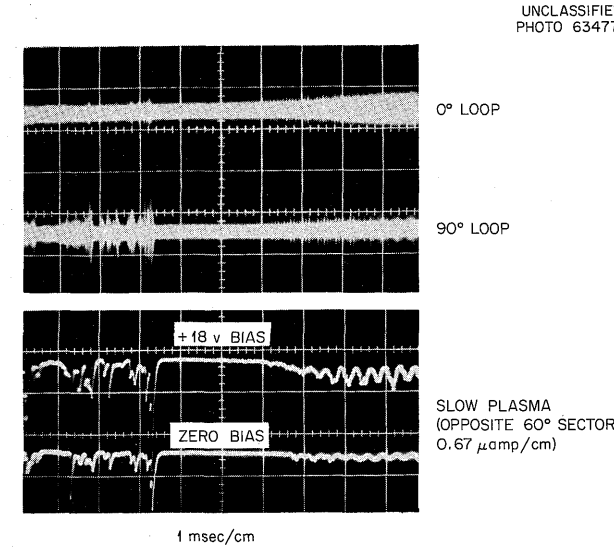

Fig. 1.9. Median-Plane Magnetic Probe Signals and Slow Plasma Currents to Sectors with Different Bias. 2 ma H_2^+, 4×10^{-9} torr.

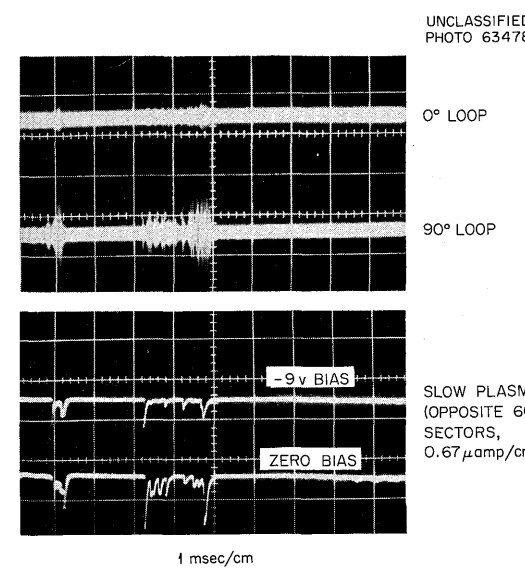

Fig. 1.10. Median-Plane Magnetic Probe Signals and Slow Plasma Currents to Sectors with Different Bias. 2 ma H_2^+, 4×10^{-9} torr.

of the 90° loop signals (Fig. 1.11). (Note that Fig. 1.11 compares two events; simultaneous observations of the same event yield similar results.) The current polarities are such that a decrease in slow ion current may be involved in these observations.

UNCLASSIFIED
PHOTO 63479A

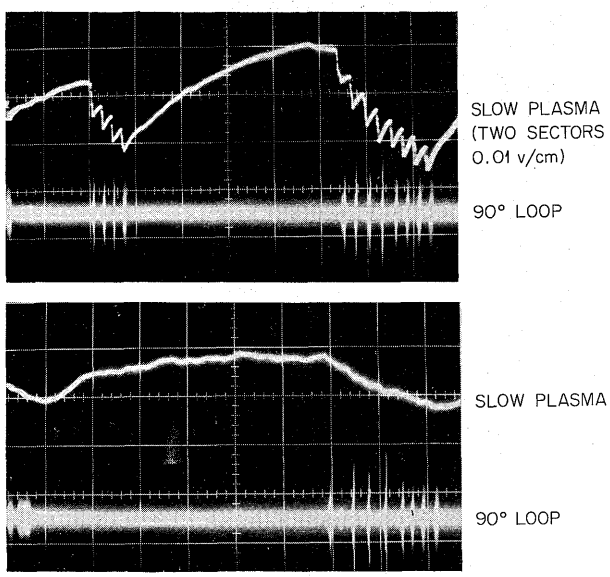

Fig. 1.11. RF Signal from Median-Plane Magnetic Probe and Slow Plasma Signals to an Integrating Detector. 1.5 ma H_2^+, 8×10^{-9} torr. The two oscillograms were not recorded simultaneously.

Comparisons of the slow plasma current traces to different collector sectors operated at the same bias (Fig. 1.12) show the expected gross correlations but also differences in detail that indicate a lack of complete azimuthal symmetry in the mechanism producing the current fluctuations.

The faster time resolution available in these recent experiments has permitted the observation of two phenomena not noted in our work of a year ago. The first is a low-frequency (kilocycles) modulation of the electron component of slow plasma which becomes noticeable a millisecond or so after the cessation of a series of electron pulses and which persists for a millisecond or so thereafter. The increase of oscillation amplitude with positive bias that denotes the oscillation as one in electron current is shown in Fig. 1.9. The oscillation frequency can be 2 to 4 kc (Fig. 1.9), 8 to 12 kc (lower oscillogram of Fig. 1.13), predominantly the lower frequency modulated by the higher (Fig. 1.14), or predominantly the higher frequency modulated by the lower (upper oscillogram of Fig. 1.13).

Radio-frequency traces that are associated with this oscillation are illustrated in Figs. 1.9, 1.14, and 1.15. Modulation patterns at 10 kc are present on the median-plane 0° loop and more clearly on the 90° loop where there is often a 3-kc modulation of the 10-kc patterns. The median-plane electric probe signal does not appear to have either frequency component, but this may be only the consequence of the frequency dependence of the probe response.

Measurements of the phase differences of the oscillating currents to different sectors (upper oscillogram, Fig. 1.13) show that the initiating disturbance is rotating at 3 kc in the direction of the proton cyclotron rotation.

The second new phenomenon was observed in studies of the fluctuations in the transmitted lithium-ion current. Figure 1.16 illustrates a typical response with burst mode rf signals. As usual, the rapid ejection of electrons that accompanies the rf activity increases the plasma potential and the transmitted beam current falls quickly to zero. The behavior of the current as the plasma potential recovers was, however, unexpected.

UNCLASSIFIED
PHOTO 63476A

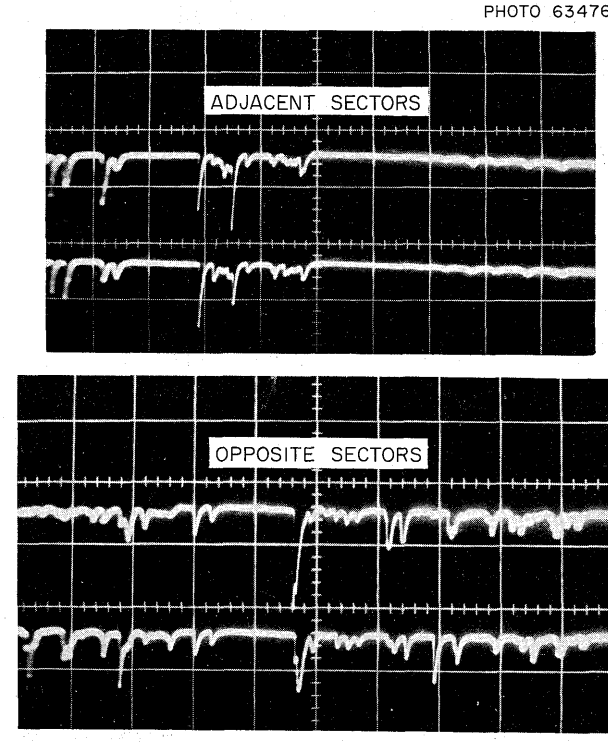

Fig. 1.12. Comparisons of Slow Plasma Currents to Different Sectors. 2 ma H_2^+, 4×10^{-9} torr, zero bias.

UNCLASSIFIED
PHOTO 63474A

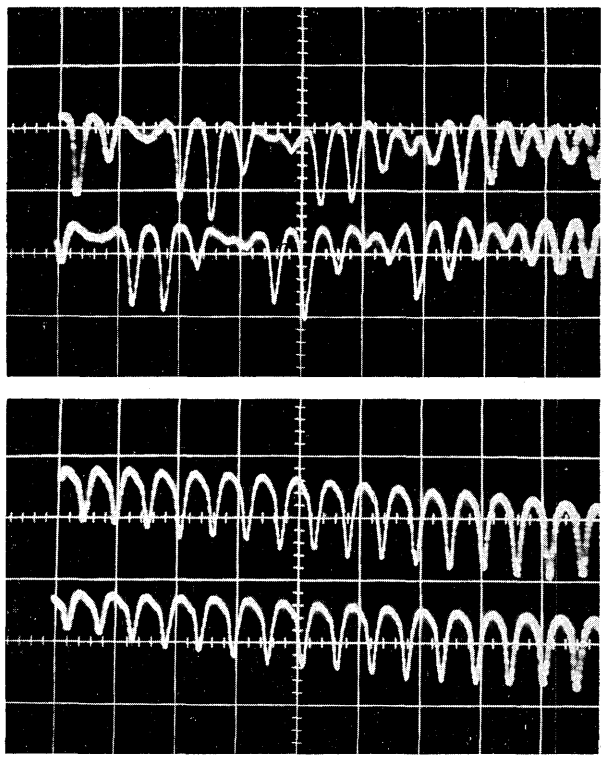

0.2 msec/cm, 0.17 μamp/cm

Fig. 1.13. 10-kc Ripple Patterns in Slow Plasma Currents to 60° Sectors, 120° Apart. 2 ma H_2^+, 4×10^{-9} torr, zero bias.

UNCLASSIFIED
PHOTO 63475A

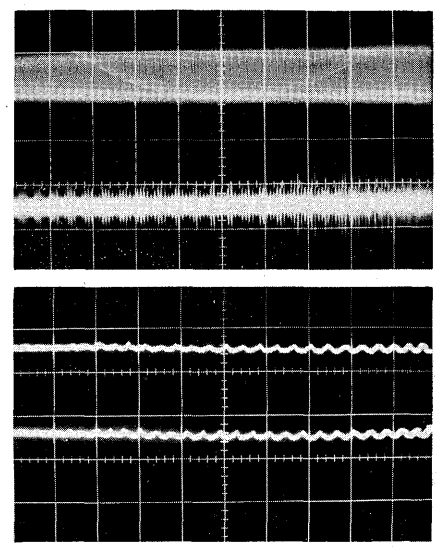

1 msec/cm

Fig. 1.14. 3-kc Ripple Patterns in Slow Plasma Currents with Median-Plane Magnetic Probe Signals. 2 ma H_2^+, 4×10^{-9} torr.

The current *gradually* builds up to full value, all the while modulated at a rate in the order of 10 kc. One identifies this modulation as a potential modulation associated with the 10-kc oscillations of the slow plasma current, but one must inquire why the potential fluctuations did not provide 100% modulation of the ion beam. (The current detectors used had a response time of a few microseconds.)

A possible explanation is that during the recovery interval the lithium beam current is being continuously modulated at megacycle rates, perhaps by the rotating potentials of the proton clusters. The combination of a slow (milliseconds) recovery in the time-averaged value of the potential, a 10-kc oscillating component of potential, and another component oscillating at about the same amplitude but at much higher frequency would result in the observed lithium beam trace. The

UNCLASSIFIED
PHOTO 63471A

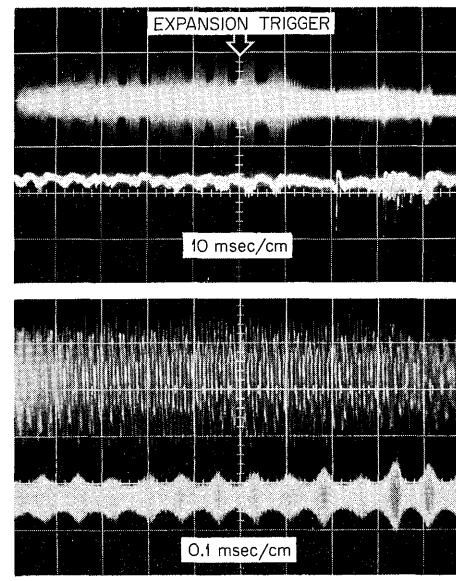

Fig. 1.15. Median-Plane RF Signals and Slow Plasma Current with Time Scale Expansion of the RF. 2 ma H_2^+, 7×10^{-9} torr.

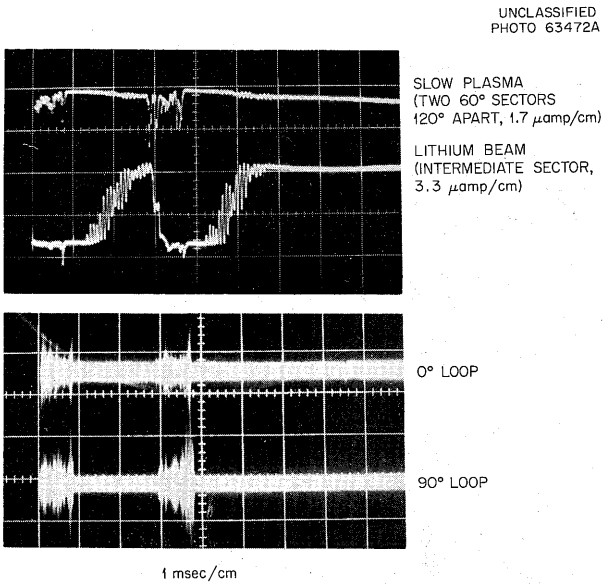

Fig. 1.16. Slow Plasma Current, Transmitted Lithium Beam Current, and RF Signals from Magnetic Probes on the Median Plane. 2.5 ma H_2^+, 5×10^{-9} torr.

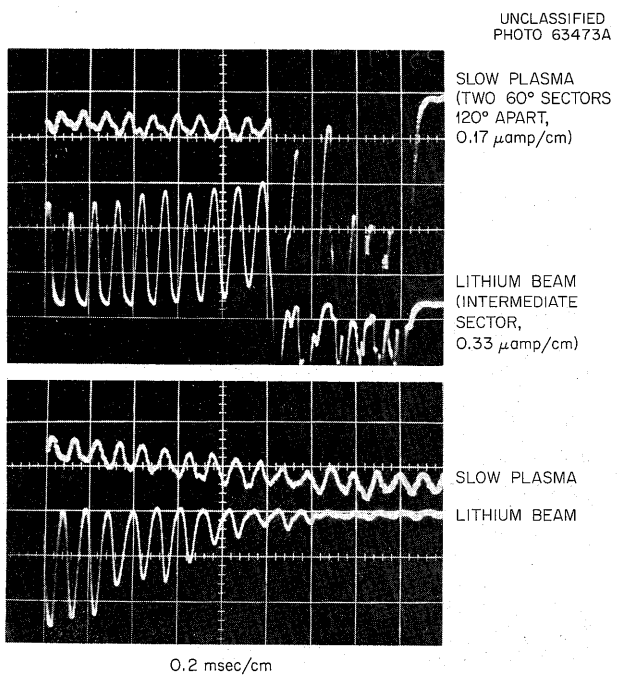

Fig. 1.17. 10-kc Ripple Patterns in Slow Plasma Current and Transmitted Lithium Beam Current. 2 ma H_2^+, 4×10^{-9} torr. An electron pulse occurred at 6 cm in the upper oscillogram. The progressive shift in phase relation is predominantly, if not entirely, due to characteristics of the dual-gun oscilloscope employed.

observed 10-kc beam oscillation would be associated with the oscillation of electron current out of the plasma in the vicinity of the ion beam, and the lithium beam should lag the slow plasma current by 90°. Figure 1.17 shows that the phase difference between the beam current and the slow plasma collected at the same azimuth is more nearly 180°. The difference in beam and electron velocities may introduce the additional 90° lag in the lithium beam trace.

Additional experiments are planned to determine the origin of the low-frequency oscillations and to evaluate the extent to which they influence the gross characteristics of the plasma.

1.4 ELECTRON-CYCLOTRON HEATING

Microwave power tubes have recently been used to irradiate the plasma contained in DCX-1. These tubes give a maximum power of about 25 w and are of the proper frequency to be used in conjunction with injection of 600-kev H_2^+. These tubes are thus of higher power and higher frequency than the tube used previously,[8] which required operation with 400-kev H_2^+.

The two tubes which were used had center frequencies of 26.6 kMc and 35 kMc. These frequencies correspond to the electron cyclotron frequency for magnetic field values of 9.6 kilogauss and 12.5 kilogauss, respectively. The regions for which the magnetic field has these values are shown in Fig. 1.18. Region 1 is the resonant zone for 26.6 kMc and includes the stable orbit for 300-kev protons. If heated in region 2, the resonant zone for 35 kMc, the electrons must travel along field lines if they are to reach the main plasma volume located near the midplane.

Several plasma parameters are altered when the microwave power is applied. The changes produced are much more evident, however, when using the lower frequency, which results in electron heating in the center zone. The following comments concern center zone heating.

One of the more marked changes produced is a reduction in the plasma potential, which was measured in the usual way, using the transmission

[8] *Thermonuclear Div. Semiann. Progr. Rept. Oct. 31, 1962*, ORNL-3392, p. 8, sect. 1.5.

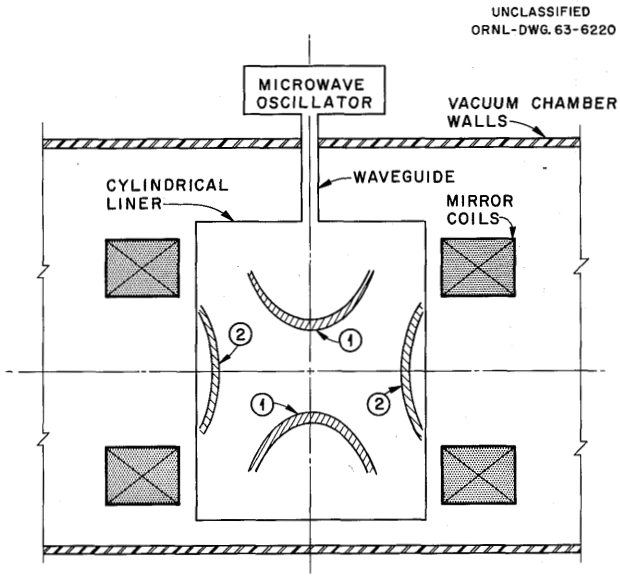

Fig. 1.18. Schematic of Microwave Heating Zones.

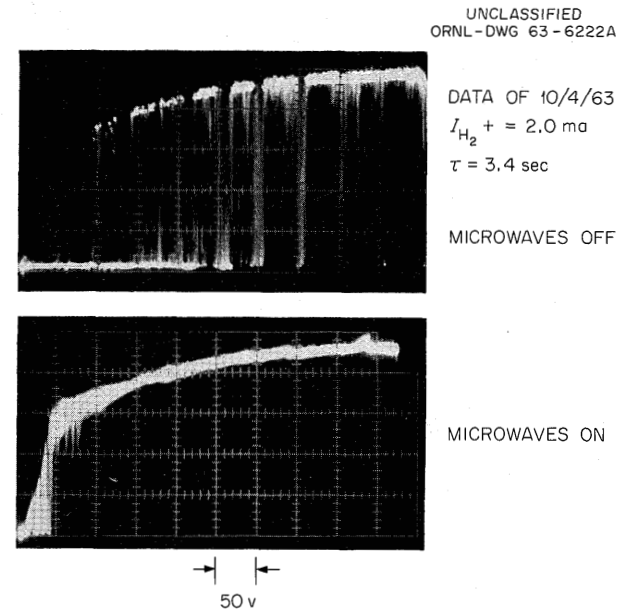

Fig. 1.19. Lithium Beam Transmission With and Without Central Zone Microwave Heating. 2.0 ma H_2^+, $\tau = 3.4$ sec.

of a beam of lithium ions. Figure 1.19 illustrates the results of these potential measurements. Without microwave heating the plasma potential fluctuates between 100 and 500 v with an average value of about 250 v. When microwave heating is added, the range of fluctuation is 10 to 70 v and the average is about 40 v.

As indicated in Sect. 1.2, magnetic signals from a 90° loop are found to be correlated with pulse-like ejection of electrons from the plasma. The application of microwave power partially suppresses these signals and reduces the amount of charge involved in the electron pulses. At the same time, the character of the azimuthal rf signals is altered in form though these signals are not suppressed. Figure 1.20 shows a particularly striking example of these changes in the rf signals; here the 90° loop signals are reduced to the noise level. (Unfortunately the lithium beam was not available during this run, and when it was available the suppression of the 90° loop signals was not as complete.)

In view of the reduction in plasma potential coincident with the suppression of the collective behavior responsible for the rf signals and electron pulses, we conclude that this collective behavior is also responsible for the anomalous electron heating which results in a large plasma potential in the absence of microwave heating.

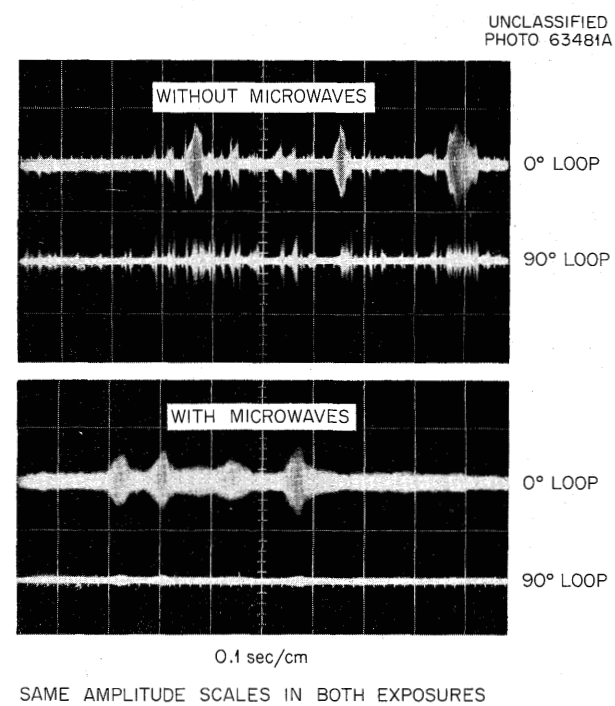

Fig. 1.20. The Effects of Central Zone Microwave Heating on Median-Plane Magnetic Probe Signals. 100 μa H_2^{+*}, 1.5 to 2×10^{-9} torr.

The plasma potential Φ is comparable to the electron temperature T, which is in turn a product of heating rate and lifetime. The lifetime, the ionization time, is essentially unchanged by applying microwaves; so a drop in Φ, and hence T, when this particular collective behavior is suppressed, implies a corresponding reduction in electron heating.

Changes in the volume of the plasma were also noted. Figure 1.21, which is derived from many measurements of the changes in the Z distribution of the charge-exchange flux, shows the effect of the microwaves on the density distribution. This figure differs from the usual distribution in having two side peaks rather than one central peak, a feature which is thought to be due to the fact that the beam did not enter on the midplane but, rather, to one side. The particles are initially formed at the position of one of the peaks and are then reflected back and forth between the two by mirror action. The additional width of the distribution is due to the usual plasma spread. The density in regions of maximum density is increased by about 10% when using the microwaves.

The results presented thus far were obtained with center zone heating. With end zone heating, no changes in plasma potential or in rf signals were observed, and there appeared to be a very slight increase in Z scattering of the trapped protons.

The region of highest plasma density is near the median plane, and it is there that the plasma is most unstable. The contrast between the effects observed using the two heating zones suggests that the heating is more effective in the region of the instability.

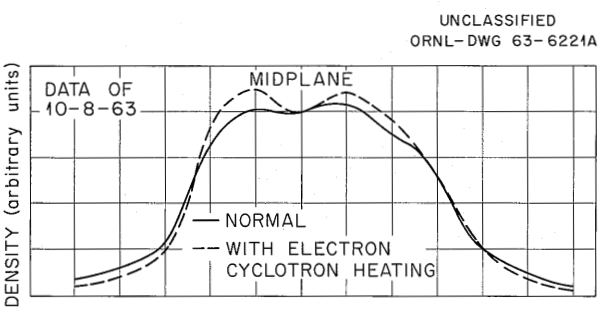

Fig. 1.21. Z Profiles of Plasma Density With and Without Central Zone Microwave Heating. 2.0 ma H_2^+, τ = 3.5 sec, 1-in. divisions on the abscissa.

A connection between these experiments and recent theoretical work of E. G. Harris is pointed out in a later section.[9]

1.5 PROTON TRAPPING BY LORENTZ DISSOCIATION OF H_2^+

The injector system shown in the previous report[10] was altered by switching the relative positions of the uppermost analyzing magnetic field and the water vapor cell. This change provided a significant reduction in the accelerator tube pressure and reduced the x-ray emission from the tube to an entirely acceptable level. Electrons from the gas cell were, however, then free to flow back to the source region where they constituted a bothersome additional load on the *einzel* lens supply. A small magnetic field is being added between the lens and the water cell to remedy this situation.

A number of runs have been made in which the responses of the charge-exchange signals to the neutral-particle detectors were measured as the H_2^{+*} current (the H_2^+ current generated from H_3^+ in the water vapor cell) and the background pressure of the plasma region were varied. Our previous work[11] had shown that Lorentz-force trapping begins to dominate at containment times of about 0.1 sec. As a consequence, the emphasis in these experiments was on the acquisition of data for containment times longer than 0.1 sec.

The neutral-particle detector consists of a longitudinal array of 12 foil-covered Faraday cups spaced at 1-in. intervals, 6 on each side of the median plane. The steady-state levels of the charge-exchange signals to these individual detectors yield a Z profile for charge-exchange loss, and Z and θ integrals of a profile yield the total charge-exchange loss current. Figure 1.22 is a plot of the ratio of this integrated charge-exchange loss current to the injected H_2^{+*} current as a function of the center detector decay time. To the extent that our measurements of the charge-exchange loss current represent the total loss current, the figure is a plot of the Lorentz-force

[9] This report, sect. 8.1.2 under the heading "Ion Cyclotron Resonance Instability."

[10] *Thermonuclear Div. Semiann. Progr. Rept. Apr. 30, 1963*, ORNL-3472, p. 7, Fig. 1.3.

[11] *Ibid.*, p. 8, Fig. 1.4.

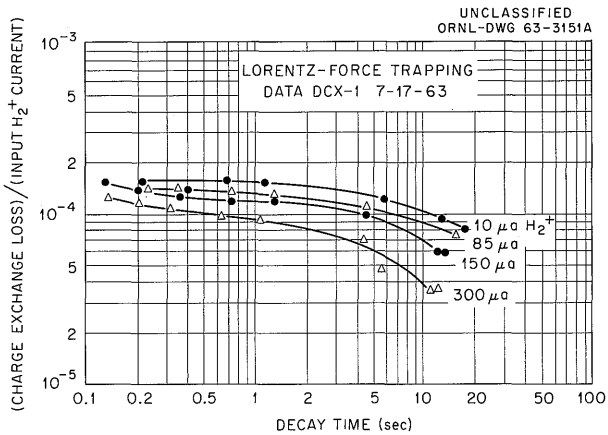

Fig. 1.22. The Ratio of Integrated Charge-Exchange Loss Current to Injected H_2^{+*} Current as a Function of Center Detector Decay Time.

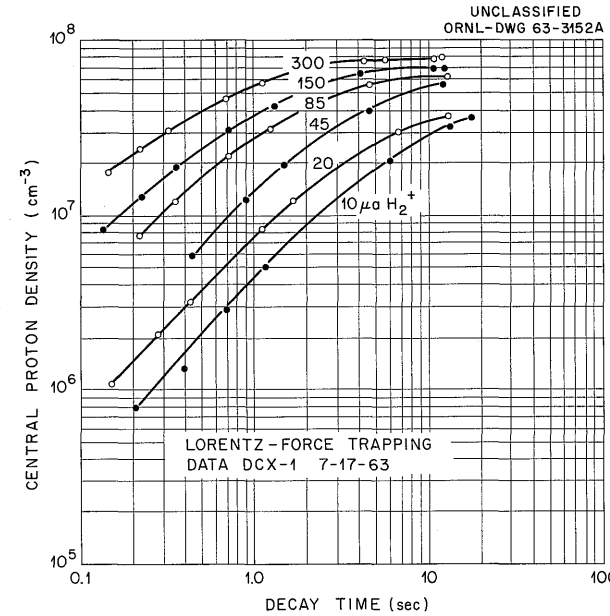

Fig. 1.23. The Central Proton Density as a Function of Center Detector Decay Time.

trapping fraction as a function of decreasing pressure. For containment times much longer than 0.1 sec, this trapping fraction should be constant as a function of τ. The dependence shown in this figure is disturbing because it indicates either that our measurements of the charge exchange are inadequate or that there is an additional loss process at the lower pressures, one which becomes more important the higher the proton injection rate.

Figure 1.23 shows the central proton density as a function of decreasing pressure. This density also was calculated from neutral-particle detector data. There is evidence of a density limit in the order of 10^8 cm^{-3}.

In Fig. 1.24 the summation quantity is the total number of fast protons stored in steady state as calculated again from the charge-exchange data. There is evidence of a limiting value of about $4 \times 10^{+11}$.

The Z profiles for the steady-state charge-exchange loss rate can be converted to density profiles by considering the difference in the containment times indicated by the individual detectors. The full width at half maximum of these density profiles is given in Fig. 1.25 as a function of the total number of stored protons. There is an expansion of the profile which becomes very pronounced at the apparently limiting value of $4 \times 10^{+11}$ particles.

The data of Figs. 1.22 through 1.25 make considerable use of the charge-exchange loss measurements, and in one respect these measure-

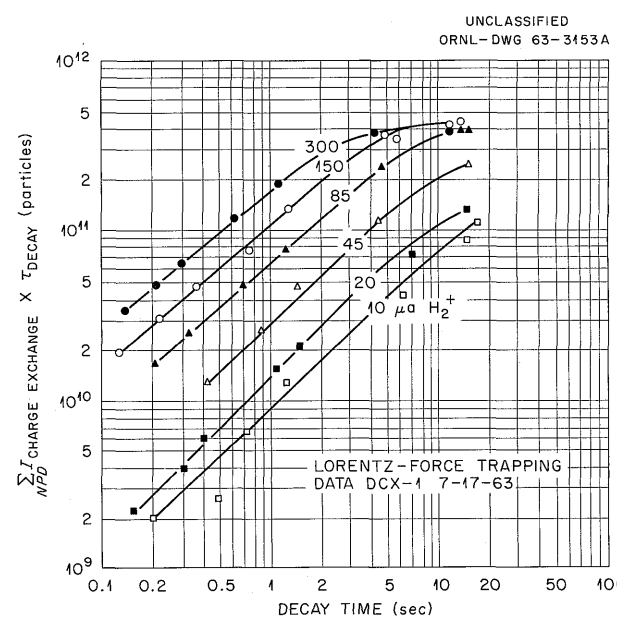

Fig. 1.24. $\sum_{NPD} I_{\text{Charge Exchange}} \times \tau_{\text{Decay}}$ as a Function of Center Detector Decay Time.

ments are known to be inadequate. At the lowest pressures the Z profiles had expanded beyond the Z limits of the detector array, so at these pressures the experimentally derived total number of stored protons is certainly less than

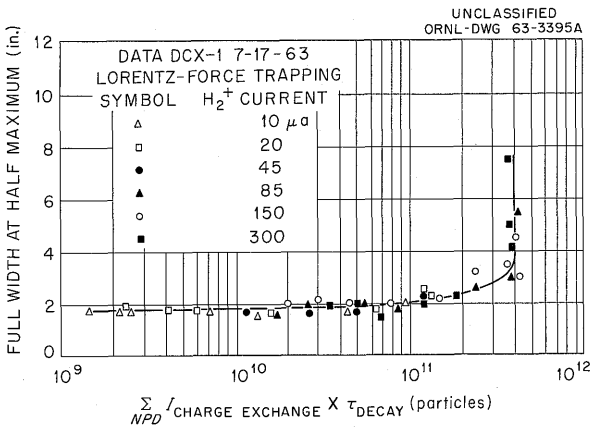

Fig. 1.25. The Full Width at Half Maximum of the Density Profile as a Function of $\sum_{NPD} I_{\text{Charge Exchange}} \times \tau_{\text{Decay}}$.

the actual number. The trapping rates are then more nearly constant than shown in Fig. 1.22; the limiting number of stored protons is somewhat more than indicated in Fig. 1.24, and the profile expansion is not as rapid as shown in Fig. 1.25. We have estimated the magnitude of this error and find that it does not affect the conclusion that at the lower pressures and higher injection rates there may be significant proton loss by a mechanism other than charge exchange. Another possible source of experimental error is recognized: severe energy degradation could result in attenuation of the current signals from the neutral-particle detectors. Experiments are in progress to determine the extent to which degradation affects the measured trapping rates.

In Figs. 1.22, 1.23, and 1.24, the data points which depart significantly from the expected behavior are those for which scattering of the plasma is most marked (Fig. 1.25). For these experiments the end walls of the plasma chamber were at the mirrors, approximately 15 in. from the median plane, and proton loss due to scattering to these walls was probably insignificant. However, in the median plane the plasma automatically extends out to the nearest radial obstruction (R = 7 in. for these experiments), and we feel at this time that any additional proton loss is the result of radial scattering of the plasma until wall collisions become important.

Other plasma parameters – rf signals, energy distribution, potential, and slow plasma fluctuations – have been measured when using Lorentz-force trapping, but these observations were confined to injection currents and containment times that did not produce the most marked scattering. The results were very similar to those previously described for gas dissociation, with differences in detail that are thought to reflect the somewhat different initial proton distributions and the increased trapping rates obtained with Lorentz-force dissociation. These same measurements need to be performed under conditions which do produce the marked scattering.

1.6 INTERPRETATIONS IN TERMS OF INSTABILITIES

Our recent data have supported the earlier conclusion that ion clustering dominates the unstable behavior of the plasma, and these data have made more clear the relationships between a number of plasma properties and the instability.

As indicated in Sect. 1.3, the general explanation for the time correlations between rf signals, the electron pulses out of the mirrors, and fluctuations in plasma potential remains the same. The rapid acquisition of electron energy can be accounted for by resonant heating of electrons in the potential wells associated with the rotating proton clusters. For the operating conditions investigated, the new low-frequency (kilocycles) phenomena are not now regarded as being of much consequence in determining the gross characteristics of the plasma.

The reduction of the plasma potential upon the application of microwave power (Sect. 1.4) is consistent with the correlations between rf signals and electron ejection displayed in Sect. 1.3. The microwaves suppress the longitudinal rf activity and the electron pulses, and these two have been shown to be closely correlated. This suppression of longitudinal rf was also observed in experiments[12] in which a stream of electrons was transmitted through the plasma region. Lithium beam studies were not made during the electron beam work, but there is no reason to doubt that rf suppression by this technique was also accompanied

[12] *Thermonuclear Div. Semiann. Progr. Rept. Oct. 31, 1962*, ORNL-3392, pp. 9–10, sect. 1.6.

by a reduction in potential. The two sets of experiments do have one other feature in common: although in each there was evidence of a significant reduction in unstable coupling to electron motion, the azimuthal rf activity was not suppressed and the decrease in plasma volume was disappointingly small.

These last observations suggest that the volume is more closely related to the azimuthal proton clustering, and this suggestion is supported by calculations which show that the observed proton scattering can be accounted for by random interactions of unclustered protons with the cluster fields. There is then the implication that protons rather than electrons dominate in determining those aspects of the instability responsible for the plasma spread. We intend to explore this implication during the next report period by continuing work with the microwaves, and by utilizing some other possibly stabilizing techniques that may couple more directly to the protons themselves.

1.7 APPENDIX: A DENSITY LIMIT FOR FAST IONS IN MIRROR FIELDS

C. E. Nielsen[13]

Neutral-particle studies of the fast-ion distribution in DCX-1 have shown that the fast ions tend to spread in the axial direction when injected beam current is increased, so that ion density does not increase in proportion to injected current. There appears to be a close correlation between the occurrence of axial spreading and the presence of rf fields produced by ion clusters.

Axial spreading by clusters may constitute a fundamental limit to the density obtainable.

Theoretically it is to be anticipated that the stability against growth of ion clusters will depend upon the energy spread – that is, upon the disorder in the assembly of fast ions. For the azimuthal clustering from the "negative mass" instability,[14] the stability criterion is that ion density n must be related to energy spread ΔE_ϕ by a relation of the form

$$n < a(\Delta E_\phi)^2$$

in which a depends upon magnetic field gradient, shape of the charge distribution, and charge and mass of the ions. Other electrostatic instabilities will have an instability threshold of the same type; and we may assume, in general, the necessity of a spread in momentum or energy for stability.

In order to estimate the significance of collective behavior for attainable density, assume that whenever n exceeds the stability threshold collective fields develop and rapidly spread the energy distribution that amount required for stabilization. Collective behavior is thus self-limiting. Assume further that axial energy spread in DCX-1 is of the same order as the spread necessary for stabilization, and that ΔE_z and ΔE_ϕ have comparable influence on stability. On these assumptions we should expect the density in DCX-1 to vary as the square of the axial energy. Any attempt to increase the density by increasing trapping rate or decreasing loss rate will simply increase energy spread and axial spreading. Eventually axial or radial spread in energy and momentum will become great enough so that escape from mirrors or to side walls will replace charge exchange as the primary loss process.

Calculations of axial oscillation energy of centered orbits show that an oscillation amplitude of approximately 3 in. corresponds to $\Delta E_z/E_\perp \sim 0.1$, while escape from mirrors occurs with ΔE_z just 5 times greater. Then the density limit is estimated as of the order of 25 times greater than density when axial oscillation has approximately 3-in. amplitude.

It must be noted that the assumption of axial energy equal to stabilization energy is crude, and the preceding estimate could easily change by a factor of 10. There will, however, be *some* density limit for stability against collective behavior merely by virtue of the anisotropy produced by escape from mirrors, and it will be possible to make a better estimate by including the effects of ΔE_z, ΔE_ϕ, and radial distribution of orbits.

[13]Consultant from Ohio State University.

[14]C. E. Nielsen, A. M. Sessler, K. R. Symon, *Proc. Intern. Conf. High-Energy Accelerators*, p. 239, CERN, 1959.

2. DCX-2

P. R. Bell
L. J. Bledsoe
J. S. Culver
R. C. Davis
S. M. DeCamp
J. C. Ezell
J. U. Guillory[1]
R. A. Gibbons
G. G. Kelley
N. H. Lazar
O. B. Morgan
T. F. Rayburn
R. F. Stratton
C. W. Wright
A. J. Wyrick
J. D. G. Rather

2.1 INTRODUCTION

The major results in DCX-2 during this reporting period have been obtained with axial lithium and hydrogen arcs.[2] These arcs are run along flux lines passing through the central volume 1 in. south of the machine axis (Fig. 2.1). The injected molecular ions, therefore, pass through the arc in each revolution as they spiral down the machine. The arc electrodes are located at the ends of the machine beyond the mirrors and the intermediate differential pumping region (Fig. 2.2).

With gas breakup, the pressure in the plasma region is typically about $p_g = 1 \times 10^{-6}$ mm Hg with beam injected, but it has been as low as $p_g = 4 \times 10^{-7}$. With a hydrogen arc running, the pressure has been $p_g = 4 \times 10^{-6}$ or greater. Increased pumping is required in the cathode region and is being added. A lithium arc reduces the pressure not only when the arc is running by direct plasma pumping, but also when the arc is off after extensive running. The base pressure with the lithium arc running and the beam present is 1.5×10^{-7} mm Hg.

Improved measurements of the injected beam have been carried out in an attempt to establish a complete account of the total accelerator current. It appears that a maximum current of only ~40 ma of H_2^+ injected current is reached even when the accelerator current is increased to more than 100 ma, for reasons that still are not clearly understood.[3] Minor difficulties associated with intermittent turn-to-turn shorts or grounds in the coil system continue to plague operations. However, improved monitoring of critical coil parameters has permitted relatively rapid diagnosis and

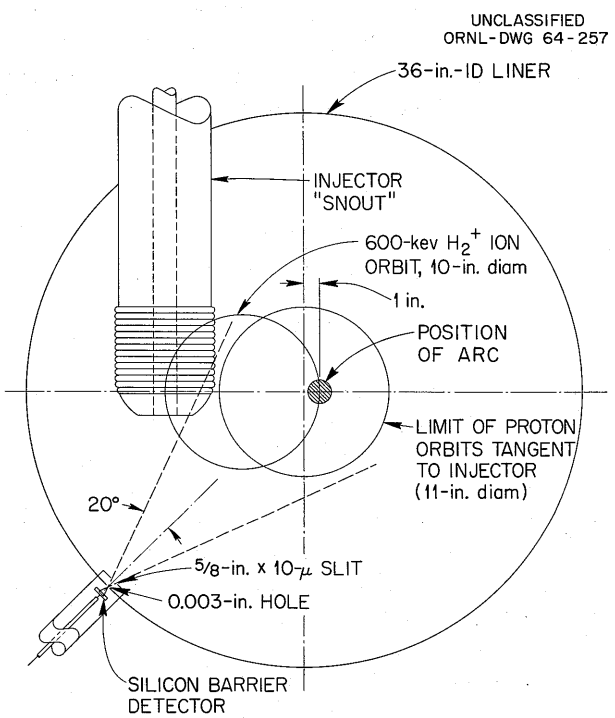

Fig. 2.1. Transverse Section Through Plasma Region of DCX-2.

[1]Summer employee, University of California, Berkeley.

[2]P. R. Bell and J. E. Francis, this report, sect. 5.2.

[3]R. C. Davis *et al.*, this report, sect. 7.1.

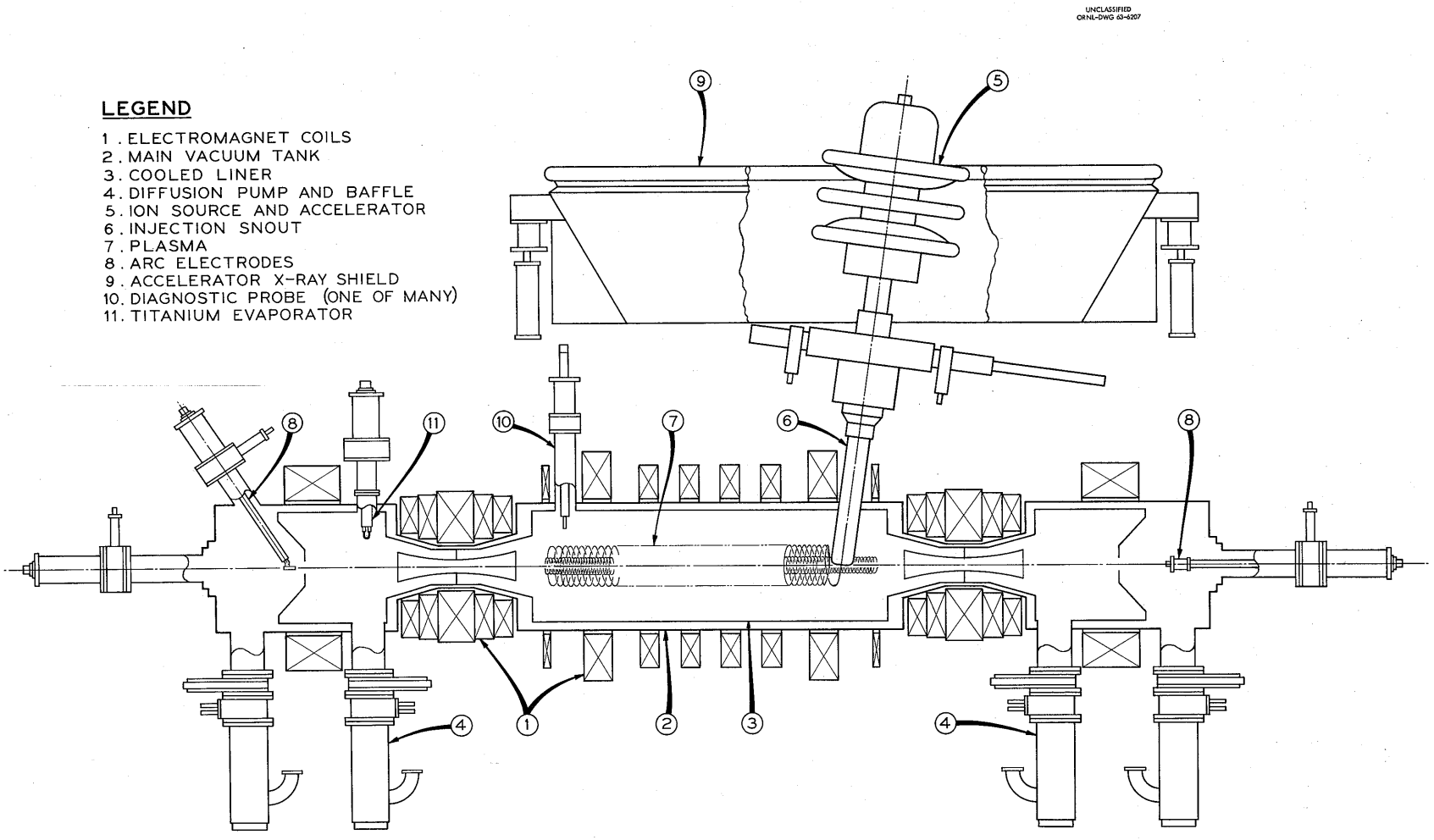

Fig. 2.2. Longitudinal Section Through DCX-2.

repair of these difficulties. Significant improvement of the drift in the field has also been accomplished by reducing the regulator amplifier drifts.

Diagnostic improvements have also been continued. Most importantly, the energy analyzer used to study the fast-neutral flux was made pivotable at a point near the detector so that scans over either radial or axial directions could be carried out. As a result, as will be described below, detailed energy and positional information of the trapped particles is now available and enables us to establish the plasma density profile with some degree of certainty.

No rotational instabilities such as are seen in other machines have yet occurred in DCX-2 – even at the highest density obtained ($\sim 10^{10}$ hot ions per cm^3). As a consequence of this absence of any source of plasma loss except charge exchange we have no present intention of adding Ioffe bars or other minimum B arrangement to DCX-2. Some engineering studies are, however, being carried out to permit such additions with reasonable speed should higher ion density produce some form of instability that minimum B could be expected to cure. Principal efforts are now directed toward lowering the pressure of residual gas in the liner and improving the operating condition with both the hydrogen and the lithium arc.

2.2 DENSITY AND ENERGY OF CONFINED PLASMA

The density of trapped plasma in DCX-2 has been calculated by a consideration of particle balance in equilibrium:

$$n_+ = I\overline{\tau}/V ,$$

where I is a particle current through the volume V, and $\overline{\tau}$ is the mean lifetime of the particles in this volume. The meaning of the equation depends on which current and lifetime are considered. If, for example, $\overline{\tau} = \overline{\tau}_x$ (the mean lifetime for charge exchange), and the current is I_x (the output of particles removed by charge exchange), then n_+V is the number of particles in the machine destined to be lost by charge exchange. If I is the total trapping rate, $\overline{\tau}$ must include an averaging over all forms of loss and in this case n_+V is the total number of trapped particles. The averaging done in DCX-2, however, is only for charge-exchange loss since other loss mechanisms apparently are unimportant.

A comparison of the foil neutral-particle detector currents (corrected for solid angle) with the trapping rate of particles shows that in DCX-2 the trapped plasma indeed is lost by charge exchange. These measurements of particle accountability in the case of arc dissociation are discussed elsewhere in this report. With gas dissociation, the flux of neutrals leaving the plasma in steady state is the sum of those directly produced by dissociation of the molecular ion beam and those resulting from charge exchange in the trapped plasma. Immediately after beam turnoff, the charge-exchange component remains, but within 10 to 20 μsec the molecular ions are gone and the dissociation-produced current falls to zero. For the DCX-2 geometry, assuming no losses except charge exchange,

$$I_x \approx 0.64\, I_w \text{ (nitrogen background gas)}$$

$$\approx \frac{9}{17} I_w \text{ (hydrogen background gas)} ,$$

where I_w is the total wall current in steady state and I_x is the charge-exchange component.[4,5] The difference in the factor for hydrogen and nitrogen is due to a difference in the ratio of proton production cross section to dissociation cross section for the two gases. It was reported previously that the value of I_x determined by the fall of neutral current at beam turnoff was much less than $^9/_{17}\, I_w$, implying other losses, but the actual situation was obscured by the use of very slow current amplifiers (rise time ≈ 200 μsec). When faster amplifiers were used, it was found that the ratios were within about a factor of 2 of the values predicted. Since the efficiency, averaged over the energy spectrum, of a foil detector typically is about 0.5 (see below), the behavior is consistent with the absence of large additional losses. With arc breakup, the foil neutral detector signals show no sudden drop if the detector is positioned where it does not intercept the dissociation neutrals from the arc, since the gas dissociation is relatively very small.

[4]P. R. Bell *et al.*, *Thermonuclear Div. Semiann. Progr. Rept. Oct. 31, 1962*, ORNL-3392, p. 13.

[5]P. R. Bell *et al.*, *Thermonuclear Div. Semiann. Progr. Rept. Apr. 30, 1963*, ORNL-3472, p. 9.

A solid-state particle detector is used in DCX-2 along with a multichannel pulse-amplitude analyzer to obtain both the energy distribution of the fast neutral particles leaving the plasma and the radial distribution of these particles. The angular resolution of the detector permits a determination of the spatial distribution of the trapped plasma, but it also is a necessary consequence of the fact that the particle flux must be reduced by a factor of more than 10^8 to permit counting without a serious distortion due to pulse summing. The arrangement used is shown in Figs. 2.1 and 2.3. The acceptance solid angle is a fan 40° wide by about 0.2° high. The slit may be oriented either horizontally or vertically and scanned in the plane perpendicular to it through an angle of about ±34°. At any given orientation the detector views a region of the plasma defined by its acceptance fan. Particles in this fan strike the detector only, of course, if they are directed at the sensitive area visible through the apertures. It is possible in spite of this selectivity to get a reasonably unbiased average spectrum measurement by sweeping up and down at a constant rate while counting with the slit horizontal. The angles tangent to the molecular-ion orbits must be excluded to exclude dissociation neutrals. By measuring the spectrum at fixed angles, the neutral flux may be determined as a function of "impact parameter" and energy, where the term "impact parameter" means the distance of closest approach to the machine center of a line through the trajectory of a particle (Fig. 2.4).

At any energy

$$\tau_x(E) = \frac{1}{n_0 \sigma_x(E)\, v(E)},$$

where n_0 is the neutral density, σ_x is the charge-exchange cross section, and v is the particle velocity. If the energy distribution of charge-exchange current, i_x, is a true average over the plasma, then the energy distribution of protons in the plasma must be

$$\bar{\nu}_+(E) = \frac{k\, i_x(E)\, \tau_x(E)}{V} = \frac{k\, i_x}{n_0 \sigma_x v V},$$

where $\bar{\nu}_+$ is the proton density per unit energy interval at energy E averaged over the volume V, and k is the ratio of total current to the measured current over a given energy interval dE. The value of k depends on the configuration of the system but is difficult to evaluate directly. It may be found by equating the solid state detector current to the neutral-particle current as measured by the foil neutral detectors properly corrected for energy cutoff and area. If k' is the area correction factor for a foil detector and $g(E)$ is its efficiency at a given energy, then

$$I'_w = k' \int_0^\infty i_w(E)\, g(E)\, dE\ ,$$

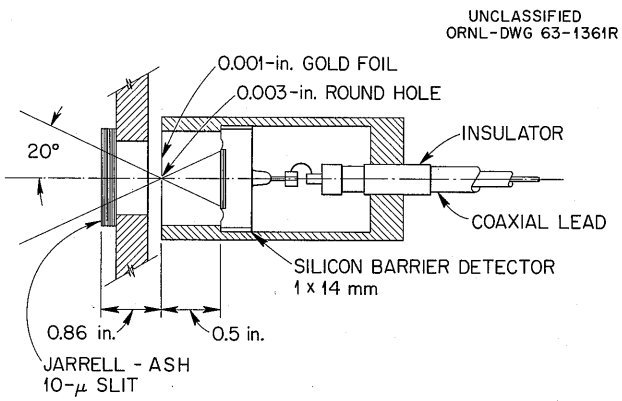

Fig. 2.3. Section Through Fast Neutral-Particle Energy Analyzer. The slit assembly used was a Jarrell-Ash 82000 optical spectrometer slit. The silicon barrier detector was an ORTEC No. 14A-25.

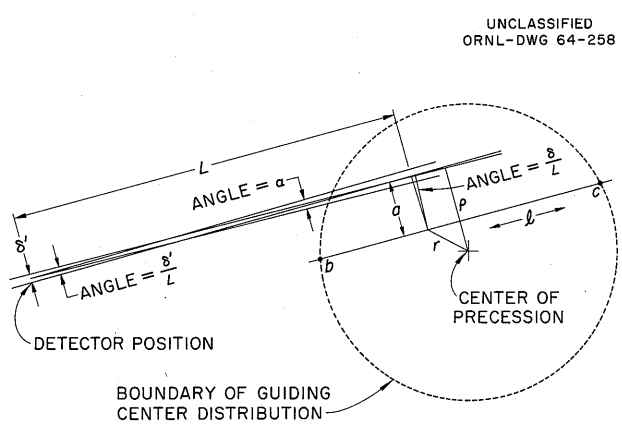

Fig. 2.4. Neutral Spectrometer Counting Geometry. The angles are exaggerated for the purpose of illustration. (See text.) The "impact parameter" is the distance ρ.

where i_w is the current at energy E per unit energy interval incident on the foil detector and I'_w is the measured foil detector current. Since

$$i_w(E) = \frac{k}{k'} i_x(E) ,$$

$$I'_w = k \int_0^\infty i_x(E)\, g(E)\, dE$$

and

$$k = \frac{I'_w}{\int_0^\infty i_x(E)\, g(E)\, dE} .$$

Then

$$\bar{n}_+ = \int_0^\infty \bar{\nu}_+(E)\, dE = \frac{I'_w}{V} \frac{\int_0^\infty \frac{i_x(E)}{n_0 \sigma_x(E)\, v(E)}\, dE}{\int_0^\infty i_x(E)\, g(E)\, dE} ,$$

where $\bar{n}_+$ is the density of trapped protons averaged over V. Since only particles with energy greater than a certain value can be measured, it is necessary to extrapolate to zero energy or to leave out the contribution of lower-energy particles to the density. In the measurements for DCX-2 a low-energy cutoff of about 50 kev is used. It is necessary, in fact, to know the energy spectrum at least down to the cutoff energy of the foil detectors. Those used in DCX-2 are 10-μin. nickel having a cutoff at about 50 kev and an efficiency which rises nearly linearly from this energy to 100% at 150 kev.[6]

If the equation above (with lower integration limits changed to E_{min}) is multiplied and divided by

$$\int_{E_{min}}^\infty i_x(E)\, dE ,$$

it may be seen that it is equivalent to

$$\bar{n}_+ = \frac{I_w}{V} \bar{\tau}_x ,$$

where

$$I_w = I'_w \frac{\int_{E_{min}}^\infty i_x(E)\, dE}{\int_{E_{min}}^\infty i_x(E)\, g(E)\, dE} = \frac{I'_w}{\bar{g}}$$

is the charge-exchange current corrected for foil detector efficiency and

$$\bar{\tau}_x = \frac{\int_{E_{min}}^\infty \tau(E)\, i_x(E)\, dE}{\int_{E_{min}}^\infty i_x(E)\, dE} .$$

With a lithium arc in DCX-2, one particular spectrometer scan gave a value of $\bar{\tau}$ = 14 msec assuming nitrogen background gas. At this time I'_w = 12 ma was determined from the current of a single detector multiplied by the ratio of its area to the area of a cylinder surrounding the plasma at the radius of the detector. Measurements in other ports indicate that this value may be too high, but not by more than a factor of 2. Correction for detector efficiency gave I_w = 23 ma. Then $\bar{n}_+ V = 0.014 \times 0.023 \times 6 \times 10^{18} = 1.9 \times 10^{15}$ particles with energy greater than 50 kev.

The spatial distribution of plasma can be determined from the value of i_x as a function of impact parameter if axial symmetry may be assumed. First, the density of guiding centers is found in the following way. By reference to Fig. 2.4 it may be seen that

$$i_x(\rho,E)\, \tau_x(E) = \int_b^c \delta \alpha L \frac{\delta'}{2\pi L} \nu_g(r,E)\, dl ,$$

where δ is the width of the sensitive region of the detector, and δ' is the height of the sensitive region, both averaged over the acceptance fan; α is the angular thickness of the fan; L is the distance from the point of emission to the detector; r is the radial distance to the guiding centers of the emitting particles; ν_g is the density of guiding centers per unit energy interval; and ρ is the impact parameter. The integration is over a line through the plasma parallel to the ray through the detector but displaced by a distance a (the Larmor radius) as shown in Fig. 2.4. This equation may be solved stepwise. The plasma region is divided into m circular zones having equal

[6] R. J. Kerr, R. A. Dandl, and C. F. Barnett, *Thermonuclear Project Semiann. Progr. Rept. Jan. 31, 1959*, ORNL-2693, p. 4.

radial increments Δr, concentric with the plasma center (Fig. 2.5). The density of guiding centers is assumed to be constant in each zone. If there are no guiding centers beyond the mth zone,

$$i_{xm}\tau_x = \beta\nu_{gm} l_{m,m} ,$$

$$\beta\nu_{gm} = \frac{i_{xm}\tau_x}{l_{m,m}},$$

where $l_{m,m}$ is the length of the chord in the mth zone made by a line passing the origin at a distance $m\Delta r - \Delta r/2$, $\beta = \delta\delta'\alpha/2\pi$ is a geometry factor, and the subscripts on ν_g and i_x mean the values at $m\Delta r - \Delta r/2$ and $m\Delta r - \Delta r/2 + a$ respectively. Then

$$i_{x,m-1}\tau_x = \beta(\nu_{gm} l_{m-1,m} + \nu_{g,m-1} l_{m-1,m-1}) ,$$

and

$$\beta\nu_{g,m-1} = \frac{i_{x,m-1}\tau_x - \beta\nu_{gm} l_{m-1,m}}{l_{m-1,m-1}} .$$

The general term is

$$\beta\nu_{g,m-j} = \frac{i_{x,m-1}\tau_x - \beta\nu_{g,m} l_{m-1,m} - \beta\nu_{g,m-1} l_{m-1,m-1} - \cdots - \beta\nu_{g,m-j+1} l_{m-1,m-j+1}}{l_{m-j,m-j}} .$$

Since $\iint \nu_g \, dE \, dV = \int n_g \, dV = \bar{n}_+ V$, the value of β may be determined directly:

$$\beta = \frac{\int \beta n_g \, dV}{\bar{n}_+ V} .$$

UNCLASSIFIED
ORNL-DWG 64-259

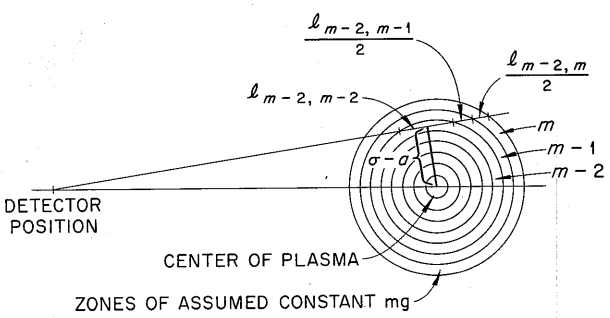

Fig. 2.5. Illustration Showing Quantities Used in Determining Guiding Center Distribution from Partial Flux. (See text.)

The actual particle distribution is found from the distribution of guiding centers. Consider a small region about the point at which the density is to be determined (coordinates r,θ). Particles passing through this region have guiding centers in a ring about the point at a distance a. If Φ is the angle around this ring from some reference direction, then

$$\nu_g(r,\theta,\Phi,a)\frac{a\,d\Phi}{2\pi a} = d\nu_+(r,a)$$

at r,θ produced by the segment $d\Phi$. Then

$$\nu_+(r,a) = \frac{1}{2\pi}\oint \nu_g \, d\Phi ,$$

where the integration is over a circle of radius a about r,θ. With concentric rings of uniform n_g,

$$\nu_+(r) = \frac{1}{2\pi}\sum \nu_{g,i}\Delta\Phi_i ,$$

where the sum is over all zones passed through by a circle of radius a at r and $\Delta\Phi_i$ is the angular extent of the ith zone.

Figure 2.6 shows the counting rate as a function of impact parameter for several energies with a hydrogen arc. Figure 2.7 is the corresponding distribution of guiding centers, and Fig. 2.8 is the proton distribution calculated from this guiding-center distribution. As can be seen from Fig. 2.8, the peak density of ions is about 5×10^8 cm^{-3}. If we assume that the radial distribution of ions is the same for the lithium arc as for the hydrogen arc, the peak density in the lithium case would be about 2×10^{10} cm^{-3}.

Figures 2.9(*a*) and (*b*) are vertical scans through the plasma region with a hydrogen arc and a lithium arc respectively. The ordinate is the counting rate of pulses from the neutral spectrometer above a 50-kev threshold. The spike at 26° is the response to the neutral flux from dissociation of the molecular ions. The spike is much smaller with the lithium arc because the lower background pressure made the gas dissociation contribution relatively much less. The peak near zero angle (the direction of the machine

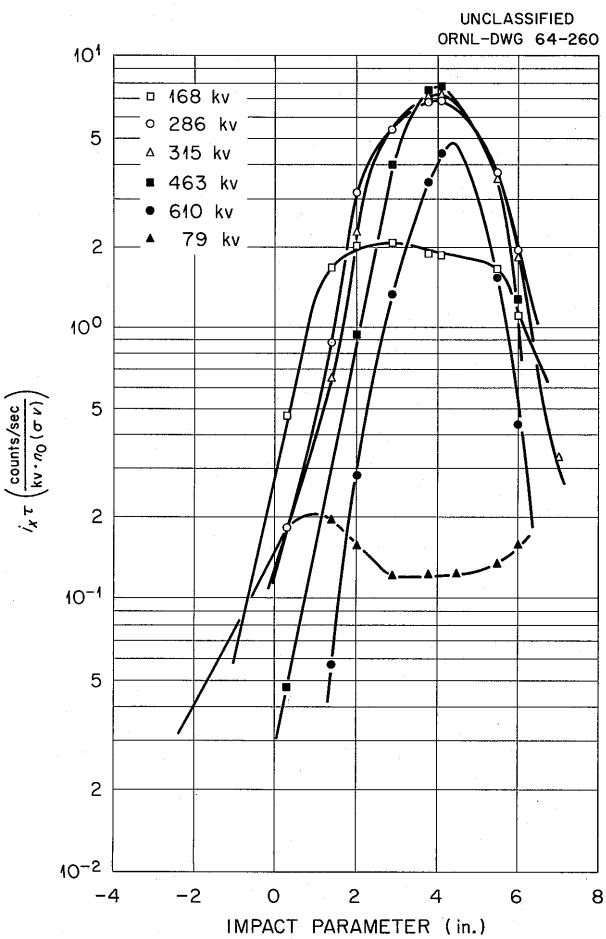

Fig. 2.6. Energy-Sensitive Detector Response to Neutral Flux, with Hydrogen Arc as a Function of the Perpendicular Distance from the Particle Flight Path to the Machine Axis (Impact Parameter).

axis) with the lithium arc is due to charge exchange in the arc.

Figure 2.10 is a horizontal scan with the hydrogen arc (detector slit vertical). Because the fan cuts off at ±20°, the dissociation neutrals are excluded. The charge-exchange neutrals are seen to have only a small spread in angle about the pitch angles of the initial and reflected molecular-ion helix. They have experienced very little "Z" scattering in spite of the fact that their total energy is spread greatly.

When the beam is turned off, the molecular ions leave the plasma volume within 10 to 20 μsec. The proton density begins to decrease at the rate

$$\left(\frac{dn_+}{dt}\right)_{t=0} = -\frac{I_x}{V},$$

where I_x is the steady-state charge-exchange current. If there were no energy mixing after beam turnoff, the time dependence of the neutral flux could be predicted from a knowledge of the equilibrium energy spectrum and the neutral pressure and composition. The energy spectrum can be broken up into a convenient number of equal intervals, with the essentially exponential decay of charge-exchange current for each added to give the total current

$$i(t) = \sum i_0(E_j)\, e^{-[n_0 \sigma_x(E_j) v(E_j) t]}\, \Delta E_j\,,$$

where $i_0(E_j)$ is the initial current contributed by the energy interval ΔE_j.

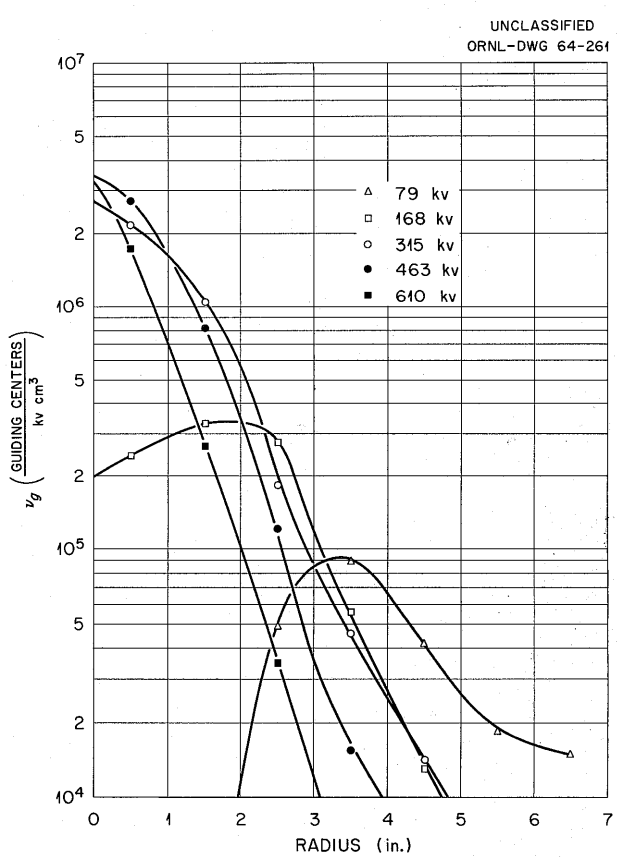

Fig. 2.7. Guiding Center Density with Hydrogen Arc.

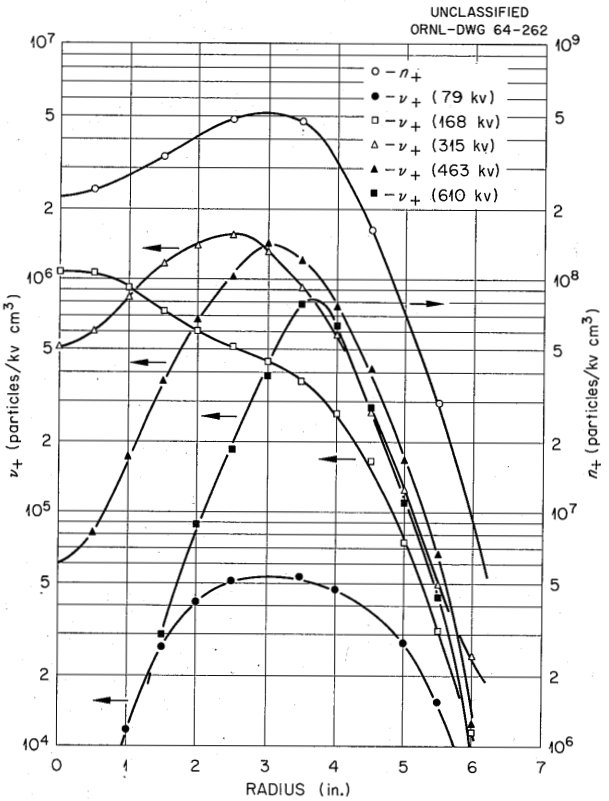

Fig. 2.8. Proton Density with Hydrogen Arc.

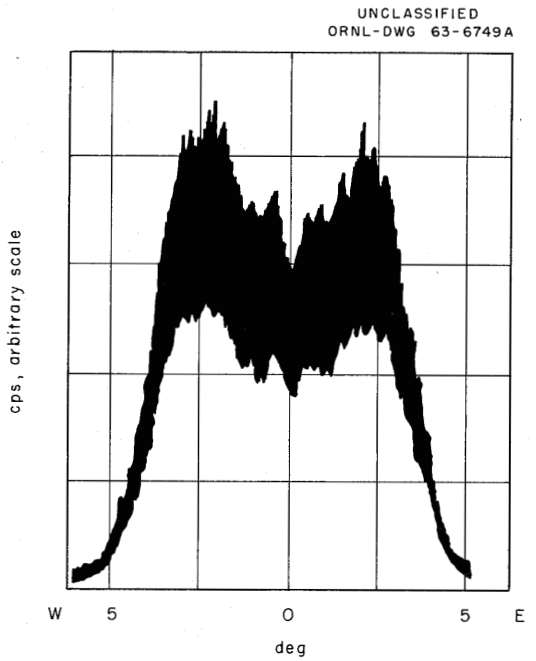

Fig. 2.10. Horizontal Angular Distribution of Charge-Exchange Neutrals in DCX-2 with Hydrogen Arc.

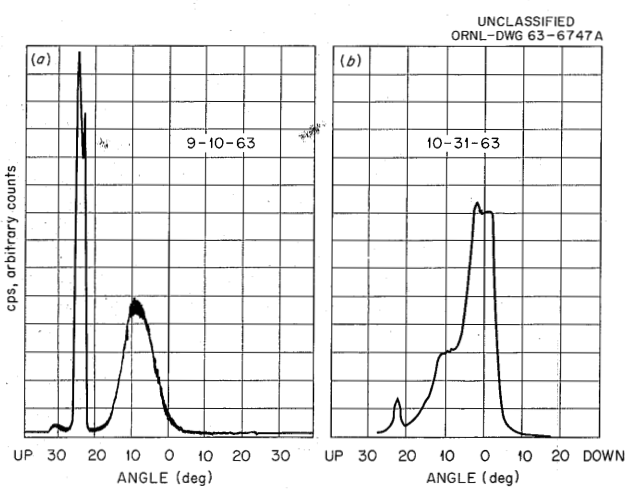

Fig. 2.9. Charge-Exchange Flux to Energy-Sensitive Detector as a Function of Viewing Angle, (*a*) with Hydrogen Arc, (*b*) with Lithium Arc.

Because the low-energy protons decay most rapidly, the spectrum should harden in time and the relative rate of decrease of current should become lower. Energy mixing will modify this shape, but it can do so only in a way which leaves the time integral of the current constant, since this integral, properly normalized, is the total number of trapped protons. Figure 2.11 is a comparison of the actual shape of a charge-exchange current decay with the predicted shape, assuming no energy mixing. Some mixing is expected because of the continuance of rf after beam turnoff. The actual shape is not understood, since the current falls more steeply than expected. A feeding of the low-energy end of the distribution by mixing would raise the rate of loss of plasma and, hence, the current. The energy spectrum of particles emitted at times greater than 10 msec and less than 50 msec after beam turnoff was measured by gating the analyzer on at the proper time and accumulating counts during many off intervals. The trapped-proton distribution is compared with the equilibrium distribution in Fig. 2.12. If there were no energy mixing and all the trapped particles charge-exchanged during the observation period, the two curves should be identical. Since the

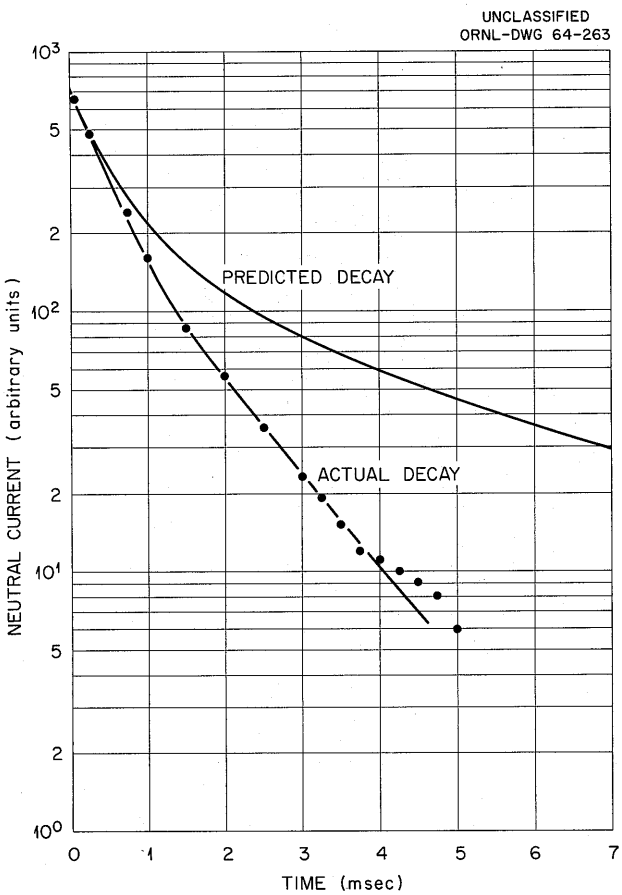

Fig. 2.11. Comparison of Actual Foil Neutral Detector Signal After Beam Turnoff with That Predicted Assuming No Energy Mixing. The amplitude of the predicted curve was adjusted to equal the actual current at $t = 0$. The assumed pressure was that which makes the initial slopes equal. It is about 5× the gage reading.

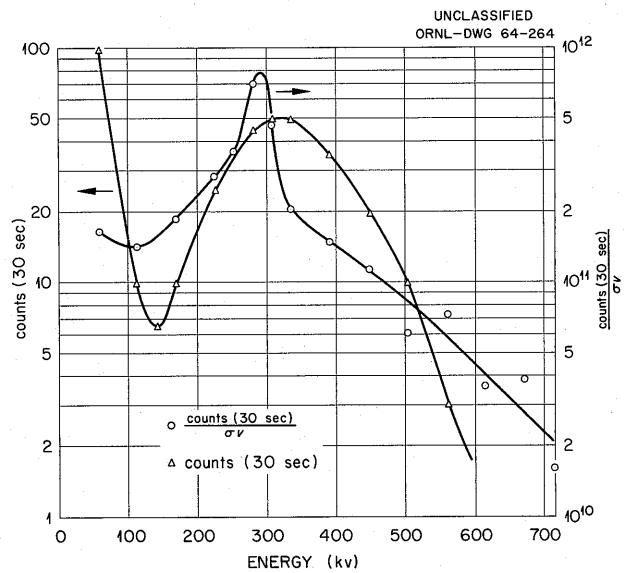

Fig. 2.12. Comparison of the Equilibrium Trapped Energy Distribution (O) with the Spectrum of Particles Emitted from 10 msec to 50 msec After Beam Turnoff (Δ).

measurement interval was delayed and was not sufficiently long, some differences are expected. However, the existence of the considerable number of low-energy particles indicates considerable energy mixing.

2.3 TRAPPING OF MOLECULAR BEAM

One of the more critical parameters necessary for assessing how close we are to attaining burnout in DCX-2 is the "mean path length," $\mathfrak{L}$, which the beam traverses in the plasma region before returning to the injector duct.[7] In the elementary theory, it may be remembered, with no arcs present, the shape of the so-called "S-curves" is relatively independent of $\mathfrak{L}$, but the magnitude of the density which one obtains for a given beam current is strongly dependent on $\mathfrak{L}$.

Two procedures may be used to determine $\mathfrak{L}$. The first is the most direct. The energy analyzer is used with the slit aligned vertically and pivoted to scan horizontally. The detector subtends an angle which prevents any of the direct dissociation neutrals from entering; so we are able to see only the neutrals from charge exchange of the trapped protons. The angle they make with respect to the axis, however, is observed to be quite small (Fig. 2.10). The average pitch angle of the beam may be deduced from the angles at which the neutrals are emitted. The pitch angle observed under certain field conditions is ~2.8°, which is close to the value expected from the injection pitch angle and the depth of the dip. By using this figure, the total path length in the flat field region is 52 m. One may take into account the

[7] P. R. Bell *et al.*, *Thermonuclear Project Semiann. Progr. Rept. July 31, 1960*, ORNL-3011, p. 17.

path length in the dips at each end as well, and assuming that three-eighths of the orbit passes through the plasma, then $\mathcal{L} = 24$ m. An even more direct measurement, not yet carried out, would be the use of a single-channel analyzer to select 300-kev particles with the detector positioned so as to view the dissociation neutrals from the beam directly.

The second procedure is connected with the cross section for dissociation, σ_d. The fraction of the beam which is dissociated is given by $n_0 \sigma_d \mathcal{L}'$, where $\mathcal{L}'$ is the total path length of the molecular-ion beam. The values for dissociation and proton production at 600 kev were taken from results accumulated by Barnett,[8] and are given in Table 2.1. Several difficulties may be commented on. Neither n_0 nor the gas composition is known well. The amount of the beam which is dissociated is determined by integrating the neutral currents from dissociation observed on the foil detectors over the proper surface area of the machine. Assuming that the gas composition has the dissociation properties of molecular nitrogen, and taking the measured path length obtained in the first procedure, then apparently in this condition only about one-third of the molecular-ion beam left the dip. Under other conditions evidence indicates that most of the beam left the dip. It is apparent that a target downstream is probably an essential tool when the dips are adjusted to optimize the proton production rate.

Perhaps an even more important aspect of a measurement of the dissociated fraction of the beam relates to a comparison of the current input to the plasma and the charge-exchange current emitted. It would be significant if all the protons injected into the plasma could be accounted for in charge-exchange current. This would give further assurance that macroscopic instabilities do not produce significant particle loss in the DCX-2 plasma. Further, if the loss rate by charge exchange were no faster than that calculated if all the particles remained at 300 kev, then our confidence in being able to attain burnout, or at least exponentiation to a high density, would remain unaltered. Here, again, experimental difficulties limit our confidence to factors of 2 or

[8] C. F. Barnett, W. B. Gauster, and J. A. Ray, *Atomic and Molecular Collision Cross Sections of Interest in Controlled Thermonuclear Research*, ORNL-3113, p. 9 (May 10, 1961).

Table 2.1. Dissociation and Proton Production Cross Sections of H_2^+ and H_3^+ in Nitrogen and Hydrogen for 600-kev Injection Energies

	σ_d (cm^2/gas molecule)	σ (Proton Production)[a] (cm^2/gas molecule)
	$\times 10^{-16}$	$\times 10^{-16}$
H_2^+ in H_2	0.73	1.1
H_2^+ in N_2	4.0	6.6
H_3^+ in H_2		2.6

[a] σ (proton production) for nitrogen assumed $1 \times \sigma(H^+ + H^0) + 2 \times \sigma(H^+ + H^+)$.

3. In one case, with the lithium arc used as the dissociating medium, the power returning to the injector could be compared to the value with the arc off. The average of two measurements yielded 8.8 ma dissociated out of the ~24.6-ma H_2^+ beam injected (32.6% dissociation). This was compared to a charge-exchange current in the middle of the machine of 2×10^{-7} amp/cm^2 striking the walls or a total charge-exchange current of 26 ma, including a correction of a factor of 2 for the aforementioned foil detector efficiency. Taking 8.8 ma of H_2^+ dissociated, one expects 13.2 ma of protons injected into the plasma if the ratio of dissociation modes in the arc is the same as in H_2.

2.4 ARC AND PLASMA PUMPING

The large pressure reduction produced by the lithium-arc operation provides an excellent method for determining a number of factors affecting the vacuum conditions in DCX-2. The foil neutral detector signal seen while the beam is on but the arc off is partly dissociation neutrals and partly charge-exchange neutrals, both components being proportional to neutral gas density, assuming that the gas composition is constant. Thus the amplitude of this signal can be used as a measure of neutral-gas pressure over a short time interval. Figure 2.13 shows the response of the foil detector signal following a sudden (within several hundred microseconds) shutoff of the lithium arc.

UNCLASSIFIED
PHOTO 64017

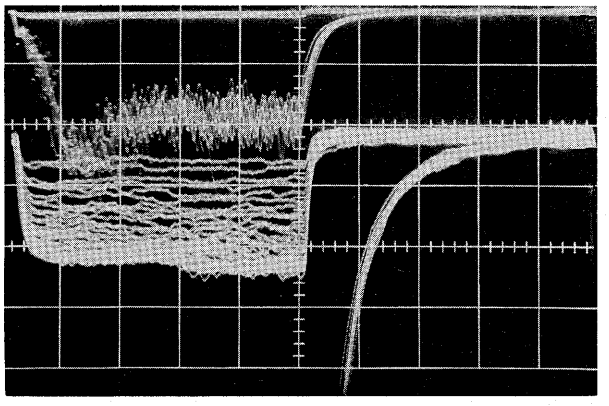

Fig. 2.13. Foil Detector Signals Showing a Shutoff of the Lithium Arc. The upper curve at low sensitivity (0.2×10^{-6} amp/cm) shows the charge-exchange current with the arc on. The lower set of traces at a sensitivity of 10^{-8} amp/cm shows the current pulse on successive $1/50$ sec intervals while the pressure is rising toward an equilibrium value after the arc has been turned off. The curve sweeping down at lower right is an arc-on signal at the higher gain.

The upper trace at low oscilloscope gain shows the large plasma signal obtained when the arc is on. This part of the signal is far off-scale on the lower (high-gain) trace. When the ion beam is turned on $1/50$ sec later, the smallest current is produced on the lower trace. Successive $1/50$-sec intervals produce progressively larger signals as the pressure rises, and the signals slowly converge (downward in the figure) to the larger equilibrium signal. The pressure in the DCX-2 liner is read from an ordinary ion-gage tube after equilibrium has been reached, giving a calibration for the foil detector signal. A constant rate of gas input from the beam is assured since all the constant injected current of molecular ions becomes gas inside the liner volume whether it is dissociated and then charge-exchanged, or whether it strikes the snout beam catcher. The portion of the input coming from outgassing may be variable, but we will, for the present, assume it to be constant. The rate of change of neutral-gas molecule density is given by

$$\frac{dn_0}{dt} = \frac{I}{V} - \frac{S}{V} n_0 , \qquad (1)$$

where I is the rate of influx of particles from all sources, V is the volume of the system, S is the pumping speed of any pumping processes, and n_0 is the neutral-gas density. The density at any time is

$$n_0 = \frac{I}{S} + \left(n_1 - \frac{I}{S}\right) e^{-(S/V)t} , \qquad (2)$$

where n_1 is the initial low pressure after arc shutoff. If the equilibrium pressure after a long time is called n_∞, then

$$n_0 = n_\infty - (n_\infty - n_1)\, e^{-(S/V)t} . \qquad (3)$$

Since the foil neutral detector current is proportional to n_0, these currents were determined from Fig. 2.13, and the equilibrium current minus the current at each pulse was graphed (Fig. 2.14). The rise-time constant obtained is 0.24 sec. The nearly exponential nature of the plot gives some justification for assuming that I was constant.

UNCLASSIFIED
ORNL-DWG 64-265

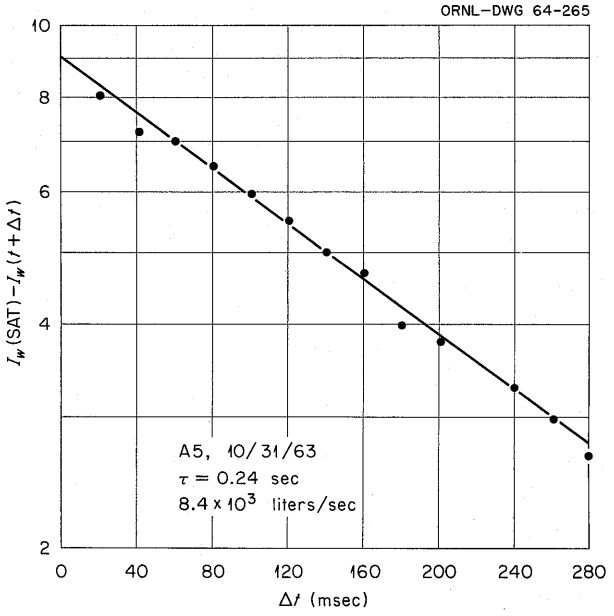

Fig. 2.14. Plot Showing the Difference Between the Saturation or Equilibrium Signal and Individual Beam-On Signals as a Function of Time After Turning Off the Lithium Arc. The curve yields the rate of pressure rise after the lithium arc is turned off and hence leads to an estimate of the plasma pumping speed with beam on and arc off (see text).

The constants of the system and the operating conditions at this time were:

$I_{H_2^+ \text{beam}} = 32$ ma, 50% duty cycle,

$V_{\text{liner}} = 2 \times 10^6$ cm^3,

p_g arc off $= 9 \times 10^{-7}$ mm Hg $= p_{g\infty}$,

Pumping speed of venturis for nitrogen $= 1.7 \times 10^3$ liters/sec (calculated),

Equilibrium foil neutral detector current, arc and beam on $= 0.4 \times 10^{-6}$ amp,

Equilibrium foil neutral detector current, arc off and beam on $= 0.2 \times 10^{-7}$ amp.

Thus $V/S = 0.24$ sec, and $S = (2 \times 10^6)/0.24 = 8.3 \times 10^3$ liters/sec total pumping speed. Since this is much larger than the normal venturi pumping speed, the excess must be attributed to the plasma pumping with gas breakup. From Eq. (2), $n_\infty = I/S$, and $I = 8.3 \times 10^3(10^3)9.0 \times 10^{-7}(3.2 \times 10^{16}) = 2.4 \times 10^{17}$ molecules/sec. This current (I) is considerably larger than the beam input, which is 1.0×10^{17} molecules/sec. The fact that the beam input is smaller than I justifies the use of p_g as a measure of n_∞ without the correction that would have to be applied if the gas had been mostly hydrogen. The excess of I over I_{beam} is, of course, the gas evolved from the beam bombardment at the injector snout and from the walls due to bombardment by the charge-exchange and dissociation neutrals.

With the arc in operation the liner pressure falls to n_1 ($\sim 1.7 \times 10^{-7}$ mm Hg). If we assume that I remains constant, then the pumping speed with the arc (S_1) is

$$S_1 = S\frac{n_\infty}{n_1} = 8.3 \times 10^3 \frac{9 \times 10^{-7}}{1.7 \times 10^{-7}}$$

$$= 44 \times 10^3 \text{ liters/sec} .$$

It is more likely, however, that I actually increases with arc dissociation, since 20 to 100 times greater current of high-energy neutrals falls on the liner wall and less current falls on the much-bombarded snout beam catcher. The liner wall, which has had little bombardment, probably produces much more outgassing.

It is perhaps constructive to compare this assumed input current of gas with the plasma pumping speed expected from the higher density trapped plasma. From the foil neutral detector current and the foil geometry factor, the total charge-exchange current to the wall is 12.8 ma. Using a $\overline{\tau}$ of 20 msec calculated from a neutral particle spectrum, we find

$$\overline{n}_+ V = i\overline{\tau} = 1.6 \times 10^{15} \text{ ions} .$$

The rate of ionization of gas (assumed to be nitrogen) by protons at the base pressure with arc on (1.7×10^{-7} mm Hg) is

$$I_{\text{ions}} = \overline{n}_+ V n_0 \sigma_i v = 1.6 \times 10^{15}(6 \times 10^9)1.7 \times 10^{-16}(7.8 \times 10^8)$$

$$= 1.26 \times 10^{18} \text{ molecules/sec} .$$

If we assume the electrons in the plasma to be $\sim$100–200 ev, and our plasma potential with arc off would correspond to such a range, then electrons would ionize a similar amount:

$$I_{\text{total}} = 2.5 \times 10^{18} \text{ molecules/sec} .$$

This expected plasma pumping rate is 10 times the rate, I, we have assumed, possibly because I is greater owing to more outgassing of walls with the denser plasma or because $\overline{n}_+ V$ is smaller than we have assumed owing to a reduced mean ion lifetime.

2.5 RADIO-FREQUENCY EMISSIONS

As reported in previous semiannuals, the DCX-2 plasma emits almost exclusively the ion cyclotron fundamentals and harmonics of both H_2^+ and H^+. The intensity is rapidly fluctuating with statistically well correlated simultaneous increases on probes at different positions along the length and around the circumference of the long plasma cylinder. There is, however, only a very poor detailed correlation of intensity peaks.[9] The radio frequency does not cease after beam shutoff in a time short compared to an ion mean lifetime, as is usually seen in DCX-1. The time behavior of this rf can be seen from Figs. 2.15(*a*), (*b*), (*c*), and (*d*). The beam was keyed on and off at 50 cps for (*a*) and (*b*) and at 20 cps for (*c*) and (*d*), and the traces began when the beam ceased. Note that the rf lasts for $\sim$2 msec when the arc is off, the plasma density low ($\sim 10^7$ ions/cm^3), and the pressure relatively high (2×10^{-6} mm Hg). When the arc is on, the pressure is low ($\sim 1.5 \times 10^{-7}$ mm Hg), the plasma density is high ($\sim 10^9$ to

[9] *Thermonuclear Div. Semiann. Progr. Rept. Apr. 30, 1963*, ORNL-3472, p. 19.

UNCLASSIFIED
PHOTO 64018

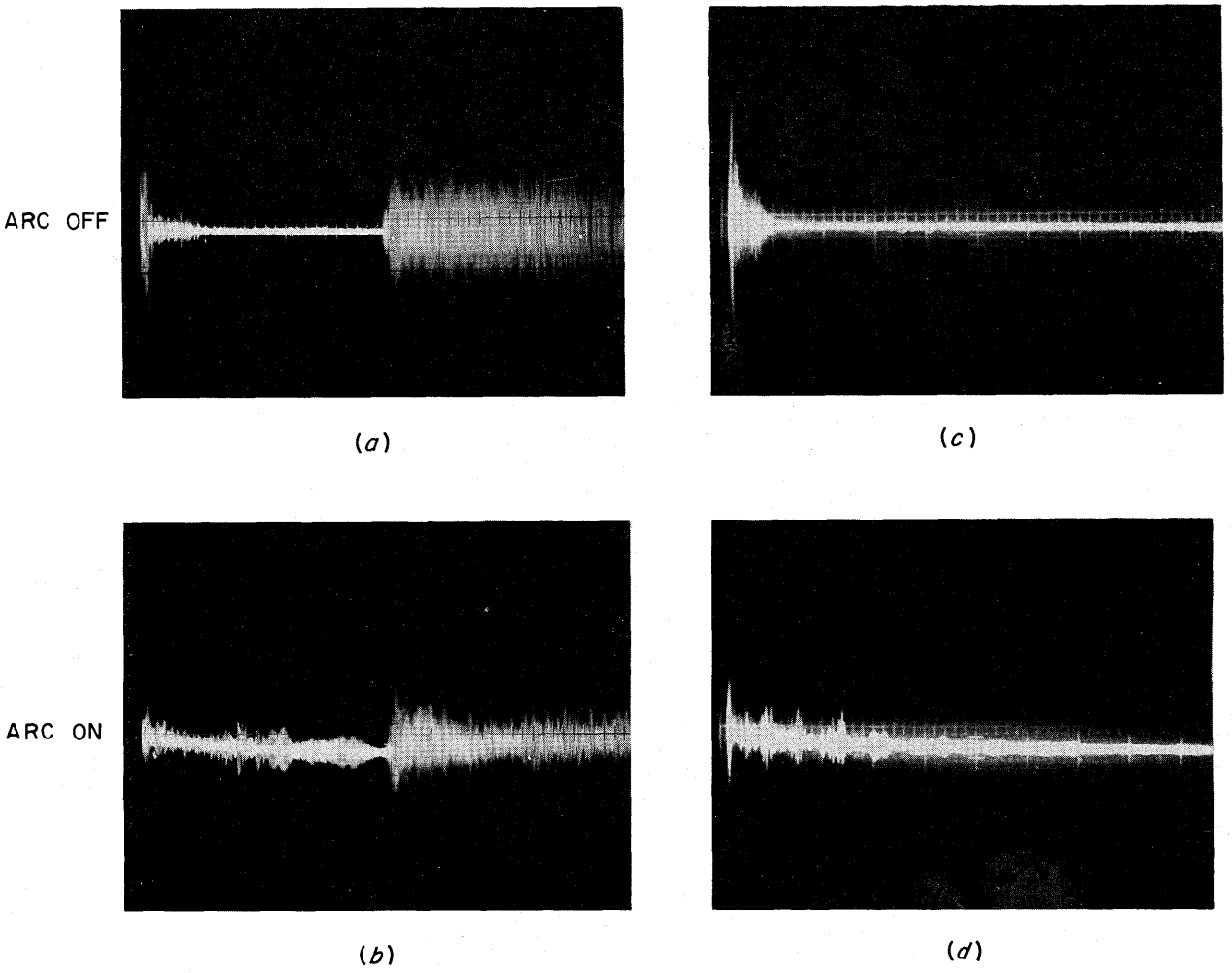

Fig. 2.15. Electrostatic Probe Signals With and Without the Lithium Arc. Sensitivity 0.1 v/cm and sweep speed 2 msec/cm. Traces (*a*) and (*b*) were taken with repetition rate 50 cps and (c) and (*d*) with 20 cps.

10^{10}), and the rf lasts to 10 to 20 msec. The intensity of the rf with the beam on, after an initial burst, is considerably less with the arc on than with the arc off despite the higher plasma density.

The spectrum of radiations emitted while the ion beam is on is altered by the operation with the arc. Figures 2.16(*a*) and (*b*) show the effects. The fundamental and second harmonic of the proton cyclotron frequency and the fundamental and odd harmonics of the molecular ions are somewhat reduced when the arc is turned on, while the third harmonic of the proton cyclotron frequency is greatly increased so that it becomes the dominant component of the radio frequency. It was noted also that the rather weak white noise background was also somewhat decreased. The spectrum emitted by the plasma after the ion beam is shut off is not only weaker and decaying, but consists almost entirely of the proton ion cyclotron fundamental when gas breakup is used (low plasma density). The higher-density plasma produced by arc breakup shows, after beam turnoff, only the second harmonic of the proton frequency, the fundamental being undetectable. Whether this is an effect due to higher density or to the presence of the arc is not yet known.

UNCLASSIFIED
PHOTO 64019

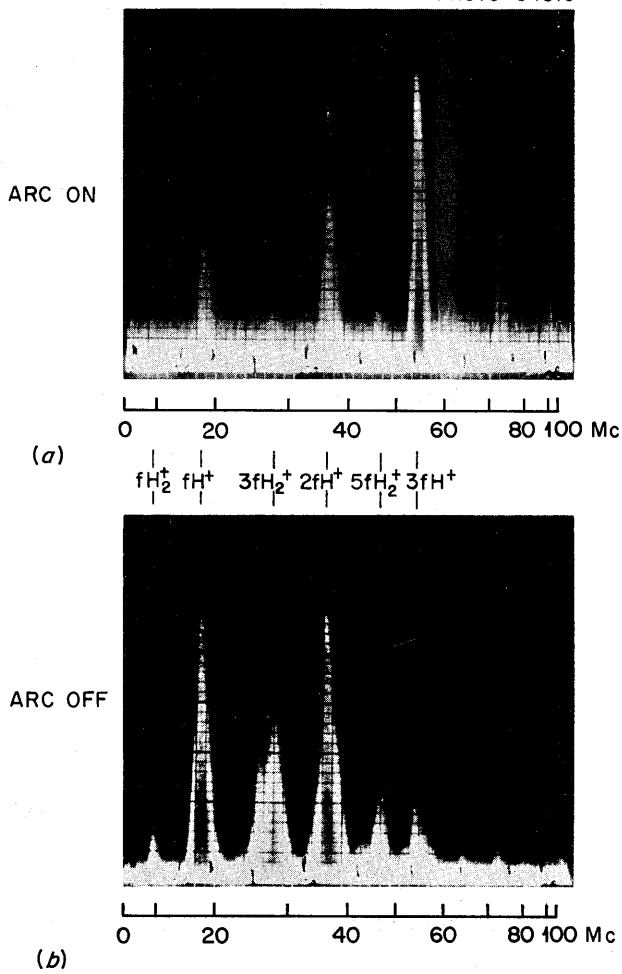

Fig. 2.16. Radiofrequency Spectrum Emitted by DCX-2 Plasma With (*a*) and Without (*b*) a Lithium Arc of about 40 Amp Intensity.

3. Electron-Cyclotron Heating

3.1 ELECTRON-CYCLOTRON HEATING EXPERIMENTS IN THE EPA FACILITY

W. B. Ard
M. C. Becker[1]
R. A. Dandl[1]
H. O. Eason
A. C. England
H. C. Hoy
R. L. Knight
N. H. Lazar
R. L. Livesey
O. D. Matlock
M. W. McGuffin

3.1.1 Introduction

The scale-up of the electron-cyclotron plasma (ECP) has been completed and operated in the EPA facility. The plasma is created in a 3:1 magnetic mirror by a 10.6-Gc (gigacycle) microwave power source capable of delivering 50 kw CW (continuous wave). Preliminary results show that at 25 kw CW the plasma has a volume of $\sim$40 liters, a total stored energy of several hundred joules, and a $\beta \cong 0.3$.

The plasma is more controllable than in the PTF in the sense that the range of operating parameters which give a stable plasma is much broader than in the PTF. Other interesting plasma properties peculiar to the scale-up will also be described.

3.1.2 EPA Experimental Facility

The scaled-up electron cyclotron resonance heating experiments are being conducted in the EPA facility. The EPA vacuum tank, originally constructed for the 1958 Geneva exhibit, was modified by addition of several large radial ports for improved diagnostic access. The experimental arrangement is shown in schematic form in Fig. 3.1. Except for size and certain details relating to the microwave power feed, the experimental arrangement is identical to that of the PTF facility.[2,3]

Magnetic field is supplied by DCX-1 type mirror coils located for a 3:1 mirror ratio. Continuous-wave microwave power at 10.6 Gc is fed into a cylindrical water-cooled copper liner or cavity of perforated copper construction. The central section of the cavity between the mirror coils is 36 in. in diameter and 21 in. long. Additional sections (16 in. in diameter and 9½ in. long) extend into the mirror throats and are terminated by clusters of plasma-pumping tubes. The cavity axis and the magnetic axis coincide. Tight metallic joints are used throughout to minimize microwave leakage. Diagnostic access for probes is gained through coaxial filters. The vacuum system is divided into three regions connected only by the plasma-pumping tubes. Vacuum pumping is afforded by two 20-in. diffusion pumps in the central region of the tank and a single 20-in. pump on either end. Water-cooled surfaces are provided for collection of the plasma which streams out into the ends of the tank.

Deuterium gas is fed into the central region of the cavity at rates of $\sim$1 atmospheric cm^3 per sec. Operation is simplified through use of a servo-controlled gas feed arrangement, which maintains constant pressure in the central region and thus compensates to a first order for the varying gas feed demands as microwave input power is varied.

The entire EPA tank is surrounded by a lead x-ray shield, 12 ft high and of 2 in. nominal thickness. The shield weighs $\sim$42 tons. The wall thickness is 3 in. adjacent to the operating area to provide additional protection for personnel

[1]Instrumentation and Controls Division.

[2]*Thermonuclear Div. Semiann. Progr. Rept. Oct. 31, 1962*, ORNL-3392, sect. 3.1.

[3]*Thermonuclear Div. Semiann. Progr. Rept. Apr. 30, 1963*, ORNL-3472, sect. 3.1.

UNCLASSIFIED
ORNL-DWG 63-7563A

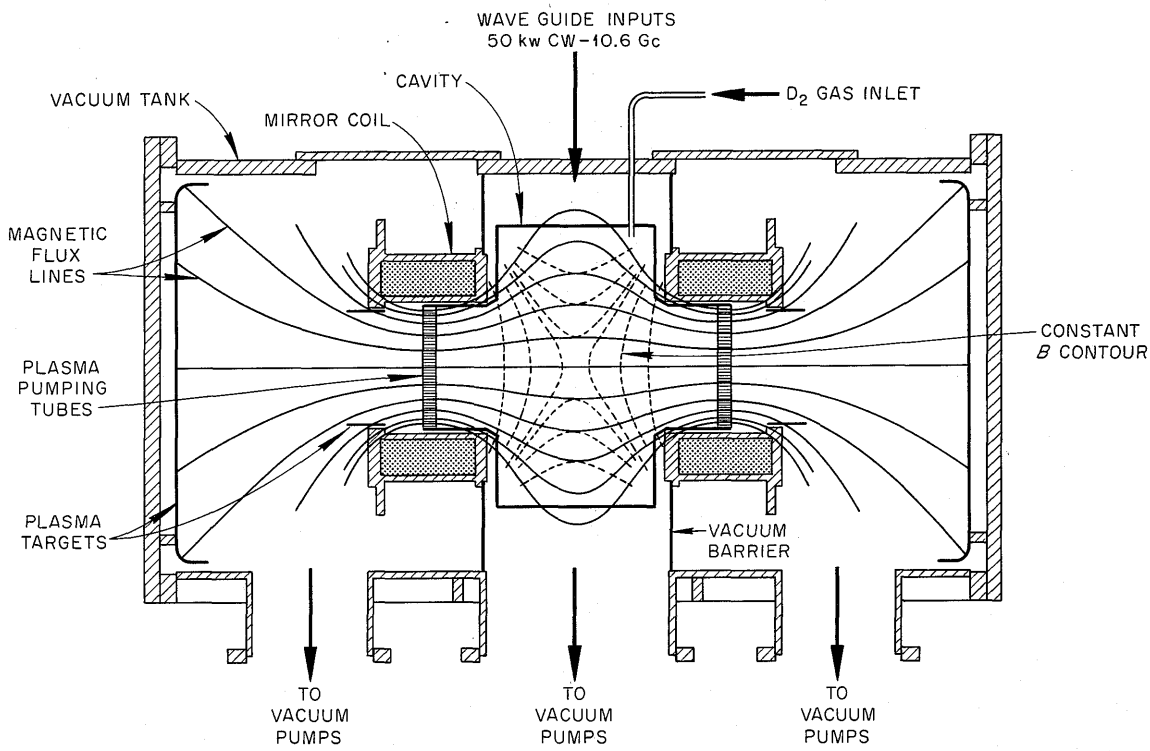

Fig. 3.1. Schematic Diagram of EPA-Microwave-Heating Experiment.

involved in experiments. The shield can be seen in Fig. 3.2, which is a photograph of the facility. The operating and diagnostic area is visible along the right side, and the microwave power source is shown outside the shield to the left.

Continuous-wave microwave power at levels up to 50 kw is supplied by three SAX-418 four-cavity klystron amplifiers operating at 10.6 Gc. These tubes are water-cooled, electromagnetically focused types having a saturated gain of ~50 db when tuned for high efficiency. Each tube requires a 20-kv, 3-amp dc beam supply which is remotely located.

The three klystrons are driven by a common oscillator located in the operating area. Output power is controlled by adjusting the drive level. An extensive system of interlocks protects the klystrons against damage due to waveguide arcs, cooling-system failure, magnet failure, waveguide pressurization failure, internal arcs, and improper operating procedure. The design is such that any tube or combination of tubes may be operated individually if desired without alterations to the system. Provisions are included for installation of a fourth tube if required at a later date.

The output waveguide circuitry for a single tube is shown in schematic form in Fig. 3.3. Identical circuitry is used for each of the three tubes. Waveguide arc protection is accomplished by a combination of photoelectric and reflected-power sensors which act through auxiliary circuitry to actuate a crystal switch for removal of drive power from the tube within a few microseconds after an arc is detected. Directional couplers are provided for monitoring output power and reflected power. All waveguides and components in the klystron output circuits are water-cooled and operate either at high vacuum or at 10-psig dry-nitrogen pressure to discourage breakdown. All mating flange surfaces are lapped, and all internal waveguide surfaces and mating flange surfaces are carefully cleaned before assembly as a further precaution against breakdown. A four-port ferrite circulator connected as an isolator protects each klystron from effects of load mismatch by diverting reflected power into the water load. Since half-wavelength waveguide windows of the type employed here are quite susceptible to failure from thermal stresses when operated under high VSWR (Voltage Standing

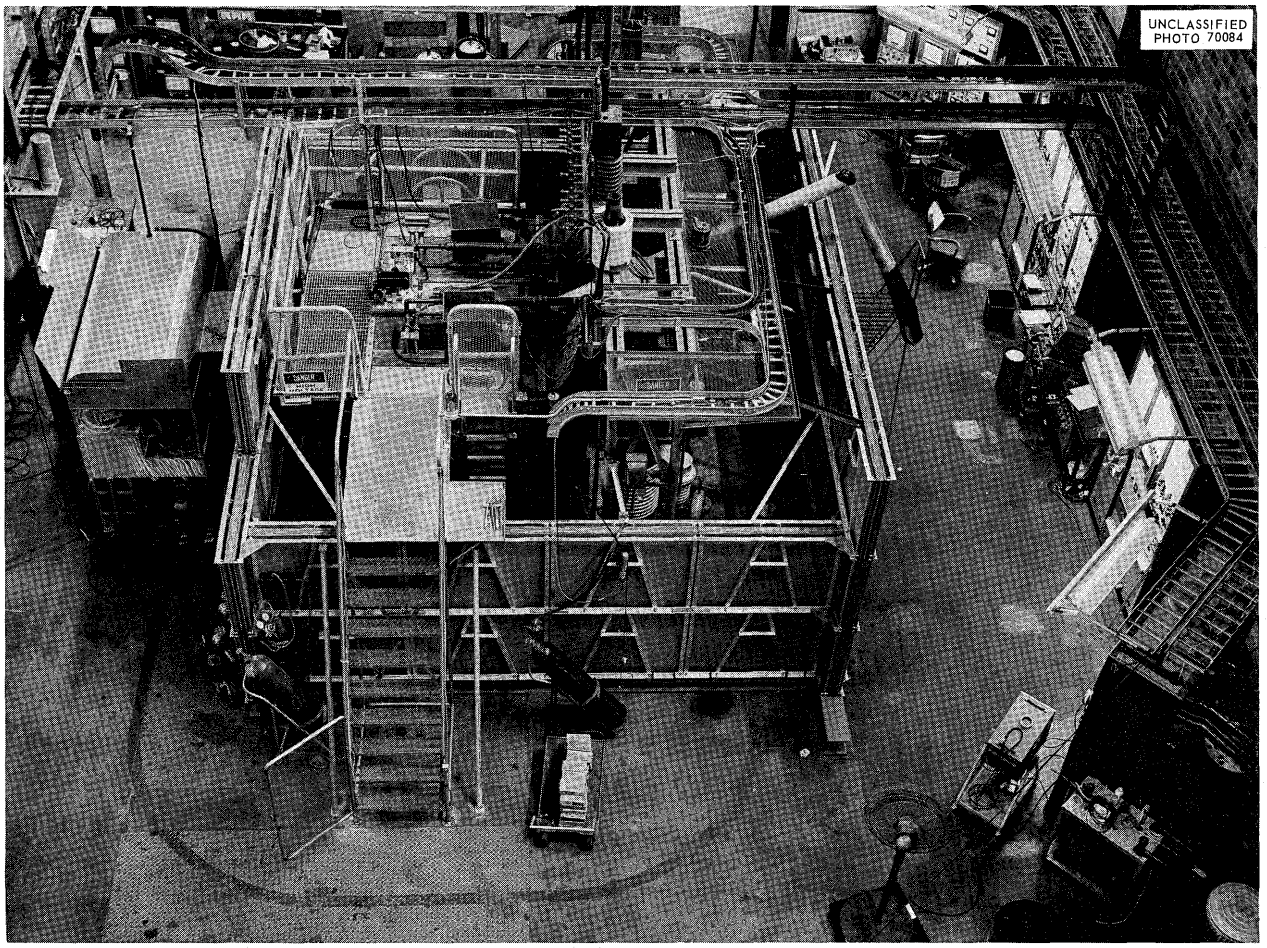

Fig. 3.2. Photograph of the Layout of the Apparatus.

Wave Ratio) conditions, the circulators are placed inside the vacuum chamber in order that all waveguide windows may be located in bilaterally matched waveguide sections. The circulators are rated to provide complete protection for the klystron amplifiers at the 20-kw CW level with a matched load at the cavity, or at the 10-kw CW level under short-circuit conditions at the cavity.

Each klystron feeds an array of two diametrically opposite pairs of waveguide ports in the cavity wall. These pairs of ports are spaced at 60° intervals to provide uniform illumination of the plasma. Each pair is symmetrically spaced in the Z direction with respect to the midplane. The total feed array is thus composed of 12 waveguide ports having both θ and Z symmetry. The only interconnection between klystron outputs is mutual coupling through the cavity. This effect is quite small since the plasma is a very lossy medium at electron cyclotron resonance. The arrangement of waveguide feed ports is clearly visible in Fig. 3.4, which is a photograph of the center section of the cavity mounted in an assembly jig prior to installation in the vacuum chamber. The magnetically shielded circulator enclosures are visible on the right side of the photograph.

Due to the relatively high cost of microwave power on a per-watt basis, impedance matching, that is, containing the microwave power in the cavity, is quite important from an economic viewpoint even though the klystrons and waveguide components are capable of operating with severe output mismatch. Power division and matching for the output of each klystron are accomplished

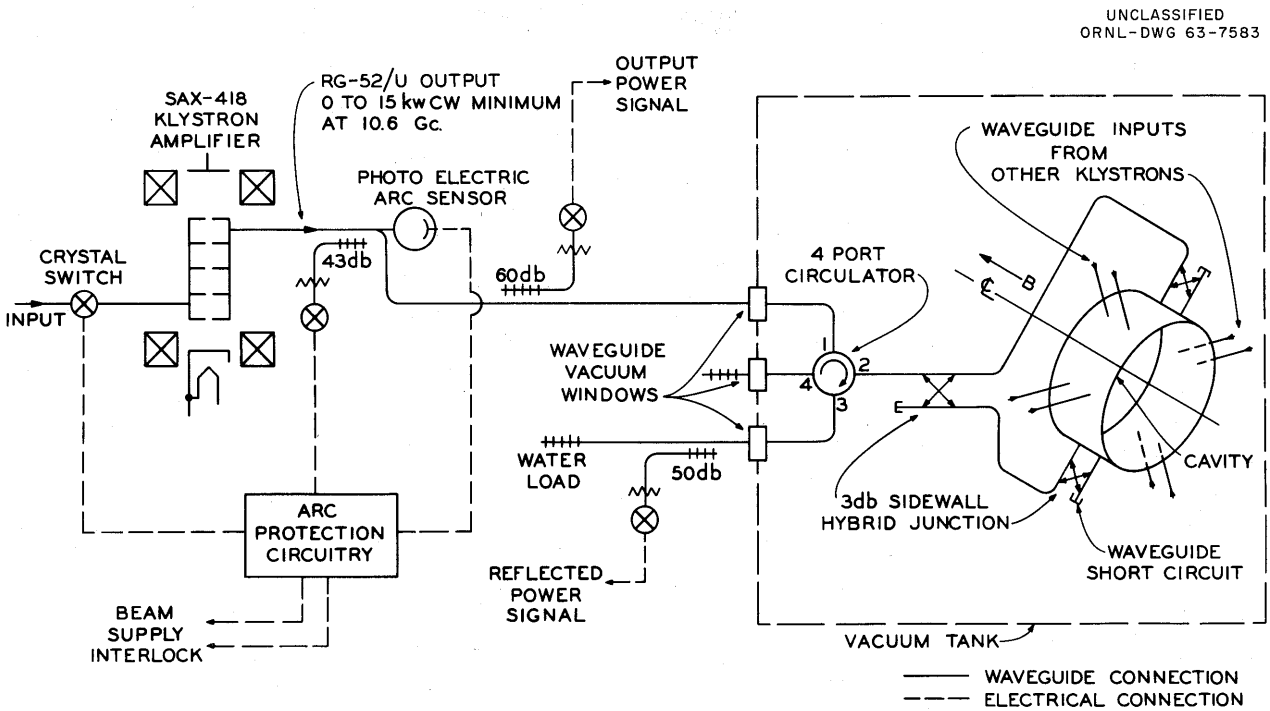

Fig. 3.3. Output Waveguide Circuitry for a Single Tube.

by three sidewall-hybrid junctions of the quadrature type.[4] These hybrids are well adapted to high-power application due to the absence of strong internal electric field gradients. They are four-port broad-band devices which have the important characteristic that when power is fed into one of the terminals, it divides equally between the opposite pair of terminals such that the outgoing voltages at equidistant points are 90° out of phase. Thus if the two outputs are terminated at equidistant terminals in equal impedances $Z_1 = Z_2 = Z$, then destructive interference for reflected power will occur in the primary input arm and the reflections will reinforce in the fourth arm so that all the reflected power exits via the fourth terminal. The input to the hybrid is thus matched for any value of output impedance Z so long as the balance and symmetry remains undisturbed. This important property has long been used in balanced duplexers, phase shifters, broad-band switches, etc., and is used to advantage here in matching the plasma to the waveguide system.

[4]H. J. Riblet, *Proc. Inst. Radio Engrs.* **40**, 180–84 (1952).

In this application, each pair of the aforementioned waveguide ports in the cavity wall is fed by a single short-slot hybrid junction having equal-length output arms. In addition, the individual ports of each pair are located symmetrically with respect to internal cavity surfaces and to the plasma itself. The equivalent impedances terminating the output arms of individual hybrids are thus made to be approximately equal for both static and dynamic (plasma-related) conditions. The fourth arm of each hybrid is terminated in a low-loss short circuit which re-reflects most of the primary reflected power back into the plasma chamber. The equivalent mismatch at the input of the hybrid (expressed in decibels as return loss) is thus improved by a factor of 2 over that existing at a given waveguide port at the cavity wall.

This method of matching the waveguide system to the plasma chamber has proved to be quite effective in practice. Total power absorbed in the water load of Fig. 3.3 due to mismatch and mutual coupling from other klystrons is typically about 100 w when operating at full output under stable plasma conditions.

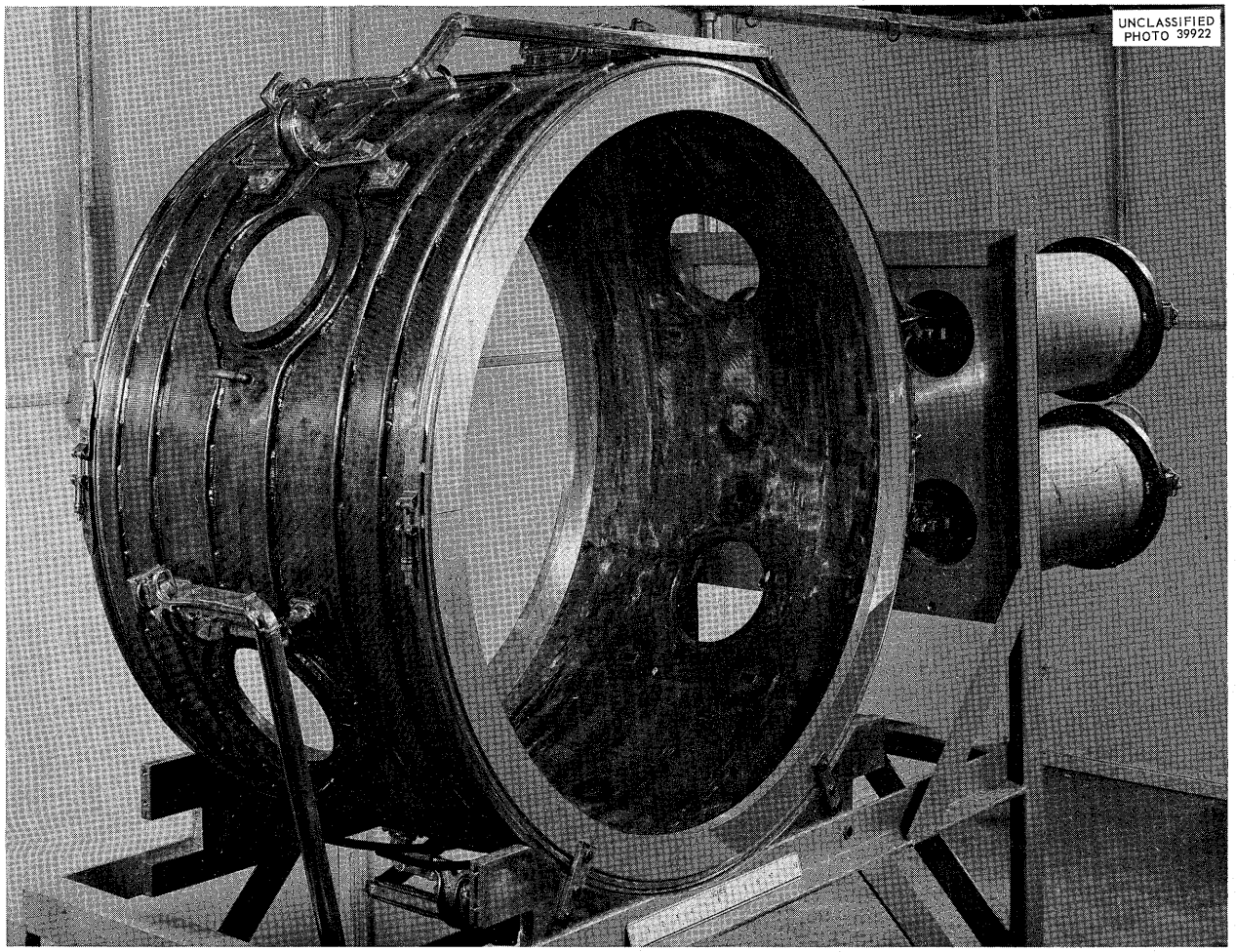

Fig. 3.4. Center Section of the Microwave Cavity Showing the Waveguide Connections and Circulator Housings.

A number of continuous monitors are provided at the operating console in addition to the necessary controls and monitors for microwave power, magnetic mirror field, and gas feed rate. Microwave noise radiated by the plasma into a 1.25-cm waveguide provides a continuous indication of electron noise "temperature," and Hall-probe measurements of diamagnetic B_z in the midplane provide continuous indication of stored-energy–density product. These two plasma parameters serve as a very important yardstick for gaging performance and stability of operation. In addition, ionization gages provide continuous indication of pressure conditions in the three regions of the vacuum system, and ion-chamber–electrometer combinations provide indication of x-ray radiation levels at strategic locations around the facility.

Typical operating procedure for the performance of plasma experiments in this facility is as follows: With no microwave power applied, the current in the magnetic mirror coils is adjusted to the proper value for electron cyclotron resonance at 10.6 Gc along the desired constant-B contours within the cavity, as indicated by a magnetic field vs current plot for the mirror region. Best operation is normally attained with field current adjusted to place the resonance zones near the entry to the mirror-coil throats. Deuterium gas is then fed into the central region of the cavity at a rate sufficient to raise the gage pressure in this region to $\approx 2 \times 10^{-5}$ torr (base pressure of vacuum system $\approx 10^{-7}$ torr). This gas feed rate generally results in a stable "overfed" plasma condition as indicated by measurements of plasma parameters. Microwave power is then

applied, increasing very slowly from zero to the desired input level. The plasma is initially formed when the deuterium gas ionizes at a very low input power level. When this occurs, the pressure in the ends of the vacuum chamber promptly rises due to "plasma-pumping" through the mirrors. A corresponding increase in the gas feed rate maintains the center pressure constant after the plasma forms.

Plasma electron noise "temperature" and stored energy are monitored continuously for stable operation as microwave power is increased, and if necessary the gas feed rate is adjusted slightly for stability. Stable operation is indicated by smooth variation and absence of violent fluctuations in the observed parameters. When the desired microwave input power level is reached, the gas feed rate is *reduced* gradually to maximize the indicated plasma parameters under stable conditions. Both parameters usually peak at the same gas feed rate corresponding to a central gage pressure reading of $\approx 1 \times 10^{-5}$ torr. Plasma decay measurements as a function of time are made by simply switching off the drive power to the klystron amplifiers. Once the proper gas feed rate has been determined for optimum stable operation with a given combination of mirror field and microwave power, the feed rate can be left fixed for a series of decay measurements by control of microwave power alone.

Extreme care must be exercised in gas feed control to prevent reducing the pressure too much. There exists at very low pressures ($<5 \times 10^{-6}$ torr) a region of highly unstable operation accompanied by extremely high levels of x-ray radiation and extreme mismatch at the waveguide feeds. Once this region is entered, no amount of gas feed variation will stabilize the operation. The only solution then is to reduce the microwave power input to zero, increase the gas feed, and then readjust the microwave power to the desired level. An interesting characteristic of the instabilities generated in this region is discussed in Sect. 3.1.8.

Operation of this facility has proven to be quite straightforward and noncritical as compared to some of the earlier systems, since stable plasma conditions occur for a wide range of operating parameters. This has permitted the successful performance of a wide variety of plasma experiments in the facility within a very short period after its completion.

3.1.3 Bremsstrahlung Measurement

The energy radiated per centimeter of path by an electron of kinetic energy E is given in the nonrelativistic limit by[5]

$$-\frac{dE}{dx} = \frac{16}{3} Z^2 n_+ \frac{r_0^2}{137} mc^2 \text{ ergs/cm} , \qquad (1)$$

where n_+ is the density of nuclei. The energy radiated per unit path length is independent of the electron energy. The energy radiated per second is Eq. (1) multiplied by the electron velocity:

$$-\frac{dE}{dt} = \frac{16}{3} Z^2 n_+ \frac{r_0^2}{137} mc^2 \sqrt{\frac{2E_0}{m}} \qquad (2)$$

$$= 1.19 \times 10^{-19} Z^2 n_+ E_0^{1/2} \text{ ergs/sec} .$$

To a good approximation, this energy is radiated more or less uniformly over the whole range of photon energies up to the electron energy E_0. Thus the spectral intensity of radiation of photons at an energy E due to an electron with energy E_0 is, for $E < E_0$,

$$i_{(E)} = \frac{1.19 \times 10^{-19} Z^2 n_+ E_0^{1/2}}{E_0} \text{ sec}^{-1} (E_0 \text{ in ergs}) \qquad (3)$$

$$= \frac{3.0 \times 10^{-15} Z^2 n_+ E_0^{1/2}}{E_0} \text{ sec}^{-1} (E_0 \text{ in kev}) .$$

Given a distribution of electrons such that the number of electrons per cubic centimeter with energy between ϵ and $\epsilon + d\epsilon$ is $f(\epsilon)\, d\epsilon$, then the total spectral intensity of radiation at the energy E is given by

$$I_{(E)} = \int_E^{\infty} \frac{3.0 \times 10^{-15} Z^2 n_+ f(\epsilon)\, d\epsilon}{\epsilon^{1/2}}$$

$$\text{sec}^{-1} \text{ cm}^{-3} (\epsilon, E \text{ in kev}) . \qquad (4)$$

This integral can be evaluated if $f(\epsilon)$ is known; or if the energy spectrum is obtained experimentally, the distribution function $f(\epsilon)$ can be determined.

[5] W. Heitler, *The Quantum Theory of Radiation*, 3d ed., p. 252, The Clarendon Press, Oxford, England, 1960.

For a Maxwellian distribution,

$$f(\epsilon) = \frac{2n_- \epsilon^{1/2}}{\pi^{1/2} T^{3/2}} e^{-\epsilon/T} , \qquad (5)$$

and Eq. (4) becomes

$$I_{(E)} = \int_E^\infty \frac{6.0 \times 10^{-15} Z^2 n_+ n_-}{\pi^{1/2} T^{3/2}} e^{-\epsilon/T} d\epsilon \qquad (6)$$

$$= \frac{3.38 \times 10^{-15} Z^2 n_+ n_-}{T^{1/2}} e^{-E/T} \quad \text{sec}^{-1}\ \text{cm}^{-3} .$$

The number of photons per kev per sec per cm^3 at energy E (kev) is given by

$$n = \frac{5.42 \times 10^{-24} Z^2 n_+ n_-}{T^{1/2} E \times 1.6 \times 10^{-9}} e^{-E/T} . \qquad (7)$$

The total number of photons per sec per cm^3 above the energy E_1 is given by

$$N = \frac{3.38 \times 10^{-15}\ Z^2 n_+ n_-}{T^{1/2}} \int_{E_1}^\infty \frac{e^{-E/T}}{E} dE . \qquad (8)$$

For $E_1 = T$, the integral in Eq. (8) has the value 0.2194.

In several previous semiannual reports, plasma-bremsstrahlung measurements have been reported. An improved collimator was built during the period of this report, and extra care was taken to eliminate scattering from the collimator walls and x-ray transmission through the sides of the collimator. In addition, high-intensity gamma-ray sources were placed in the EPA facility to locate the volume scanned by the collimator.

The bremsstrahlung was observed by a 3 × 3 in. NaI(Tl) crystal which was mounted 23 ft away from the axis of the machine and viewed ~40 cm^3 of plasma through thin aluminum windows. The fractional solid angle subtended by the crystal through the collimator was $\sim 6.5 \times 10^{-7}$. Figure 3.5 shows a 1-min count of the plasma bremsstrahlung at 25 kw with D_2 gas feed at a magnetic field of 2000 amp. Also shown is a spectrum taken after turnoff. The sum of counts made after ten turnoffs between 1 msec and 1 sec after turnoff is also shown. The two spectra have the same shape.

To achieve this, it was necessary for the analyzer to look into a "black" hole on the opposite side of the cavity. This hole consisted of an 0.010-in. aluminum window at the end of a tube which in turn was surrounded by lead to shield the surface seen by the collimator from the intense soft x rays produced at the mirrors. It was previously noticed that the spectra before turnoff were distorted in the vicinity of ~100 kev due to the scattering of the soft

UNCLASSIFIED
ORNL-DWG 63-7283A

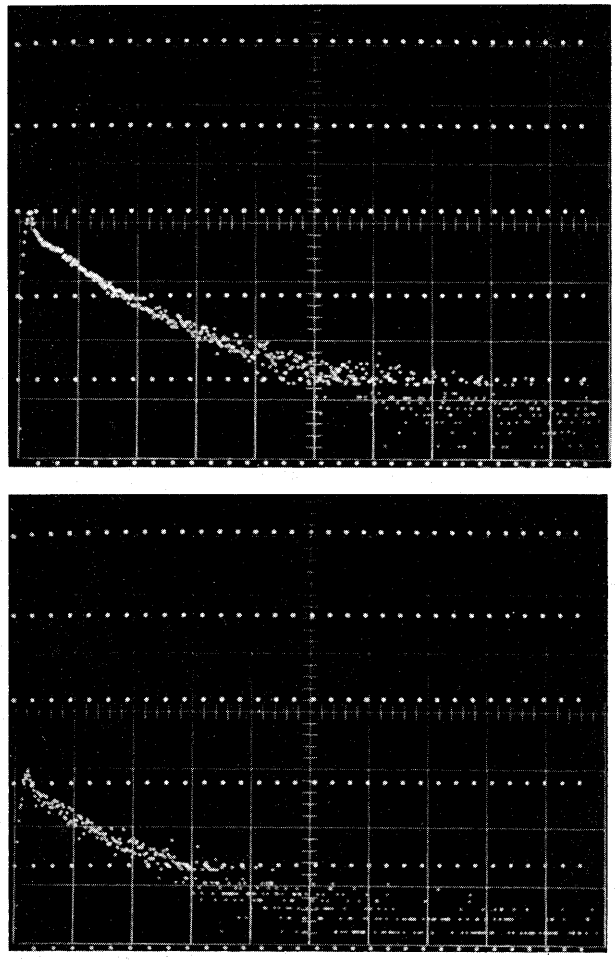

25-kw MICROWAVE POWER
2000-amp FIELD CURRENT
DEUTERIUM PLASMA
1 Mev FULL SCALE

Fig. 3.5. The Spectra of X Rays Produced by the ECP in the EPA Facility as Analyzed by a 512 Channel Analyzer. There is a logarithmic ordinate and a linear abscissa. The upper spectrum is a 1-min count with the machine on while the lower is a composite spectrum of the counts taken after 10 turnoffs between 1 msec and 1 sec after the turnoff.

x rays by the back wall. After turnoff, this intense x-ray source disappeared within a few milliseconds and this effect was not observed in the spectrum. The above mentioned "black" hole largely eliminated this effect. Comparison of this spectrum with Eq. (7) indicates a temperature of ~120 kev. The density as determined from the solid angle, the counting rate above 120 kev, and the total plasma volume viewed by the collimator is 4–7 × 10^{11} electrons/cm^3.

Defining $\beta = 8\pi nE/B_0^2$, where B_0 is the undisturbed (vacuum) magnetic field on the axis at the midplane, and nE is the energy density of the plasma, then $\beta \cong 0.4$ for this plasma.

One difficulty with the measurement is bremsstrahlung production from plasma ions with $Z > 1$, in particular, copper which is sputtered off the walls. Although no Cu II light is seen from the cavity, this cannot be ruled out as a source of error. In addition, scattering in the collimator itself is known to be present and probably influences the spectrum shape.

3.1.4 Flux Measurements of the Total Energy

For the purpose of measuring the total energy stored in the plasma, a 50-turn 36-in.-diam coil was wrapped around the cavity ~10 in. from the midplane. The voltage induced in this coil by the decaying plasma was monitored for the turnoffs. The total area under the voltage vs time curve is proportional to the total flux change through the coil in this system. Assuming that the plasma volume consisted of a cylinder whose cross-sectional area was small compared to the flux coil (as estimated from radial Hall-probe scans and x-ray pinhole photographs), then a good estimate of the net number of flux lines passing through the flux coil could be made, that is, the number through the plasma minus the number returning around the plasma inside the flux coils.

If the plasma is assumed to be a cylinder of length $2l$, with total magnetic moment M and a radius which is not large compared with the radius of the coils, the emf induced in the coil by a change in M is given by Eq. (9):

$$\mathcal{E} = \frac{n\,d\phi}{10^8\,dt} = \frac{n\pi}{10^8 l}\left[\frac{Z+l}{\sqrt{R^2+(Z+l)^2}} - \frac{Z-l}{\sqrt{R^2+(Z-l)^2}}\right]\frac{dM}{dt}, \quad (9)$$

where $n = 50$ turns, $Z = 10$ in., $R = 18$ in., and l is the length of the plasma.

A calculation shows that the voltage induced in this coil is given by $\mathcal{E}(v) = 4.65 \times 10^{-8}\ dM/dt$, approximately independent of the length of the plasma. This calculation only assumes that the plasma area is small compared to the coil area. For this plasma at 25 kw, we have $\mathcal{E}\Delta t \cong 3.2 \times 10^{-2}$ v-sec so that the change in magnetic moment is ~7 × 10^5 gauss-cm^3. Using a plasma cross-sectional area of 1250 cm^2, this gives an average field reduction inside of 250 gauss or an average $\beta \cong 0.3$ provided by a plasma energy density of ~7.5 × 10^{16} ev/cm^3.

The value of the plasma cross-sectional area when used here is calculated assuming a plasma of ~8 in. radius. This radius has been estimated from radial Hall-probe scans and from the pinhole x-ray photographs. These measurements are discussed in Sect. 3.1.6 and 3.1.7 respectively. The value of β is in fair agreement with the value determined by the bremsstrahlung measurement.

3.1.5 Decay Times After Power Turnoff

The containment time of the plasma in EPA has shown an increase over that obtained at a few kilowatts in the PTF. Figure 3.6 shows a logarithmic plot of a number of parameters after power turnoff. The decay time of both the Hall-probe signal and the voltage induced in an external coil (labeled $d\phi/dt$) are ~0.4 sec as opposed to decay times of ~0.1 to 0.2 sec for the same parameters in the PTF. In addition the light, detected by a multiplier phototube, shows a long decay component, not observed at all in the PTF. As in the PTF, there is a burst of neutrons after turnoff, about an order of magnitude increase over the neutron rate observed with the power on. These neutrons are largely due to Coulomb dissociation of deuterium. The decay time of the

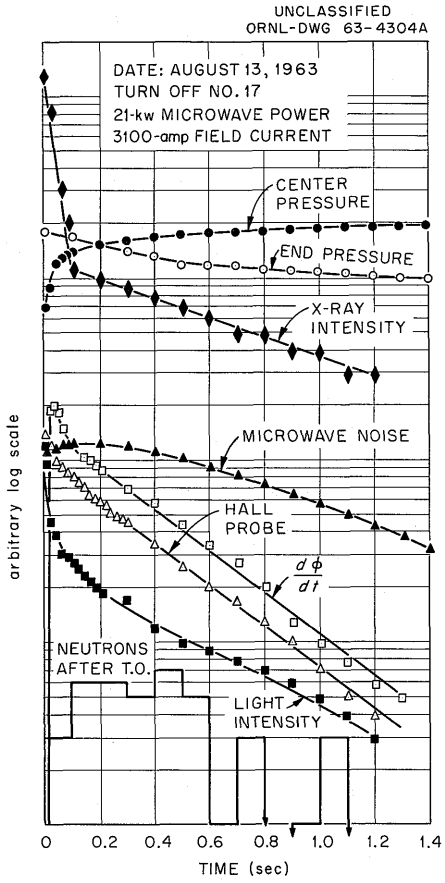

Fig. 3.6. A Semilog Plot of the Variation of a Number of Parameters After Turnoff in the EPA Facility. The curve labeled $d\phi/dt$ is the voltage induced in a coil wrapped around the cavity. The curve labeled Hall Probe is the magnetic field measured near the cavity surface.

energy density is appropriate to the self-collision time[6] for a hot-electron plasma of a density of $\sim 10^{12}$ and a temperature of ~100 kev.

3.1.6 Radial and Axial Hall-Probe Scans

Scans of the radial and axial variation of the Z component of the plasma magnetic field were performed as mentioned in Sect. 3.1.1. These were done in a similar manner and with similar apparatus to those performed on the PTF and described in a previous semiannual report.[7] Figure 3.7 shows axial scans at several values of external magnetic field coil current. This variation in coil current changes the resonant-heating-zone position quite drastically; for example, at 2000 amp the resonant-heating zone crosses the axis at ~9 in. from the midplane, while at 3200 amp the zone crosses the axis at ~3 in. It is seen that the general shape of the curves does not depend strongly on the heating-zone position. The plasma would appear then to have approximately the same effective axial length regardless of the heating-zone position. However, the influence of the inserted axial probe wall on these curves may be considerable.

Figure 3.8 shows a plot of the variation of the external Z component of the plasma magnetic field as a function of radius at the midplane. This was measured by a Hall probe in a water-cooled well. The probe well remained fixed at a point far outside the plasma while the Hall probe was moved inside of it to make the measurement. While the magnitude changes, the functional dependence on radius is not significantly affected by the variation in external magnetic field coil current. This implies that the plasma radius is not a strong function of the position of the cyclotron resonant magnetic heating surface.

[6] L. Spitzer, Jr., *Physics of Fully Ionized Gases*, 2d ed., chap. 5, p. 133, Interscience, New York, 1962.

[7] *Thermonuclear Div. Semiann. Progr. Rept. Apr. 30, 1962*, ORNL-3315, sect. 3.1.

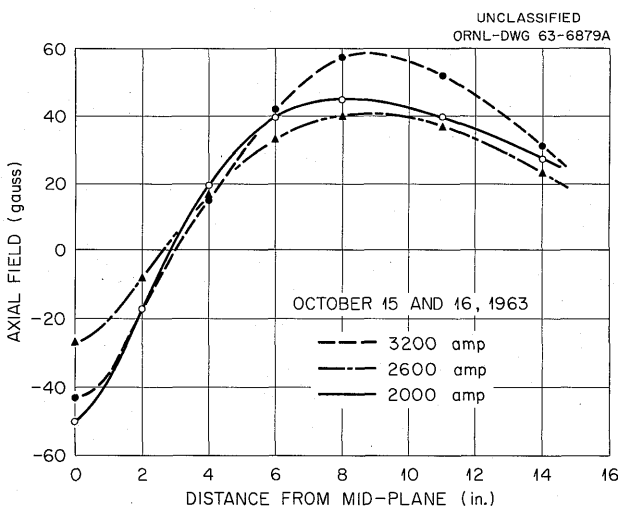

Fig. 3.7. The Axial Variation of the Z Component of the Plasma Magnetic Field. The Hall Probe is moved inside a stationary water-cooled well.

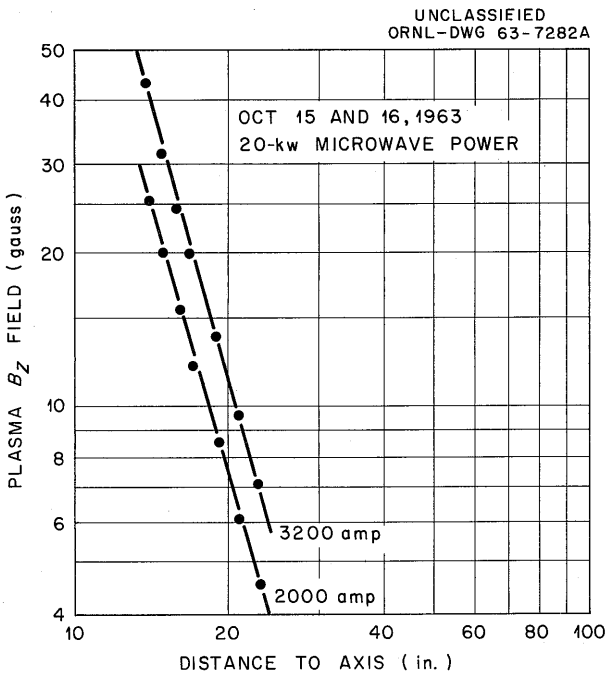

Fig. 3.8. The Radial Variation of the Z Component of the Plasma-Magnetic Field on the Midplane. The Hall Probe is moved inside a stationary water-cooled well. Both are kept far outside the plasma.

Another scan was made, not shown here, which consisted of inserting both the well and probe deeper into the cavity. The same type of behavior was observed with the exception that when the radius of the end of the well was less than 8 in., a sharp drop in the energy density occurred. This is taken as further evidence of the plasma radius being ~8 in.

3.1.7 Pinhole-Camera X-Ray Photographs

Figure 3.9 shows a pinhole photograph of the x rays from the plasma. The camera consisted of a lead box mounted in a well in the vacuum system on the midplane. The camera looked through a 0.010-in. aluminum window into the cavity. The camera had a ¼-in.-diam pinhole in a ½-in.-thick gold collimator which fitted into an aperture in a 1-in.-thick lead box. The film used was a Polaroid 4 × 5 film packet with a speed rating of 3200 ASA. The bright semicircles seen at the sides are produced by x rays from electrons striking the mirror throats as they escape out the mirror loss cone. The plasma is the fuzzy region near the center. From the known size reduction in the photograph and densitometer scans of the film, the plasma radius appears to be ~8 in. and the length appears to be approximately 10 to 15 in.

The film is most sensitive to low-energy x rays (the $K\alpha$ absorption edges of iodine and silver) so that there is discrimination against higher energies. For this reason, the scattered radiation from the back wall of the cavity, which distorts the bremsstrahlung spectrum near ~100 kev, should not be a serious source of error.

3.1.8 "Quantized" Instabilities

A peculiar type of instability can be generated in this plasma. This type of instability was seen in the PTF, but not previously reported. An instability can be produced which dumps a large and relatively repetitive amount of energy on the walls of the cavity. As a consequence, certain detectors will see large, separated bursts of x rays. Under a given set of operating conditions (fixed microwave power and location of constant-B surface) the x-ray bursts have a remarkably uniform distribution in size, although their rate of emission may vary greatly with pressure.

Figure 3.10 shows the pulse-height spectrum from an ionization chamber mounted close to the plasma and encased in ~½ in. of lead. Note the scarcity of small burst pulses. Based on a calibration from other known energy sources, the peak of the burst spectrum appears to be ~300 Mev; that is, each plasma instability dumps enough energy on the cavity walls to produce a burst of ionization in the chamber equivalent to a single particle of ~300 Mev depositing all of its energy by ionization in the chamber.

The full width at half maximum of the spectrum is ~200 Mev. The breadth of the spectrum is partly due to the resolution of the chamber and partly due to the fact that the instability does not dump a truly constant amount of energy out of the plasma.

From these data alone, it is almost impossible to determine the total amount of energy dumped from the plasma in one burst. However, from a measurement of the voltage induced in the coil wrapped around the cavity, it is estimated that between 1 and 10 j is dumped during an instability.

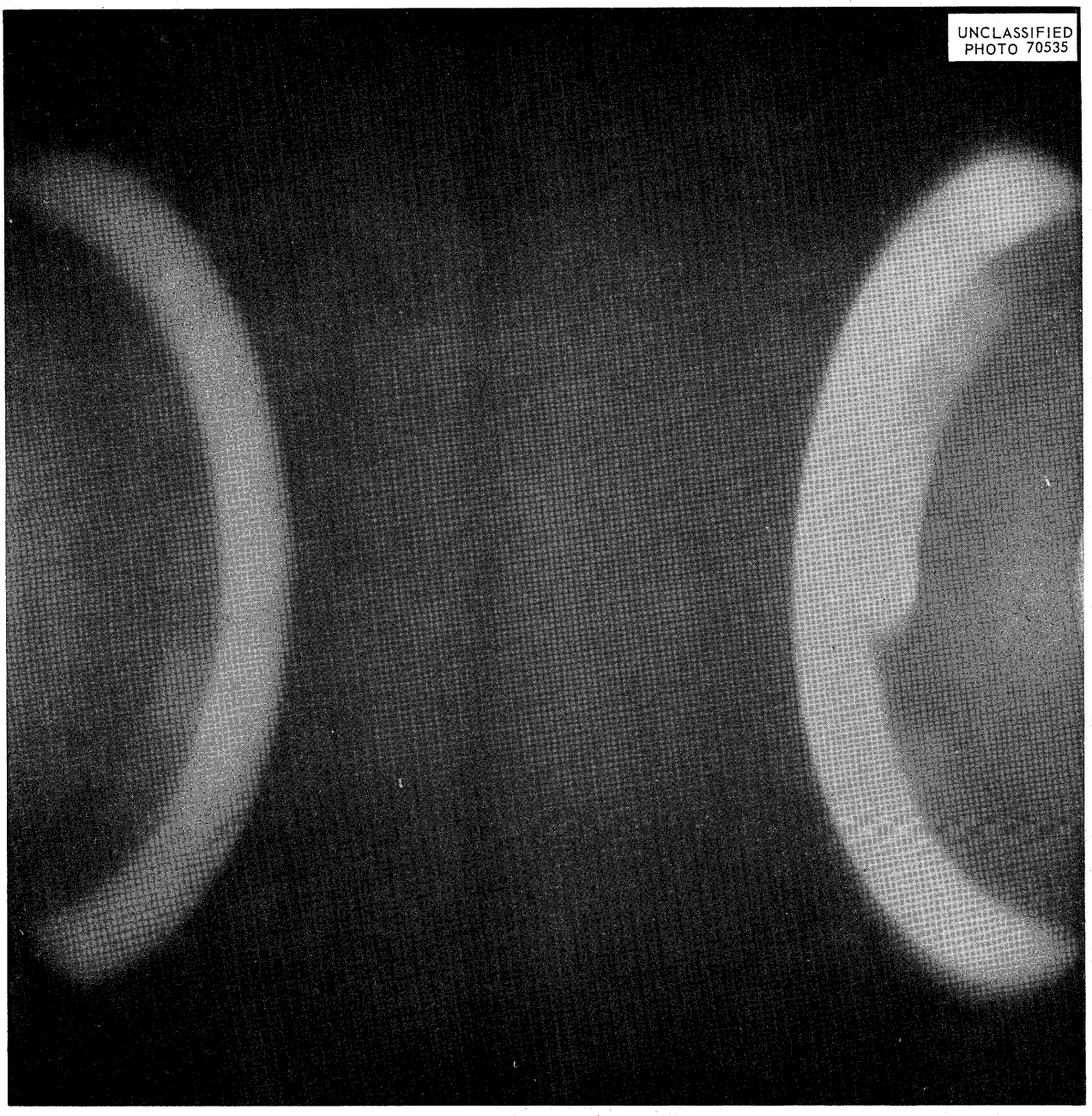

Fig. 3.9. Pinhole Photograph of X Rays from the ECP in the EPA Facility.

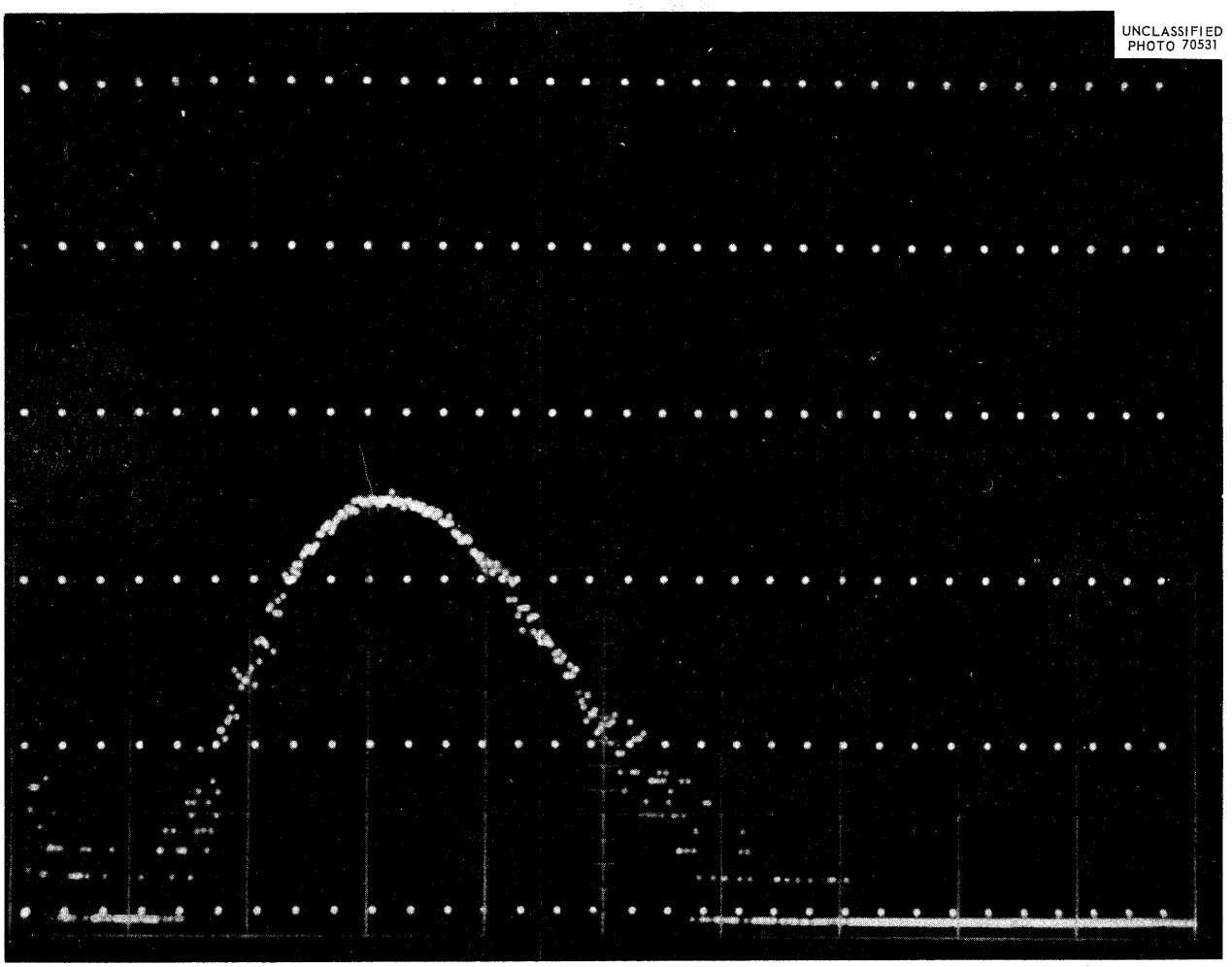

Fig. 3.10. Pulse-Height Spectrum of the Output Pulses from an Ionization Chamber in the EPA Facility. The ordinate is a logarithmic display of the counts per channel while the abscissa is the linear pulse height display. The peak of the spectrum corresponds to a pulse given by depositing ~300 Mev in the chamber.

3.2 EXPERIMENTS ON THE ELECTRON-CYCLOTRON PLASMA IN THE PHYSICS TEST FACILITY (PTF)

W. B. Ard
M. C. Becker[8]
R. A. Dandl[8]
H. O. Eason
A. C. England
G. M. Haas
R. L. Livesey
M. W. McGuffin

3.2.1 Introduction

During the period of this report, further experimentation involving microwave interferometry and instability measurements has been performed on the ECP. Another experiment involving the determination of radial energy-density distribution has been completed and is reported separately in Sect. 3.3.

3.2.2 Plasma Density Measurement by Microwave Interferometry at 8 mm

An 8-mm microwave interferometer with cast metallic gold lenses was installed in the PTF. This interferometer was similar in all respects other than wavelength to the 4-mm interferometer described in the last semiannual report.[9] The results obtained with the new interferometer are not significantly different from those obtained at 4 mm. The measured plasma density is 3 to 10 times lower than that measured by the neutral-

[8]Instrumentation and Controls Division.

[9]*Thermonuclear Div. Semiann. Progr. Rept. Apr. 30, 1963*, ORNL-3472, sect. 3.1.

beam technique,[10] and the density decays in ~100 μsec after turnoff, in disagreement with the decay times of all other parameters. Specifically, the decay times of microwave noise, Hall-probe signals, and voltages from coils wrapped around the cavity all are on the order of ~100 msec or longer. The visible light decays in ~3 msec, about 30 times more slowly than the interferometer decay.

3.2.3 Instability Measurements with Small Coils

Small-diameter, low-inductance flux coils were used to study instabilities in the ECP. By the proper choice of parameters, these instabilities could be completely eliminated or made to occur with almost any desired frequency. The flux coils were mounted in water-cooled, thin-walled stainless steel tubing and inserted axially into the microwave cavity. These coils could detect instabilities removing as little as 3% of the stored energy of the plasma per millisecond. The stainless steel cans used were thin enough so that the coils could detect flux changes with a rise time of 1 μsec or longer without appreciable distortion.

When the plasma was made unstable, the amount of energy dumped could be made as much as 10% of the total energy stored in the plasma. The instabilities lasted up to 10 μsec. As the parameters were adjusted so as to decrease the time between instabilities, the amount of energy dumped decreased from this limit while the frequency of the instabilities increased until the instabilities could no longer be resolved. If the instabilities were made to occur frequently, the interval between them was approximately constant. As the instabilities were made to occur less frequently, the time between them became random.

Production of x rays during the instability indicated that, initially, electrons are lost radially from the plasma. A short x-ray burst at the start of the instability was clearly observed. Later in the instability, a longer x-ray burst appeared at the mirror throat.

Rough absorber measurements on the axial x-ray detector showed that the more energetic x rays occur later in time than the soft x rays. Absorber measurements on the center detector show predominantly soft x rays. This implies that the more energetic x rays are emitted later in the instability and are emitted predominantly through the mirror coils.

Two identical flux-coil probes inserted equal distances axially into both ends of the cavity monitored simultaneous flux changes. These signals indicated that the plasma instabilities were symmetric with respect to the midplane, that is, that there was no net axial displacement of the stored energy.

Observations of the flux-coil signals were also made after power turnoff. Although the probes were too insensitive to see the total slow plasma decay, small rapid fluctuations within a few milliseconds after turnoff could be observed. Both axial probes produced identical signals indicating no net axial plasma displacement after turnoff.

3.3 DETERMINATION OF SPATIAL DISTRIBUTION OF ENERGY DENSITY OF THE ECP IN THE PTF[11]

W. B. Ard
R. A. Dandl[12]
A. C. England
R. J. Kerr[13]

A method of determining the spatial distribution of energy and density in a hot-electron plasma has been used, which consists of dropping through the plasma a probe which collects essentially all the electrons. The probe is a small metallic sphere which is allowed to fall through the plasma. The particle current to the sphere is monitored indirectly by observing the x rays emitted from the sphere and at the same time measuring the rate at which energy is lost by the plasma.

In the experiment, $\frac{1}{8}$-in.-diam stainless steel spheres are dropped from a distance of 2 ft above the center of the plasma. A well-collimated x-ray counter aimed along the axis of the magnetic field records a burst of x rays when the sphere crosses the axis of the field. This x-ray burst serves as a timing marker. The change in energy in the plasma is determined by measuring the emf induced in a

[10] R. J. Kerr, *Nuclear Fusion* (in press).

[11] This section of this report was given as a contributed paper by W. B. Ard at the Sixth International Conference on Ionization Phenomena in Gases (Paris, 1963) and will be published in the Proceedings of that conference.

[12] Instrumentation and Controls Division.

[13] Deceased.

coil surrounding the plasma. The total x-ray production is measured by a scintillation counter located near the plasma. The outputs from these detectors are displayed simultaneously on a fast multichannel recorder.

The rate at which the electrons strike the sphere depends on the rate at which the sphere sweeps out plasma rather than on the velocities of the particles. This is due to the fact that the orbits of the energetic electrons precess in the magnetic field gradient in a time which is several orders of magnitude smaller than the time required for the sphere to fall a distance equal to its diameter. The precessional velocity of the electron is given to first order by

$$v = \frac{\mu c}{eB}\frac{\partial B_z}{\partial r}, \tag{1}$$

where μ is the magnetic moment due to the electron orbit and is equal to $E_\perp/B$. Equation (1) then becomes:

$$v = \frac{c}{e}\frac{E_\perp}{B^2}\frac{\partial B_z}{\partial r}. \tag{1a}$$

The time required for an electron whose orbit is at a distance r from the axis of the field to precess around the axis once is given by

$$T = \frac{2\pi r}{v} = \frac{2\pi r e B^2}{c E_\perp (\partial B_z/\partial r)}. \tag{2}$$

For a simple magnetic mirror field, a good approximation for the field at the midplane is $B_z = B_0 - \alpha r^2$ and $\partial B_z/\partial r = -2\alpha r$. These approximations are good as long as r is smaller than the confining field coil radius. Equation (2) therefore becomes

$$T = \frac{\pi e B^2}{c E \alpha} \simeq \frac{\pi e B_0^2}{c E \alpha}, \tag{3}$$

if r is small.

Equation (3) shows that the precessional period T is, to first order, independent of the distance of the electron from the axis of the field.

In this experiment B_0 is 3000 gauss and α is 3.67 gauss/cm^2. The metal spheres fall at the rate of one sphere diameter in 10^{-3} sec. From Eq. (3), the energy required to give an electron a precessional period this small is 1.7×10^{-10} ergs or about 100 ev. It therefore appears that all the electrons with energy above 100 ev will be swept out by the metal sphere as it falls through the plasma, since the transit time for the electrons between the magnetic mirrors is several orders of magnitude smaller than 10^{-3} sec. Therefore, most of the plasma will have been swept out by the time the sphere reaches the axis of the field.

The change in magnetic field that results from the loss of energy by the plasma is measured by a 50-turn coil with a 12-cm radius located 12 cm from the midplane of the magnetic mirror field. If the plasma is assumed to be a cylinder of length $2l$, with total magnetic moment M and a radius which is small compared with the radius of the coils, the emf induced in the coil by a change in M is given by Eq. (4):

$$\begin{aligned}\mathcal{E} &= \frac{n\,d\phi}{10^8 dt} = \frac{n\pi}{10^8 l}\left(\frac{12+l}{\sqrt{288+24l+l^2}} - \frac{12-l}{\sqrt{288-24l+l^2}}\right)\frac{dM}{dt} \\ &= \frac{1.57\times 10^{-6}}{l}\left(\frac{12+l}{\sqrt{288+24l+l^2}} - \frac{12-l}{\sqrt{288-24l+l^2}}\right)\frac{dM}{dt};\end{aligned} \tag{4}$$

in the limit of small l, Eq. (4) becomes

$$\mathcal{E} = 9.25\times 10^{-8}\frac{dM}{dt}. \tag{5}$$

If l is 12 cm, such that the plasma extends to the plane of the coil, Eq. (4) becomes

$$\mathcal{E} = 1.17\times 10^{-7}\frac{dM}{dt}. \tag{6}$$

Equations (5) and (6) show that the emf induced in the coil is approximately independent of the extent of the plasma in the direction of the magnetic field.

If we assume again that the plasma is a cylinder of length $2l$, then the radial dependence of energy density in the plasma can be determined. As the sphere falls through the plasma, it sweeps out cylindrical shells of plasma. The volume of plasma swept out as the sphere falls a distance dr is given by Eq. (7):

$$dV = (2l)(2\pi r\,dr). \tag{7}$$

The time rate of change of total magnetic moment is then given by

$$\frac{dM}{dt} = \frac{E_r}{dt} = -4\pi l r \frac{E_r}{B_0} \frac{dr}{dt}, \qquad (8)$$

where E_r is the energy density at the radius r and dr/dt is the velocity of the sphere.

3.3.1 Results

Figure 3.11 is a schematic diagram of the cross section of the apparatus showing the relative location of the various detectors, etc. The plasma is produced in the magnetic mirror by a few kilowatts of microwave power at the electron cyclotron frequency.[14] Stainless steel spheres are dropped one at a time from the hopper above the plasma and are collected through the funnel at the bottom.

Figure 3.12 is a multichannel-recorder trace of the outputs of the various detectors during the time it takes a sphere to fall through the plasma. The response of the side x-ray detector looking at the whole midplane of the plasma shows that the peak x-ray production from the sphere occurs earlier than when the peak emf is induced in the coil. This indicates that there is a group of very energetic electrons whose orbits extend outside the main plasma. The low emf produced at the time of maximum x-ray production indicates that these very energetic electrons account for only a small part of the total energy stored in the plasma. The presence of these fast electrons is also evident from the production of neutrons by electron dissociation of the deuterium nuclei.[15]

Figure 3.13*a* is a plot of the emf induced in the coils as a function of time. The minimum in the curve occurs at the time that the sphere crosses the axis of the field (viz., 60 ms). This can be seen in Fig. 3.12 from the output of the collimated x-ray detector which looks down the axis of the field. The emf produced after the sphere has crossed the axis is either due to plasma that the sphere has missed in falling to the axis or to the fact that the microwave power continues to produce plasma while the sphere is falling through the plasma. At any rate, the area under the second part of the curve is only 10 to 15% of that under the first part. The area under the first part of the curve is 1.05×10^{-3} v-sec. Using Eq. (5), this corresponds to a decrease in the total magnetic moment of the plasma of 1.1×10^4 gauss-cm^3. This gives a total energy change of about 4 j.

Shown in Fig. 3.13*b* is a plot of the emf divided by the distance of the sphere from the axis.

[14] *Thermonuclear Div. Semiann. Progr. Rept. Apr. 30, 1962,* ORNL-3315, sect. 3.1.

[15] W. B. Ard *et al., Phys. Rev. Letters* **10**, 87 (1963).

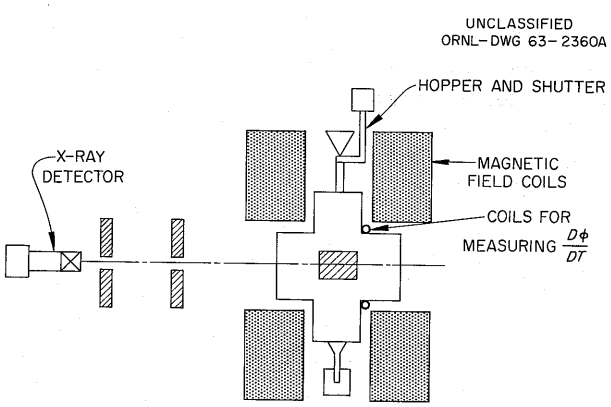

Fig. 3.11. Schematic Diagram of Metal-Sphere Dropping Experiment.

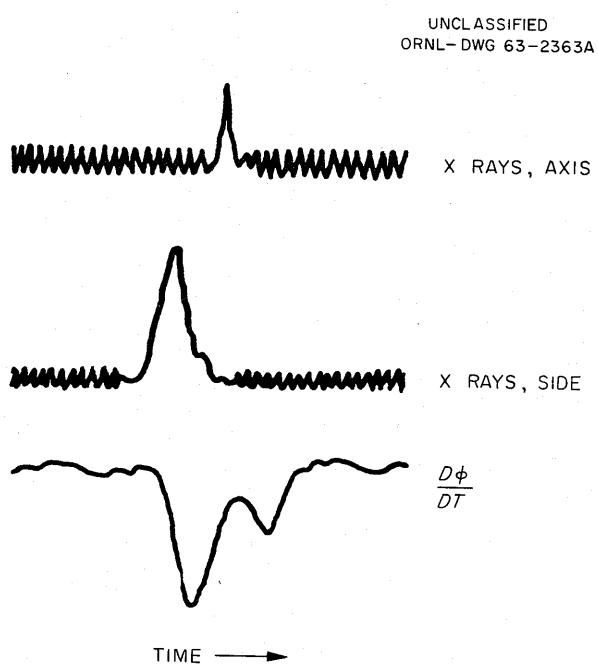

Fig. 3.12. Multichannel-Recorder Trace During the Dropping of a Metal Sphere.

According to Eq. (7) the height of this curve at a given distance from the axis is proportional to the energy density at that distance. This gives an effective radius for the plasma of about 10 cm. The apparent rise in energy density as r approaches 0 is probably due to losses in plasma from processes other than the collision of electrons with the surface of the sphere. Possible processes that would produce nonlocal losses of plasma are losses due to gas being boiled off the surface of the sphere or changes in space charge in the plasma. Even small nonlocal losses produce a large error in Eq. (7) at small radii.

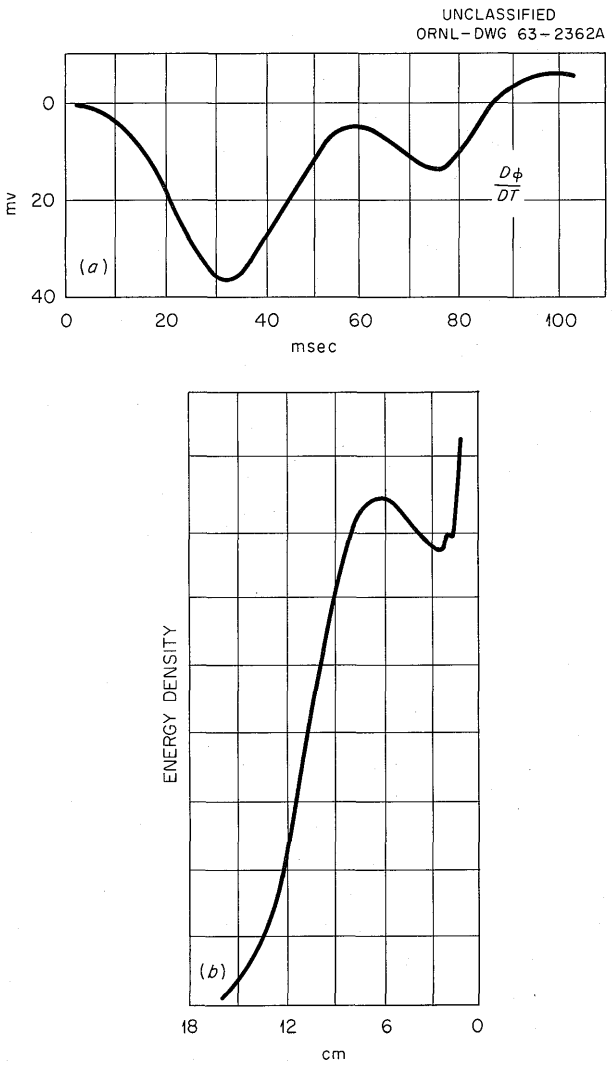

Fig. 3.13. (*a*) **Plot of EMF Induced in Coil as a Function of Time;** (*b*) **EMF Divided by the Distance of the Sphere from the Axis of the Magnetic Field.**

3.3.2 Conclusions

It appears that this method of determining various properties of hot-electron plasmas can be used along with other methods to give information about the spatial structure of the plasma. It should be possible to extend these measurements to give both temperature and number density. This could be done by measuring the x-ray energies as a function of the position of the sphere. Since the x-ray production from the sphere in this plasma is very large, the x-ray energies would have to be measured by placing various absorbers in front of the detector. Since the results obtained are extremely reproducible from drop to drop, the absorber measurements should prove adequate.

One discrepancy in these results should be pointed out. The change in total magnetic moment produced by turning off the microwave heating power is ~2.5 times larger than that produced by the spheres falling through. Part of this discrepancy is due to the fact that the rate at which energy is stored in the plasma by the microwave power is not small compared with the rate at which the sphere sweeps out energy, and the emf is a measure of the net rate of energy loss rather than the rate at which energy is lost on the sphere.

4. Plasma Physics

4.1 STABILIZED PLASMAS

Igor Alexeff R. V. Neidigh

4.1.1 Introduction

The experiments described in this section were attempts to evaluate several combinations of magnetic-mirror and cusp field configurations for their ability to contain plasma. In some thermonuclear experiments,[1-3] plasma between two simple magnetic mirrors has been found to be unstable, escaping from between the mirrors by moving across the magnetic field. Since it is thought to escape more easily across a magnetic field of decreasing strength in the escape direction than across one of increasing strength in the escape direction, the mirror machine in laboratories elsewhere has been modified by adding cusp-shaped fields.[4,5]

In our evaluation, as described in the following paragraphs, we measured the noise, density, and loss rate of a cold plasma contained in some combinations of cusps and mirrors. We found that the basic two-mirror device, with cusps formed by adding axially parallel but oppositely directed uniform field, had better containment characteristics than with axially perpendicular cusps added after the manner of Ioffe.[4] We also found that the simple two-mirror device without added cusps is a good container if the plasma electrons are hot. Our criterion for stability is a plasma loss rate from the device which for the cold plasma is not greater than that permitted by ion-ion multiple scattering and which for the hot-electron plasma is not greater than that permitted by multiple scattering of the electrons in collision with atomic nuclei. In the two-mirror device with hot electrons, this criterion was met – even though multiple scattering of hot electrons with atomic nuclei requires the very long decay time of about 0.1 sec.

It should be emphasized that ours is a small-scale experiment with a plasma of cold ions. The usefulness of the apparatus is its flexibility. We suspect that magnetic-field configurations which contain cold plasma poorly will also contain hot plasma poorly, and therefore these results are pertinent where larger machines are contemplated.

This paper presents our criterion for stability first, and then describes three groups of experiments. The first experiments were the measurements of noise, density, and decay time with four- and six-pole axially perpendicular cusps and mirrors – the Ioffe field. The next experiments were measurements of the same parameters with the axially parallel cusps. The last experiments studied hot electrons as a stabilizing feature in the simple two-mirror system.

4.1.2 Stability Criterion

A basic problem in the study of plasma contained between magnetic mirrors is whether or not the plasma is *stable*. By *stable*, we mean that the plasma shows no rapid particle losses due to cooperative effects such as turbulence, flutes, etc. For a quantitative, objective criterion of stability, the above definition can be recast in the following

[1] *Thermonuclear Div. Semiann. Progr. Rept. Oct. 31, 1962*, ORNL-3392, sect. 1.4, p. 7.

[2] W. A. Perkins, R. F. Post, and N. W. Carlson, *Controlled Thermonuclear Research Semiann. Rept.*, UCRL-9969, p. 10 (January 1962).

[3] M. S. Ioffe, R. I. Sobolev, *et al.*, *Zh. Eksperim. i Teor. Fiz.* **39**, 1602 (1960); **40**, 40 (1961).

[4] Y. B. Gott, M. S. Ioffe, *et al.*, "Some New Results on the Confinement of Magnetic Traps," Paper CN-10/262, *Conference on Controlled Nuclear Fusion*, Fontenay-aux-Roses, July 1963.

[5] E. M. Little and W. E. Quinn, *Phys. Fluids* **6**, 875 (1963).

form: A plasma is considered stable if the experimentally measured rate of plasma loss is equal to the theoretically computed rate of plasma loss under the assumption of single-particle, noncooperative, loss mechanisms.

The manner in which the above stability criterion – plasma is lost primarily through single-particle loss mechanisms – is applied to an experimental case is as follows:

First, the various single-particle loss processes for the two components of the plasma, the electrons and the ions, are separately considered. For the electrons, these processes include electron-electron scattering, resulting in the velocity vectors of the electrons rotating into the escape cones of the mirrors; electron-ion scattering; and electron–gas-atom scattering. For the ions, these processes include ion-electron scattering; ion-ion scattering; and ion–gas-atom scattering. For each process a decay constant τ(sec) is defined. This number would correspond to the time required for the plasma density to drop from its initial value to $1/e$ of this value if the loss process being considered were the only loss process present. Notice that this definition does *not* require that the density decay follow an exponential law.

The second step is applying the stability criterion is to consider separately for ions and electrons the various values of τ – the decay time constants for different loss processes. Obviously, the shortest time constant for a given component dominates the particle loss rate. In the case of our hot-electron plasmas, for example, the electron–gas-atom scattering time constant is shorter than the electron-ion and electron-electron time constants, and dominates the electron loss process.

The third step in applying the stability criterion is to compare the shortest time constant, τ, for the electrons with the shortest time constant for the ions, and select the longer of the two as the theoretical time constant of the plasma as a whole. The reason for this third step is that, in general, the more slowly escaping component of the plasma – the electrons or the ions – electrostatically confines the more rapidly escaping component and thereby determines the rate of plasma decay. Thus, in our hot-electron plasmas, the electrons escape more slowly, and determine the plasma decay constant. Conversely, in our plasmas having both ions and electrons cold, the ions determine the decay constant.

If the above stability criterion is applied to the hot-electron plasmas, one finds that the electrons are dominating the plasma decay, and that the primary electron loss process is due to scattering with the atoms of the gas. The experimental decay constant τ agrees quite well with the theoretical decay constant,

$$\tau = \frac{\theta^2 E^2}{2\pi n v e^4 \log_e(a_0 E/e^2)},$$

where E is the electron temperature in ergs, θ is the scattering angle in radians (0.91 was used for a 2.5 mirror ratio), n is the neutral-gas density, v is the electron velocity, e is the electronic charge, and a_0 is the atomic radius. This equation is easily derived from the discussion of the multiple scattering of charged particles given by Fermi.[6] Note that the theoretical τ depends inversely on gas density. The experimental τ also shows an excellent inverse dependence on gas density, confirming the basic loss assumption of electron scattering with gas atoms.

In the case of plasma having both ions and electrons cold – a few ev in temperature – the stability criterion shows that the ions determine the plasma decay and that ion-ion scattering is the dominant ion loss process. The above scattering equation can be modified to correspond approximately to the ion-ion scattering process. The right-hand side is multiplied by $2\sqrt{2}$ to compensate for the collision of identical particles, n is redefined as the ion density, v is the ion velocity, and a_0 is the nearest-neighbor distance. The calculated τ from this modified formula is in fair agreement with the longest experimental values of τ, as will be discussed. The equation of Spitzer[7] for ion-ion scattering also gives τ values in agreement with the longer experimental values. Note that in the theoretical formula for τ, the background gas density does not appear. The experimental values for τ are found to be approximately independent of gas density, supporting the model of plasma loss due to ion-ion scattering.

[6] "Fermi's Nuclear Physics Notes," p. 37 in *Nuclear Physics*, ed. by Orear, University of Chicago Press, Chicago, 1950.

[7] Lyman Spitzer, Jr., *Physics of Fully Ionized Gases*, p. 78, Interscience, New York, 1956.

4.1.3 Cold Plasma with Ioffe Fields

The experimental technique for measurement of noise, density, and decay time of a cold plasma has been described and tested extensively.[8] Its application to this experiment is shown schematically in the inset to Fig. 4.1. Coils which form the magnetic mirrors are indicated. The Ioffe field is produced by the four or six bars which thread the coils. Plasma is generated between the mirrors by the electron beam from a heated, negatively biased cathode. Gas fed into the collimating hole in the anode generates a noisy, unstable plasma. The noise is observed as a fluctuating potential across the small resistance connecting the negatively biased electrodes to ground. The plasma density and decay time can be obtained by time-analyzing this potential after the beam turn-off. S_1 observes the plasma near the axis; S_2 observes the plasma boundary; and S_3 catches the plasma which drifts out radially between the Ioffe bars.

[8]Igor Alexeff, R. V. Neidigh, and E. D. Shipley, *J. Nucl. Energy: Pt C* **4**, 263–66 (1962).

The graph of Fig. 4.1 is a plot of the strength of the Ioffe field vs the distance from the axis at the midplane for four- and six-pole systems. Note that for a given current in the Ioffe bars the magnetic field penetrates further into the plasma region with the four-pole system, but the six-pole system has a greater field strength between the bars. In this experiment the current in the Ioffe bars was increased until the steepest radial field gradient was neutralized as shown in Fig. 4.2. These are calculated field strengths at the midplane; practically, the Ioffe bars were not positioned so that the field could be known to this accuracy. We can only say that at the location of greatest radial falloff in field (between the bars in the midplane), the gradient was essentially zero. Elsewhere, the gradient was reversed. The radial mirror ratio or alpha of Ioffe[4] was essentially unity for the maximum current in the bars. However, the optimum noise reduction, density increase, and longer decay time occurred with much less than the maximum current, as will be shown.

On applying the Ioffe fields to the plasma, the noise reduction, density increase, and longer decay time are impressive. Some typical results are shown in Fig. 4.3, this being a four-pole Ioffe

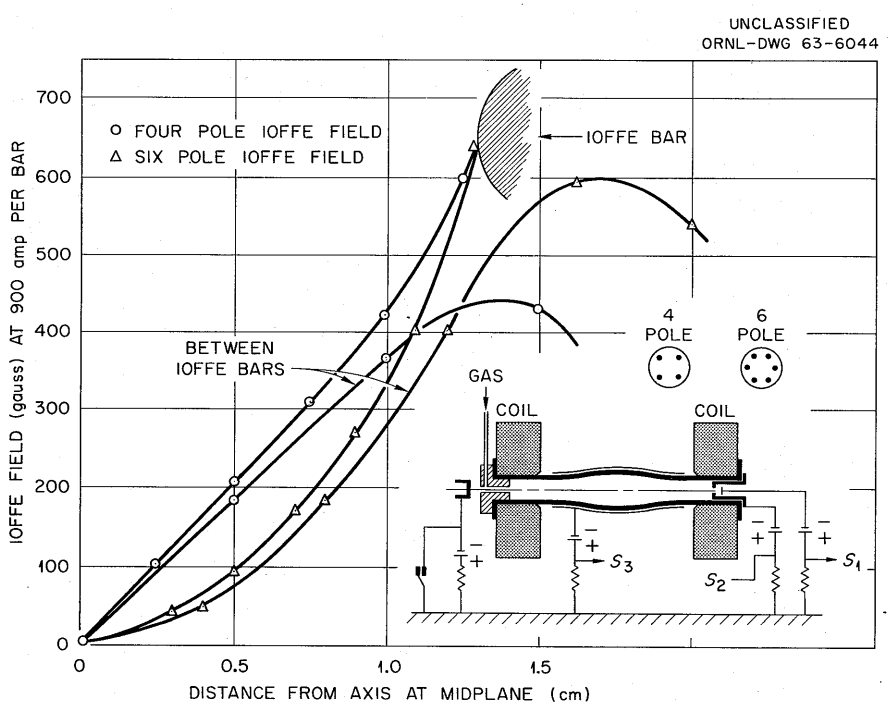

Fig. 4.1. Axially Perpendicular Cusps – the Ioffe Field. Graph: field strength vs distance from the axis. Inset: schematic diagram of the apparatus. Coils are 15 cm apart. All battery potentials are less than 100 v.

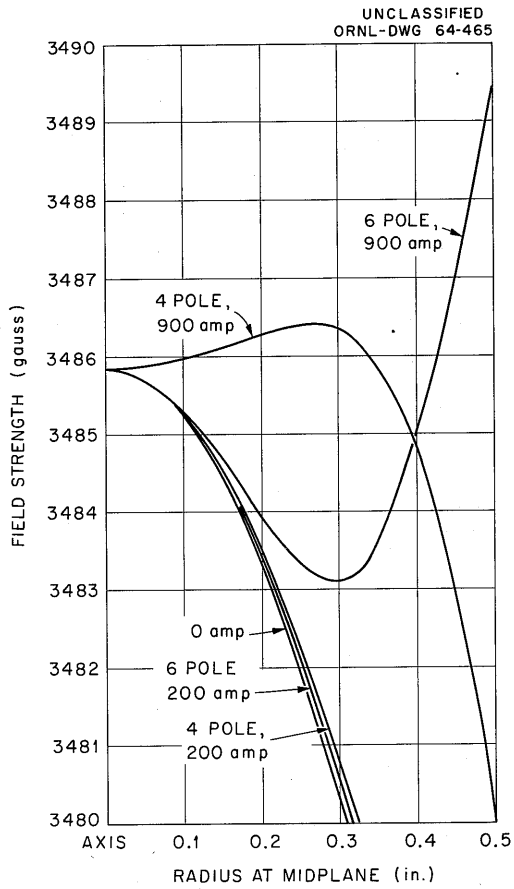

Fig. 4.2. Calculated Total Field Strengths vs Radius Between Ioffe Bars at the Midplane. Curves are shown for 900 amp and 200 amp in 4- and 6-pole systems.

system. The signal to the axial and boundary collectors is compared with the signal to the radial collector. Notice the noise reduction in both the axial and radial collectors (right-hand column). The decaying signal after turnoff is in the left-hand column. Three signals are superimposed to show the nonreproducibility due to plasma noise. The area under the curves, proportional to the plasma density, is seen to increase as the Ioffe field strength is increased. The lower trace is the signal to the radial collector. The plasma lost radially appears to be less and leaks out at a lower rate when the optimum Ioffe field is applied.

The axial and boundary collector signals are observed separately in Fig. 4.4. The application of the optimum Ioffe field reduced the plasma noise on the boundary and significantly increased the plasma density near the axis as well. The optimum effect appears to be at a Ioffe field strength equal to about 15% of the midplane field, or a bar current of about 200 amp.

From this type of data, density and decay time may be graphed against the Ioffe field strength as in Fig. 4.5. This is a six-pole system, but is typical of the four-pole system as well. The density is seen to maximize at 10 to 15% with an increase of almost a factor of 3. The decay time τ maximized at about the same place and has a value of 35 μsec. The radial loss has decreased continuously with increasing Ioffe field. The effect of Ioffe fields on the density of a plasma in a uniform field is shown here for comparison. The mirrors have increased the plasma density, and the Ioffe fields have given further increase to the density and decay time. However, the calculated plasma decay time, for multiple-scattering losses only, is of the order of several hundred microseconds. The implication is that the dissipative mechanism has been only partially removed by the addition of the weak Ioffe fields, but stronger fields appear to be even less effective within the range tested.

4.1.4 Cold Plasma in Cusp Fields

Cusps may be formed by a uniform field added parallel to the axis of a two-mirror system but with opposite direction (Fig. 4.6*b*).[9] The point of zero field strength will be on the axis at the midplane if the uniform field is equal and opposite at this point. A ring of zero field in the midplane will occur if the uniform field is weaker; if it is stronger there will be two points of zero field on the axis between the midplane and the coil throats.

The cusp field of Fig. 4.6*b* with two zero points on the axis has been evaluated, and its ability to contain the cold plasma is compared with that of uniform and two-mirror configurations.[8] Some of the data are shown in Fig. 4.7. The plasma density in the cusp is not accurately known because the volume changes, but it is thought to be greater than between mirrors. The decay time can be found accurately from the data, and is 100 μsec. Note the exact retrace of the five shots in Fig. 4.7, right column, indicating minimal plasma noise.

The cusp field of Fig. 4.6*d* was formed by adding uniform field to the simple cusp of Fig. 4.6c. Its

[9] *Thermonuclear Div. Progr. Rept. Oct. 31, 1961*, ORNL-3239, sect. 3.1.2, pp. 20–22.

UNCLASSIFIED
ORNL-DWG 63-3793A

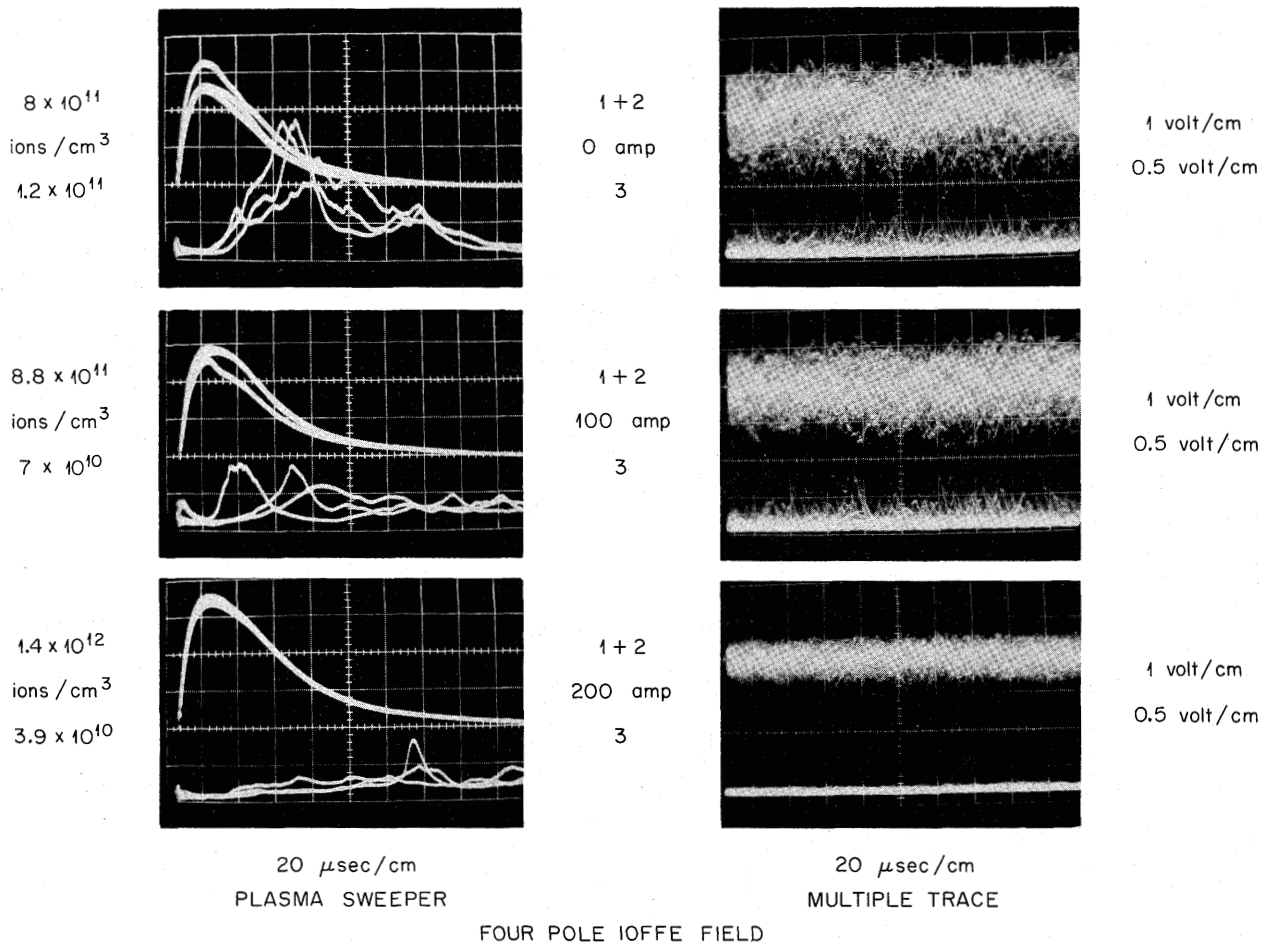

Fig. 4.3. Noise and Density of Plasma Between Magnetic Mirrors with Ioffe Fields Added. Upper traces on each photo are from electrodes S_1 plus S_2. Lower traces on each photo are from electrode S_3. A Ioffe current of 200 amp is a Ioffe field strength, measured between the bars, equal to 15% of the main field, measured on the axis at the midplane.

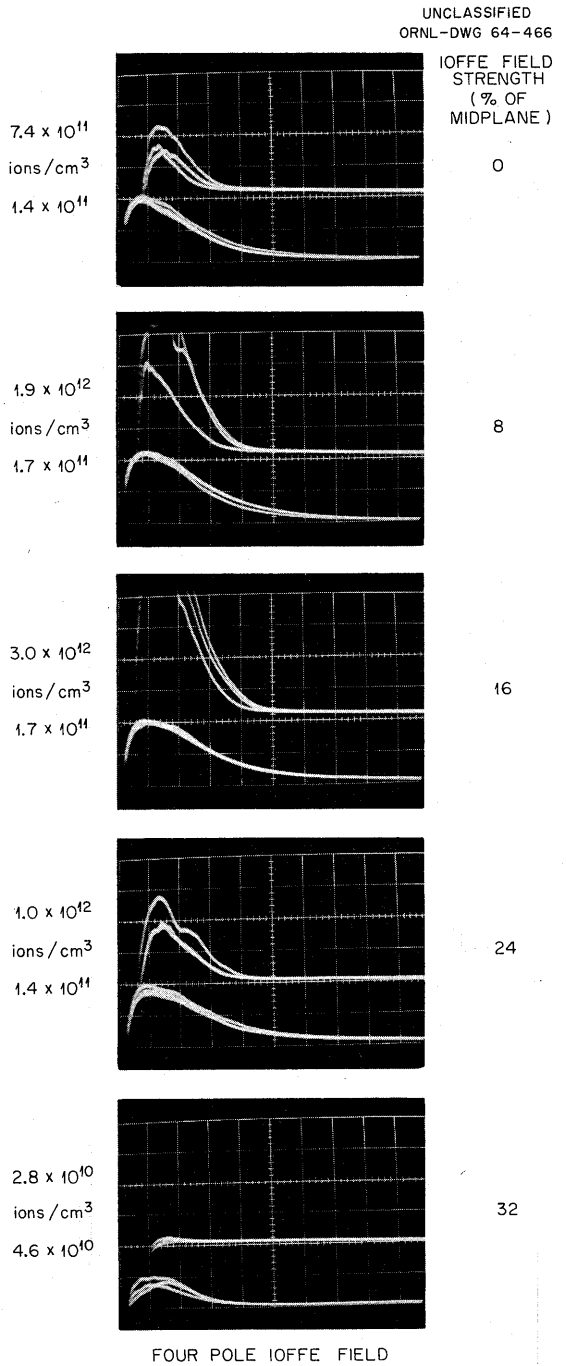

Fig. 4.4. Ion Current to Collectors S_1 (Upper Traces) and S_2 (Lower Traces) After Beam Turnoff. Note that the density (area under the curves) on the axis (upper traces) increased by a factor of about 4 as the Ioffe current was increased from zero (lower traces). At the plasma boundary (lower traces) the density hardly changed, but the addition of the Ioffe field produced less noise (curves retrace). The optimum Ioffe field strength was about 16% of midplane field strength.

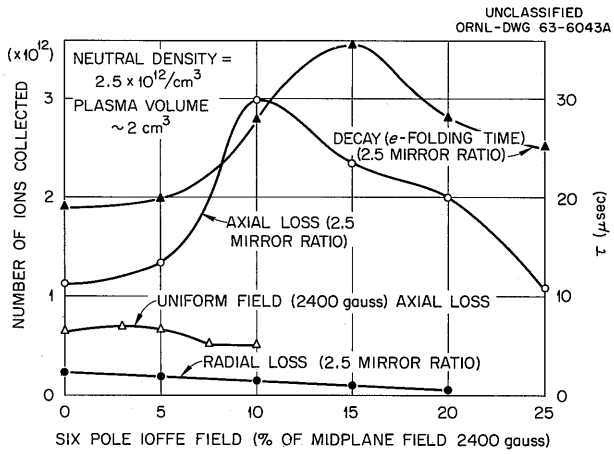

Fig. 4.5. Six Pole Ioffe Field. Note the maximum decay time is 35 μsec. The density of the plasma between mirrors was greater than in a uniform field and the added Ioffe field gave an additional increase in density.

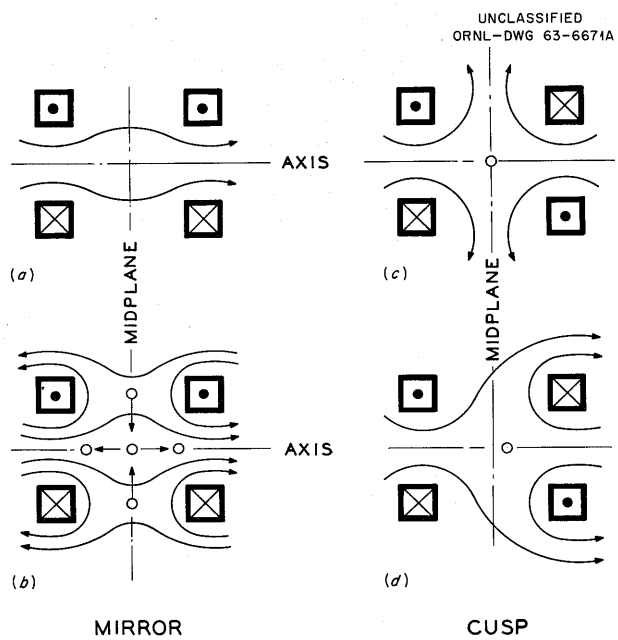

Fig. 4.6. Mirror and Axially Parallel Cusp Magnetic Fields. (*a*) Mirrors only; (*b*) mirrors with uniform field added in opposite direction; (*c*) cusp only; (*d*) cusp with added uniform field.

UNCLASSIFIED
ORNL-LR-DWG 64468A

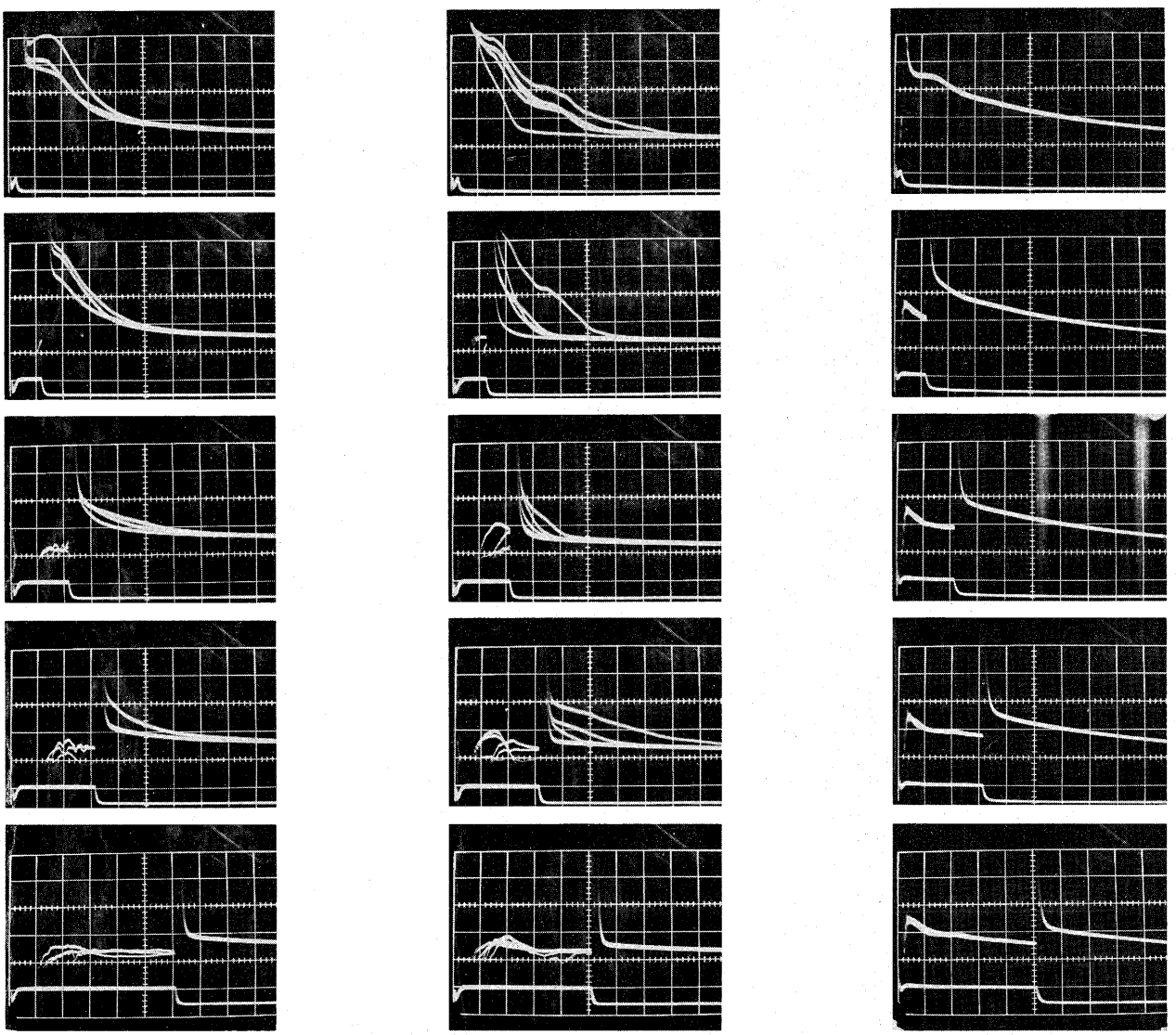

SWEEP = 20 μsec/cm
UNIFORM MAGNETIC FIELD
→ 1400

SWEEP = 20 μsec/cm
MAGNETIC MIRROR GEOMETRY
→ 4300 → 1400 → 4300

SWEEP = 20 μsec/cm
FIELD CUSP GEOMETRY
← 5000 → 50 ← 5000

Fig. 4.7. Comparison of Uniform, Mirror, and Cusp Magnetic Fields for Their Ability to Contain Plasma. In the uniform and mirror fields the plasma is noisy (curves do not retrace). In the cusp the curves retrace and the decay time is 100 μsec. The plasma density is also increased in the cusp though this increase is not apparent due to a vertical scale change.

plasma-containment characteristics are graphed in Fig. 4.8. Here the density and decay time are graphed as a function of the added uniform field. They maximize at a uniform field strength equal to the maximum field strength in the cusp. The subsequent decrease is probably caused by the increasing uniform field which opens one mirror. The plasma noise was minimal and its density was comparable to that achieved with mirrors and Ioffe bars, but the decay time is several times longer and is about equal to the calculated decay time, which considers multiple scattering only.

4.1.5 Hot-Electron Plasma

Apparatus for testing the stabilizing effect of hot electrons in the plasma was essentially the same as for the cold plasma. The Ioffe bars were adjusted to enclose a larger volume, and insulation of the filament was improved to accommodate a 5-kv bias instead of the 100-v bias. Now the plasma is apparently 100% ionized in the defining hole, and beam-plasma interaction heats the plasma electrons between the mirrors to kilovolt temperatures.[10]

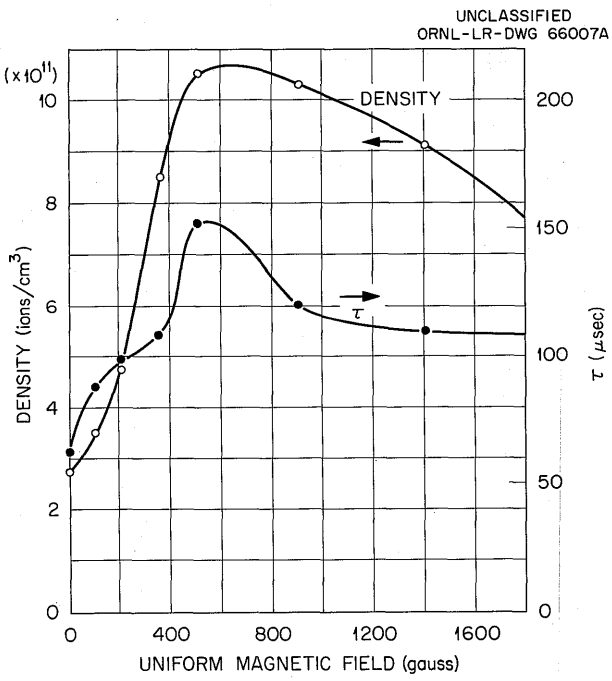

Fig. 4.8. Density and Decay Time of Plasma in Simple Cusp with Added Uniform Field. The maximum field in the cusp annulus was 600 gauss.

The cusp of Fig. 4.6*b* with a ring of zero field in the midplane was tested. The visible light appeared as in Fig. 4.9. An image by bremsstrahlung radiation on x-ray film using a pinhole camera of lead is shown in Fig. 4.10. The x-ray image of the visible plasma is barely seen on the film – it is in the center, on the axis. The large ellipses mark the intersection of the cusps with the vacuum chamber walls. An electron temperature of 25 kev and a decay time of 6 msec were determined from a logarithmic display of the output of an x-ray-excited sodium iodide crystal on a multichannel analyzer. The multiple-scattering equation is approximately satisfied by these values indicating minimal losses by cooperative phenomena. The plasma decay was observed with the multichannel analyzer in a scaling mode. A readout illustrating the method is shown in Fig. 4.11. Essentially it counts x-ray flux every 2 msec after turnoff.

In the simple mirror geometry the beam-plasma heating mechanism[10] is very effective, and the plasma makes an x-ray image similar to the visible image.[11] Here the electron temperature was 130 kev, and the decay time was 70 msec. A hot-electron density of about $10^{11}/cm^3$ was measured by a neutral-beam technique, the x-ray flux intensity, and a diamagnetic probe.[11]

The effect on the decay constant and the electron temperature by the addition of Ioffe fields to this kind of plasma is shown in Fig. 4.12. The solid line is the multiple-scattering formula with decay time plotted against temperature. All the data points except the maximum and minimum ones were obtained with Ioffe bars in place but with different Ioffe field strengths. We think the scatter in the points above and below the line is primarily due to our present inability to measure the decay time accurately – an error which we believe we can reduce. The distribution along the line is just a measure of the effectiveness of the electron heating mechanism, which is disturbed by the presence of the Ioffe bars. Maximum temperature and decay time were obtained with mirror containment only. The stability of the hot-electron plasma appears

[10] Igor Alexeff and R. V. Neidigh, *Phys. Rev. Letters* **10**, 273 (1963).

[11] *Thermonuclear Div. Semiann. Progr. Rept. Apr. 30, 1963*, ORNL-3472, sect. 3.2, pp. 31–37.

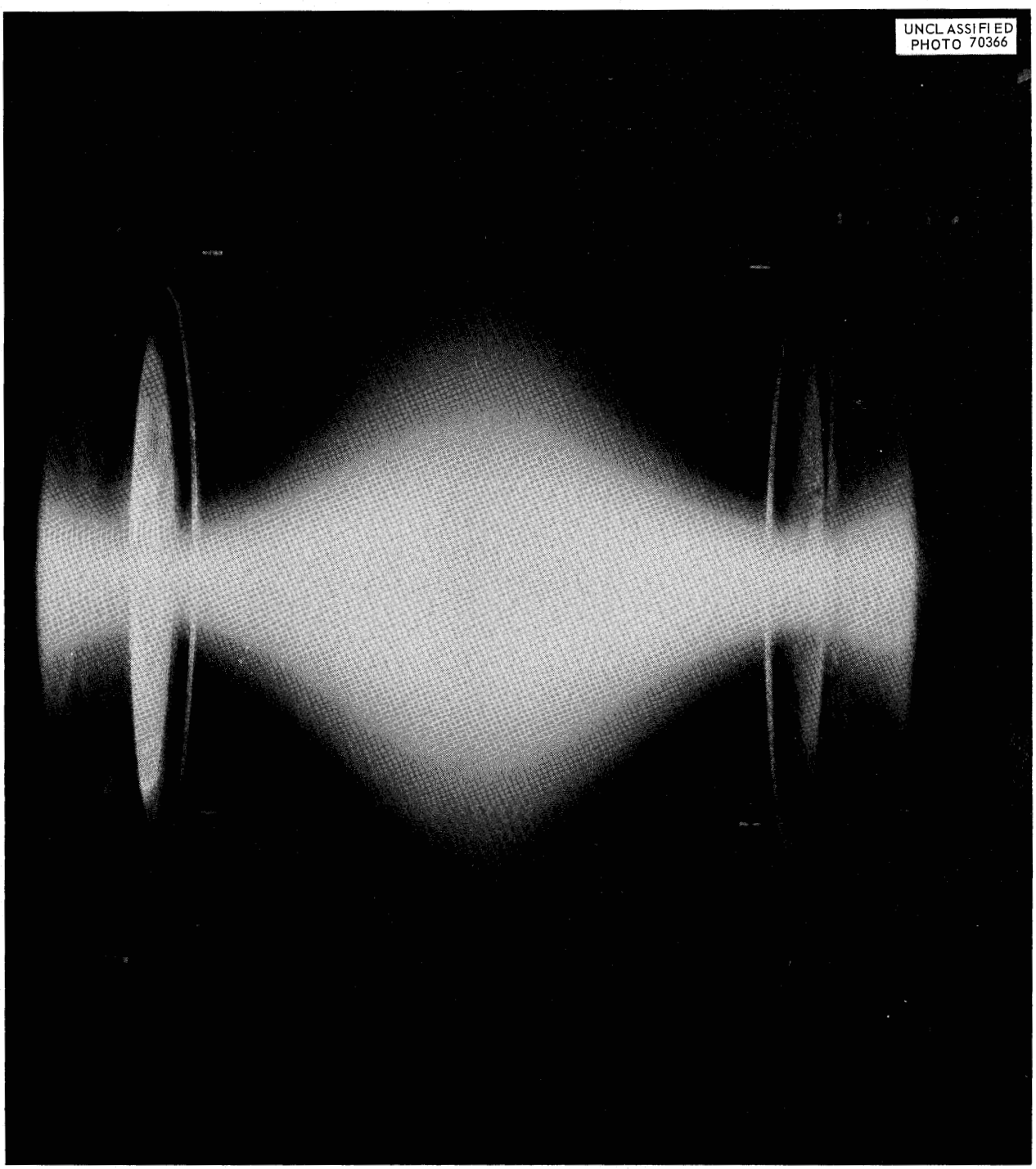

Fig. 4.9. Hot-Electron Plasma in the Cusp Magnetic Field of Fig. 4.6*b*. A ring of zero field lies in the midplane.

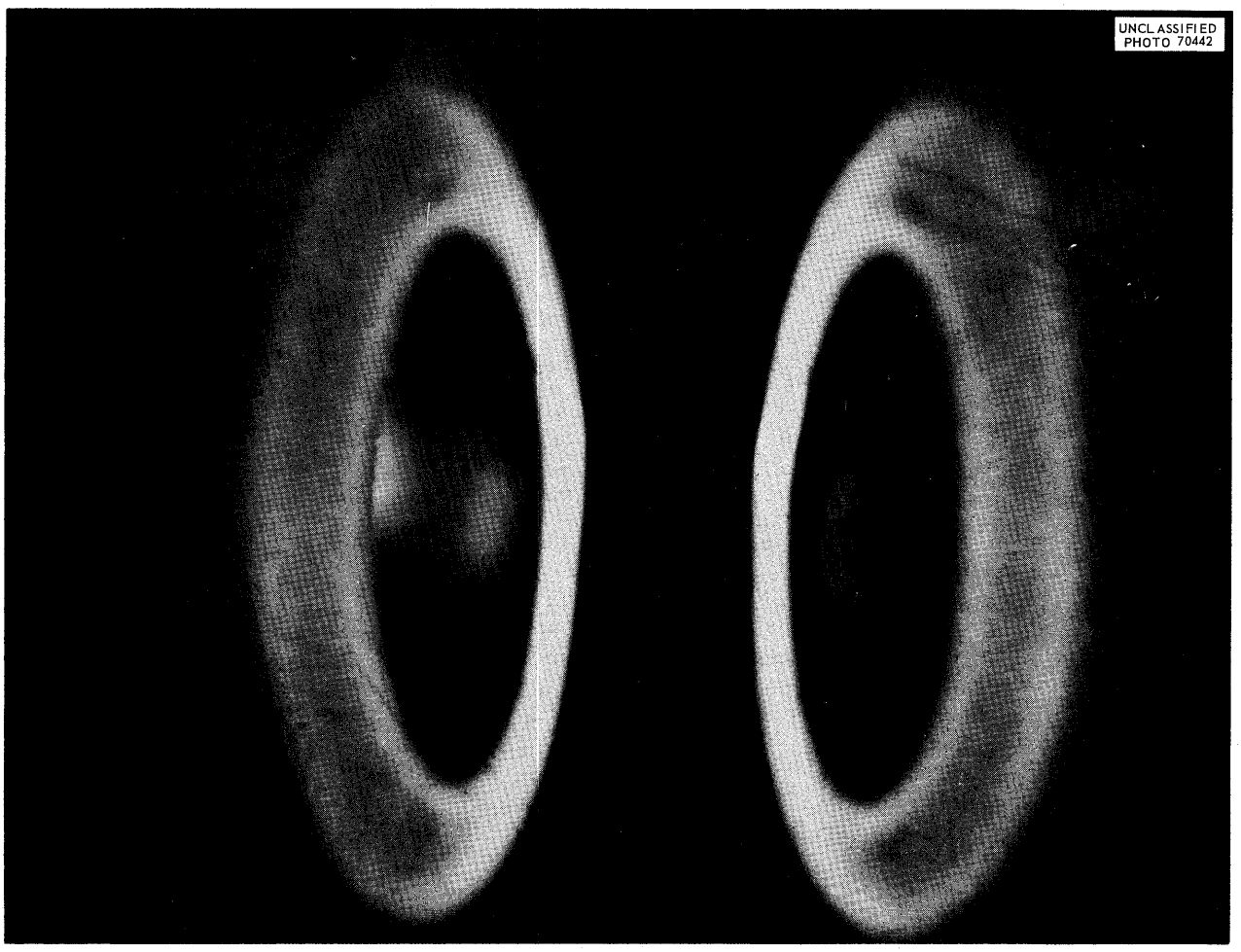

Fig. 4.10. X-Ray Image of the Plasma of Fig. 4.9. The visible plasma is barely seen in the x-ray image in the center on the axis. The large ellipses locate the cusp intersection with the vacuum chamber wall.

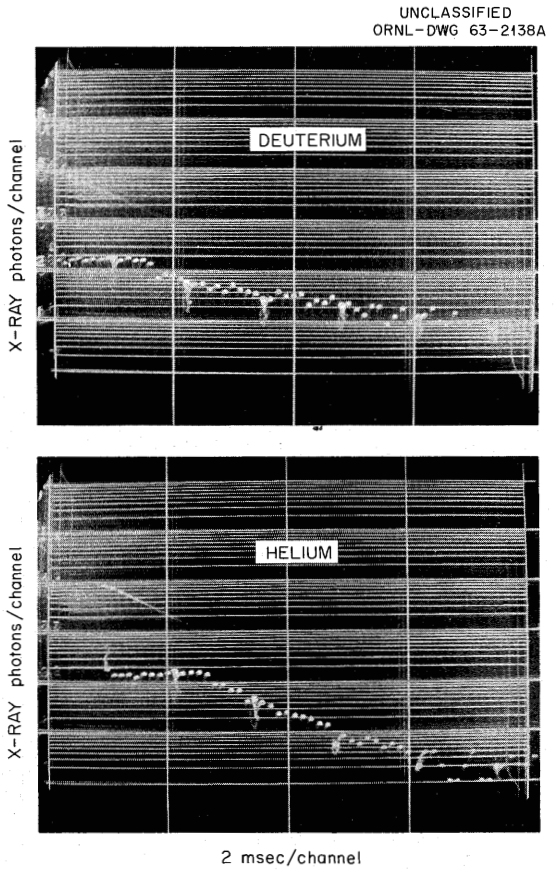

Fig. 4.11. Typical X-Ray Decay of Hot-Electron Plasma. The multichannel analyzer, used in a scaling mode, switches channels every two msec. About 28 msec of steady-state x-ray flux is shown before electron beam turnoff.

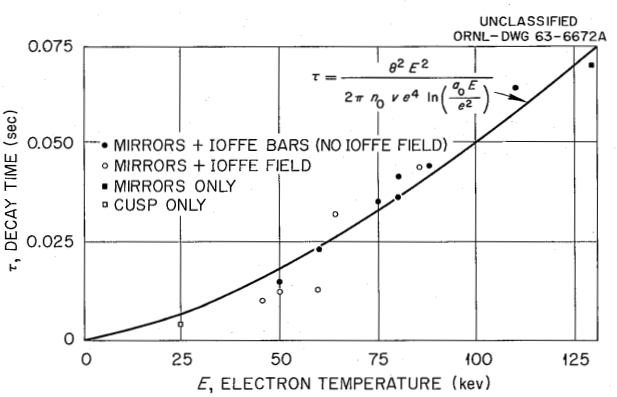

Fig. 4.12. Decay Time vs Electron Temperature of the Hot-Electron Plasma. Scatter of experimental decay time from that predicted by the formula is thought to reflect our inaccuracy in measurement. Scatter of data along the curve reflects the effect on the heating mechanism by the magnetic field shape and strengths.

to be independent of added cusps, either the axially parallel or Ioffe type.

There is additional evidence that this plasma with kilovolt electrons is stable. The decay time has been measured as a function of the neutral pressure. An extrapolation to zero pressure gives an infinite decay time ($1/\tau = 0$). To magnetic and electrostatic probes, the plasma appears noisy in the steady state. This may be due to the high beta. As the plasma decays, the noise abates without any change in the decay time. We feel that the stabilizing effect of hot electrons should not be overlooked in the future planning of thermonuclear experiments.

4.2 MEASUREMENT OF PLASMA DECAY TIME AND DENSITY WITH A CAVITY RESONATOR

Igor Alexeff

In previous studies of the plasma-containment time and the plasma density in a magnetic-mirror apparatus, some inconsistencies were obtained.[12] These inconsistencies are now apparently understood. In this work, plasma density was measured in two ways: first, by measuring the frequency shift of a cavity resonator surrounding the plasma volume; and second, by collecting and measuring the ion current escaping through the magnetic mirrors. The discrepancy observed was that the plasma density as measured by the cavity resonator was always lower by a factor of between 30 and 400 than that as measured by the charge collection technique. However, the decay time constants measured by the two methods were identical.

The explanation of the discrepancy is quite simple – the plasma in the apparatus is now considered to be a hot-electron rather than a cold-ion plasma. Such hot-electron plasmas having electron temperatures of many electron kilovolts were indeed later observed in the same apparatus. This hot-electron plasma gives a decay time constant of the correct order of magnitude. In addition, each hot electron produces many secondary ions and electrons by ionizing the background gas in the apparatus. These secondary ions and electrons are scattered very rapidly out of the magnetic mirrors.

[12] *Thermonuclear Div. Semiann. Progr. Rept. Oct. 31, 1962*, ORNL-3392, sect. 3.5, p. 38.

Thus the cavity resonator apparently measured the actual density of plasma contained in the apparatus, while the ion-current collection technique apparently measured the current of secondary ions produced. The theoretical studies show that, as was observed, the secondary ions should be about 100 times as abundant as the primary electrons, and that the decay time constants for the two measuring processes should be identical. Because of this ionization-chamber effect, the plasma sweeper will not give a reliable measurement of plasma density when hot electrons are present, and its use under such conditions has been avoided.

4.3 FURTHER MEASUREMENT OF IONIC-SOUND-WAVE VELOCITY IN PLASMA BY A TIME-OF-FLIGHT TECHNIQUE

Igor Alexeff W. D. Jones

Further experiments concerning the time-of-flight technique of measuring ionic-sound-wave velocity[13] support the conclusions of our previous report.[14] In this previous work, the ion waves were transmitted through a discharge tube run in an ordinary glow mode (see Fig. 4.13). Ion waves are generated in the tube by a pulser, which increases the anode-cathode potential for a period of a few microseconds. Presumably, ionic sound waves are thereby produced by sheath interactions at the anode and cathode. Now, if the cathode is operated in a space-charge-limited regime, the floating potential of the plasma is observed to go suddenly negative after an appropriate delay, as shown in Fig. 4.14. Presumably, an ion wave from the anode arriving at the cathode neutralizes the cathode space-charge sheath and causes a drastic increase in cathode emission. This negative pulse is very strong and is easily observed above the background noise level of the discharge. The time delay between the initial and the response pulse is proportional to the distance between the anode and the cathode, as would be expected if a wave of constant velocity were propagating between them. The experimental wave velocity (cm/sec) is computed by dividing the distance (cm) between the anode and cathode by the time delay (sec) between the start of the initial pulse and the start of the response pulse.

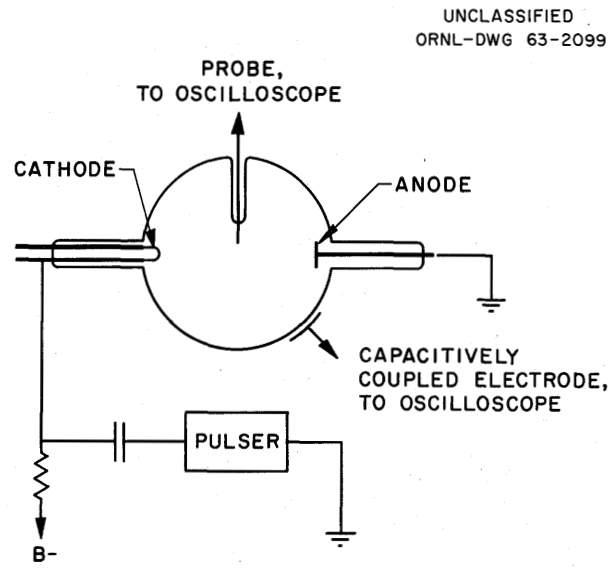

Fig. 4.13. Schematic Diagram of Apparatus.

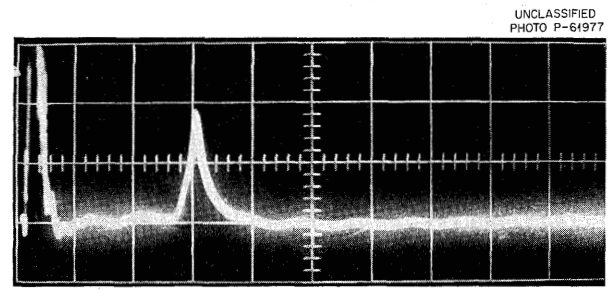

Fig. 4.14. Typical Response Pulse. Neon gas, pressure "high," 5 μsec/large division, 5 cm gap, T_e = 2.1 ev.

Further work has been done which clearly supports the above model of ionic sound waves crossing the discharge tube. The new observations are listed below. Later, a separate paragraph is devoted to each observation.

1. That the experimental value for the ion wave velocity is independent of anode-cathode spacing was verified for many more observations.

2. That the experimental value for the velocity depends on $m_i^{-1/2}$, where m_i is the mass of an ion in the plasma, was verified for many more observations and under better-controlled conditions.

[13] L. Tonks and I. Langmuir, *Phys. Rev.* **33**, 195 (1929).

[14] *Thermonuclear Div. Semiann. Progr. Rept. Apr. 30, 1963*, ORNL-3472, sect. 3.5, p. 45.

3. At the intermediate gas pressures used, a value for the adiabatic compression coefficient for the electron gas was experimentally found to be $^5/_3$, in agreement with theory.

4. Ion wave pulses were produced simultaneously at two anodes, separated by different distances from the cathode. As expected, two ion wave pulses apparently arrived at the cathode at two different times, giving rise to two response pulses.

5. Multiple reflections of the ion wave pulses from the glass walls of the discharge tube were observed.

6. At high gas pressures the response pulse occurred much later in time, corresponding to a wave propagating with ordinary sound velocity in the background gas; apparently, at high pressures, the plasma is carried along with the background gas. At intermediate pressures, both the ionic-sound-wave pulse and the ordinary sound wave pulse were observed.

7. The direction of propagation of the wave front between the cathode and the anode was investigated with a specially designed probe. Preliminary investigations support the hypothesis that the wave front moves from anode to cathode.

These further measurements of the experimental ion wave velocity were made in the same apparatus as used previously (Fig. 4.12). For these measurements, the gas pressure was kept higher than in the earlier work[14] to reduce ion drift velocities by means of ion–gas-atom collisions. To ensure that the ion drift velocity was low, the electric field inducing the drift was experimentally measured by using both cold and hot Langmuir probes. Under the conditions of electric field and of gas pressure present in the discharge tube, the ion drift velocity should have been quite low compared with the ionic-sound-wave velocity.

A second consequence of the higher gas pressures used in the later work – 10 μ and higher – is that the mean collision frequency of an electron with background gas atoms is higher than the ion plasma frequency. As a consequence, the adiabatic compression coefficient of the electron gas, γ, should be $^5/_3$ or 1 in the Tonks-Langmuir velocity equation, $v = (\gamma, kT_e)^{1/2}\ m_i^{-1/2}$. Here, v is the wave velocity (cm/sec), γ is the adiabatic compression coefficient of the electron gas (1, $^5/_3$, or 3), k is Boltzmann's constant (ergs per electron volt), T_e is the electron temperature (electron volts), and m_i is the ion mass (grams).

The following paragraphs discuss in somewhat greater detail the above-listed observations.

1. Experimental results which indicate that the experimental values of the ionic-sound-wave velocity are independent of electrode spacing are shown in Fig. 4.15. For these measurements a discharge tube 20 cm in diameter was used. However, the anode-cathode spacing was varied from 1 cm to 20 cm. Each experimental velocity is normalized to an electron temperature of 1 ev and an ion mass of 1 amu, by multiplying the experimental velocity by $T_e^{-1/2}\ m_i^{1/2}$. Here, T_e is the electron temperature, as obtained by a Langmuir probe measurement, and m_i is the ion mass used. Since the ion wave velocity is independent of electrode spacing, the time interval between the driving and the response pulse is proportional to the distance between the anode and the cathode. Thus the response pulse is *not* due to a relaxation of the plasma in the whole tube, but involves the anode-cathode gap.

2. Experimental results which indicate that the ionic-sound-wave velocity is proportional to $m_i^{-1/2}$ are shown in Fig. 4.16. These measurements were made for a variety of anode-cathode spacings ranging from 1 cm to 20 cm. Each experimental velocity was normalized to an electron temperature of 1 ev by multiplying the experimental value by $T_e^{-1/2}$. Here, T_e is the electron temperature in electron volts, as measured during that run by a Langmuir probe. The experimental results do indeed show that the velocity is proportional to $m_i^{-1/2}$.

3. An experimental value for γ, the adiabatic compression coefficient of the electron gas, can

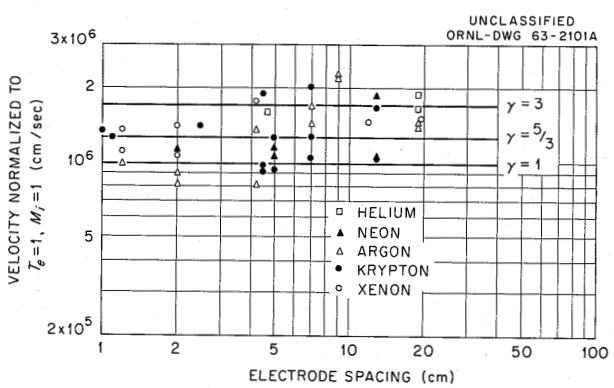

Fig. 4.15. Normalized Experimental Velocity vs Anode-Cathode Distance.

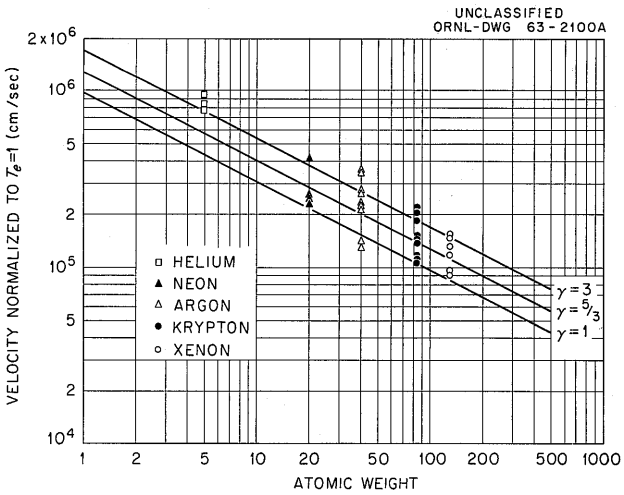

Fig. 4.16. Normalized Experimental Velocity vs Atomic Mass.

be obtained by a statistical treatment of the data shown in Fig. 4.15. The value obtained from such a treatment is $\sqrt{\gamma} = 1.40 \pm 0.38$, giving an rms scatter of 27%. The permitted values are $\sqrt{3} = 1.732$, $\sqrt{5/3} = 1.29$, and $\sqrt{1} = 1.00$. The permitted value $\sqrt{3}$ is improbable at the rather high pressure used, since the electron–gas-atom collision rate is higher than the ion plasma frequency. The experimental value agrees best with $\sqrt{5/3}$, suggesting that the plasma electrons are being compressed adiabatically and are being heated in all three degrees of freedom.

4. Ion-wave pulses produced by using two anodes having spacings with respect to the cathode in the approximate ratio 2:1 are shown in Fig. 4.17. The initial driving pulse is at the left edge of the figure. The second and third pulses are the two response pulses. As expected, they are spaced in time by an approximate ratio of 2:1, corresponding to a velocity of ionic sound waves independent of electrode spacing. Multiple response pulses, as shown here, are generally difficult to obtain; the production of the first response pulse appears to "drain away" temporarily the driving mechanism of the response pulses. The second and subsequent response pulses are generally weak or absent.

5. In Fig. 4.17, a second pair – and traces of a third pair – of response pulses can be seen. A geometrical analysis of the discharge tube indicates that the second pair corresponds to ion wave fronts reflected once from the walls of the discharge tube, and the third pair corresponds to two reflections. In fact, the narrow first pulse of the first pair corresponds to the narrow second pulse of the second pair, and conversely, as would be expected on the basis of the preceding interpretation. These multiple reflections are not frequently observed, since, as noted above, the first response pulse generally drains away temporarily the driving mechanism of the subsequent response pulses.

6. As the gas pressure in the discharge tube is increased, a second, later response pulse appears, corresponding to ordinary sound waves in the background gas. This second pulse is shown in Fig. 4.18. At very high pressures, the ionic-sound-wave pulse disappears, and only the slow, ordinary sound-wave pulse remains. This effect is shown in Fig. 4.19.

7. The direction of propagation of the ionic-sound-wave front was investigated with a special probe, a "discharge probe." No ordinary Langmuir probe seemed to be satisfactory, as the noise level present on ordinary probes obscured the

UNCLASSIFIED
PHOTO P-61979

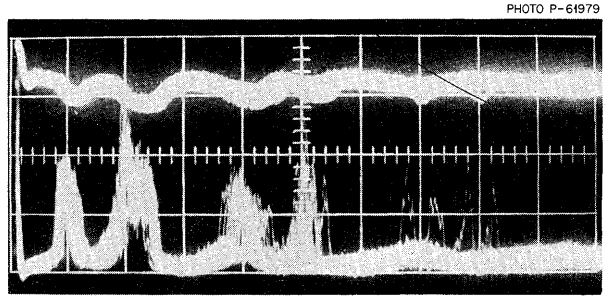

Fig. 4.17. Multiple Pulses plus Wall Reflections. Krypton gas at $\approx 100\mu$, 50 μsec/large division, 7.13 cm gap, $T_e = 2.1$ ev.

UNCLASSIFIED
PHOTO P-61976

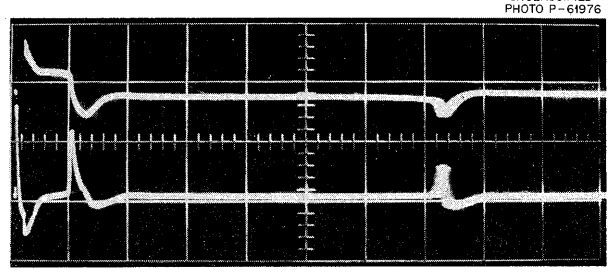

Fig. 4.18. Ionic and Acoustic Wave. Helium at $\approx 125\mu$, 20 μsec/large division, 19 cm gap, $T_e = 1$ ev.

arrival of the ion waves. Also, an ordinary Langmuir probe, being coupled to ground, could generate ion waves during the electrical disturbance caused by the driving pulse.

To detect the arrival of an ion wave at a given point in the discharge tube, the apparatus shown in Fig. 4.20 was used. The detector used was an auxiliary discharge, marked *discharge probe*. This probe consists of a hot filament surrounded by a perforated anode. Presumably, an ion wave penetrating the perforated anode would reach the cathode and cause a momentary increase in emission; this increase of emission would be observed as a response pulse in the battery-operated oscilloscope.

UNCLASSIFIED
PHOTO P-61978

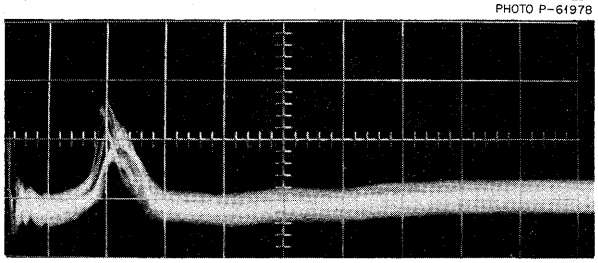

Fig. 4.19. Acoustic Wave Only. Helium, pressure "high," 5 μsec/large division, 1.7 cm gap, $T_e \approx 6$ ev.

Note that the entire discharge-probe circuitry was battery operated and could rise to any potential toward which the probe tended to move. Thus, when the driving pulse was applied to the discharge tube, we hoped that the probe would remain close to the plasma potential and not generate additional, confusing ion waves. The electrical isolation between the probe circuit and the discharge-tube circuit was quite good. In fact, a small wire had to be attached to the oscilloscope trigger input to provide a trigger signal, by capacity coupling, from the driving pulse.

UNCLASSIFIED
ORNL-DWG 64-467

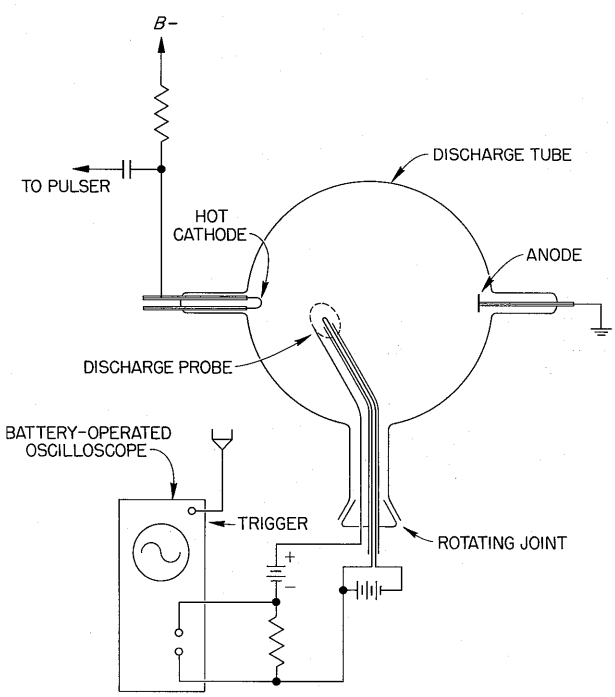

Fig. 4.20. Schematic Diagram of Discharge Probe.

The results of the experiment were sufficiently good that the ion wave arrival at the discharge probe could generally be detected. By moving the probe via a rotating joint, the wave could be followed across the tube. The wave definitely was moving from anode to cathode, as had been postulated previously. That the results of the experiment are not extremely clear-cut is due to the problems involved in operating two discharges simultaneously in the same plasma. The two discharges interfere with each other, although the interference can be minimized by reducing the size and number of holes in the perforated anode.

In conclusion, it is now clear that ionic-sound-wave velocities can be measured in simple discharge tubes by a time-of-flight technique. These waves can be detected traveling from anode to cathode in the discharge tubes. The wave velocity follows the predicted dependence on ion mass and is independent of electrode spacing. Several wave fronts can be generated simultaneously at different points in the discharge tube. The waves are reflected from the tube walls and can be damped by high gas pressures. At high gas pressures, ordinary sound waves are observed traversing the tube.

4.4 OBSERVATIONS OF DISCHARGE TUBE STRIATIONS USING AN IMAGE CONVERTER

Igor Alexeff W. D. Jones R. V. Neidigh

Extensive use has been made of a modified Snooperscope[15] to study moving striations of light in the inert gases in cylindrical discharge tubes. These moving striations are observed to occur when the plasma is undergoing self-excited oscillatory motion. As the pressure is increased, they begin to appear at about 10 μ and move down the tube with velocities in the neighborhood of 10^5 cm/sec. The Snooperscope shows that a well-defined pulse of light is produced at the anode and is gradually dispersed as it moves down the tube. Present evidence suggests that the striations are produced by ion waves propagating down the tube.

Most of the work was done in a Pyrex glass tube about 4 cm in diameter and 60 cm in length. The interelectrode spacing varied from about 10 to 40 cm. A rather limited amount of work done in a tube 1 cm in diameter seemed to indicate that the results were unaffected by the size of the diameter of the tube. The tubes were normally operated in the space-charge-limited regime, in the ordinary glow mode, with interelectrode potentials in the range of from 50 to 350 v. Electron temperature measurements were made by use of an ordinary Langmuir probe swept with a 60-cycle collecting voltage.[16]

A block diagram of a typical setup is shown in Fig. 4.21. A reference signal – which may be electrical, such as would be obtained from a floating probe (as shown); or optical, such as would be obtained from a photomultiplier tube – is obtained from the oscillating plasma in the cylindrical tube. This reference signal is displayed on an oscilloscope which is either internally triggered or externally locked to the signal. The oscilloscope supplies a positive gate pulse which is used to actuate the rest of the electronics. The gate pulse is attenuated to about a volt and then phase-inverted by a simple, commercially available amplifier.[17] Next, the pulse is used to trigger a General Radio unit pulser,[18] which serves to provide a delayed pulse by means of its "delayed pulse" output. The purpose of this pulser is to provide a variable time delay between the triggering of the oscilloscope and the gating on of the modified Snooperscope. From the first unit pulser, the delayed pulse goes to a second General Radio unit pulser. This second pulser then provides the actual gate pulse, variable in length, which activates the image converter for an adjustable period of time. The second pulser does not provide enough voltage to activate the image converter directly; so the pulse is first amplified by a General Radio unit-pulse amplifier.[19] The output of this amplifier now provides a negative pulse of 250 v, adjustable in duration and delay, for the control of the image-converter tube.

A reference signal is also taken from the second unit pulser and displayed on the trigger oscilloscope. This reference pulse indicates the period in which the Snooperscope is gated on relative to the reference signal obtained from the oscillating plasma.

Figure 4.22 shows the results of a series of snapshots taken of what the Snooperscope sees when it is gated on at different times. In this figure, time increases from top to bottom. Also, the anode was located on the right and the cathode on the left. Note the formation of the "glob" of light at the anode and the progression of this glob down the tube as the Snooperscope was gated on at longer and longer times. The figure shows that additional globs of light are formed at the anode before the first glob has traveled the length of the tube. The bottom picture in the figure shows what the Snooperscope sees when randomly gated. This agrees, as might be expected, with what was observed with the naked eye.

---

[15]The modified Snooperscope is an image-converting device which can be used to stroboscopically "stop" and study periodic fluctuations in the light output of a plasma in the 10^3–10^6 cps range. See Igor Alexeff and R. V. Neidigh, *Thermonuclear Div. Semiann. Progr. Rept. Oct. 31, 1962*, ORNL-3392, p. 41; also discussed in Paper L8, presented at the Plasma Physics Section, Meeting of the American Physical Society, San Diego, Calif., Nov. 6–9, 1963 (abstract to be published in the *Bulletin of the American Physical Society*).

[16]Igor Alexeff and W. D. Jones, *Thermonuclear Div. Semiann. Progr. Rept. Apr. 30, 1963*, ORNL-3472, p. 47.

[17]The amplifier is obtained from Kane Engineering Laboratories, 845 Commercial St., Palo Alto, Calif., catalog number C-5A.

[18]The General Radio unit pulser is obtained from General Radio Co., West Concord, Mass., catalog number 1217-B. This device requires an additional General Radio power supply, number 1201-B.

[19]The General Radio unit pulse amplifier is obtained from General Radio Co., West Concord, Mass., catalog number 1219-A. The power supply is self-contained.

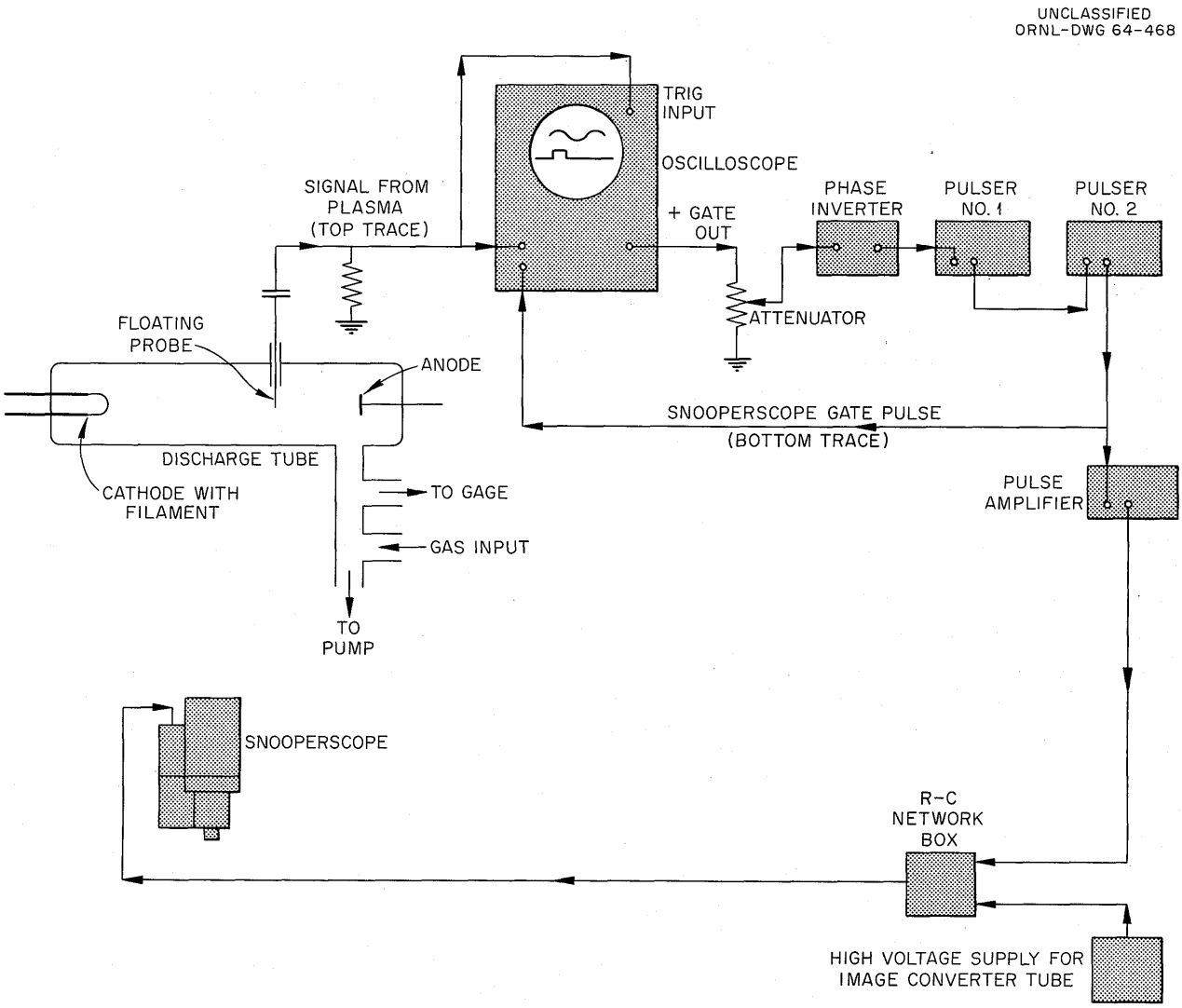

Fig. 4.21. Block Diagram of Setup Used to Study Moving Striations.

Figure 4.23 shows the manner in which the Snooperscope is used to obtain the velocity of the moving light striations. The upper trace shows the reference signal from the plasma used to trigger the oscilloscope, while the lower trace shows the Snooperscope gating pulse. The reference signal in this case was the signal from a floating probe. The series of unit pulsers (see Fig. 4.21) allows the Snooperscope to be gated on at any arbitrary time, relative to the reference signal, for an arbitrary length of time. By taking a series of simultaneous time and striation-position measurements, a graph such as the one shown in Fig. 4.24 for krypton can be constructed. The slope of the curve gives the velocity of the moving striations. Note that the striations seem to slow down as they proceed down the tube. The initial velocity is found to correspond quite closely to the theoretical *signal* velocity which would be expected for ion waves moving down the tube, whereas the average velocity is only about one-half the ion-wave signal velocity, corresponding, perhaps, to the ion-wave *group* velocity.

Moving striations were observed in all the inert gases. Figure 4.25 shows a plot of the average velocity of the striations as a function of the atomic

UNCLASSIFIED
PHOTO 64087

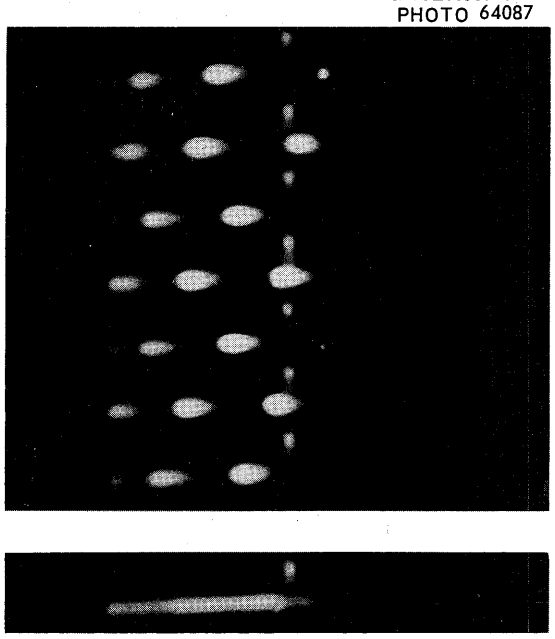

Fig. 4.22. (*Top*) Series of snapshots for the Snooperscope gated on at different times. Time increases from top to bottom. The striations move from the anode on the right to the cathode on the left. (*Bottom*) Snapshot for the Snooperscope gated on randomly.

UNCLASSIFIED
PHOTO 64088

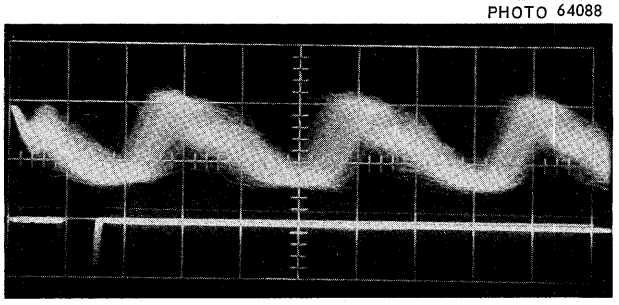

NEON AT 25 μHg
SWEEP = 10 μsec / cm
VERTICAL SCALE FOR TOP TRACE = 5 v/cm

Fig. 4.23. (*Top*) Plasma reference signal from a floating probe. (*Bottom*) Snooperscope gating pulse.

mass number of the gases. Here the experimental velocities have been normalized to an electron temperature of 1 ev, the normalization being made, however, in accordance with the theoretical formula of Tonks and Langmuir[20] (see Fig. 4.25) for ionic-sound-wave velocities. In the formula, γ is the adiabatic compression coefficient of the electron gas, K is Boltzmann's constant (ergs per electron volt),

UNCLASSIFIED
ORNL-DWG 64-469

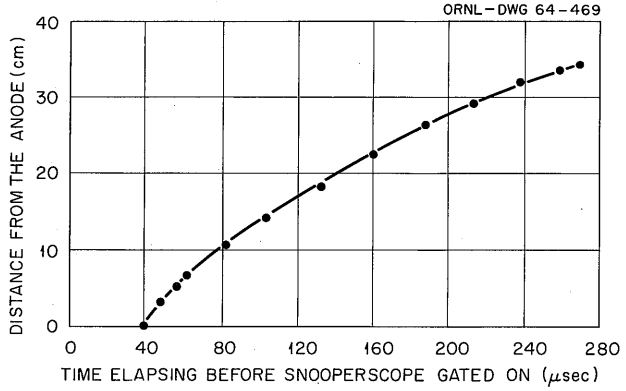

Fig. 4.24. Striation Position vs Time (Krypton).

UNCLASSIFIED
ORNL-DWG 64-470

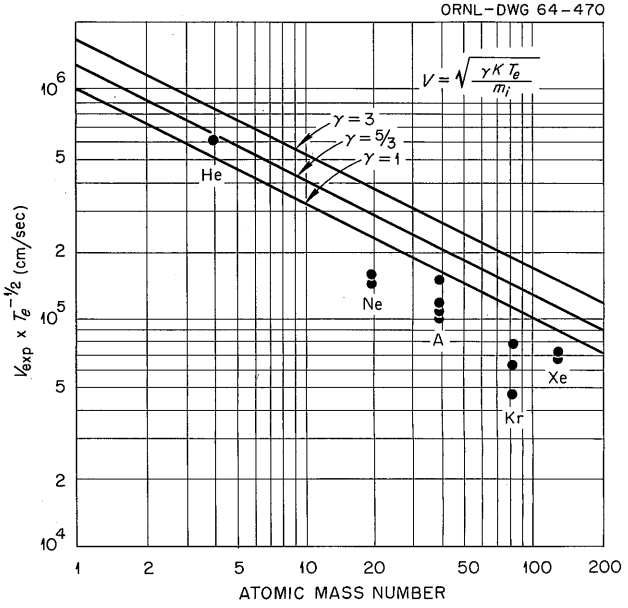

Fig. 4.25. Experimental Striation Velocity vs Atomic Mass Number. Experimental velocities normalized to an electron temperature of 1 ev.

T_e is the electron temperature (electron volts), and m_i is the ionic mass (grams). The straight lines give the theoretical dependence of ionic-sound-wave signal velocity on atomic mass for the three possible values of γ, again in accordance with the Tonks-Langmuir formula. The agreement of the experimental points with the theoretical lines shows that the striation velocities exhibit

[20] L. Tonks and I. Langmuir, *Phys. Rev.* **33**, 195 (1929).

the same general dependence on atomic mass as do the ionic sound waves. Also, calculations show that the electron-temperature normalization causes the rms scatter of the experimental points to decrease by more than a factor of 2, thus implying that the striation velocities also have the same electron-temperature dependence as ion waves.

The preceding mass and electron-temperature dependence exhibited by these preliminary striation-velocity data would suggest that the striations are triggered by ionic sound waves propagating down the tube with group velocity. The dispersion effects which have been noted would seem to add strength to this suggestion.

4.5 POSITIVE-ION CURRENT COMPENSATION FOR THE AUTOMATIC CONVERTER CIRCUIT FOR A LANGMUIR PROBE

Igor Alexeff W. D. Jones

In a previous report,[21] we discussed an automatic converter for a Langmuir probe which allows the characteristic of a Langmuir probe to be continuously displayed on an oscilloscope. Although being very useful in its original form, the converter circuit was incomplete in that no compensation was made for the collection of positive ions by the probe. As the probe is made more and more negative, the number of electrons capable of reaching the probe decreases, whereas the number of positive ions collected is constant. For large, negative voltages, therefore, a significant portion of the probe current is contributed by the collection of the positive ions. This produces the characteristic departure from linearity at large negative potentials usually observed for Langmuir probe characteristics for which no positive-ion correction has been made.

A simple addition has now been made to the original converter circuit which allows correction to be made for the collection of positive ions. This addition, shown in the modified circuit in Fig. 4.26, consists of coupling a variable-voltage power supply through a large resistor (large relative to the variable resistor) to the original circuit between the transformer and the variable resistor, as shown. By simply varying the power-supply voltage, an electron current equal to the current to the probe produced by the positive-ion collection can be made to flow through the variable resistor, thus canceling the voltage which would normally be seen by the log converter due to the positive-ion current flow. Thus the power-supply voltage can be adjusted so that the Langmuir probe characteristic, observed visually on the oscilloscope screen, returns to its expected linear shape. The amount of positive-ion correction necessary can be read directly from a current meter in series with the power supply.

[21] Igor Alexeff and W. D. Jones, *Thermonuclear Div. Semiann. Progr. Rept. Apr. 30, 1963*, ORNL-3472, p. 47.

UNCLASSIFIED
ORNL-DWG 64-471

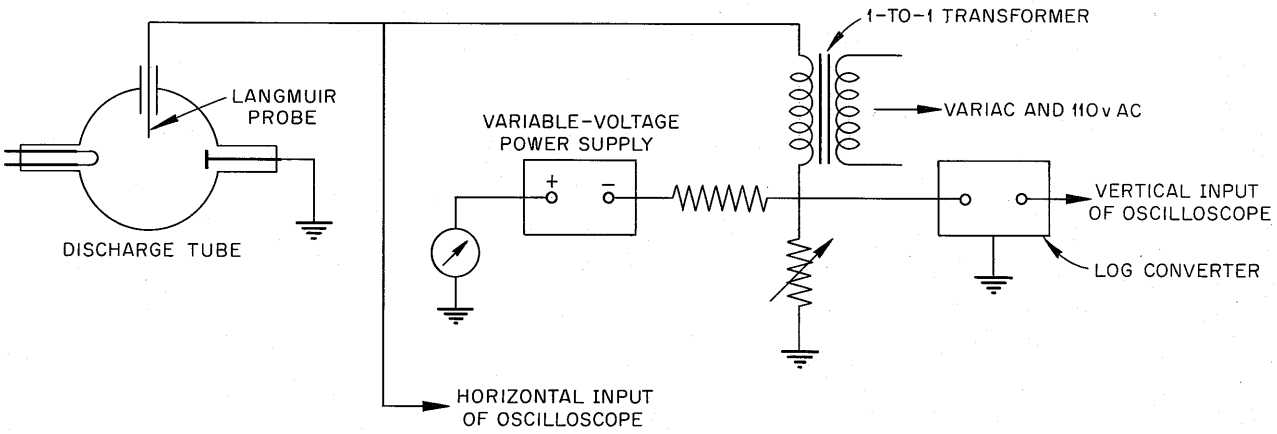

Fig. 4.26. Modified Automatic Converter Circuit for a Langmuir Probe.

5. Vacuum Arc Research

5.1 DEUTERIUM-ARC STUDIES

R. A. Gibbons N. H. Lazar
T. F. Rayburn

5.1.1 Introduction

The magnetically constrained high-density deuterium-arc plasma has been shown previously to be highly ionized and relatively quiescent. It appeared to be a good plasma for the study of plasma diffusion across a magnetic field in the regime where only charged-particle collisions were important. However, Langmuir-probe measurements of the region outside the main arc plasma indicate that the particle transport across the magnetic field is dominated by flutes generated by the main arc plasma. The flutes, with a cross-sectional area of about 0.2 cm^2, apparently extend the full length of the arc through a 2:1 magnetic mirror. They have both radial and azimuthal velocities of (1 to 5) $\times$ 10^5 cm/sec across the magnetic field that are dependent on the magnetic field strength, the arc current, and the radius at which the measurement is made.

5.1.2 Direct-Current Probe Measurements

The main deuterium-arc plasma column has an ion density of $\sim 10^{14}$ cm^{-3} in the center region of the Gas Arc Facility (GAF), where the neutral gas density is $\sim 10^{12}$ cm^{-3}. The electron and ion temperatures for this arc approximately follow the relations T_e (ev) = 0.145 I_{arc} (amp) and T_i (ev) = T_e − 6. Earlier experiments indicated that the plasma was relatively quiescent with ~1% current modulation, negligible radiated power, and an azimuthal drift velocity of 1.5 $\times$ 10^5 (~3% of the ion thermal velocity).[1] Since the plasma seemed suitable for cross-field diffusion studies, a Langmuir probe (0.010 in. in diam by 0.125 in. long) was used for dc measurements of the ion density as a function of radius in the center region of the GAF.

The ion densities were found to be exponentially decreasing functions of radius, with an e-folding length of ~1.0 ± 0.1 cm, when plotted in an equivlent one-dimensional form ($r^{1/2}$ correction for cylindrical spreading.[2] The very weak dependence of e-folding length on magnetic field strength is shown in Fig. 5.1. The e-folding length was similarly insensitive to changes in arc current and center-region pressure. Since the plasma particle temperatures are essentially independent of the magnetic field (within a factor of 2), the results shown in Fig. 5.1 do not seem to be explainable on the basis of either collisional or Bohm (anomalous) diffusion.

5.1.3 Time-Resolved Probe Measurements

Time-resolved measurements of the ion and electron currents to the probe indicated that the plasma density outside the main arc fluctuates by several orders of magnitude, up to about the main arc plasma density. The current (either ion or electron) to similar probes placed along the same magnetic field line were almost exactly correlated in time and magnitude. This correlation persisted, even when one of the probes was moved through one of the mirrors until it almost touched the face of the anode, so long as the two probes remained on the same field line. The quality of the correlation in ion currents is shown in Fig. 5.2 for a probe separation of 30 cm.

---

[1] C. L. Cocke *et al.*, *Thermonuclear Div. Progr. Rept. Oct. 31, 1961*, ORNL-3239, pp. 58–61.

[2] A. Simon, *Proc. U.N. Intern. Conf. Peaceful Uses At. Energy, 2nd, Geneva, 1958*, **32**, 343 (1959).

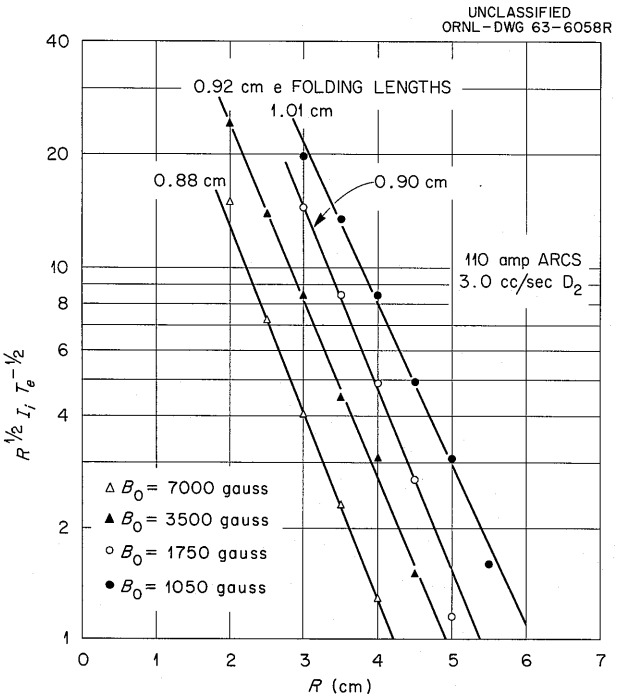

Fig. 5.1. DC Ion Density vs Radius – Dependence on Magnetic Field Strength.

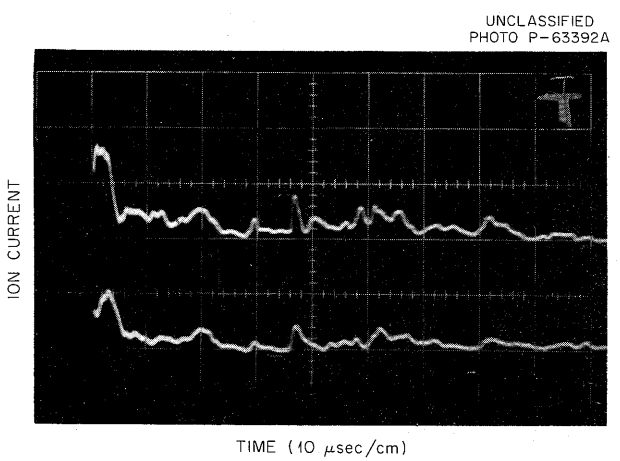

Fig. 5.2. Ion Current to Langmuir Probes 30 cm Apart Along the Magnetic Field.

Insulated end plates were inserted in the central region of the GAF close to the mirror coils and surrounding the differential pumping baffles. Simultaneous observation of the ion currents to a probe and to the end plate provides evidence for a flute which is relatively long-lived, decaying exponentially to the end wall with a lifetime of ~20 μsec, as shown in the upper trace of Fig. 5.3. The current to the probe persists for only 5 μsec (lower trace of Fig. 5.3), indicating that the flute passes by the probe. The decay rate of ions to the end plate is quantitatively consistent with the expected thermal drift ($\bar{v}/4$) of the ions in the flute along field lines as the flute moves across field lines.

Correlation of currents to two probes near the midplane of the facility was also examined. The nearly exact correlation found between probes on the same magnetic field line was never seen when the probes were separated either radially or azimuthally. However, a real correlation exists in almost every case, in the sense that almost every large pulse on one probe is correlated with the appearance of some signal to the second. When a time-averaged photograph of many traces is examined (Fig. 5.4, taken with two probes spaced 0.26 cm), an average delay is apparent between the two signals. From a comparison of the magnitude of the delay for similar radial and azimuthal separations of the two probes, it appears that the flute is spiraling across field lines in a direction that makes an angle of 40° to a radius.

The radial and azimuthal velocities deduced from data of the type shown in Fig. 5.4 are given in Fig. 5.5 as a function of the arc current at a radius of ~2 cm. The magnetic field on axis in the midplane is 7 kilogauss. The lines shown are visually

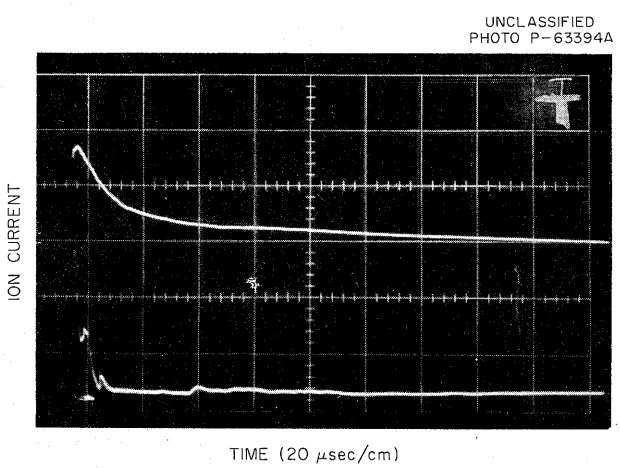

Fig. 5.3. Ion Currents to End Plate (Upper Trace, 200 ma/cm) and Langmuir Probe (Lower Trace, 10 ma/cm).

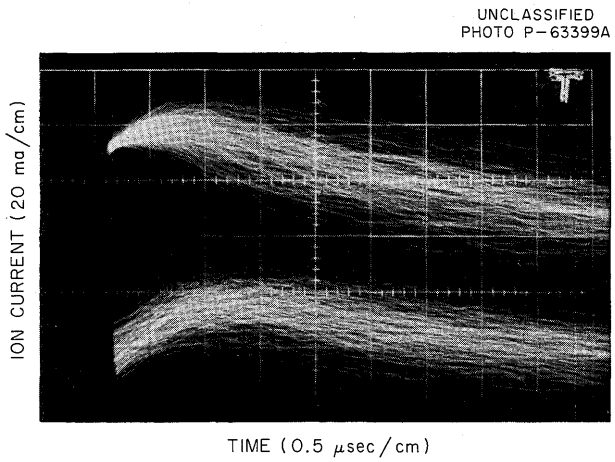

Fig. 5.4. Multiple Flute Ion Currents to Langmuir Probes with 0.26-cm Radial Separation and No Azimuthal Separation.

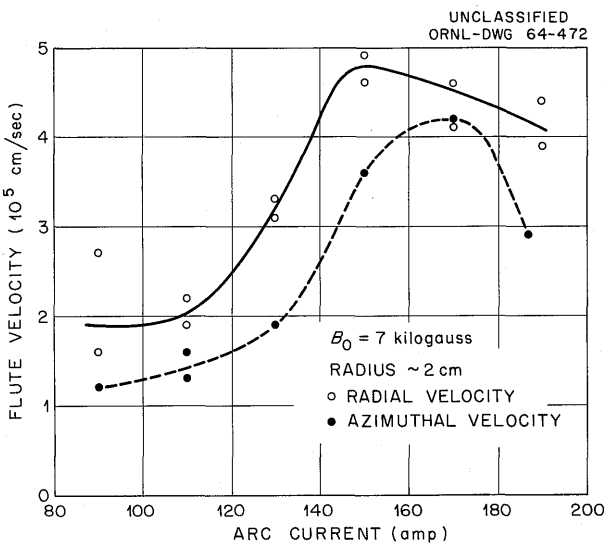

Fig. 5.5. Radial and Azimuthal Flute Velocities as a Function of the Arc Current.

fitted to the experimental points. The sense of the azimuthal velocity is appropriate for $E \times B$ drift, with E directed positively outward. Previous arc studies have demonstrated that variation of the arc current affects primarily the electron and ion temperatures. Thus, from Fig. 5.5, the flute velocity across the magnetic field may be said, generally, to increase with increasing electron temperature.

The azimuthal flute velocity as a function of radius is shown in Fig. 5.6 for a 150-amp arc in a midplane magnetic field of 7 kilogauss. By equating the electron and ion currents flowing out the ends along a field line, both the space potential and electron temperature variations vs time may be demonstrated. One may also include the additional cooling of the electrons through ionization of the background gas. The calculated electron temperature decreases roughly exponentially with an e-folding time of ~10 μsec. If the radial velocity is assumed to be equal to the azimuthal velocity over the range shown in Fig. 5.5, then the radial decrease in velocity would be consistent with the decrease in electron temperature. On the other hand, the ion temperature is expected to decrease with time less rapidly than the electron temperature (~30% in 10 μsec).

The results above suggest that the plasma motion across the magnetic field might be due to $E \times B$ drift for an E field roughly proportional to the electron temperature. However, the radial velocity as a function of magnetic field strength (Fig. 5.7) does not indicate that the velocity is proportional to $1/B$ except possibly above 7 kilogauss. For these measurements the probe position was fixed at ~2.5 cm and the arc power was constant; this

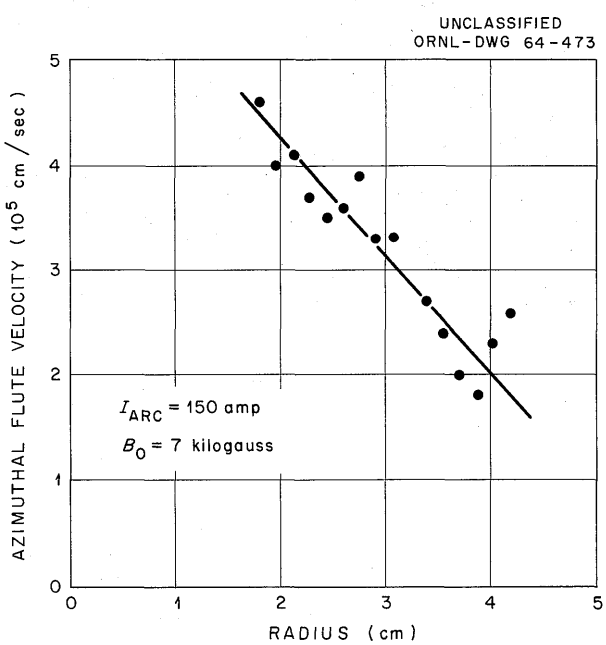

Fig. 5.6. Azimuthal Flute Velocity as a Function of Radius.

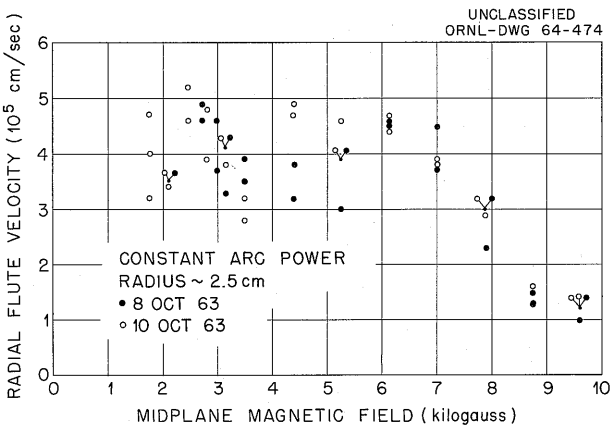

Fig. 5.7. Radial Flute Velocity as a Function of the Magnetic Field Strength.

should give a roughly constant electron temperature in the arc core. The effect of more rapid electron cooling by the higher pressure around the arc at lower magnetic fields has not been evaluated.

The width of the plasma flutes may be estimated from the probe-current pulse width, the flute velocity, and the probe length. For the data of Fig. 5.4 the average flute width was 0.40 cm, and the multiple exposures show that the fluctuations in width are relatively small. The area of the flutes may be estimated from the probe area and the ratio of ion currents to the end plate and to the probe at the peak of the pulse. This method gives a cross-sectional area for the flute of ~0.20 cm^2, which is in good agreement with the flute width above. It should be noted that the Larmor diameter of a 16-ev D_1^+ ion (roughly the average temperature) is 0.24 cm in the normal 7-kilogauss field; therefore the flute is only about two Larmor diameters wide.

5.1.4 Discussion

Several features of these flutes must be pointed out in any attempt to understand their generation by the main arc plasma. There appears to be no axial variation of the current intensity to probes along the same field line; so helical-type instabilities described by Hoh and Lehnert[3] seem to be ruled out. The more likely explanation seems to be in the class of hydromagnetic flutes, described originally by Rosenbluth and Longmire.[4]

In applying their theory, the effect of the finite Larmor radius of the ions must be included. Rosenbluth, Krall, and Rostoker[5] give the criterion for stability at low β as

$$\left(\frac{r_L}{\lambda}\right)^2 > \frac{\sqrt{(v_D^2/r_p)\,(1/\lambda)}}{\omega_L},$$

where

r_L and r_p = Larmor and plasma radii,

v_d^2/r_p = centrifugal acceleration of the plasma at the surface due to an azimuthal drift, v_D,

$\omega_L = v/r_L$ = ion Larmor frequency,

λ = wavelength of the perturbation.

This may be rewritten as

$$\frac{r_L}{\lambda} > \frac{v_D}{v}\sqrt{\frac{\lambda}{r_p}}.$$

The drift velocity due to the gradient of the magnetic field in the GAF has been calculated and is not large enough to cause instability for the measured ion energies. A rotation of the main arc plasma was observed spectroscopically, however, and the value $v_D \approx 1.5 \times 10^5$ cm/sec was deduced. Taking $r_p \approx 1$ cm, $r_L = 0.1$ cm, and $\lambda \sim 1.0$ cm,

$$r_L/\lambda = 0.1; \qquad \frac{v_D}{v}\sqrt{\frac{\lambda}{r_p}} \sim 0.05 .$$

With this drift velocity the arc would be marginally stable. It is impossible to state categorically whether this, then, is or is not the source of the instability.

[3]F. C. Hoh and B. Lehnert, *Proc. Intern. Conf. Ionization Phenomena Gases, 4th Uppsala*, vol. II, p. 604 (1960).

[4]M. N. Rosenbluth and C. L. Longmire, *Ann. Phys. (N.Y.)* 1, 120 (1957).

[5]M. N. Rosenbluth, N. A. Krall, and N. Rostoker, *Nucl. Fusion, 1962 Supplement*, part 1, p. 143.

5.2 LITHIUM ARC

J. E. Francis P. R. Bell

New electrodes have been developed so that a lithium arc can be operated under pulsed conditions.

The cathode assembly is shown in Fig. 5.8. The cathode consists of a 0.170-in. tantalum rod that has been machined down to 0.040 in. over the area to be covered by the arc. The operating temperature of the cathode is obtained by means of an external welding machine that supplies 300 amp in addition to the power supplied by the arc.

The anode is also heated externally to maintain sufficient lithium vapor for the arc. A cross section of the anode is shown in Fig. 5.9. The lithium is heated by a heater that supplies 700 w in the heater tube *A*. Lithium is vaporized in the boiler *B*, and vapor flows through a short tube to the arc chamber *C*, where it is ionized by the electrons from the cathode. A unique feature of this anode is that the heater leads do not have to pass through a vacuum seal. Also, the lithium vapor can nowhere contact the heater elements and corrode the heater.

The use of these electrodes makes it possible to control the arc operating conditions. By changing the power input to the boiler, the lithium pressure is varied so that the voltage required to maintain a 40-amp arc in a uniform magnetic field can be varied from 100 v to 250 v. If the arc is operated with a high lithium pressure (low voltage), the ion species is all Li^+. When the lithium pressure is reduced (high voltage), the arc contains both Li^+ and Li^{2+}. By use of a 10-sec-on 10-sec-off duty cycle, the arc current has been varied over a range of 10 to 100 amp.

Investigation of the operating characteristics of these electrodes is being continued in an effort to obtain better control over the ion species in the arc and to obtain long electrode life.

UNCLASSIFIED
ORNL-DWG 64-475

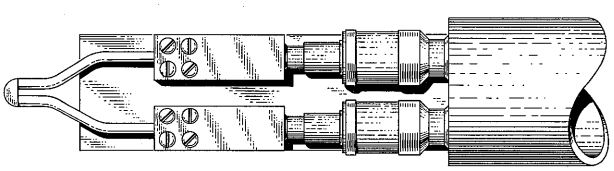

Fig. 5.8. Cathode Structure for Lithium Arc.

UNCLASSIFIED
ORNL-DWG 64-476

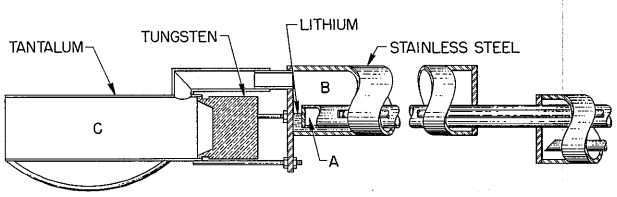

Fig. 5.9. Heated Lithium Anode.

5.3 CHARGE-EXCHANGE AND ENERGY-TRANSFER MECHANISM FOR IONS IN THE ENERGETIC CARBON ARCS – ATOMIC *Q* VALUES

J. R. McNally, Jr. M. R. Skidmore

5.3.1 Introduction

The steady-state, high-current, magnetically confined, low-pressure, carbon and gas-fed carbon arcs exhibit relatively high mean ion energies (up to 220 ev in 8-ft-long arcs and up to 430 ev in a 16-ft-long arc)[6] but relatively low electron excitation temperatures (3 ev from C^{2+} and 7 ev from C^{3+} in a 5.5-ft-long arc).[7] The singly ionized species also reveal, at least in long arcs, spectral line profiles with significantly lower temperatures. The line profiles obtained for observations transverse to the magnetic field are all closely Gaussian, indicating equipartition of energies in this plane among doubly and trebly ionized species at a temperature higher than the equilibrium for singly ionized particles. This section discusses mechanisms for heating and equilibration in the energetic carbon arcs, with particular emphasis on the possible role of charge-exchange phenomena.

The ionic species observed spectrographically in the carbon arc include C^+, C^{2+}, and C^{3+}, with C^+ generally weakest; the predominant species detected by Neidigh with a mass spectrometer[8]

[6] J. R. McNally, Jr., and M. R. Skidmore, *Appl. Optics* 2, 699 (1963).

[7] J. R. McNally, Jr., in *Proceedings of Symposium on Optical Spectrometric Measurements of High Temperatures*, p. 70, University of Chicago Press, Chicago, 1960.

[8] R. V. Neidigh, *Thermonuclear Proj. Semiann. Progr. Rept. July 31, 1959*, ORNL-2802, pp. 31–36.

were C^{3+} and C^{4+} (presumably only ground-state C^{4+} ions are present since electrons having 299 ev or more energy are required to populate the first excited state of C^{4+}). The presence of numerous ionic charge states suggests the possibility of charge-exchange reactions which may "mix" the energy distributions of the trapped ions, and, further, in the case of non-resonance, exothermic charge-exchange reactions will lead to actual heating of ions in the arc. If, in addition, cyclic processes involving inelastic collisions with electrons (ionizations and recombinations) together with exothermic charge-exchange collisions are indicated, then electron kinetic energy may be "pumped" into the ions.

The high energies and energy distributions observed for the ions may therefore result from several combined mechanisms:[6,7,9] (1) the slant line or "tornado" effect, which depends on the $E \times H$ product; (2) resonance radio-frequency heating and, especially, mixing of the individual ion energy distributions at the ion gyrofrequency and its harmonics in the magnetic field; (3) irreversible heating by ion-ion collisions in the accelerating electric fields of the arc; and (4) the charge-exchange heating and mixing to be discussed in Sect. 5.3.2.

5.3.2 Charge-Exchange Reactions

Charge-exchange reactions analogous to those of interest in the carbon arc do exhibit cross sections that are quite large. Figures 5.10 and 5.11, taken from an ORNL compilation of cross-section data,[10] illustrate the energy dependence of several reactions studied by Hasted *et al.*[11,12] The ground-state reactions can be expressed as

$$C^{2+} + Ar^0 \longrightarrow C^+ + Ar^+ + 8.6 \text{ ev}$$

$$C^{2+} + Ne^0 \longrightarrow C^+ + Ne^+ + 2.8 \text{ ev}$$

$$C^{2+} + He^0 \longrightarrow C^+ + He^+ + -0.2 \text{ ev}$$

$$Kr^{2+} + Ne^0 \longrightarrow Kr^+ + Ne^+ + 3.0 \text{ ev}$$

$$Kr^{3+} + Ne^0 \longrightarrow Kr^{2+} + Ne^+ + 15.3 \text{ ev}$$

$$Kr^{4+} + Ne^0 \longrightarrow Kr^{2+} + Ne^{2+} + (26.8 \text{ ev})$$

The excess energy is the net difference[13,14] in the ionization potentials (I.P.) and, in analogy with nuclear reaction Q values, will appear as an increase in kinetic energy of the reaction products whenever Q is positive. Datz[15] has also found evidence for a quite large charge-exchange cross section in the bombardment of Ar^0 with energetic Ar^{4+} ions. Other charge-transfer reactions involving both positive, zero (symmetrical type reactions), and negative Q values have been studied by Hasted.[16] The symmetrical reactions have very large cross sections, especially at energies below about 1000 ev.

Ground-state, non-resonance, charge-exchange reactions to be expected among carbon ions and neutrals (C^0 from incandescent carbon particles) in the energetic carbon arc are

$$C^{4+} + C^0 \longrightarrow 2C^{2+} + 76.7 \text{ ev} \quad (1)$$

$$C^{4+} + C^0 \longrightarrow C^{3+} + C^+ + 53.2 \text{ ev} \quad (2)$$

$$C^{4+} + C^+ \longrightarrow C^{3+} + C^{2+} + 42.1 \text{ ev} \quad (3)$$

$$C^{4+} + C^{2+} \longrightarrow 2C^{3+} + 16.6 \text{ ev} \quad (4)$$

$$C^{3+} + C^0 \longrightarrow C^{2+} + C^+ + 36.6 \text{ ev} \quad (5)$$

$$C^{3+} + C^+ \longrightarrow 2C^{2+} + 23.5 \text{ ev} \quad (6)$$

$$C^{2+} + C^0 \longrightarrow 2C^+ + 13.1 \text{ ev} \quad (7)$$

All these processes are exothermic and can lead to significant heating of the product ions. Symmetrical charge-exchange reactions, for which Q is zero, can contribute to a mixing of energies

[9] J. R. McNally, Jr., and M. R. Skidmore, *Thermonuclear Div. Semiann. Progr. Rept. Apr. 30, 1963*, ORNL-3472, pp. 52–55.

[10] C. F. Barnett, W. B. Gauster, and J. A. Ray, *Atomic and Molecular Collision Cross Sections of Interest in Controlled Thermonuclear Research*, ORNL-3113, pp. 50, 52 (1961).

[11] J. B. Hasted and R. A. Smith, *Proc. Roy. Soc. (London)* **A235**, 354 (1956).

[12] J. B. Hasted, J. T. Scott, and A. Y. J. Chong, *Proc. Intern. Conf. Ionization Phenomena Gases, 4th, Uppsala*, vol. I, p. 34 (1960).

[13] C. E. Moore, *Atomic Energy Levels*, NBS-467, June 1949.

[14] The ionization potential for Kr IV is estimated at 52.5 ev by W. Finkelnburg and W. Humbach, *Naturwissenschaften* **42**(2), 35 (1955).

[15] S. H. Datz, oral discussions, October 1963.

[16] J. B. Hasted, *Proc. Phys. Soc. (London)* **A205**, 28 (1950).

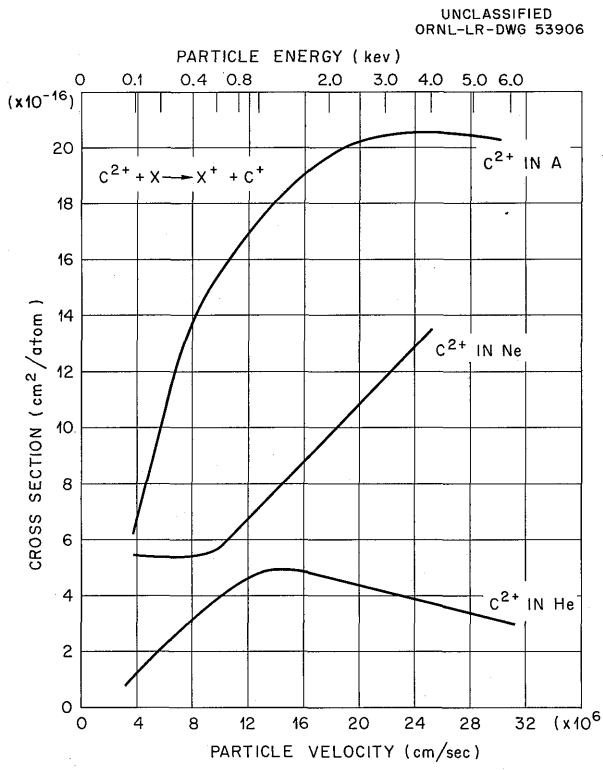

Fig. 5.10. Electron Capture Cross Sections of Doubly Charged Carbon Ions in Noble Gases.

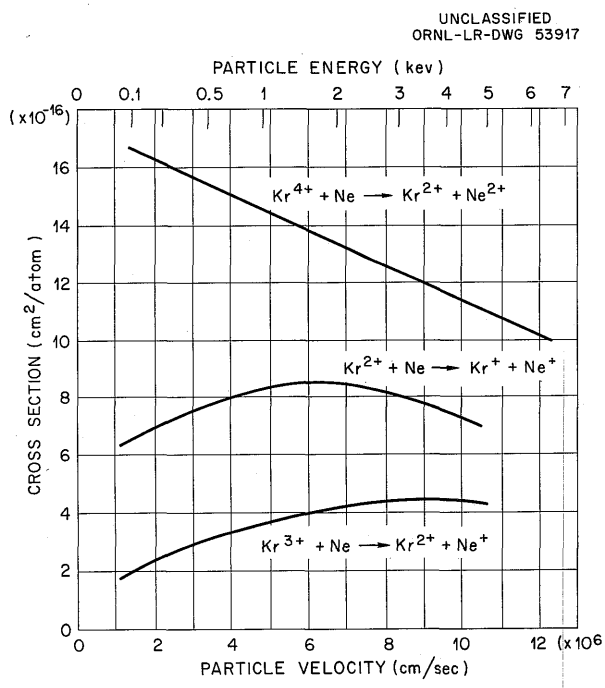

Fig. 5.11. Electron Capture Cross Sections for Highly Ionized Krypton in Neon Gas.

of the ions of different charge states. In the exothermic reactions [(1) to (7)] we note that, neglecting polarization effects, the Coulomb repulsion force $Z_1 Z_2 e^2/r^2$ increases markedly, thus requiring that a significant fraction of Q must appear as an increase in kinetic energy of the reaction products. Excitation and ionization effects may also occur, although only reactions (1), (2), and (5) have sufficiently large Q to "shake off" one or more electrons. From the study of β-decay effects causing the nuclear charge of an atom to change by unity, followed by "shaking" of the bound electrons, Carlson[17] has concluded that about 70% of the beta decays end in the ground state, about 10% result in excited states, and about 20% end in the ionization of one or more electrons. Thus, if the analogy to beta decay is valid, most of the exothermic charge-exchange reactions will be ground-state reactions.

5.3.3 Discussion

The competition between electron collisional ionization ($T_e \sim 5$ ev) vs charge-exchange reactions (we assume $\sigma_{cx} \cong 10^{-15}$ cm^2) in the promotion of C^0 to C^+ is estimated as being about equal except near the electrodes, where ionization by electrons probably dominates. The charge-exchange processes probably become increasingly important in promoting C^+ to C^{2+} (I.P. = 24.38 ev) and C^{2+} to C^{3+} (I.P. = 47.86 ev) provided, of course, higher stages of ionization are already present in the arc. The C^{4+} ion can only be produced by ionization processes or by zero- or negative-Q charge-exchange reactions since C^{5+} has not been detected in the carbon arcs (the I.P. of C^{4+} is 392 ev). Probe measurements suggest a somewhat higher electron temperature than do the spectroscopic excitation temperatures; thus, no firm interpretation of the actual competition rates can be made at present.

The spectral line profiles for each charge species are quite Gaussian,[6] indicating a rapid energy-mixing mechanism.[18] Charge-transfer col-

[17] T. A. Carlson, oral discussions, October 1963. See also T. A. Carlson, *Phys. Rev.* 131, 676 (1963).

[18] Such mixing effects have been observed in the DCX-1 and DCX-2 proton energy distributions and apparently for electrons in beam-plasma experiments and electron cyclotron heated plasmas, although the Debye distances are much greater in the DCX cases.

lisions as well as elastic collisions tend to make the individual ion energy distributions coincide. This is true in the cases of doubly and trebly ionized species studied to date, but the singly ionized species are always significantly cooler. Ion temperatures reported[6] for gas-fed carbon arcs are $N^+ = 1.5 \times 10^6$ °K; $Ar^+ = 1.4 \times 10^6$ °K; $C^+ = 2.0 \times 10^6$ °K; $N^{2+} = N^{3+} = C^{2+} = 2.5 \times 10^6$ °K; and $Ar^{2+} = 2.6 \times 10^6$ °K. The closer match of the two carbon ion temperatures may be due to resonance charge-transfer processes which cause these ions to lose their specific charge identity more rapidly. The lag in ion temperature of the singly charged ions is probably due to their prior history as cold neutrals and to the fact that they had insufficient residence time to thermalize with the higher charge states before being promoted to higher charge states themselves.

It would be of considerably interest if an energy transfer cycle could be visualized which permitted pumping electron kinetic energy into the ions via recombination, ionization, and charge-exchange processes. In the case of the carbon arc we required $\tau_{cycle} \lesssim \tau_{res}$, where τ_{res} is the average residence time of ions in the arc (estimated to be of order 300 cm/$v_{drift} \sim 0.3$ msec). This would require a smallest cross section for any step in the cycle (ionization, recombination, and exothermic charge exchange) to be of order

$$\sigma \gtrsim \frac{1}{(3 \times 10^{-4}) n_i v_i}$$

$$\sim \frac{1}{(3 \times 10^{-4})(3 \times 10^{13})(10^7)} \sim 1 \times 10^{-17}\ \mathrm{cm}^2$$

for ion-ion reactions or about 2×10^{-19} cm^2 for ion-electron reactions. Since ion-electron-electron (three-body) recombinations have cross sections generally much less than 10^{-20} cm^2 at $T_e = 4$ ev, it would be necessary to invoke specialized ion-ion-electron three-body recombinations, possibly of the type

$$C^{2+} + C^{3+} + e \longrightarrow C^+ + C^{3+}$$

or

$$2C^{3+} + e \longrightarrow C^{2+} + C^{4+} + e',$$

although such collisions probably result in a gross decrease of the Coulomb potential energy and hence could lead to significant ion cooling. The longer collision time and large effective radius of the heavy ions in such collisions suggest that the electron may have a greater probability of inducing such reactions compared to ion-electron-electron three-body reactions, but it is difficult to envisage sufficiently large cross sections. Unfortunately, one is therefore led to conclude on the basis of fragmentary data that cyclic processes of a purely atomic nature may not be important as a mechanism for rapid pumping of electron energy into kinetic energy of the ions in the carbon arc. It may be possible, of course, that portions of the arc (peripheral and interfilamentary regions) are sufficiently cool to permit rapid recombination processes to take place.[19] In any case, one may readily visualize particles picking up about 50 ev of kinetic energy as C^0 proceeds stepwise by charge-exchange processes alone to C^{3+}. (Charge exchange or de-excitation collisions between two metastable C^{2+} ions give a Q of 13.0 ev per event.) In long-lived systems, such as possibly the solar corona, where the ions appear to be hotter than the electrons[20] and high degrees of ionization are found, such cyclic processes may contribute to the high ion temperatures.

At present it seems that the tornado effect contributes about 30 ev to the ion kinetic energy, charge-exchange effects may contribute up to about 50 ev (or more) energy and also contribute strongly to the mixing of the ion energy distributions, and some radio-frequency heating and mixing may occur; but the predominant mode of heating apparently comes from accelerations of multiply charged ions in the axial electric field and the strong radial electric field of the arc. Mixing of the energy distributions then occurs by charge-exchange processes (resonance, exothermic, and endothermic), elastic collisions, and some reso-

[19] E. Hinnov and J. G. Hirschberg [*Phys. Rev.* **125**, 795 (1962)] give a $T^{-4.5}$ dependence for the three-body recombination coefficient.

[20] See, for example, discussion by D. E. Billings, *Temperature — Its Measurement and Control in Science and Industry*, vol. 3, Part 1, pp. 713–22, Reinhold, New York, 1962.

nance mixing of the individual ion energy distributions at the ion cyclotron frequencies and harmonics thereof. This model will be tested further by spectral studies of a greater variety of ions in the energetic carbon and gas-fed carbon arcs. It may be that a major contributing factor in producing the strong radial electric field is the existence of energetic ions – in other words, the electric fields may result from the large ion energies, rather than being their cause.

6. Cross Section Measurements

C. F. Barnett J. A. Ray
J. C. Thompson

During the present period, major emphasis has been placed on modifications of existing apparatus to facilitate measurements of atomic collision cross sections. The successful operation of the 600-kev accelerator has been plagued for the past four years with two problems: breakdown of the auxiliary power insulating transformer stack, and voltage regulation. The first problem has been solved by replacing the transformer with a generator driven with a Fiberglas rod. A fast voltage regulator utilizing a derivative amplifier and filter circuit has been fabricated and installed. For output voltages of 300 kev the short-time variation in voltage is now less than 500 v, and the voltage drift is within this value for periods of several hours.

The fabrication and initial vacuum tests of the cross-beam apparatus have been completed. After bakeout at 120°C, the pressure was 10^{-8} torr without titanium pumping. The addition of titanium pumping on liquid-nitrogen-cooled surfaces lowered the pressure to 7×10^{-10} torr. Minor design changes are now being made to improve the efficiency of the titanium pumping.

Throughout the history of atomic collision cross-section measurements, a need has existed for a low-current detector and energy analyzer of neutral particles in the kev range. Common scintillators and solid-state detectors provide a suitable detector for protons or neutral hydrogen atoms above 20 kev. A proportional counter has been designed and fabricated to provide for detection of hydrogen particles down to 2 kev. The entrance of the counter consists of a 0.001×1.5 in. slit covered with a thin film of Formvar. The slit is scanned laterally over the spatial extent of the beam. The counter is filled with approximately 1 torr of methane. Preliminary results with high-energy alpha particles indicate good energy resolution, and tests are proceeding in determining the energy resolution and minimum energy for protons.

A complete revision has been made of ORNL-3113, *Atomic and Molecular Collision Cross Sections of Interest in Controlled Thermonuclear Research.* The collection now includes 135 graphs of evaluated data, along with a bibliography of 1800 references. These references have been collected and filed for further evaluation.

7. Production, Acceleration, and Injection of Ionic and Atomic Beams

7.1 HIGH-CURRENT ION-BEAM PRODUCTION AND INJECTION

R. C. Davis
R. R. Hall
G. G. Kelley
O. B. Morgan
R. F. Stratton
D. C. Weaver[1]

This group continues to divide its efforts between operating, evaluating, and improving the DCX-2 ion-beam injector system and doing basic studies on producing and handling high-current beams.

The H_2^+ current limitation at approximately 60 ma (ref. 2) has been studied with the 600-kv High-Intensity-Beam Facility. The problem proved to be a decreased relative production of H_2^+ ions from the duoplasmatron ion source as the total extracted current was increased above 100 ma. Various modifications of the ion source were evaluated to try to improve this limitation. From these studies it was found that the H_2^+ current could be increased up to approximately 100 ma by increasing the size of the aperture in the source anode. This aperture (*A* in Fig. 7.1) was increased from 0.052 in. in steps to 0.080 in. The maximum H_2^+ current was obtained from a 0.070-in. aperture with the other source geometry as shown in Fig. 7.1, and the source operating with the minimum hydrogen gas flow needed to obtain the total output current. After a 95-ma H_2^+ ion beam (Fig. 7.2) had been passed through a 4-cm aperture located 350 cm from the source and 250 cm from the magnetic solenoid lens, work was suspended in favor of other problems.

After obtaining 95 ma of H_2^+ ions on the test stand, an attempt was made to achieve similar results with the DCX-2 injector system. Here the beam requirements are more stringent in that it must pass through a 4-cm-diam tube 70 cm long located approximately 250 cm from the magnetic lens. Possibly a more serious difference in the two systems is that the DCX-2 injector system is immersed in the stray magnetic field of the machine. After considerable shielding, the component of this field transverse to the path of the injected beam[3] is still great enough to require the addition of small magnetic guiding coils to pass the beam through the restricting duct. There is also a magnetic-field component along the axis of the beam varying in intensity from a few hundred gauss up to 1 kilogauss through most of the region below the magnetic lens. All beam accountability studies on both systems are done with calorimeters. On the test stand,[4] where one is working with a simple conical copper duct and one target, the beam accountability has been from 90 to 100% of the drain on the 600-kv power supply in the current range of 0 to 250 ma. However, on the DCX-2 system the diagnostics must be performed on a system including the magnetic shielding duct, which involves a large quantity of magnetic shielding material, a coil system dissipating approximately 200 kw of power, and a more complex water system. The calorimetric beam accountability on this system is only 80% of the drain on the power supply. Until this accountability is improved, one cannot be absolutely certain of any of the beam diagnostics that have

[1]On loan from the Y-12 Plant.

[2]R. C. Davis *et al.*, *Thermonuclear Div. Semiann. Progr. Rept. Apr. 30, 1963*, ORNL-3472, p.70.

[3]R. C. Davis *et al.*, *Thermonuclear Div. Semiann. Progr. Rept. Apr. 30, 1962*, ORNL-3315, p. 17.

[4]R. C. Davis *et al.*, *Thermonuclear Div. Semiann. Progr. Rept. Oct. 31, 1962*, ORNL-3392, p. 53.

UNCLASSIFIED
ORNL-DWG 63-4368

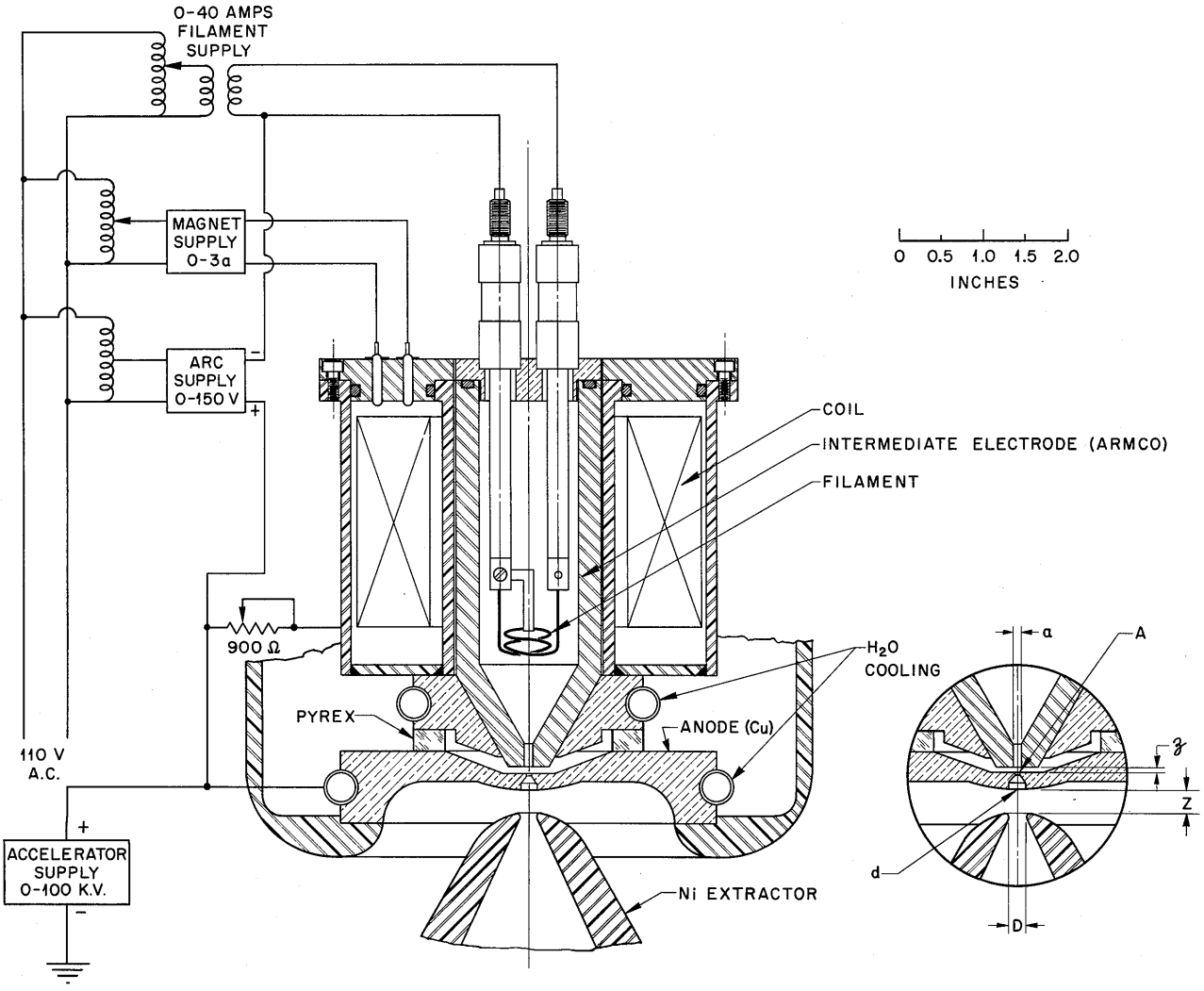

Fig. 7.1. Modified Duoplasmatron Ion Source

been performed. The calorimetric measurement of the H_2^+ beam being injected into the machine has been limited to 36–40 ma (Fig. 7.2). A very recent recalibration of one of the two independent water-flow measuring devices used indicates the possibility that these currents are low by 10%. Since the accountability is poor, it is not certain that the injected current in DCX-2 really is lower than expected. More effort will be spent trying to remove the uncertainty involved in these measurements and trying to increase the H_2^+ current injected into the machine. These efforts will progress at a rate determined primarily by the time

UNCLASSIFIED
ORNL-DWG 63-6759

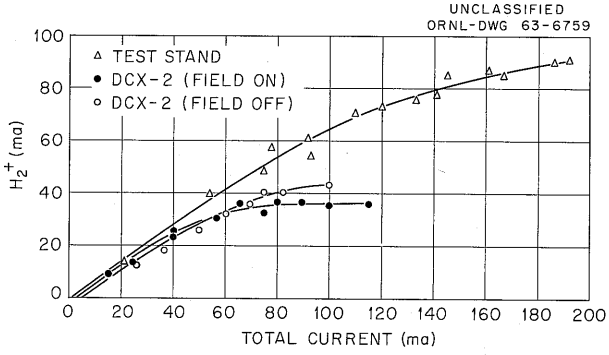

Fig. 7.2. Calorimetric Ion Beam Accountability Data at 600 kv.

available for the incorporation of various improvements and modifications so as not to drastically interrupt the overall machine program.

Minor modifications have continued to improve the voltage-holding capacity of the accelerating column on the atmospheric side. The most recent version of the arrangement of the epoxy "skirts," Fig. 7.3, provides a system operating in a non-controlled atmosphere that operates for many hours continually without breakdown with no beam or with small beams. With beams of 50 to 250 ma operating with a 50% or greater duty cycle, the tube is continuing to improve but is limited at present to periods of 10 min to 1 hr between voltage breakdowns. Even when these breakdowns occur across the epoxy, there is no damage, and with some of the sections in intermittent service for $1\frac{1}{2}$ yr there has not been a fault through the epoxy.

Considerable effort was devoted on the 600-kv test stand in an attempt to reproduce the anomalous spreading of a beam beyond a crossover reported earlier.[5] These efforts included a step-by-step return to the components and conditions utilized at the time of the observation with the exception of the magnetic lens. The lens used at the time has been damaged and could not be used. Other than the different lens there is also a possibility of a more obscure change or variation having been made in the system that has not been reproduced. Despite the rather intense effort, this beam behavior, which would be very interesting to study, has not been reproduced.

Two new projects have been started on the 100-kv ion-source test facility. The first includes an

[5]P. R. Bell *et al.*, *Thermonuclear Div. Semiann. Progr. Rept. Jan. 31, 1961,* ORNL-3104, p. 19.

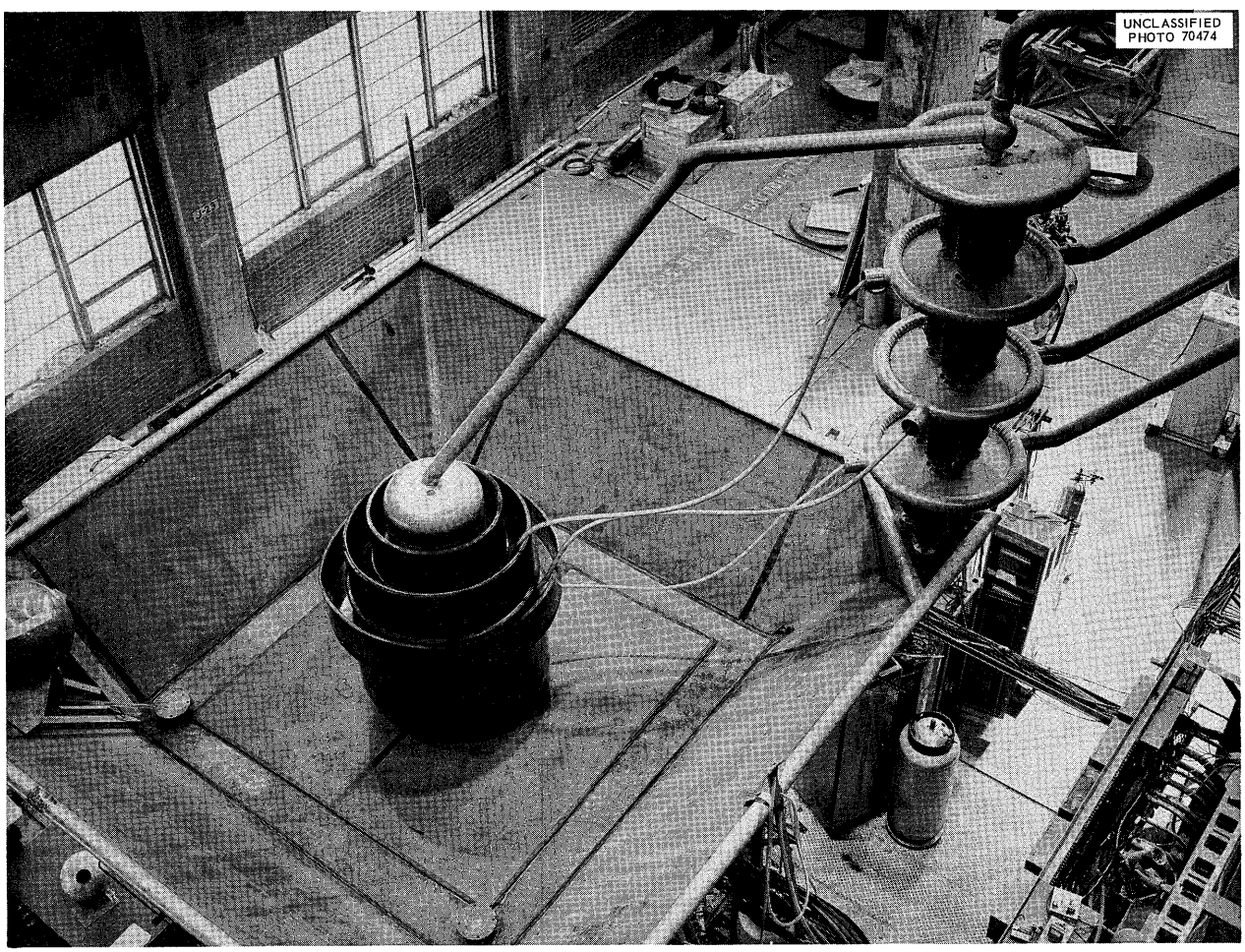

Fig. 7.3. 600-kv High Intensity Beam Facility with Epoxy "Skirts" on the Accelerating Column.

accelerator column with an accel-decel electrode arrangement. This facility will be used to try to produce a small, well-collimated, neutralized, 50- to 100-kv beam from a duoplasmatron ion source. This facility is now ready for testing. A second project that has been planned is a multi-aperture duoplasmatron ion source that will be used in an attempt to extract currents in excess of the 350 ma obtained from a single aperture. The components of this source are being built.

7.2 ION-SOURCE DEVELOPMENT

C. W. Blue N. H. Lazar
O. D. Matlock

The ion-source development work reported previously[6] has been continued. The principal changes made in the experimental unit, and shown in Fig. 7.4, are:

1. A water-cooled copper anode has replaced the carbon anode. The tungsten insert in the face of the anode prevents erosion of the copper by back-streaming electrons.

2. The target has been relocated at a distance L = 18 in. from the source and a small target added as shown. A 1-in. hole in the larger target, axially aligned with the source, allows the ion beams to focus on the small target according to the following equation:

$$L = \frac{2\pi}{B}\left(\frac{2mV}{q}\right)^{1/2}, \qquad (1)$$

[6] *Thermonuclear Div. Semiann. Progr. Rept. Apr. 30, 1963*, ORNL-3472, p. 71.

UNCLASSIFIED
ORNL-DWG 63-1403R

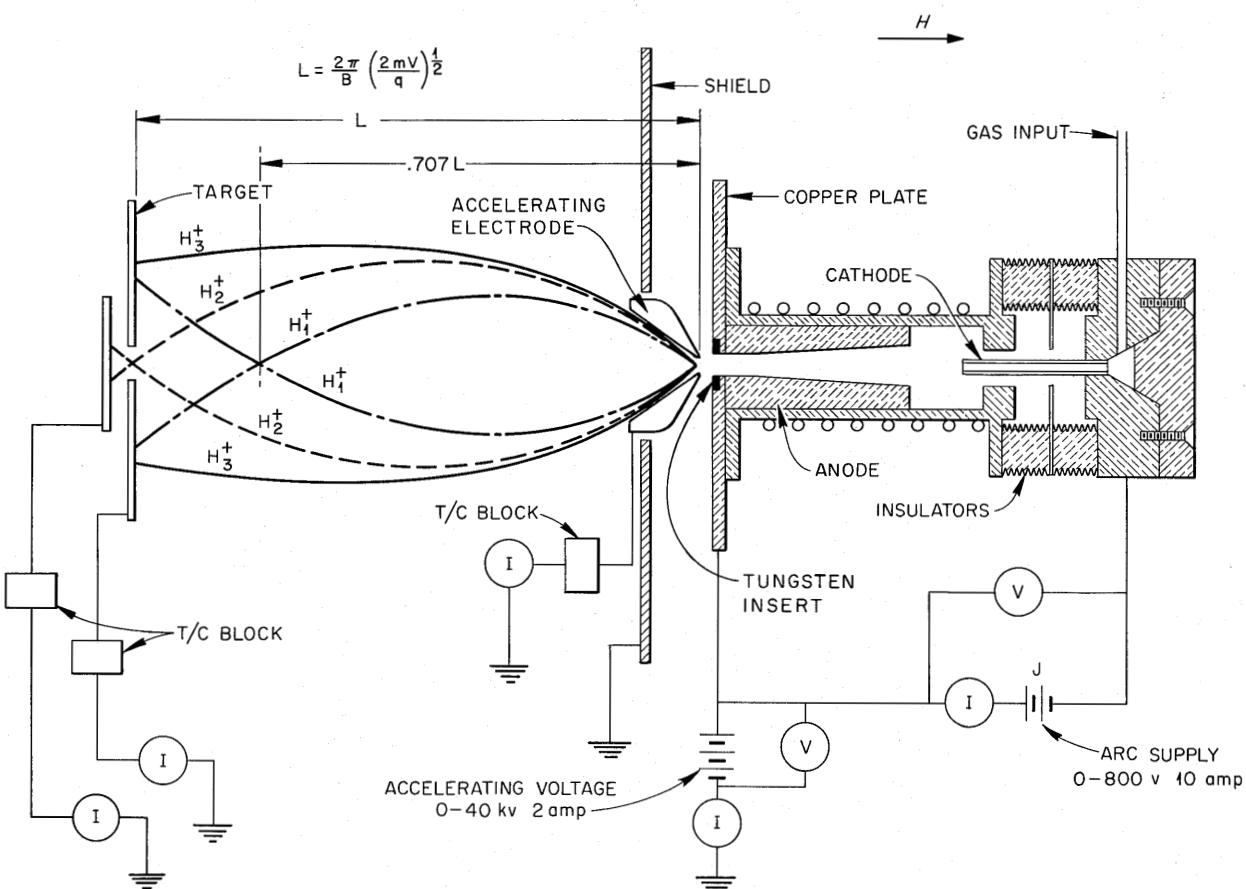

Fig. 7.4. PIG Ion Source.

where m/q is the mass-to-charge ratio of the accelerated ions.

By varying the magnetic field and the accelerating potential, either the H_1^+ or H_2^+ beams may focused on the small target. Figure 7.4 illustrates the typical beam trajectories of the H_1^+ and H_3^+ components when the H_2^+ beam is focused on the small target. Limitations of the magnetic field prevent focusing of the H_3^+ ions onto the small target, and since the ratio of the H_1^+ and H_2^+ are expected to vary with magnetic field, deductions of the H_3^+ beam cannot be made from the present data. However, 75% of a total output of 175 ma has been shown to be H_2^+, with gas efficiency of 51.3%. All power measurements were made calorimetrically.

Figure 7.5 shows voltage-current characteristics of the arc for three different feed rates of hydrogen. With further increase of the feed rate, the characteristics became negative. Thoriated tungsten cathodes were tried, with the hope that lower arc currents and, possibly, plasma density could be sustained with the present voltages; but after the initial bakeout the arc operated with the same voltage-current characteristics of those of pure tungsten.

Up to the limits imposed by space-charge requirements in the accelerating-gap electric field, the total ion output of the source increases with increased gas-feed rate. Figure 7.6 shows the total ion current vs arc current for three different gas feed rates. The decrease of ion current with increase of arc current must be related to a decrease of plasma density due to increased temperatures of ions and electrons in the arc as a function of increasing arc current. The gas efficiencies, beginning with the smallest feed rate, are 35.8, 41.2, and 44.0%, assuming ion beams composed of 40% H_1^+ and 60% H_2^+. The magnetic field and accelerating potential were held constant.

Figure 7.7 shows the total ion current vs accelerating potential with all other parameters held constant. In this case, the gas-feed rate

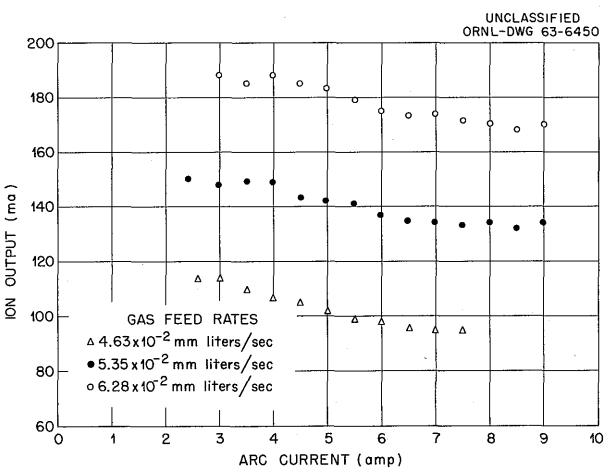

Fig. 7.6. Ion vs Arc Current.

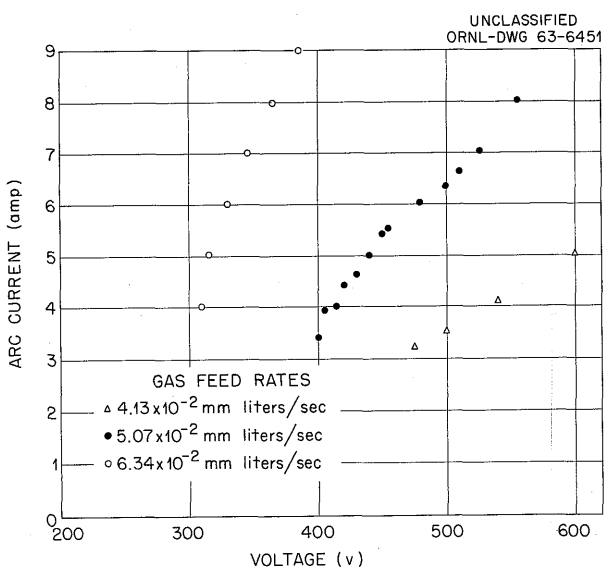

Fig. 7.5. PIG Ion Source – Arc Current vs Arc Voltage.

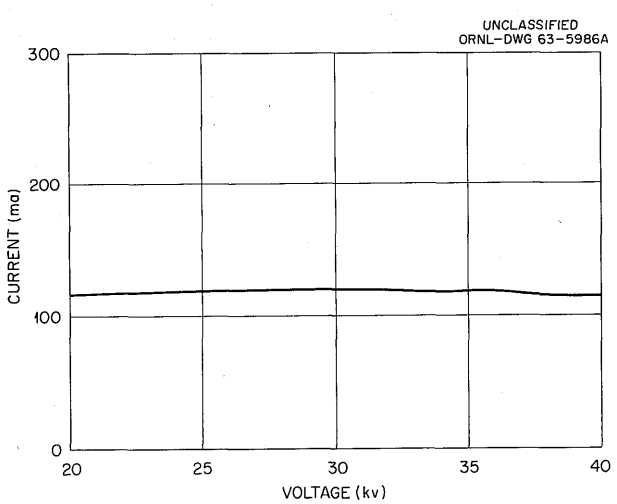

Fig. 7.7. Ion Current vs Accelerating Voltage.

was 4.57×10^{-2} mm-liter/sec, and the gas efficiency was 38.2%. From the data in Figs. 7.6 and 7.7, it may be inferred that the ion output of the source is primarily a function of plasma density, which seems to be determined by the gas feed rate. However, a limit to the output is imposed by ions striking the accelerating electrode, which inevitably results in voltage breakdown across the accelerating gap. Thus the gas feed rate must be limited so that the ion output does not exceed the space-charge-limited ion current for a parallel beam in the accelerating gap, given by[7]

$$I = \frac{1.71 \times 10^{-7}\, V^{3/2}}{(Z/r_0)^2 A^{1/2}}, \qquad (2)$$

where

V = accelerating potential in volts,

Z = beam accelerator spacing given by mechanical spacing plus r_0,

r_0 = initial beam radius,

A = mass number of extracted ions,

I = ion current in amperes.

A plot of total ion current vs $V^{3/2}$ is shown in Fig. 7.8. The gas feed rate was varied from 5.06×10^{-2} mm-liter/sec to 7.52×10^{-2} mm-liter/sec, which resulted in the efficiency increasing from 37.7% to 47%. In making the adjustments, it was difficult to determine just when the ions began to strike the accelerating electrode. The H_1^+-to-H_2^+ ratio was also changing as the gas-feed rate was changed, thus introducing uncertainties in the exact application of Eq. (2). Therefore the points are somewhat dispersed.

All the above data were taken on an experimental unit having the following parameters: The cathode was of tungsten, $2\frac{1}{2}$ in. long, 0.150-in. OD, and 0.030-in. wall thickness. The hole in the copper anode had a minimum radius (r_0) of $\frac{3}{32}$ in.; the length of the anode was $3\frac{5}{8}$ in.; the accelerating gap was 0.100 in.; and the inside diameter of the accelerating electrode was $\frac{1}{4}$ in. The unit was operated in the 32-in. magnetic gap of tank D with a maximum field of 4500 gauss. The base pressure of the vacuum system was

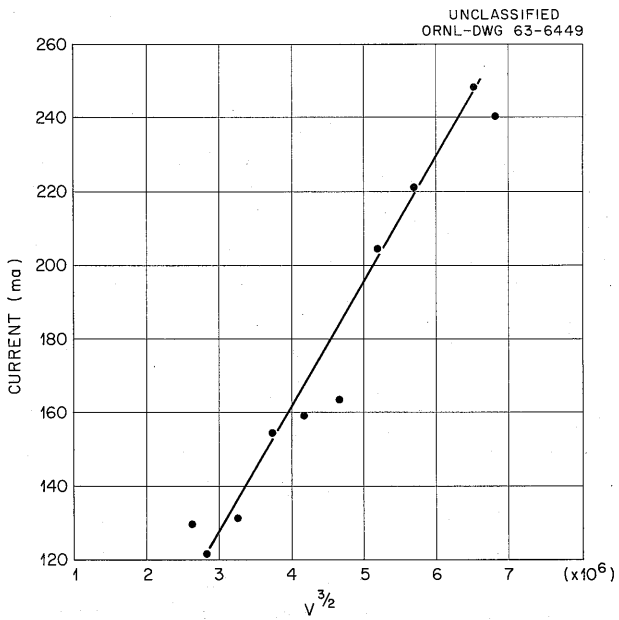

Fig. 7.8. Total Ion Current vs $V^{3/2}$.

6×10^{-7} mm, and the operating pressure was 4 to 8×10^{-6} mm.

A new ion source, designed with integral magnetic coils, has been built and is ready for testing.

7.3 NEUTRAL SOURCE DEVELOPMENT

V. J. Meece W. L. Stirling

Reliable operation of the ion-source[8] hollow-cathode arc has been achieved with acceleration voltages in the 30-kv range. The source runs stably at hydrogen gas feeds from 0.1 to 0.04 cc/sec. Typical operation is with 30 to 35 ma of total current on target, measured calorimetrically, at 30 kv for 1 cc in 15 sec.

Three parameters have been observed to have a strong effect on the beam output: gas feed rate, arc current, and magnetic-field strength.

In the gas feed range given above, the lower the gas feed, the higher the ion output. However, the beam spread increases with increasing output. The 30- to 35-ma beam has a half-angle divergence of 10°. At feed rates below about 0.04 cc/sec, the

[7] *Thermonuclear Project Semiann. Progr. Rept. Jan. 31, 1960,* ORNL-2926, p. 62.

[8] E. L. Earley *et al., Thermonuclear Div. Semiann. Progr. Rept. Apr. 30, 1963,* ORNL-3472, p. 73.

arc becomes unsteady; at feed rates above 0.1 cc/sec, it is hard to hold the accelerating voltage.

The arc electrodes have been designed so that electrons back-streaming through the anode from the accelerating gap cannot hit the emitting surface of the ion-source tungsten cathode. It has been found that these electrons can maintain emission of the cathode without aid of an arc power supply once the source has started operating. However, momentary high-voltage sparks to ground usually extinguish the arc. For this reason, an arc supply is being used, at least for the present. For stable operation, the optimum arc current depends strongly on gas feed rate for a cathode of given size. The tungsten cathode used here has a 0.200-in. OD and a 0.140-in. ID and runs smoothly for current variations between 7 and 20 amp for the feed rates given above. The arc voltage is about 150 v for the 30- to 35-ma beam, and the arc current is about 15 amp. Beam output is directly proportional to arc current.

Total ion current output varies markedly with magnetic-field strength. For the 30- to 35-ma beam, the field is about 1300 gauss, At 1500 gauss, with all other parameters held constant, the current increases by 15%, but the beam divergence increases above the 10° limit. At 900 gauss, the current is down 20 to 40%. Both the gas feed and magnetic-field effects on current output are being further investigated.

The dissociating or converter arc, through which the ion beam passes in order to produce the final beam of neutrals, has been run several times, but the operation is not reliable enough to yield reproducible results. Voltage insulation difficulties still exist across the cooling-water lines. Preliminary tests with a new arrangement for supporting the arc electrodes look promising.

8. Plasma Theory and Computation

8.1 STABILITY OF ORNL PLASMAS

T. K. Fowler

This section summarizes what is known about stability of the hot-electron and hot-ion plasmas created in ORNL thermonuclear experiments.

8.1.1 Stable Hot-Electron Plasmas

Cyclotron Heating. – It has been speculated that stable hot-electron plasmas created by magnetic compression owe their stability against flutes to conduction to end walls.[1] In the hot-electron plasmas generated by electron-cyclotron heating at ORNL, this speculation may be confirmed inasmuch as a prominent characteristic of these experiments is a critical gas pressure above which complete ionization takes place and a stable high-density plasma is confined.[2] Actually, the reason for stability may be more complicated than the simple idea of conduction implies. For example, the stable mode is also characterized by a positive space potential, whereby a large, low-energy electron component (<1 kev) becomes electrostatically confined. According to thermodynamic energy principles, a distribution which is a monotonically decreasing function of particle energy is completely stable.[3] It may be that filling out the low-energy spectrum by electrostatic trapping approximates this ideal. Theoretical progress along these lines awaits a better understanding of the steady state. Aside from a crude prediction of the critical pressure and positive potential,[4] little has been accomplished calculationally in this direction, despite effort. Note that, while the existing theory[5] is not strictly applicable to our high-β plasmas, finite orbit effects do not appear to be sufficient to stabilize flutes in this case.

In addition to the clearly important role of background gas, another characteristic of our hot-electron plasmas, in comparison with the compression experiments, is a somewhat higher β, perhaps 0.25. It is interesting that this is of the order of magnitude of the critical β for the mirror instability and other magnetic pinching instabilities catalogued by Furth.[6]

As for other instabilities, in light of evidence now available the electrostatic microinstabilities discussed by Harris[7] would be expected to be eliminated or weakened by the large thermal spread. Universal modes occurring at the surface are probably suppressed by the short length, which invokes strong Landau damping. However, since this is not effective if $T_e >> T_i$, one must again call upon the surrounding cold plasma to dilute the electron temperature at the surface.[8]

Beam Plasmas. – The hot-electron plasmas created by beam-plasma interaction also occur in a large neutral-gas background.[9] An additional

[1] R. F. Post *et al.*, *Phys. Rev. Letters* **4**, 166 (1960).

[2] *Thermonuclear Div. Semiann. Progr. Rept. Jan. 31, 1961*, ORNL-3104, sect. 3.1; *Thermonuclear Div. Progr. Rept. Oct. 31, 1961*, ORNL-3239, sect. 3.1.

[3] W. A. Newcomb, in Appendix of I. B. Bernstein, *Phys. Rev.* **109**, 10 (1958); T. K. Fowler, *J. Math. Phys.* **4**, 559 (1963).

[4] *Thermonuclear Div. Semiann. Progr. Rept. Apr. 30, 1962*, ORNL-3315, sect. 6.2.

[5] R. F. Post, *Bull. Am. Phys. Soc.* **8**, 166 (1963). Post's theory is an elaboration of that of M. N. Rosenbluth, N. A. Krall, and N. Rostoker, *Nuclear Fusion*, 1962 Supplement, Pt. 1, p. 143.

[6] H. Furth, *Phys. Fluids* **6**, 48 (1963).

[7] E. G. Harris, *J. Nucl. Energy: Pt. C* **2**, 138 (1961).

[8] M. N. Rosenbluth, Fontenay Study Group on Mirror Machine Configurations, Fontenay-aux-Roses, France, 1963.

[9] *Thermonuclear Div. Semiann. Progr. Rept. Apr. 30, 1963*, ORNL-3472, p. 31.

stabilizing feature may be the small plasma radius, only of the order of the Debye length.

8.1.2 Review of DCX Instabilities

The DCX-1 and DCX-2 experiments differ from most other thermonuclear devices in two important respects: the ion orbits are large, and the plasma is accumulated slowly. The very large orbits appear to restrict collective phenomena to the microinstability regime (frequency $\omega > \omega_{ci}$, the ion cyclotron frequency). On the other hand, the associated large diamagnetic current is a classic source of microinstabilities. And, because of the slowness of plasma accumulation characteristic of injection machines in general, even weak instabilities are potentially dangerous. For example, DCX-1 is presently limited in density by a microinstability whose macroscopic consequences (diffusion) occur on a slow time scale measured in seconds.

The absence of the superdangerous macroinstabilities – that is, low-frequency ($\omega \ll \omega_{ci}$) oscillations – in DCX-1 and DCX-2 is well established.[10] Since this is true even at the lowest pressures achieved in DCX-1, end conduction is probably not the explanation in this case. Rather, this is probably an extreme "finite-orbit effect." Indeed, Post's finite-orbit theory,[5] though perhaps not well tailored to DCX geometry, does suggest stability against flutes in DCX-1 and even more strongly in DCX-2. One may also give a qualitative argument against macroinstabilities in general in DCX devices. To conserve momentum in ion-electron interactions, a charge perturbation to which the ions and electrons contribute tries to follow the center of mass of the heavier particles, the moving ions. Exactly what the charge wave speed is depends, for example, on the relative contribution of ions to the wave. But to the extent that ions participate strongly (E not parallel to B), the wave speed is almost but not quite the ion speed. Then electrons (and ions) stream relative to the wave frame, and hence they respond oppositely (number-density perturbations out of phase, charge in phase) as in the two-stream instability.[11] The macroinstabilities, such as the flute mode, in which electron and ion number densities are perturbed together (number densities in phase, charges almost out of phase) simply cannot occur. Rather, the wave, tugged along by the streaming ions, would generally move faster than the electron thermal speed, and the response is the two-stream type above.

Thus we shall limit further discussion to microinstabilities. In particular, we shall discuss just the electrostatic, or charge bunching, type, magnetic pinching instabilities being negligible at present current levels.[6] Charge bunching can account at least qualitatively for the observed collective effects in DCX-1 and DCX-2, namely, space and energy diffusion. It is observed that the instabilities are self-limiting, as quasi-linear theory predicts for bunching in streams.[12] The further consequences of the instabilities in diffusing particles in energy and space take place at rates many orders of magnitude slower than the initial (linear theory) growth rate of the microinstability itself, but also many orders of magnitude faster than diffusion by two-body collisions. The qualitative picture is this: Charge bunches rapidly build to some fixed level and either remain intact for long times (e.g., when there is only one bunch in DCX-1) or destroy each other by what we may call higher-order nonlinear effects (wave-wave interaction). Most individual particles, moving with no particular phase relative to the bunches, scatter at random from them. How the enhanced scattering scales with density has yet to be determined.

Charge Bunching. – The most striking feature of collective oscillations (instabilities) in DCX experiments is the discrete frequency spectrum around harmonics of the ion cyclotron frequency, which suggests a resonance. That this is to be expected for any charge-bunching instability is an immediate consequence of our qualitative argument against macroinstabilities above. Merely because the ions gyrate, charge waves following the ions close on themselves. Thus, only waves returning on themselves in phase fail to be weakened by

[10] An exception, a weak 10-kc oscillation in DCX-1, probably involves only electrons and is thereby exempt from our reasoning here. But the energy drive for this mode must be indirect and weak.

[11] J. D. Jackson, *J. Nucl. Energy: Pt. C* 1, 171 (1961); for further discussion see *Thermonuclear Div. Semiann. Progr. Rept. Apr. 30, 1963*, ORNL-3472, p. 75.

[12] W. Drummond and D. Pines, *Proceedings of the Salzburg Conference on Nuclear Fusion*, Paper CN-10/134, Salzburg, 1961.

self-cancellation after many transits around the plasma. These surviving periodic waves, consisting of a circular array of alternately positive- and negative-charge "bunches," rotate almost as fast as the ions, as noted above. Hence, they are observed in the laboratory frame as oscillations at frequencies around $l\omega_{ci}$, l being the number of positive bunches.

The important point is that, if periodicity is required for continued growth of the wave to a macroscopically observable limit, then field inhomogeneity, which destroys periodicity, limits the instability. An important exception in our axially symmetric systems with large orbits is that class of particles whose orbits are concentric to the axis and therefore move in a constant field. At least two pieces of experimental evidence indicate that only such ions participate in DCX instabilities:

1. In DCX-1, probes eliminating the large population of protons *not* nearly concentric to the axis have little effect on the oscillation amplitude and character.

2. In DCX-2, protons which, via the instability, gain large amounts of energy (>300 kev), have orbits concentric to the axis.

The resonance nature of the instability has created considerable interest in the ion cyclotron resonance instability discovered by Harris.[7] We review the development of the understanding of this mechanism in Sect. 8.2. However, we first must point out a puzzle. Harris's mechanism calls for ion-electron interaction. Because the electrons do not move across the field, this requires that some component of the electric field be parallel to the magnetic field. But in DCX-2, and in certain circumstances in DCX-1, it appears that E might be perpendicular to B. In DCX-2, protons, though scattered violently perpendicular to B, are not scattered parallel to B. In DCX-1, as interpreted, evidence of an electric field perpendicular to B remains when activity along B is suppressed by electron-cyclotron heating or electron-beam stabilization. Now, there are other mechanisms, depending on density and magnetic-field gradients, which involve essentially the ions alone and $E \perp B$. For example, a radially decreasing magnetic field is expected to bunch ions ("negative mass" instability),[13] but the field in DCX-2 is uniform. Also, a density gradient brings about bunching which is a high-frequency counterpart to the universal modes in which only a little electric field along B is required.[14] But there remains the question how the expected ion-electron instability could fail to dominate. As we shall see, greater thermal spread should be required to cure Harris's instability in a long machine like DCX-2. In the case of DCX-2, the answer may lie in conduction to the ends via the sizable ionization current. But the question remains open. It is certainly an important question, since the experimental implication is that microinstabilities do not enhance end losses, the more vulnerable loss route.

Ion Cyclotron Resonance Instability. – Over the last five years, Harris has investigated the unstable interaction of electrons with ions streaming across a magnetic field in a series of idealized model calculations. The conclusion is that the instability is basically the two-stream type occurring in infinite plasmas, and should occur in DCX experiments essentially unchanged in such characteristics as thresholds, growth rate, and so forth. Correspondingly, a sufficient temperature spread in ions and electrons should limit the instability. However, it appears that only a temperature spread along B is useful, a consequence of restrictions on motion perpendicular to B.

The models calculated may be distinguished by the ion velocity distribution, f_0^i, employed. In a cylindrical coordinate system, with $\vec{B} \parallel \hat{z}$, azimuth θ about $\vec{B}$, they are (ω_{ci} = ion cyclotron frequency, $v_\perp^2 = v^2 - v_z^2$):

$$(A)^{15} \qquad f_0^i \propto \delta(v_z)\,\delta(\vec{v}_\perp - \hat{\theta} r\omega_{ci}) ,$$

describing concentric orbits, no thermal spread, a net ion "diamagnetic" current density $j_0 = en_0 r\omega_{ci}$;

$$(B)^{6} \qquad f_0^i \propto \exp\left(-\frac{v_z^2}{\alpha_z^2} - \frac{v_\perp^2}{\alpha_\perp^2}\right),$$

[13] C. E. Nielsen, A. M. Sessler, and K. R. Symon, *Intern. Conf. on High-Energy Accelerators and Instrumentation, CERN, 1959*, Geneva, European Organization for Nuclear Research, 1959, p. 239.

[14] A. B. Mikhailovskii and A. V. Timofeev, *Soviet Physics JETP* **17**, 626 (1963). This problem is also being treated by Y'akov Shima in our group.

[15] P. B. Burt and E. G. Harris, *Phys. Fluids* **4**, 1412 (1961).

describing overlapping orbits, thermal spread, no net current;

(C)[16] $f_0^i \propto \exp(-v_z^2/\alpha_z^2)\delta(\vec{v}_\perp - \hat{\theta} r\omega_{ci})$,

like (*A*) but with thermal spread along $\vec{B}$;

(D)[17] $f_0^i \propto \exp\left[\frac{-(\vec{v}_\perp - \hat{\theta} r\omega_{ci})^2}{\alpha_\perp^2}\right] \exp\left(\frac{-v_z^2}{\alpha_z^2}\right)$,

like (*C*) but with a thermal spread perpendicular to $\vec{B}$. For electrons, we have in mind a distribution

$$f_0^e \propto \exp(-m_e v^2/2T_e).$$

In all these cases, the plasma is uniform and the extent along $\vec{B}$ is infinite. For cases (*A*) and (*C*), it is possible to solve the stability problem with finite radial extent – that is, for a long plasma cylinder.

The conclusion from these studies is that the important physics is embodied in the much-simplified dispersion relation

$$\omega_{pe}^2 \int dv_z \left[\frac{m_e}{m_i} \frac{f_0^i(v_z)}{(\omega - k_z v_z - l\omega_{ci})^2} + \frac{f_0^e(v_z)}{(\omega - k_z v_z)^2}\right] = 1 , \quad (1)$$

where ω_{pe} is the electron-plasma frequency. The integer l designates the azimuthal harmonic, $\exp(il\theta)$.

The point to note is that Eq. (1) has the form of the infinite plasma two-stream dispersion relation with $\vec{k}\cdot\vec{v} \to k_z v_z + l\omega_{ci}$ for ions where $k_\perp v_\perp \to l\omega_{ci}$ expresses periodicity imposed by the magnetic field.

Equation (1) is correct for cases (*A*) and (*C*) if $k_z >> k_\perp$. Also, it is exact for the more elaborate distribution (*D*) if $\alpha_\perp = 0$ and $T_e = 0$, and it is quite accurate in any case if $k_z >> k_\perp$, the most unstable limit for small T_e. For cases (*B*) and (*D*) with $\alpha_\perp \neq 0$ and $T_e \neq 0$, the overlapping of ion orbits and electron orbits mixes harmonics so that a sum over l occurs. However, generally the electron term with $l = 0$ dominates and only one ion term (such that $k_\perp \alpha_\perp / l\omega_{ci} \sim 1$) need be considered at a time, again essentially Eq. (1). Finally, as to consequences of spatial confinement, from models (*A*) and (*C*) it has been found that, while allowed perpendicular wave numbers are limited by boundary conditions appropriate to a finite radial extent of the plasma, the infinite medium dispersion relation is otherwise not altered. In fact, for the important case $k_\perp << k_z$ [Eq. (1)], it is just the same.

The content of Eq. (1) has been conveniently displayed by Harris as a plot of stable and unstable regions in parameters ω_{pe} and $l\omega_{ci}$ for various values of T_e/T_i ($T_i \equiv \frac{1}{2} m_i \alpha_z^2$), as in Fig. 8.1. [That is, Fig. 8.1 plots the locus of real ω roots of Eq. (1), which divides the stable and unstable regions.] In Fig. 8.1, frequencies are scaled in units of $k_z \alpha_z$, whence the origin corresponds to large k_z. The regions of instability for DCX-1 and DCX-2 parameters are indicated. Note that for DCX-1 the region of instability is quite small and is limited to small wavelengths near the origin. Thus a small electron temperature should stabilize the system insofar as Harris's mechanism is concerned. This may account for the experimental observation that a very modest amount of electron-cyclotron heating stabilizes electron activity in DCX-1. A stability map similar to Harris's, but for the exact dispersion relation for model (*B*), is given by Soper (Sect. 8.2).

Finally, it is interesting to note that Harris's oscillation tends to be dominantly an electron charge wave. That is, while ions contribute to the charge wave, and the wave cannot exist without the ions, the perturbation in electron density (hence charge) is considerably greater than the ion perturbation. For large k_z, at the threshold for growth the ratio is easily computed as the ratio of terms in Eq. (1). Consider model *A* with $T_e = 0$. The frequency at threshold (that density such that a slight increase in density brings about instability) is obtained by equating to zero the derivative with respect to ω of the left side of (1) and solving for ω. Introducing this frequency into (1) and taking the ratio of the ion density perturbation (proportional to the f_0^i term) to the electron

[16] E. G. Harris, Culham Laboratory Report (in press).

[17] Y. Shima, *Bull. Am. Phys. Soc.* **8**, 175 (1963); *Thermonuclear Div. Semiann. Progr. Rept. Oct. 31, 1962*, ORNL-3392, sect. 6.4.

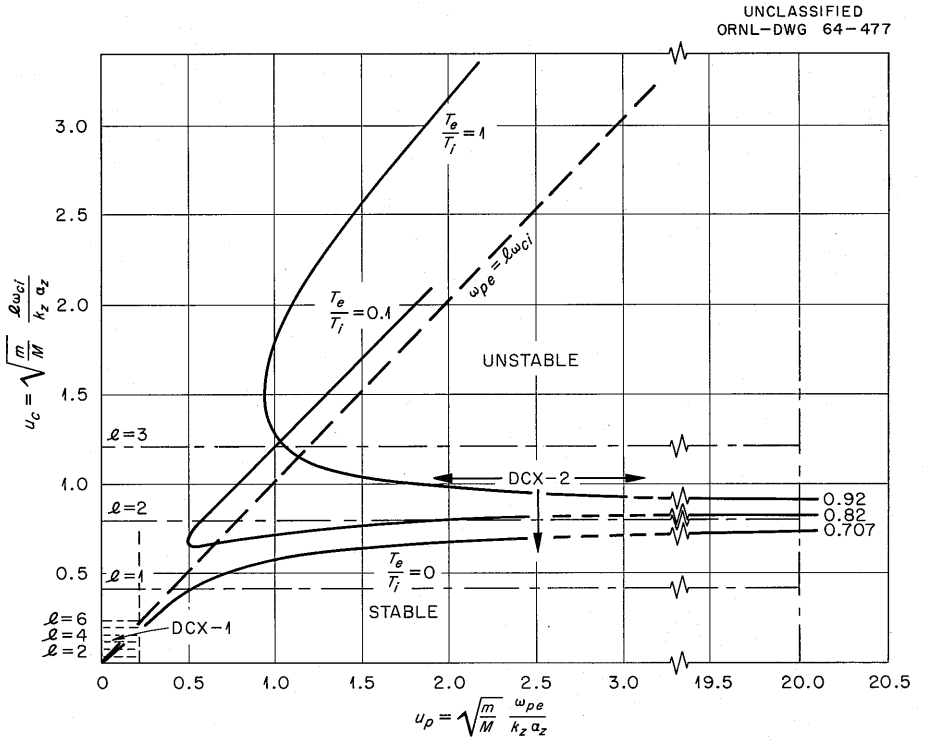

Fig. 8.1. For Model (C) in Text, Regions of Stability Against Ion Cyclotron Resonance Instability for Different Ratios of Electron Temperature, T_e, and Ion Temperature, T_i, Along the Magnetic Field. Here l is the harmonic number, ω_{ci} the ion cyclotron frequency, ω_{pe} the electron plasma frequency, k_z the wave number along the magnetic field, and α_z the ion thermal speed along the field. The zones occupied by DCX-1 and DCX-2, for different harmonics l, are indicated. At present for DCX-1, $u_p < 1/5$ and $u_c < l/25$; for DCX-2, $u_p < 20$ and $u_c < 2/5\, l$. This figure is taken from a Culham Laboratory Report by E. G. Harris, in publication.

perturbation (the other term), we obtain as the ratio of ions to electrons in a bunch,

$$\frac{\Delta n_i}{\Delta n_e} = \left(\frac{m_e}{m_i}\right)^{1/3} . \qquad (2)$$

Note that for small k_z, which is the regime in which a negative mass effect would dominate, $\Delta n_i \gg \Delta n_e$. Then the wave is an ion wave.

8.2 THE EFFECT OF FINITE ION AND ELECTRON TEMPERATURES ON THE ION CYCLOTRON RESONANCE INSTABILITY

G. K. Soper[18] E. G. Harris[19]

In a recent note Harris[20] has investigated the temperature effects in the Burt-Harris model[21] [see Eq. (1), Sect. 8.1]. He shows in a very simple manner that regions of stability and instability can be determined by calculating the curves along which the imaginary part of the frequency is zero in the u_c, u_p plane (see Fig. 8.1, Sect. 8.1). The dimensionless quantities u_c and u_p essentially are a measure of the ion-cyclotron and the electron frequencies. Harris calculated different curves for various values of the ratio of the electron to ion temperature parallel to the magnetic field.

[18] Oak Ridge Graduate Fellow.

[19] Consultant from the University of Tennessee.

[20] E. G. Harris, Culham Laboratory Report, publication in progress.

[21] P. Burt and E. G. Harris, *Phys. Fluids* 4, 1412 (1961).

Using the dispersion relation due to Harris,[22]

$$1 = \gamma(\omega) = 2\pi \sum_j \frac{\omega_{pj}^2}{k^2} \sum_n \int_{-\infty}^{\infty} dv_z \int_0^{\infty} v_\perp \, dv_\perp \left[\frac{\omega_{ij}}{v_\perp} \frac{\partial f_{0j}}{\partial v_\perp} \frac{n J_n^2(k_\perp v_\perp/\omega_{ij})}{(\omega + k_z v_z + n\omega_{ij})} + k_z \frac{\partial f_{0j}}{\partial v_z} \frac{J_n^2(k_\perp v_\perp/\omega_{ij})}{(\omega + k_z v_z + n\omega_{ij})} \right] , \quad (1)$$

where j represents the different species of the plasma, that is, the electrons and ions, and the $\perp$ and z symbols represent quantities measured perpendicular and parallel to the magnetic field, one can perform the same type of analysis as above with the two-temperature distribution function:

$$f_{0j} = \frac{1}{\pi^{3/2} \alpha_{\perp j}^2 \alpha_{zj}^2} \exp(-v_\perp^2/\alpha_{\perp j}^2 - v_z^2/\alpha_{zj}^2) , \quad (2)$$

where the parameters $\alpha_{\perp j}$ and α_{zj} represent the thermal spread of each species in the perpendicular and parallel direction. Substituting Eq. (2) into (1) and integrating gives

$$\frac{1}{\delta (k_z/k)^2 \mathfrak{z}_p^2} = \theta^{-1} Z'(\delta^{1/2}\theta^{-1/2}\mathfrak{z}) + \sum_{n=-\infty}^{\infty} e^{-\lambda_i} I_{|n|}(\lambda_i) [2n\mathfrak{z}_c \mathrm{T} Z(\mathfrak{z} + n\mathfrak{z}_c) + Z'(\mathfrak{z} + n\mathfrak{z}_c)] , \quad (3)$$

where

$Z(x)$ = the plasma dispersion function as defined by Fried and Conte,[23]

$\mathfrak{z} = \dfrac{\omega}{k_z \alpha_{zi}}$, ω is the frequency of any disturbance,

$\mathfrak{z}_p = \dfrac{\omega_{pe}}{k_z \alpha_{zi}}$,

$\mathfrak{z}_c = \dfrac{\omega_{ci}}{k_z \alpha_{zi}}$,

$\delta = m_e/m_i$,

$\theta = T_{ze}/T_{zi}$,

$\mathrm{T} = \alpha_{zi}^2/\alpha_{\perp i}^2 = T_{zi}/T_{\perp i}$,

$\lambda_i = \dfrac{2\omega_{ci}^2}{k_{\perp i}^2 \alpha_{\perp i}^2}$,

where, of course, the e and i labels represent electron and ion quantities.

The real and imaginary parts of Eq. (3) were solved following the prescription of Harris. Because of the complicated nature of the calculations, the results were obtained with the aid of the CDC 1604-A computer. Figure 8.2 shows the

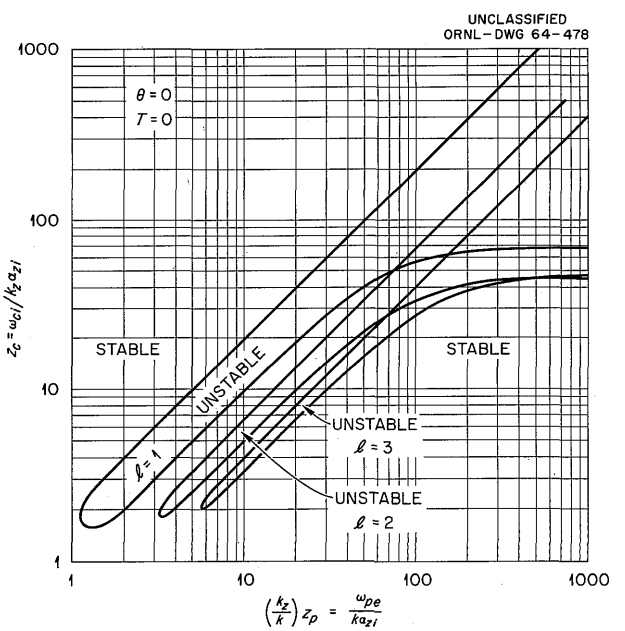

Fig. 8.2. Plot of Eq. (3) with $Im\ \omega = 0$.

[22] E. G. Harris, *J. Nucl. Energy, Pt. C* 2, 138 (1961).

[23] B. D. Fried and S. D. Conte, *The Plasma Dispersion Function*, Academic Press, New York, 1961.

regions of stability and instability for the parameters:

$\theta = 0$ (curves for other values of θ from $1/100$ to 100 are in progress),

$\lambda_i = 3.0$ (varying this parameter over a range from 1 to 20 did not appreciably alter the results),

$T = 0$ (it has been noted[24] that for values of $T \gtrsim 0.5$ no instability can occur; curves for values of T of 0.1, 0.2, and 0.4 are being prepared).

8.3 GROWTH RATES OF ELECTROSTATIC INSTABILITIES IN MIRROR CONFIGURATIONS

T. K. Fowler

A new method for obtaining exact upper bounds on instability growth rates predicted by the linearized Vlasov equation[25] has been applied to distributions resembling plasmas confined in mirror machines. Features examined include: (1) cross-field streaming of ions through electrons, in response to magnetic confinement radially; (2) ion velocity anisotropy, resulting from end confinement; (3) magnetic-field curvature, as in a mirror; and (4) density gradient. As might be expected, electrostatic instabilities arising from the first two effects appear to grow fastest. While both charge and current perturbations are examined, our bounds correspond to growth rates of electrostatic streaming and anisotropy instabilities in infinite plasmas in a uniform magnetic field, studied by Harris.[26]

Determining exact equilibria which include all the desired features has proved to be the principal limitation on the technique. We assume the electrons, confined electrostatically, and any cold plasma, to be isotropic (Maxwellian). For the hot ions, we take a distribution

$$f_0^i \propto \exp\left[-T_\perp^{-1}(\tfrac{1}{2}Mv_\perp^2 + \alpha p_\theta) - T_{||}^{-1}\tfrac{1}{2}Mv_z^2\right],$$

where M is the ion mass and p_θ is the canonical angular momentum corresponding to an azimuthally symmetric mirror field. This distribution rotates with frequency α, so that ions stream azimuthally with speed $r\alpha$. The density falls off approximately like $\exp(-r^2/R^2)$, where $R = (\bar{\Omega}_c/\alpha)^{1/2}\bar{r}_L$ and $\bar{\Omega}_c$ and $\bar{r}_L$ are the ion Larmor frequency and radius at z averaged over r within the plasma. Defining $\omega_{pi} = (4\pi ne^2/M)^{1/2}$, the maximum growth rate is bounded by

$$\gamma_{\max} < \omega_{pi}\left[\frac{MR^2\alpha^2}{T_\perp} + \frac{(T_\perp - T_{||})^2}{T_\perp T_{||}}\right]^{1/2}. \quad (1)$$

This result comes from the electric interaction. We have omitted a similar magnetic term, smaller by a factor $2\bar{v}/c$ with $\bar{v} = (R^2\alpha^2 + 3T_\perp/M)^{1/2}$. Note that growth vanishes as $\alpha \to 0$ and $T_\perp \to T_{||}$.

Result (1) does not include effects (2) and (3) simultaneously. If $T_\perp \neq T_{||}$, f_0^i is valid only over a region in which the magnetic field is approximately uniform. On the other hand, if we sacrifice anisotropy, f_0^i is valid with any degree of field curvature, and Eq. (1) is the bound with $T_\perp = T_{||}$ and taking for R its maximum value within the plasma.

The method for obtaining bounds is an application of Lyapunov theory.[27] We seek an integral, H, which is quadratic in the distribution perturbation f and field perturbations $\vec{E}$ and $\vec{B}$, such that $H > (8\pi)^{-1}\int d\vec{x}\,(\vec{E}^2 + \vec{B}^2)$ and $H^{-1}(dH/dt) < 2\mu$ for all allowed perturbations. Then $\vec{E}$ and $\vec{B}$ grow no faster than $\exp \mu t$; hence

$$\gamma_{\max} < \max_{(\text{all } f, \vec{E}, \vec{B})} \tfrac{1}{2}H^{-1}(dH/dt).$$

In our examples,

$$H = \sum_j \tfrac{1}{2}\int d\vec{x}\, d\vec{v}\, f_j^2(T_j/f_0^j) + (8\pi)^{-1}\int d\vec{x}\,(\vec{E}^2 + \vec{B}^2),$$

where the sum runs over ions and electrons. For ions, $T_j = T_\perp$, etc.

[24] Y. N. Dnestrovsky, D. P. Kostomarov, and V. I. Pistunovich, *Nucl. Fusion* **3**, 30 (1963).

[25] *Thermonuclear Div. Semiann. Progr. Rept. Apr. 30, 1963*, ORNL-3472, p. 76.

[26] E. G. Harris, *J. Nucl. Energy: Pt. C* **2**, 138 (1961); P. B. Burt and E. G. Harris, *Phys. Fluids* **4**, 1412 (1961).

[27] T. K. Fowler, *J. Math. Phys.* **4**, 559 (1963), see Theorem 4.

8.4 PLASMA DIFFUSION BY MICROINSTABILITIES

T. K. Fowler

We shall give a lower bound on the time, τ_D, for plasma diffusion across a magnetic field as a consequence of microinstabilities. The question is of special interest for closed confinement configurations, such as the toroidal multipole,[28] designed to be stable against magnetohydrodynamic (macroscopic) modes. Despite deliberate pessimism in bounding τ_D, we obtain, for the multipole in particular, optimistic results and conclude that microinstabilities, even if present, will not seriously limit confinement. For stellarators with ohmic heating, our bound is somewhat more pessimistic and is not more than an order of magnitude shorter than observed pumpout times.

We examine just electron diffusion. Since ambipolar effects limit the diffusion rate to that of the slower charge component, this certainly provides a lower bound on τ_D. Furthermore, as might be expected, we find ion diffusion (omitting ambipolar electric fields) to be faster, so that electron diffusion controls and provides the better estimate. We shall, however, take ions into account indirectly through any enhancement of electron diffusion due to drift in the ambipolar field.

The time required to diffuse a distance r (plasma radius) at a rate D_r is

$$\tau_D = r^2 D_r^{-1} . \tag{1}$$

The coefficient of diffusion of electron guiding centers, D_r, across the magnetic field $\vec{B}$ is defined by

$$D_r t = \left\langle \left(\int_0^t \frac{cE_\perp}{B} dt' \right)^2 \right\rangle = \Omega_e^{-2} \overline{v}_\perp^2 , \tag{2}$$

$$\overline{v}_\perp^2 = \left\langle \left(\int_0^t \frac{eE_\perp}{m} dt' \right)^2 \right\rangle , \tag{3}$$

where $E_\perp$ is the component of electric field perpendicular to $\vec{B}$, and Ω_e is the electron cyclotron frequency. To obtain a rigorous upper bound on D_r, in (2) we take the largest $\overline{v}_\perp^2$ (whatever t is) and the smallest t consistent with conservation laws. The resulting bound should apply both to the turbulent diffusion emphasized by Spitzer[29] and to the particle-wave resonance mechanism proposed by Drummond and Rosenbluth.[30]

We specialize to Maxwellian ion (i) and electron (e) velocity distributions with relative drift $\vec{v}_D$,

$$f_0^e = (v_e/\sqrt{\pi})^{-3} \exp[-(\vec{v} - \vec{v}_D)^2/v_e^2] , \tag{4}$$

$$f_0^i = (v_i/\sqrt{\pi})^{-3} \exp(-v^2/v_i^2) , \tag{5}$$

written in the ion drift frame. Our corresponding bounds are

$$\overline{v}_\perp^2 < v_D^2 , \tag{6}$$

$$t^{-1} < (v_D/v_e)\omega_{pe} , \tag{7}$$

where $\omega_{pe} = 5 \times 10^4 \sqrt{n(\mathrm{cm}^3)}$ is the electron-plasma frequency.

Following Gardner,[31] Eq. (6) is obtained by rearranging particles in phase space to obtain the state of lowest kinetic energy consistent with Liouville's theorem (the *nonlinear* Vlasov equation is a Liouville equation). Since we are not interested in what develops after the plasma has leaked away, we subdivide the plasma into layers and perform this rearrangement for each layer separately. Then the lowest energy state is the stable state obtained by decelerating the electrons to eliminate the drift. This yields (4), the change in v^2 being:

$$\int d\vec{v}\; v^2 (v_e/\sqrt{\pi})^{-3} \left[e^{-(\vec{v}-\vec{v}_D)^2/v_e^2} - e^{-v^2/v_e^2} \right] = v_D^2 . \tag{8}$$

To obtain (7), we assume that, because of subsequent thermalization, kinetic energy is converted to field energy (and, in turn, to $\overline{v}_\perp^2$) most rapidly during the initial phase of the instability development, whence $t^{-1} < \gamma$, the maximum growth rate in the linearized theory. Then we employ a previously developed exact upper bound on γ.[32]

[28] T. Ohkawa and D. W. Kerst, *Phys. Rev. Letters* **7**, 41 (1961).

[29] L. Spitzer, Jr., *Phys. Fluids* **3**, 659 (1960).

[30] W. E. Drummond and M. N. Rosenbluth, *Phys. Fluids* **5**, 1507 (1962).

[31] C. S. Gardner, *Phys. Fluids* **6**, 839 (1963).

[32] T. K. Fowler, *Phys. Fluids* (in press).

For this case, $\gamma < \frac{1}{2}(d/dt) \ln H$ for any perturbation, with

$$H = \frac{1}{2}\int d\vec{x}\, d\vec{v} \left[f_i^2 \left(\frac{-T_i}{f_0^i}\right) + f_e^2 \left(\frac{-T_e}{f_0^e}\right)\right] + (8\pi)^{-1}\int d\vec{x}\,(\vec{E}_1^2 + \vec{B}_1^2)\,, \quad (9)$$

where f_i and f_e are distribution perturbations, $\vec{E}_1$ and $\vec{B}_1$ are field perturbations, $T_i = \frac{1}{2}m_i v_i^2$, and $T_e = \frac{1}{2}m_e v_e^2$. The resulting bound is the right side of (6), valid for any kind of mode, electrostatic or magnetic.

Combining Eqs. (1), (2), (6), and (7) yields

$$\tau_D > (r/\rho_e)^2 (v_e/v_D)^3 \omega_{pe}^{-1}\,, \quad (10)$$

where $\rho_e = v_e \Omega_e^{-1}$ is the electron gyroradius. For the toroidal multipole, there is no acceleration along $\vec{B}$ and the diamagnetic drift is $\ll v_i$. An ambipolar electric field would increase the drift, but since ions as well as electrons would be accelerated, certainly $v_D < v_i$ by energy conservation (T_e not $> T_i$). Then, anticipating $T_e \sim T_i$, $v_e/v_D > v_e/v_i = (m_i/m_e)^{1/2}$. The radius is $r = 10\rho_i$, whence (for protons) $r = 400\rho_e$. Finally, Eq. (10) yields $\tau_D > (10^5/\sqrt{n})$ sec with n in cm^{-3}; for example, $\tau_D > 10$ msec if $n < 10^{14}$ cm^{-3}. For the stellarator, with ohmic heating $v_D \sim 4v_i$ and $T_e \sim T_i$. Again taking $r = 400\rho_e$ and the observed density $n \sim 10^{13}$ cm^{-3}, Eq. (10) yields $\tau_D > 500$ μsec. The present pumpout time is <5 msec.[33]

Formula (10) may be compared with that of Drummond and Rosenbluth,[30] who took for γ the growth rate of an ion-electron streaming instability (infinite streams) and for $\overline{v_\perp^2}$ the results of quasilinear theory for that problem. Using their result for D_r, τ_D is longer by a factor $(v_e/v_D)^3(\omega_{pe}/\Omega_e)$, much longer than the stellarator pumpout time. Of course, though less specialized, our estimate is only a bound which may not be achieved. Perhaps no mechanism gives a growth rate as fast as (7), and the proper conclusion for the stellarator is that pumpout is not a microinstability.

8.5 IMPURITY RADIATION IN HOT-ELECTRON PLASMAS

S. Cuperman Mozelle Rankin

The coupled steady-state problem of impurity de-excitation radiation (which may depend on the specific energy distribution of the free electrons)[34] and the solution of the Fokker-Planck equation for the free electrons (which may depend on the inelastic collisions between the free electrons and the partially ionized impurity atoms or the neutral particles contained in the plasma) have been studied. Specifically, situations approximating hot-electron plasmas generated by cyclotron heating have been studied.

The steady-state Fokker-Planck code[35] for free electrons (ions omitted) has been amended to include, besides mirror loss and injection of energetic electrons simulating cyclotron heating, also the effect of inelastic collisions leading to excitation and de-excitation and thus to a new source of energy losses from the plasma. We assume that the neutral or not-completely-ionized particle – here called impurity – may be characterized by just two bound (quantum) levels. Then, the term in the Fokker-Planck equation describing the change in the distribution function of the free electrons $f(E)$ because of inelastic collisions with the impurity atoms is given by

$$\left\{\frac{\partial f(E)}{\partial t}\right\}_{\mathrm{inel}} = 2\pi\, e^4 f_{12}\, \alpha \int f(E)\, dE\, \frac{1}{E^2}\sqrt{\frac{2E}{m}}\, G\, f(E)\,, \quad (1)$$

with the dimensionless quantity G defined by

$$G = \frac{n_1}{n_0}\left\{\frac{f(E+E_{12})}{f(E)}\, Z\left(1+\frac{1}{Z}\right)^{-3/2} \ln[1.25(1+Z)] - (Z-1)\ln(1.25Z)\right\} + \frac{n_2}{n_0}\left\{\frac{f(E-E_{12})}{f(E)}\, Z^{1/2}(Z-1)^{1/2}\ln(1.25Z) - Z\left(1+\frac{1}{Z}\right)^{-1}\ln[1.25(1+Z)]\right\} \quad (2)$$

[33] W. L. Harries, private communication.

[34] S. Cuperman, "Impurity Radiation from Non-Maxwellian Spherical Plasmas," to be published in *Physics of Fluids*.

[35] T. K. Fowler and Mozelle Rankin, *J. Nucl. Energy: Pt. C* 4, 311 (1962).

and

$$Z = \frac{E}{E_{12}} . \qquad (3)$$

In the above expressions E, $f(E)$, and $\int f(E)\, dE$ are the energy, energy distribution function, and the density of the free electrons; m and e are the electron mass and charge; f_{12} is the absorption oscillator strength; α is the ratio of the impurity density (n_0) to the free-electron density; n_1 and n_2 are the densities of impurity atoms in lower (1) and upper (2) states ($n_1 + n_2 = n_0$); E_{12} is the transition energy between the levels (1) – (2). If more than two levels are necessary to describe the impurity under discussion, or if more than one impurity species is contained in the plasma, expression (1) has to be replaced by a sum of corresponding contributions.

While explicit expressions for the impurity densities n_1 and n_2 as a function of the distribution function $f(E)$ (the solution of the Fokker-Planck equation) can be written down by using the results of ref. 34, because of the complexity involved in the computations, another method has been used.

First, an arbitrary value β for the ratio of excited to ground state atomic populations of the impurity atoms, β_1, is introduced in Eq. (2). Then the Fokker-Planck equation with $G(\beta_1)$ is solved as in ref. 35, and a solution $f_{\beta_1}(E)$ is obtained. Finally, using the results obtained elsewhere[34] for the de-excitation problem, the electronic plasma density (and thus the absolute values of n_1 and n_2) which corresponds to the numbers α_1 and β_1 initially chosen is found. When a sufficient number of cases (i.e., values of α, β) have been run, a direct correspondence between the electronic plasma density, impurity percentage, the injection energy, and the shape of the free-electron distribution is established.

Preliminary results refer to the critical conditions (percentage of impurity α_c, electronic density n_{ec}, transition energy E^c_{12} – for a given injection energy E_s) when inelastic collisions begin to affect the distribution function of the free electrons. The effect depends essentially on α and on the ratio $E_{12}/\bar{E}$ (ref. 36) (or E_{12}/E_s) rather than on E_{12} or $\bar{E}$ (E_s). It is stronger for values $\xi_{12} = (3/2)(E_{12}/\bar{E}) \ll 1$ and decreases as ξ_{12} increases.

On the other hand, concerning the energy loss from the plasma through the de-excitation radiation, already the use of a distribution function obtained as a solution of the Fokker-Planck equation in which inelastic collisions were neglected ($\alpha = 0$) gives results which are different from those corresponding to a Maxwellian distribution. The effect, generally a decrease of the total energy loss N, is stronger for large values of ξ_{12} and vanishes when $\xi_{12} \ll 1$.

When inelastic collisions are introduced in the Fokker-Planck equation [through Eq. (1)] and the solution so obtained is used to calculate the de-excitation energy loss, it is found again that the larger changes correspond to values $\xi_{12} > 1$.

If both $\xi_{12} \ll 1$ and $\xi'_{12} > 1$ transitions are present at the same time in the plasma and the corresponding densities of impurities n_0 and n'_0 are gradually increased, then the energy losses N and N' must increase. This will lead to a decrease of the plasma energy (and to a change in electron distribution), coming essentially from ξ_{12} transition, which will increase even more the energy loss N through the line ξ_{12} ($N \sim \bar{E}^{-1/2}$) and decrease the energy loss through ξ'_{12}, because of the depletion of the distribution function of electrons with energy able to excite the E'_{12} line. If $n_0 = n'_0$, for instance when studying an optical transition $\xi_{12} \ll 1$ and an x-ray line of the same species ($\xi'_{12} > 1$), the effect is easier to interpret. This is just the situation in the PTF experiment[37] into which xenon was introduced. The dependence of the Xe II optical line λ = 4844 A, and the Xe Kα x-ray $\lambda \cong 30$ kev as a function of Xe partial pressure exhibits the above feature. Further calculations are in progress.

8.6 STABILIZATION OF BOUNDED PLASMAS BY ELECTRON STREAMS AND ARCS

C. O. Beasley

A previous investigation[38] of a proposed stabilizing mechanism for ion cyclotron oscillations in DCX-1[39] used the concept of the transport of energy fluctuations along an electron

---

[36] $\bar{E}$ is the average free-electron energy.

[37] W. B. Ard *et al.*, *Thermonuclear Div. Semiann. Progr. Rept. Apr. 30, 1963*, ORNL-3472, p. 27.

[38] C. O. Beasley and E. G. Harris, *Thermonuclear Div. Semiann. Progr. Rept. Apr. 30, 1963*, ORNL-3472, p. 79.

[39] J. L. Dunlap *et al.*, *Thermonuclear Div. Semiann. Progr. Rept. Apr. 30, 1963*, ORNL-3472, p. 3.

stream to the absorbing walls of the machine containing the plasma. If the rate of energy transfer were sufficiently rapid, the fluctuations would not have time to grow. In other words, the condition

$$\frac{v_g}{L} > Im(\omega)$$

would guarantee stability, where v_g is the group velocity of the excited mode, L the size of the container, and $Im(\omega)$ the growth rate of the excited mode. A detailed examination of the roots of the dispersion relation, $D(\omega,k) = 0$, where k is the wave vector of the electron stream, predicted insufficient damping via this mechanism; for ion cyclotron resonance modes there was very little dependence of the roots ω on k for a given mode, hence

$$v_g = \frac{dRe(\omega)}{dk} \cong 0 .$$

(Each mode had to damp its own growth because of the noncoupling of modes in a linear theory.)

However, the infinite-plasma theory applied here is now thought to be inappropriate to describe the existing situation. One shortcoming is uncertainty in the proper definition of the velocity of transport of the energy fluctuations. For example, the group velocity, used previously, is not proper since it is not uniquely defined for growing waves, but rather exhibits explicit time dependence. Also, even assuming that one could correctly find the velocity of energy transport, there is still the problem of describing physically the absorption of such fluctuations at the walls by the application of appropriate boundary conditions. Our previous assumption of total absorption of energy is quite possibly incorrect.

On the other hand, if one uses a model which is finite in one dimension, and if proper boundary conditions are applied, any existing energy transport as well as absorption at the boundaries is automatically taken into account. In such a system the plasma is looked upon as part of a circuit. Such effects as "feedback" of oscillations, or absorption of them (resulting in convective rather than absolute instabilities), can be described by applying appropriate boundary conditions.

The particular model used to describe DCX is shown in Fig. 8.3. The fast ions (N_i, $\vec{V}_i$) present in the central region are represented by a beam streaming in the x direction. Cold electrons (N_e, $\vec{V}_e$), streaming in the z direction, are neutralized outside the ion beam by cold ions (N_i, $\vec{V}_i = 0$). Nonstreaming cold electrons can also be added. Since all particles are assumed to be cold, moment equations suffice. The equations are Fourier analyzed in x and y, and Laplace transformed in time; the general solution of the resulting differential equation in z has been found. Various boundary conditions relating to several different physical situations are currently being investigated.

UNCLASSIFIED
ORNL-DWG 64-479

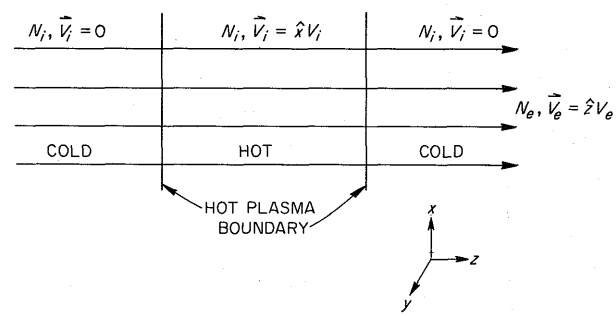

Fig. 8.3. DCX Model.

8.7 SOME EFFECTS OF A MAGNETIC FIELD ON COULOMB SCATTERING

David Montgomery[40] Igor Alexeff
R. V. Neidigh

Calculations of transport and relaxation phenomena in plasmas usually involve, directly or indirectly, the use of the Rutherford scattering cross section in the Boltzmann or Fokker-Planck collision integrals. In fact, the Rutherford scattering formula is drastically modified by the presence of a strong magnetic field, as can be verified by a perturbation calculation of the

[40]Consultant from the University of Maryland.

scattering in powers of $1/B$, the reciprocal of the magnetic-field strength. The leading term in the ratio of the perpendicular energy transfer, relative to that transferred in the absence of a magnetic field, can be calculated for a two-body collision, and is equal to $(r_L/2b)^2$, where r_L is the Larmor radius of the reduced-mass "particle," and b is the impact parameter. When this ratio becomes appreciably less than unity for a "typical" impact parameter, an asymmetry is introduced between the two directions perpendicular to the magnetic field and the parallel direction. This is offered as an explanation of the paradoxical result $\gamma = C_p/C_v = 3$ (instead of $5/3$) recently observed in collision-dominated ionic sound waves.[41]

There are possibilities that the theory can be applied to the recent experiments concerning diffusion of plasma across a magnetic field, where diffusion is normal up to a critical field and anomalous above this value.[42]

8.8 STUDIES OF ENERGY ENHANCEMENT IN DCX-2

T. K. Fowler Mozelle Rankin

We have begun an attempt to determine phenomenologically the degree of enhancement of energy diffusion in DCX-2. Though unnecessarily elaborate for the purpose, the already existing Fokker-Planck code is employed. It is simply amended by multiplying the two-body Coulomb collision terms for ion-ion energy transfer and ion loss by arbitrary numbers P and Q.

Typically we fit DCX-2 data at low densities ($n < 10^8$ cm^{-3}) with $P \sim 10^7$ to 10^8 and $Q = 1$. Though the value of P is very large, one should note that even so it represents energy diffusion on a time scale several orders of magnitude slower than that for the microstabilities presumably responsible for the enhanced diffusion. Their growth time is $\sim 10^{-7}$ sec. The corresponding transfer rate can be as much as 10^9 kev/sec, which is about 10^{12} times the appropriate Coulomb collision energy transfer rate.

[41] Igor Alexeff and R. V. Neidigh, *Phys. Rev.* **129**, 516 (1963).

[42] As an example, see R. Geller, *Phys. Rev. Letters* **9**, 248 (1962).

8.9 ORBIT STUDIES IN A IOFFE MAGNETIC FIELD

Mozelle Rankin D. A. Griffin

The MADCAP IV code for studying particle orbits in DCX-2 has been modified to include the contribution of a four-pole Ioffe bar field to the standard DCX-2 magnetic field. Calculations for the Ioffe field were made concurrently with the orbit calculations, and the Ioffe field was added to the standard stored field values to obtain the new magnetic field. Initially in the orbit code four infinitely long filaments were used to approximate the Ioffe field. Formulas for the field produced by this configuration are given in Sect. (2) of DCX-2 Technical Memorandum No. 106 by C. E. Parker and W. F. Gauster. The more complicated expressions for this field considering end connections between the bars (given on pages 2–5 of the above memorandum) are now a part of MADCAP IV, but no orbit results using these expressions are yet available.

In the orbit studies Ioffe bars were located at a radius of 13.7 in., and the current per bar was 580,000 amp. This is the current necessary to give a Ioffe field of 6000 gauss at a radius of 6 in. All particles were started at $\theta = 0°$ in a clockwise direction and were followed for 10 μsec unless they escaped earlier. Escape is here defined as having a radial value greater than 16.5 in. or an axial value greater than 58 in. To study the effects of relative position of the bars and starting point of the particle, the bars were rotated. The phrase "bars at θ_0" means the bars with current out of the plane of the paper are at θ_0 and $\theta_0 + 180°$, and the bars with current into the plane of the paper are at $\theta_0 + 90°$ and $\theta_0 + 270°$.

Three sets of orbits were run: (1) 600-kev H_2^+ orbits with $r_0 = 9$ in., $\theta_0 = 0$, $Z_0 = 42$ in., $\dot{r}_0 = 0$, $r\dot{\theta}_0 = -0.2985$ in./nsec, $\dot{Z}_0 = 0$; (2) 300-kev H^+ orbits with $r_0 = 6$ in., $\theta_0 = 0$, $Z_0 = 42$ in., $\dot{r}_0 = 0$, $r\dot{\theta}_0 = -0.2985$ in./nsec, $\dot{Z}_0 = 0$; and (3) 300-kev H^+ orbits with $r_0 = 4$ in., $\theta_0 = 0$, $Z_0 = 42$ in., $\dot{r}_0 = 0$, $r\dot{\theta}_0 = -0.2985$ in./nsec, $\dot{Z}_0 = 0$.

For the molecular orbits Table 8.1 summarizes various cases of bar position and containment time.

Figures 8.4 and 8.5 are the cases of bars at 45° and at $67\frac{1}{2}°$ respectively. In general it seems that particles initially near a bar are lost rapidly,

whereas particles remote from the bar are contained for at least 10 μsec. Small variation of the bar position resulted in noticeable orbit changes.

As a check on the reliability of the code, the velocity components of the escaping particle of Fig. 8.5 and the magnetic-field direction were reversed. The orbit properly retraced to the original starting point. Continuation of the same trajectory (now leaving the initial point in opposite direction to the original run) gave Fig. 8.6. Total containment time here is 4.4 μsec.

Table 8.2 and 8.3 summarize cases of atomic orbits. Figures 8.7 and 8.8 are H^+ orbits with an initial radius of 6 in. Figures 8.9, 8.10, and 8.11 are H^+ orbits with an initial radius of 4 in.

Table 8.1. H_2^+ with $r_0 = 9$ in.

Bar Position	Time Contained (μsec)
0°	0.62
45°	10.0
67½°	0.46
90°	0.17
135°	10.0
154½°	10.0
157½°	10.0
160°	9.8

UNCLASSIFIED
ORNL-DWG 64-480

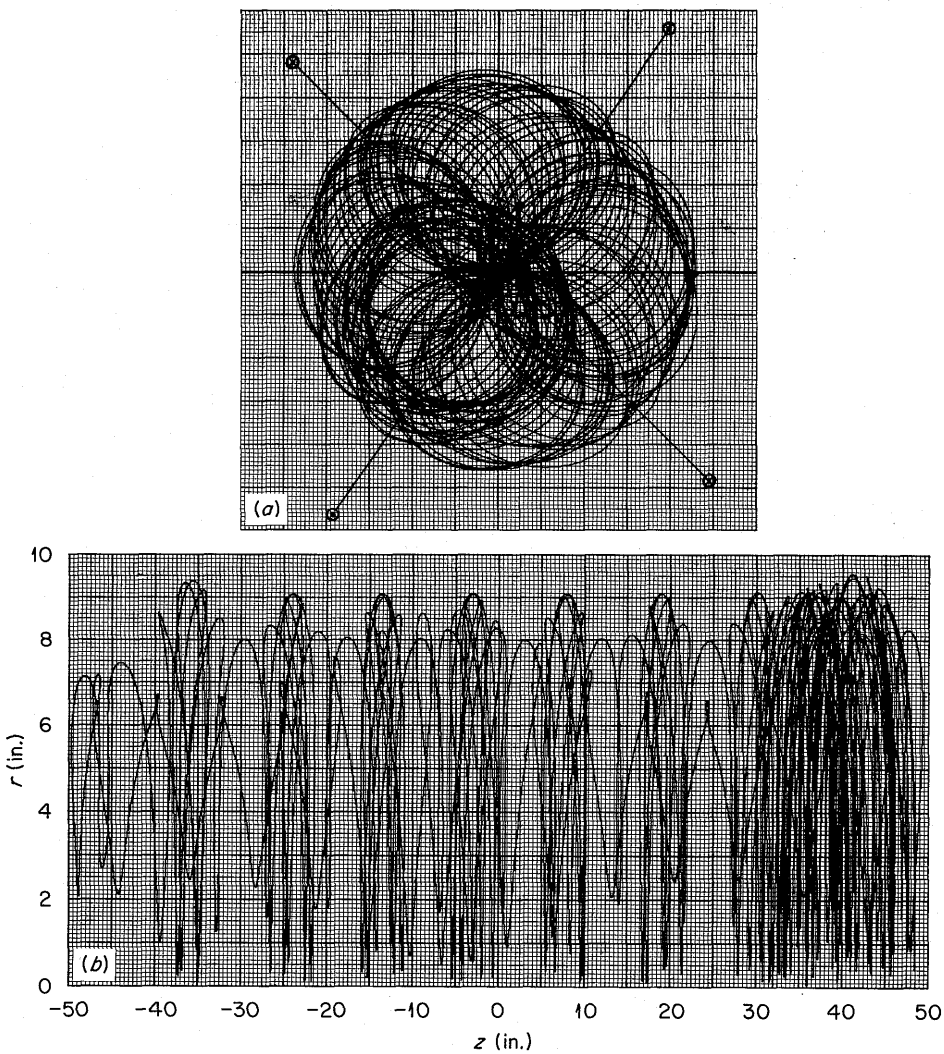

Fig. 8.4. (*a*) *X-Y* Plot of H_2^+ Orbit with $r_0 = 9$ in., $z = 42.0$ in., Bars at 45°, 10 μsec; (*b*) *R-Z* Plot of H_2^+ Orbit with $r_0 = 9$ in., $z = 42.0$ in., Bars at 45°, 10 μsec.

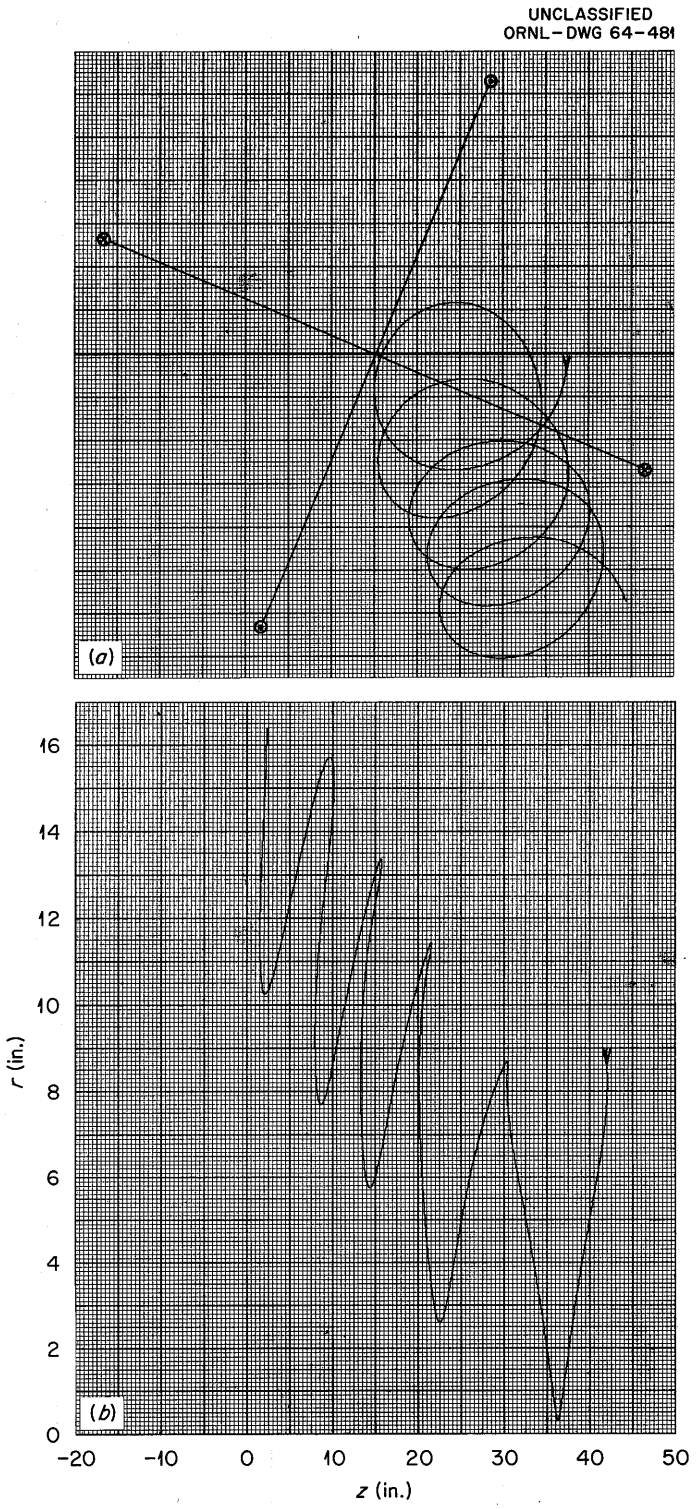

Fig. 8.5. (*a*) *X-Y* Plot of H_2^+ Orbit with $r_0 = 9$ in., $z = 42.0$ in., Bars at $67\frac{1}{2}°$, 0.46 μsec; (*b*) *R-Z* Plot of H_2^+ Orbit with $r_0 = 9$ in., $z = 42.0$ in., Bars at $67\frac{1}{2}°$, 0.46 μsec.

UNCLASSIFIED
ORNL-DWG 64-483

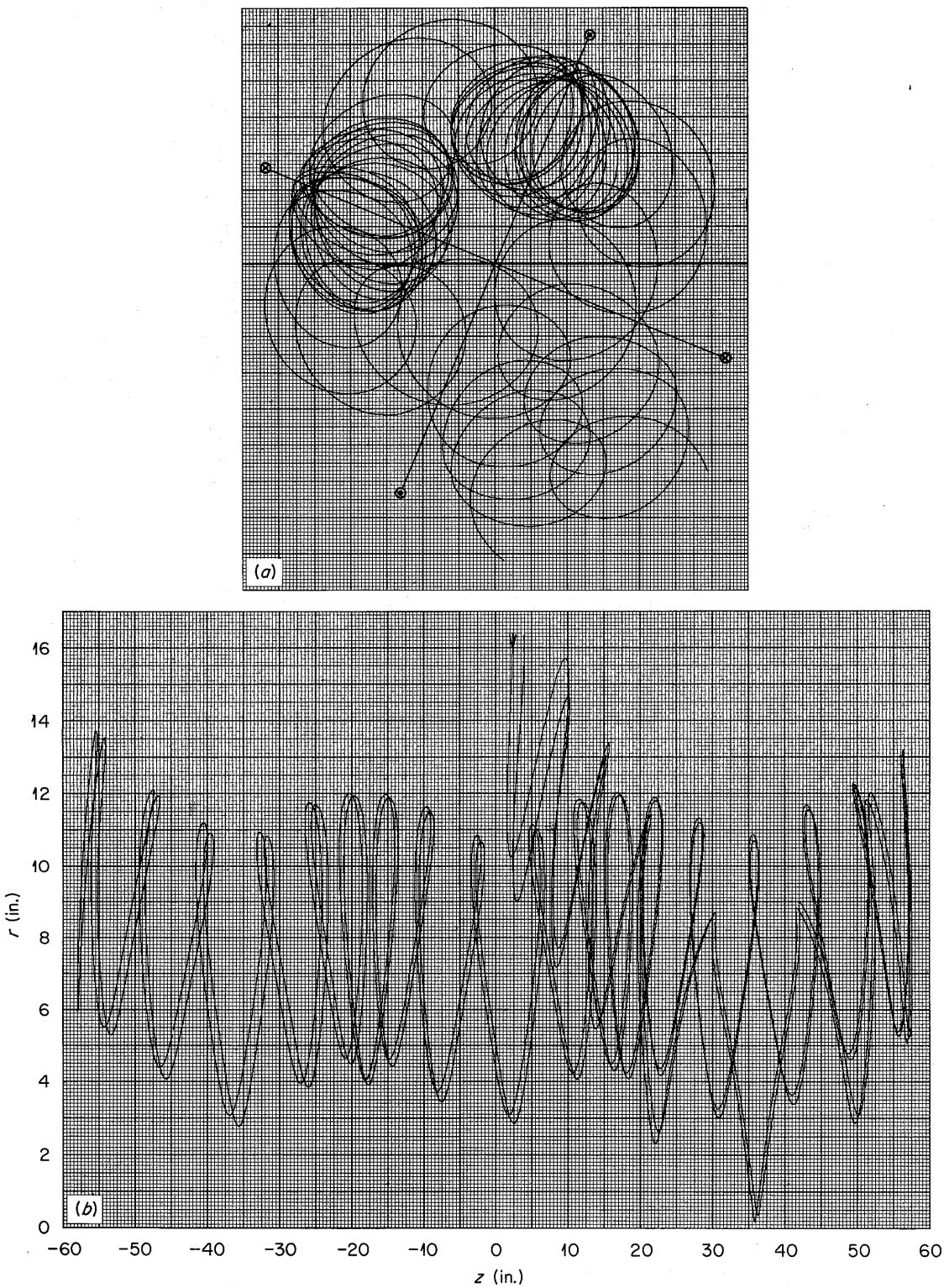

Fig. 8.6. (*a*) *X-Y* Plot of H_2^+ Orbit with $r_0 = 9$ in., $z = 2.31$ in., Bars at $67\frac{1}{2}°$, 4.4 μsec; (*b*) *R-Z* Plot of H_2^+ Orbit with $r_0 = 9$ in., $z = 2.31$ in., Bars at $67\frac{1}{2}°$, 4.4 μsec.

Table 8.2. H^+ with $r_0 = 6$ in.

Bar Position	Time Contained (μsec)
45°	10
67½°	3.29
90°	0.24
135°	10
157½°	10
180°	10

Table 8.3. H^+ with $r_0 = 4$ in.

Bar Position	Time Contained (μsec)
45°	10
67½°	10
90°	5
135°	10
157½°	10
180°	10

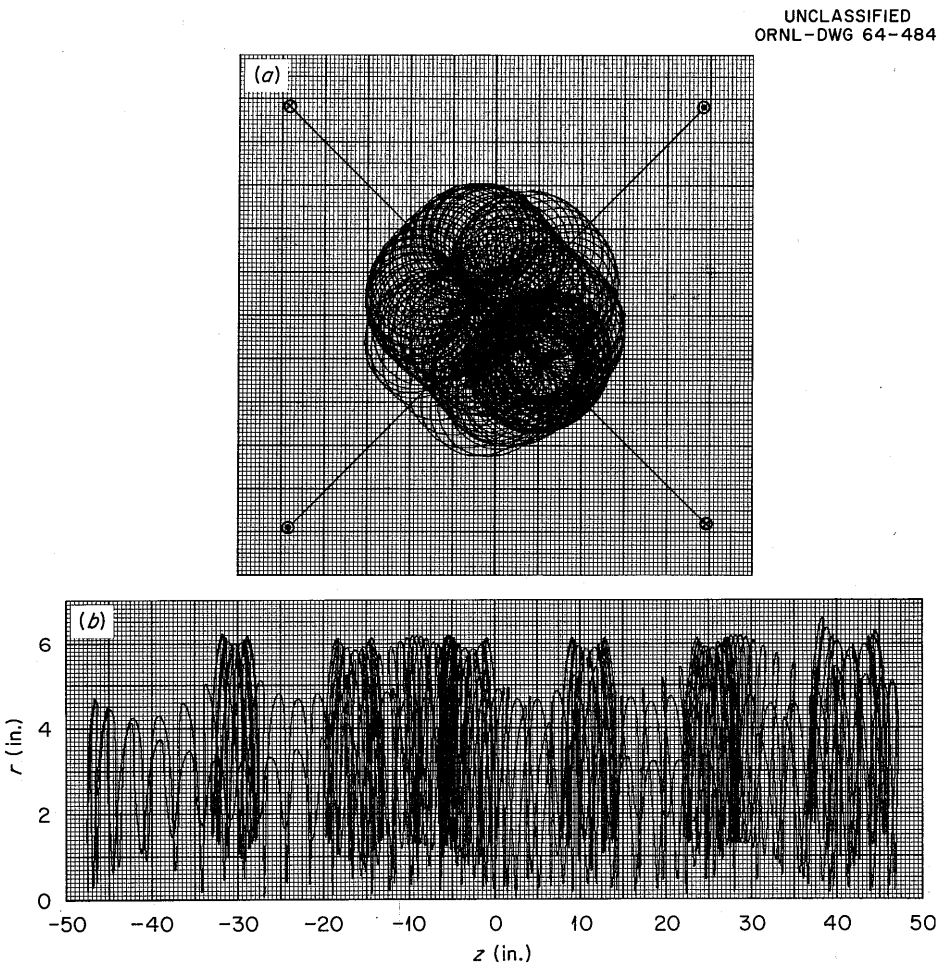

Fig. 8.7. (*a*) *X-Y* Plot of H^+ Orbit with $r_0 = 6$ in., $z = 42.0$ in., Bars at 45°, 10 μsec; (*b*) *R-Z* Plot of H^+ Orbit with $r_0 = 6$ in., $z = 42.0$ in., Bars at 45°, 10 μsec.

UNCLASSIFIED
ORNL-DWG 64-482

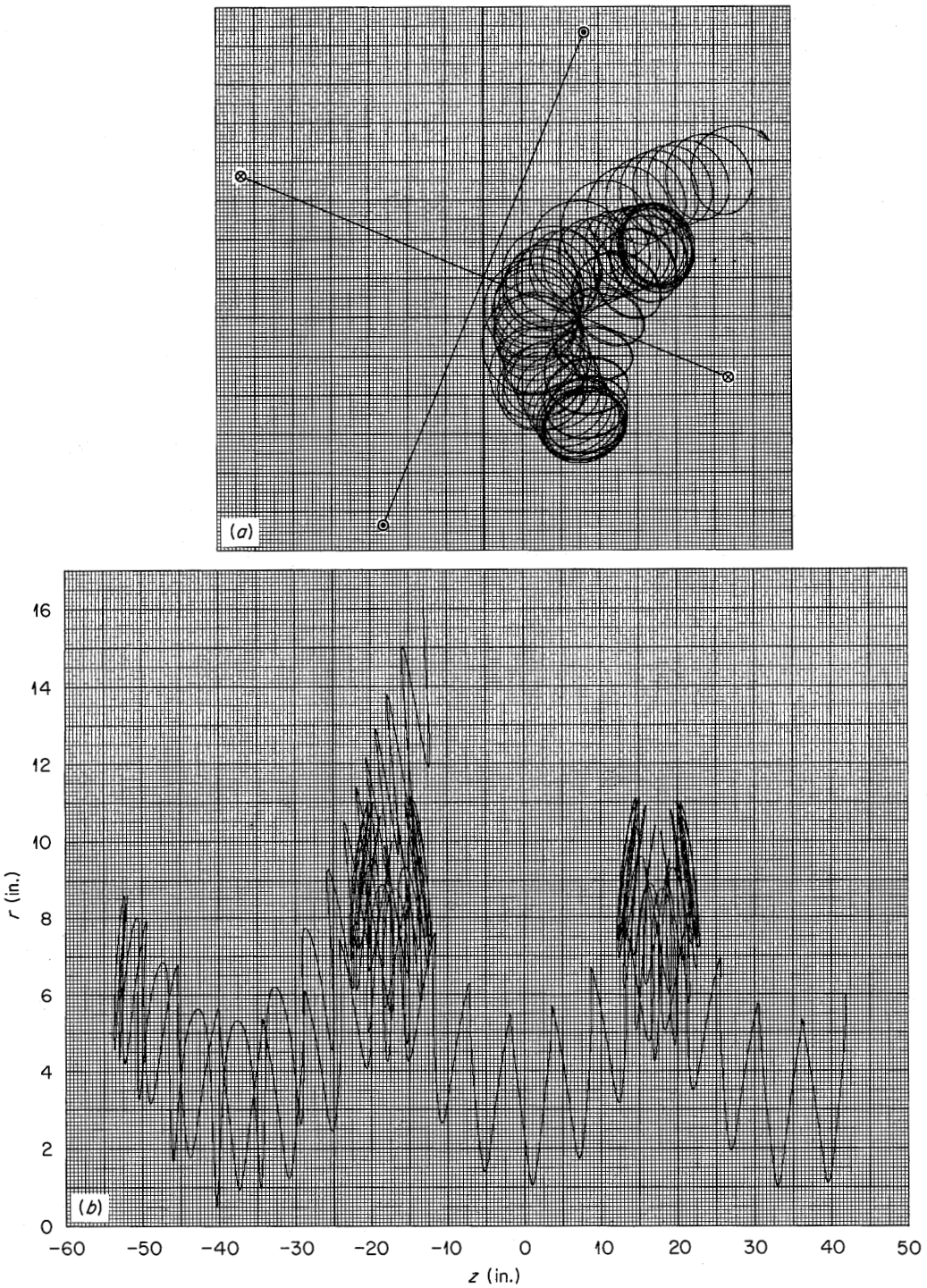

Fig. 8.8. (*a*) *X-Y* Plot of H^+ Orbit with $r_0 = 6$ in., $z = 42.0$ in., Bars at $67\frac{1}{2}°$, 3.29 μsec; (*b*) *R-Z* Plot of H^+ Orbit with $r_0 = 6$ in., $z = 42.0$ in., Bars at $67\frac{1}{2}°$, 3.29 μsec.

UNCLASSIFIED
ORNL-DWG 64-485

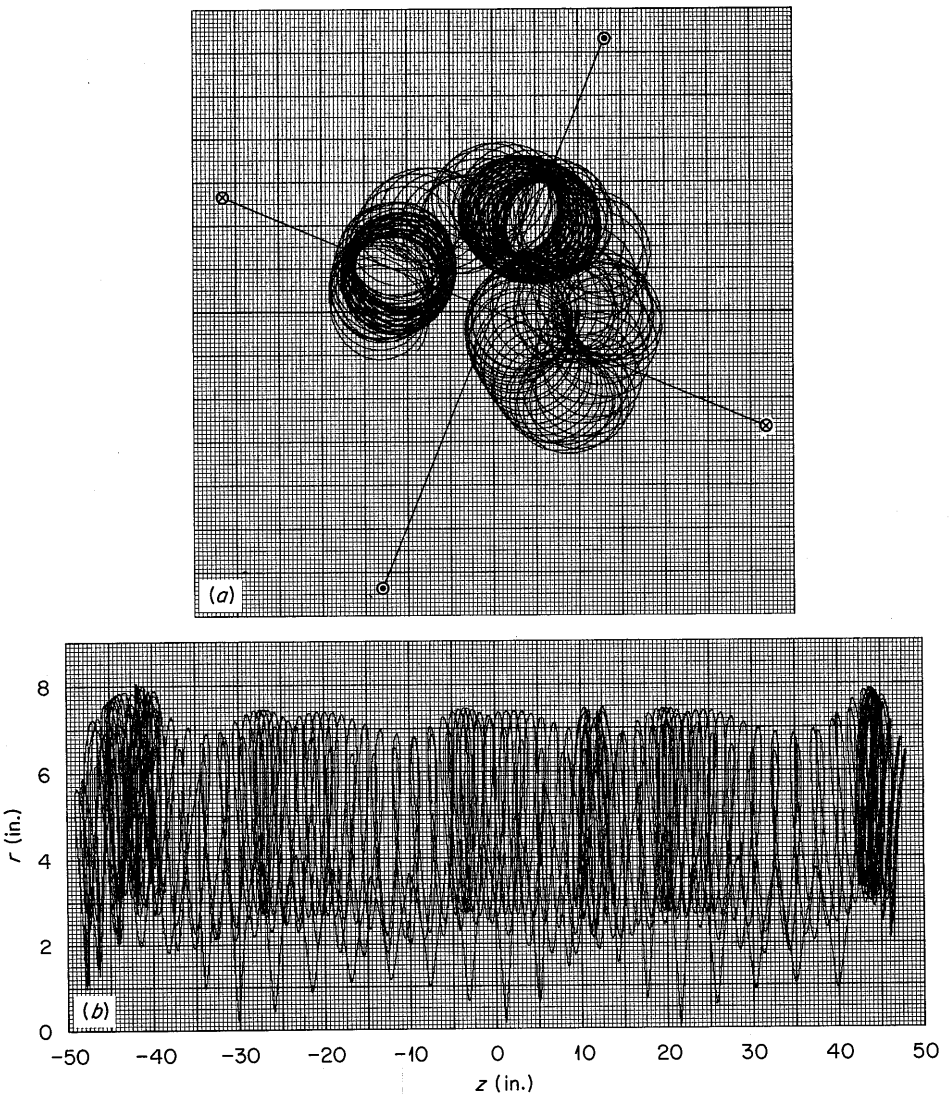

Fig. 8.9. (*a*) *X-Y* Plot of H^+ Orbit with $r_0 = 4$ in., $z = 42.0$ in., Bars at $67\frac{1}{2}°$, 10 μsec; (*b*) *R-Z* Plot of H^+ Orbit with $r_0 = 4$ in., $z = 42.0$ in., Bars at $67\frac{1}{2}°$, 10 μsec.

UNCLASSIFIED
ORNL-DWG 64-486

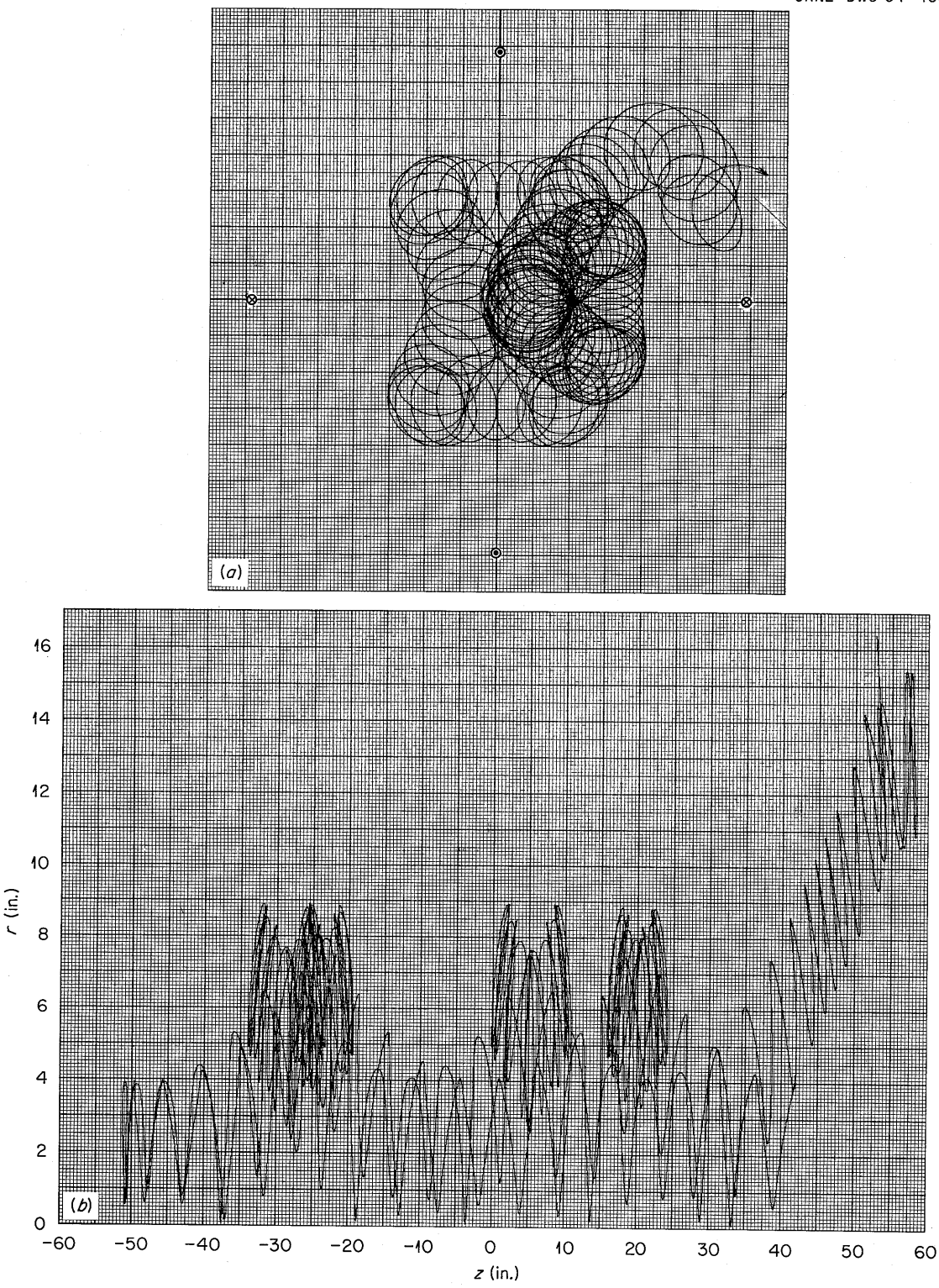

Fig. 8.10. (*a*) *X-Y* Plot of H^+ Orbit with $r_0 = 4$ in., $z = 42.0$ in., Bars at 90°, 5 μsec; (*b*) *R-Z* Plot of H^+ Orbit with $r_0 = 4$ in., $z = 42.0$ in., Bars at 90°, 5 μsec.

UNCLASSIFIED
ORNL-DWG 64-487

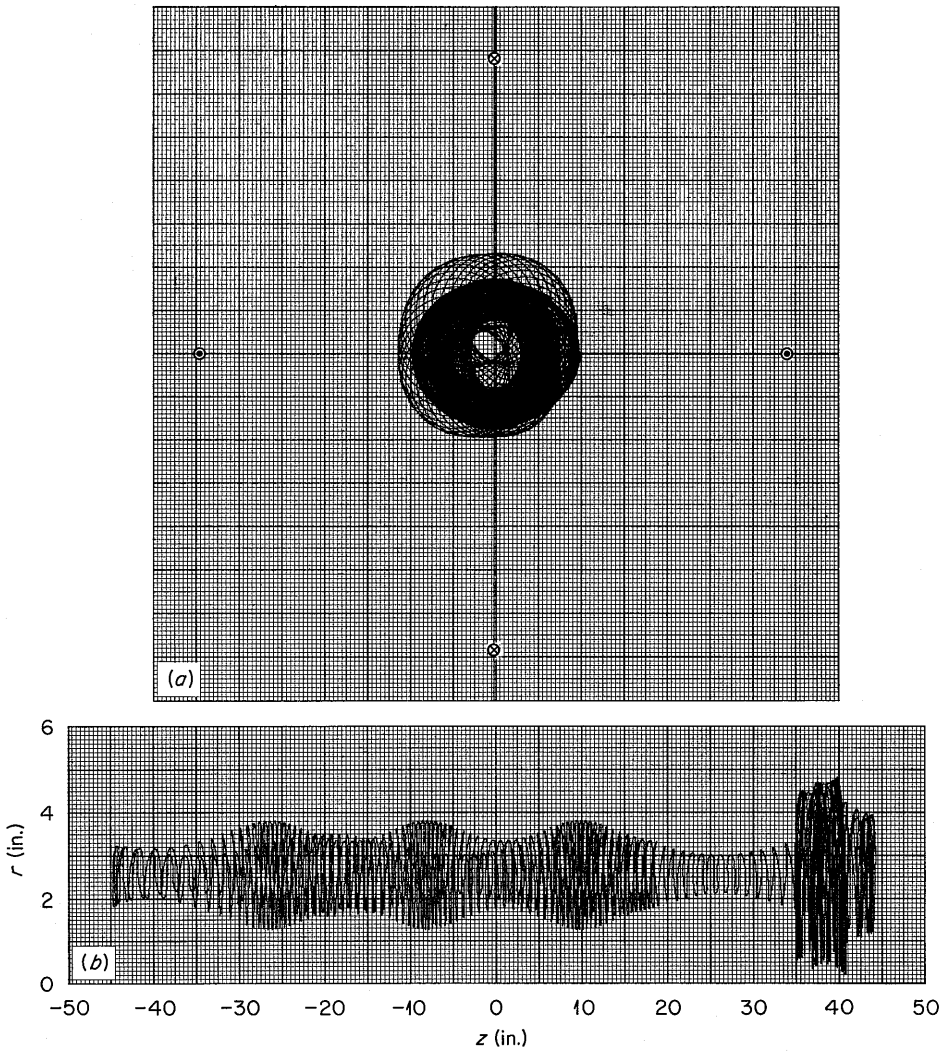

Fig. 8.11. (*a*) *X-Y* Plot of H^+ Orbit with $r_0 = 4$ in., $z = 42.0$ in., Bars at 180°, 10 μsec; (*b*) *R-Z* Plot of H^+ Orbit with $r_0 = 4$ in., $z = 42.0$ in., Bars at 180°, 10 μsec.

9. Magnetics and Superconductivity

9.1 A STUDY ON MINIMUM *B* CONFINEMENT FIELDS

W. F. Gauster
D. A. Griffin
J. N. Luton
C. E. Parker
Mozelle Rankin
P. A. Thompson

Recently much interest has been devoted to the minimum *B* confinement field configurations. This study deals with three special cases: a hypothetical application of Ioffe bars to DCX-2, a special form of J. Andreoletti's axisymmetric field designs, and a coil arrangement suggested by D. A. Baker, LASL.

9.1.1 Application of Ioffe Bars to DCX-2

A preliminary investigation was made on how the concepts of Ioffe *et al.*[1] of superimposing a multipole cusp field on an axisymmetric mirror field could be applied to DCX-2. The principal arrangement and the main dimensions are shown in Fig. 9.1. In this connection it should be remembered that the injection duct of DCX-2 (ref. 2) is so arranged that the molecular-ion beam enters the main field at a distance of 42 in. from the midplane of the machine. The distance from the injection point to the midplane of the mirror coils is 39 in. Therefore, the end connections of the Ioffe bars are well inside the mirror coils. In order to minimize the field deformations due to the end connections, the winding arrangement shown in Fig. 9.1 was considered. It corresponds to a set of two cusp coil pairs which are perpendicular to the x and y axis, respectively. Here the field deformation produced by the end connections is relatively small. Ioffe *et al.* use, for a six-bar system, another winding scheme. This arrangement, applied to a four-bar system, is shown in Fig. 9.2, but since the field deformations become larger it will not be applied here.

The field at the center of DCX-2 is 12 kilogauss and decreases near the injection duct to approximately 11.9 kilogauss. The superimposed quadrupole field required in the machine midplane at 6 in. from the center was assumed to be about 6 kilogauss. The space available in DCX-2 would be sufficient for a four-bar system – each bar occupying up to 30° in azimuth, and a radial depth determined by inner and outer radii of 11 and 17 in., respectively. In order to produce the desired field, about 5.8×10^5 ampere-turns for each bar would be necessary. This corresponds to a power of approximately 6 Mw.

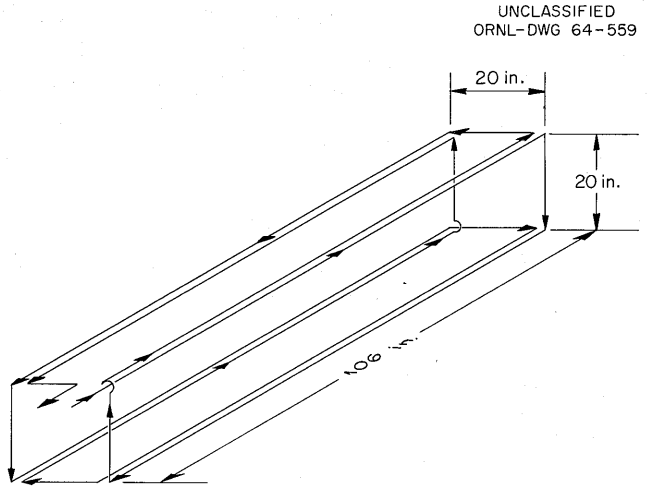

Fig. 9.1. Quadrupole Conductor Arrangement with Eight End Connections.

[1]Y. B. Gott, M. S. Ioffe, and V. G. Telkovsky, "Proceedings of the Conference on Plasma Physics and Controlled Nuclear Fusion Research, 4–9 September 1961, Salzburg, Austria," *Nucl. Fusion*, 1962 Supplement, Part 3, p. 1045–1047. See also: H. P. Furth, UCRL-6933 (Oct. 2, 1963) and UCRL-7452 (July 30, 1963).

[2]*Thermonuclear Div. Semiann. Progr. Rept. Jan. 31, 1961*, ORNL-3104, p. 21.

UNCLASSIFIED
ORNL-DWG 64-560

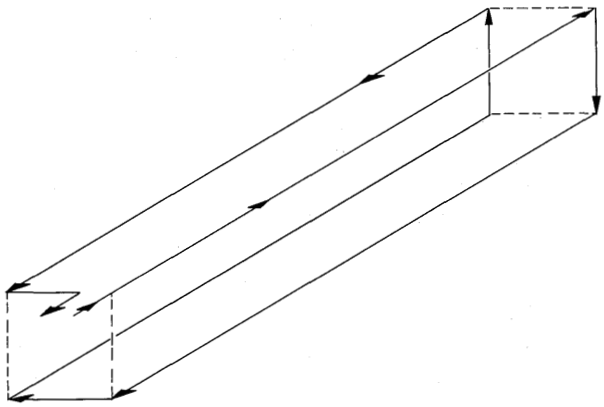

Fig. 9.2. Quadrupole Conductor Arrangement with Four End Connections.

Assuming the same cross section for each bar, a hexapole instead of a quadrupole system would need a power of about 21 Mw for producing again 6 kilogauss at 6 in. from the center. Furthermore, in DCX-2 it would be more difficult to accommodate six instead of four bars. Because of the necessary accessibility, it would not be possible to use for each bar the azimuthal angle of 30° previously mentioned for the quadrupole system; that is, the bar cross section would have to be drastically reduced. This means, of course, a very substantial increase of the necessary power beyond the mentioned value of 21 Mw. As a consequence of this power consideration, detailed field calculations were made for a quadrupole system only.

Figure 9.3 shows the lines of constant-magnitude B at the midplane of DCX-2 if four Ioffe bars are provided. The field increases monotonically from 12 kilogauss at the center to 14.2 kilogauss. The B = 14.2 kilogauss line consists of two branches, each enclosing two Ioffe bars. These B-constant line branches intersect in four singular points, S_1 to S_4. The B-line segments joining the singular points surround the center in almost square shape. Passing from the center O radially through one of these singular points, the field reaches a maximum of 14.2 kilogauss and decreases with increasing radius. For any other azimuthal angle the 14.2 kilogauss line does not represent a maximum. The points S_1 to S_4 are saddle points of the "magnitude B surface."

Finally, Fig. 9.4 shows the constant B lines in a plane perpendicular to the z axis in a distance of 40 in. from the midplane. The B distribution

UNCLASSIFIED
ORNL-DWG 64-561

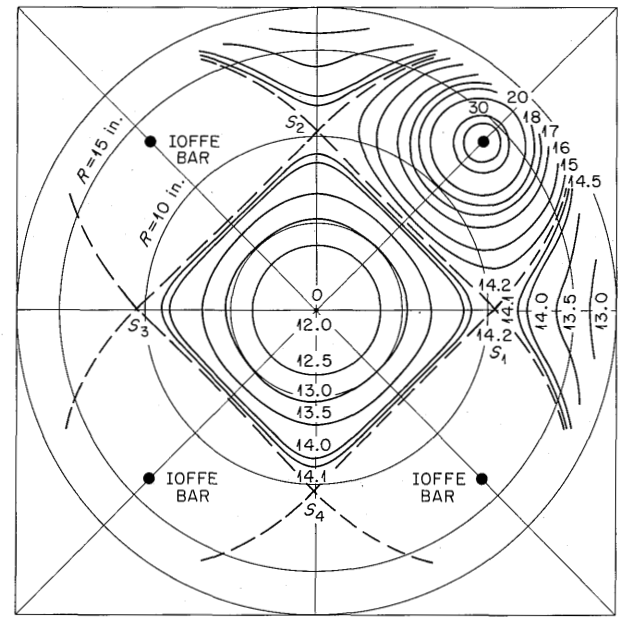

Fig. 9.3. DCX-2 Field with Superimposed Quadrupole Field. Bar current, 5.8×10^5 amp; constant B lines at midplane.

UNCLASSIFIED
ORNL-DWG 64-562

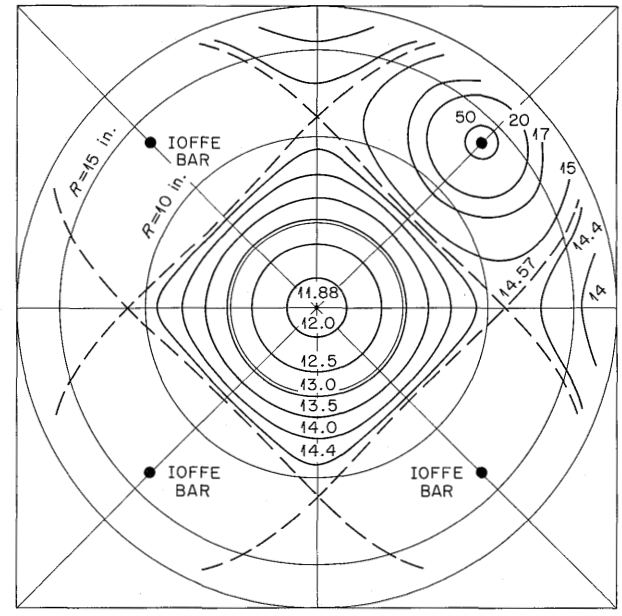

Fig. 9.4. DCX-2 Field with Superimposed Quadrupole Field. Bar current, 5.8×10^5 amp; constant B lines at plane z = 40 in.

is quite similar to that in the midplane; the critical field strength is 14.57 instead of 14.2 kilogauss.

The described brief investigation demonstrates a possible field modification of DCX-2 using a quadrupole Ioffe bar system. More detailed calculations could be done if the results of the DCX-2 experiments indicate that such a modification of the presently employed field configuration appears to be necessary.

9.1.2 J. Andreoletti's Field Configurations

J. Andreoletti[3] investigated confinement and stability properties of "magnetic wells" – magnetic fields having a finite volume inside which the energy density $B^2/2\mu_0$ has a nonzero minimum. He devised methods for a systematic search for these fields and presented several different types of solutions. Three of them are axisymmetric; one consists of pairs of especially shaped cusp coils, symmetrically arranged to a plane perpendicular to the z axis. Andreoletti made magnetic field measurements employing a model shown in Fig. 9.5. A set of five pairs of cusp coils was used, and by changing the coil currents, different field configurations were achieved.

Andreoletti describes three special cases with different ampere-turn numbers for each individual cusp coil pair (Table 9.1). In cases *a* and *b* he found, when measuring the flux density B in the midplane, two equal maximum values B_{max} and, in between, one minimum value B_{min}. These values and the mirror ratios in the r direction, $K_r = B_{max}/B_{min}$, are listed in Table 9.1. In case c, his measurements yielded one approximately constant value of 10.8 in the range $5.5 \leqq r \leqq 16.5$.

Since we were interested in the accuracy of Andreoletti's model measurements, we calculated[4] for cases *a*, *b*, and *c* the quantities B_r, B_z, and B in a toroidal volume determined by $8 \leqq r \leqq 12$ and $0 \leqq z \leqq 1.7$ in steps of 0.1. The value 1.7 represents the axial distance of the nearest surface of coil III from the midplane $z = 0$ (Fig. 9.5). The shape of the magnitude B surface is so complicated that we built, for case *a*, a model of this surface consisting of ten vertically arranged pieces of cardboard (Fig. 9.6). The upper rim of each piece is cut corresponding to magnitude B lines for $z =$ 0, 0.2, 0.4 ... 1.6, and 1.7. This model shows that in case *a* the magnitude of B around B_{min} is almost independent of z, which indicates poor containment in the z direction. As expected, case c yields no sufficient containment in the r direction. For case *b* the calculation yielded the following results: B assumes a very flat minimum of 7.3000 at $r = 10.27$; for $r = 10.20$, a minimum of 7.2994 occurs at $z = 0.5$; for $r = 10.4$ and $z =$ 1.20, the minimum value is 7.2827. Unfortunately in case *b*, therefore, similar to case *a*, there is no monotonic increase of B around a B_{min} point in all directions.

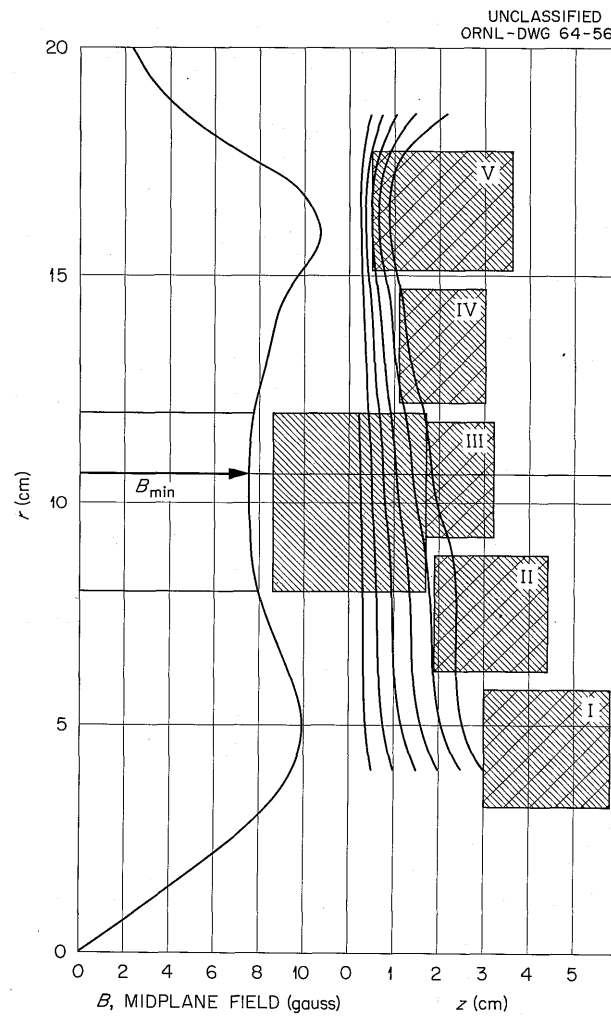

Fig. 9.5. J. Andreoletti's Coil Arrangement and Midplane Field Configuration.

[3] J. Andreoletti, *Compt. Rend. Acad. Sci. Paris* **257**, 1235–37 (1963).

[4] M. W. Garrett, *Calculations of Fields, Forces, and Mutual Inductances of Current Systems by Elliptical Integrals* (forthcoming ORNL-3575A); *J. Appl. Phys.* **34**(9), 2567 (1963).

In conclusion it can be said that Andreoletti's coil arrangement as described previously does not produce absolute B-minimum surfaces in any of his cases *a*, *b*, and *c*. Our calculations, however, do not consider the relaxed stability criterion $\int dB/B$ for these three cases. It might be possible that Andreoletti's magnetic fields satisfy this condition. Finally, we assume that with an appropriate change of the coil arrangement and in the numbers of ampere-turns for each cusp coil pair, an absolute B-minimum surface can be achieved. Such an investigation is under way.

Table 9.1. J. Andreoletti's Coil Arrangement for Minimum B Fields

Case	Ampere-Turns of Coils					B_{max}	B_{min}	K_r
	I	II	III	IV	V			
a	150	16.5	18.7	20	45	8.4	6.85	1.23
b	108	27.5	16.5	26	30	7.8	7.2	1.085
c	185	40.0	49.0	40	57	10.8	10.8	1.00

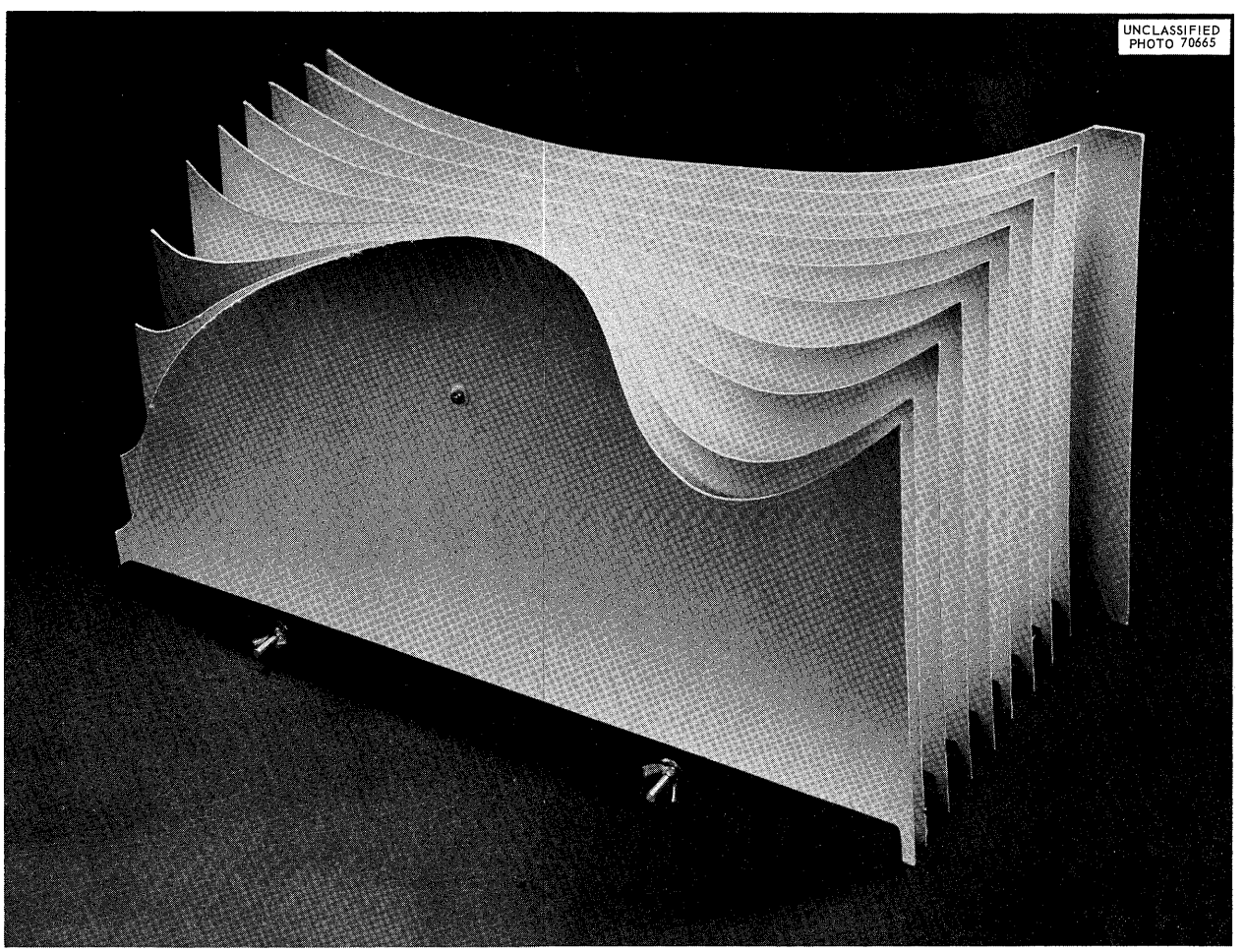

Fig. 9.6. Photo of Model Showing Field Configuration of J. Andreoletti's Coil Arrangement (Case *a*).

9.1.3 D. A. Baker's Coil Arrangement

Recently D. A. Baker made a study of the magnetic field produced by a pair of rectangular mirror coils, energized by currents in the same direction (magnetically aiding), and separated the proper distance with their planes parallel and their major axes at right angles.[5] (This is a special case of the class of noncircular mirror coils of elongated shape, which would include oval, elliptical, rectangular, etc.) His analytical investigations indicate that this arrangement can achieve a minimum B confinement field – this result was also obtained by Andreoletti, Brachet, and Berlingot. Further, his study indicates that for the limiting case of two pairs of infinitely long antiparallel wires (distance W between the wires of each pair and distance S between the planes determined by each pair) there is still the desired confinement configuration, if the following condition is satisfied:

$$\frac{1}{\sqrt{3}} < \frac{S}{W} < \frac{1}{\sqrt{2}}. \qquad (1)$$

We were interested in the details of the field produced by infinitely long filaments with the special data: W = 20 cm, S = 13 cm, and I = 1000 amp, which yields a field in the center of B_0 = 56.24 gauss. [The S/W ratio is approximately in the middle of the limits indicated by Eq. (1).] Cartesian coordinates for this case are shown in Fig. 9.7; the results of our computer calculations are given in Figs. 9.8, 9.9, and 9.10. All data are for the magnitude of B normalized by dividing by B_0. It should be noted that the symmetry of this general class of mirror coils is such that all data are included in one octant of space; for simplicity the first octant is considered using Miller indices to describe the direction of the different radial lines.

Figure 9.8 shows B vs radius in the [001] direction (i.e., along the z axis). For the case of main interest (S = 13 cm), a maximum of 1.0083 occurs at z = 3.6 cm. The dashed curves indicate how a change in the parameter S (separation of "coils") affects the magnitude of the field along this direction: For S = 14 cm, which is very nearly to the upper limit given in Eq. (1), the maximum does enlarge and move farther out; however, field increases in the other directions are adversely affected.

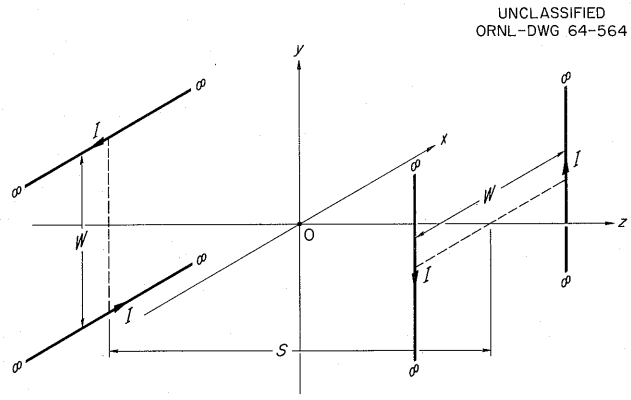

Fig. 9.7. D. A. Baker's "Absolute B Minimum" Arrangement.

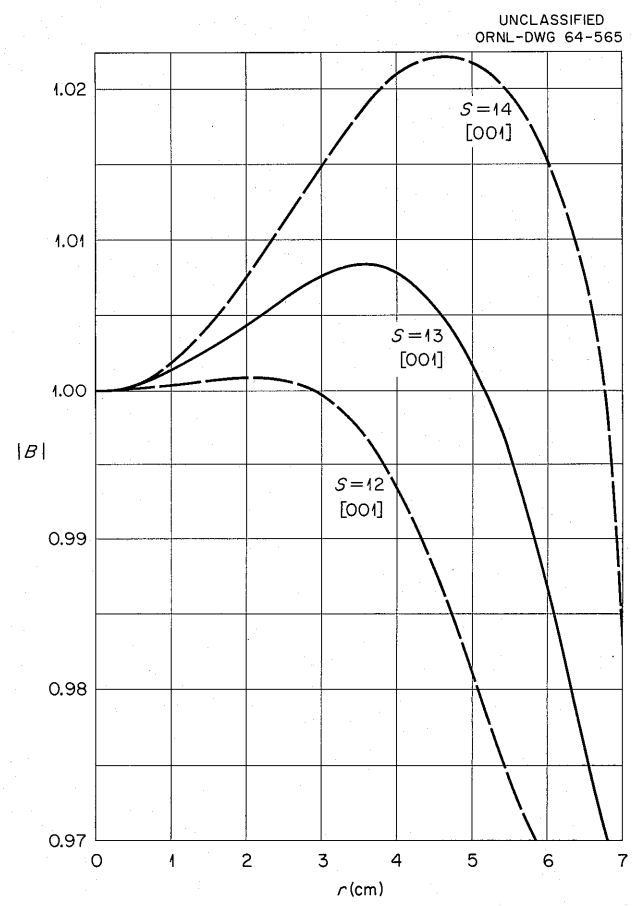

Fig. 9.8. D. A. Baker's Arrangement. Effect on $|B|$ of changing separation of coils.

[5] D. A. Baker, "A Study of the Magnetic Field Produced by a Pair of Rectangular Mirror Coils," LASL Meeting, September 12–13, 1963.

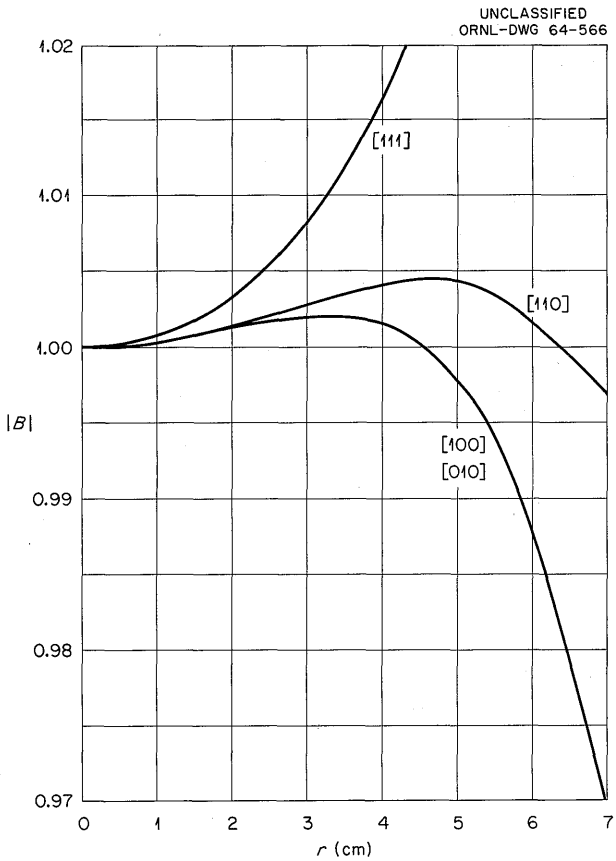

Fig. 9.9. D. A. Baker's Arrangement. $|B|$ vs r for directions indicated (S = 13 cm).

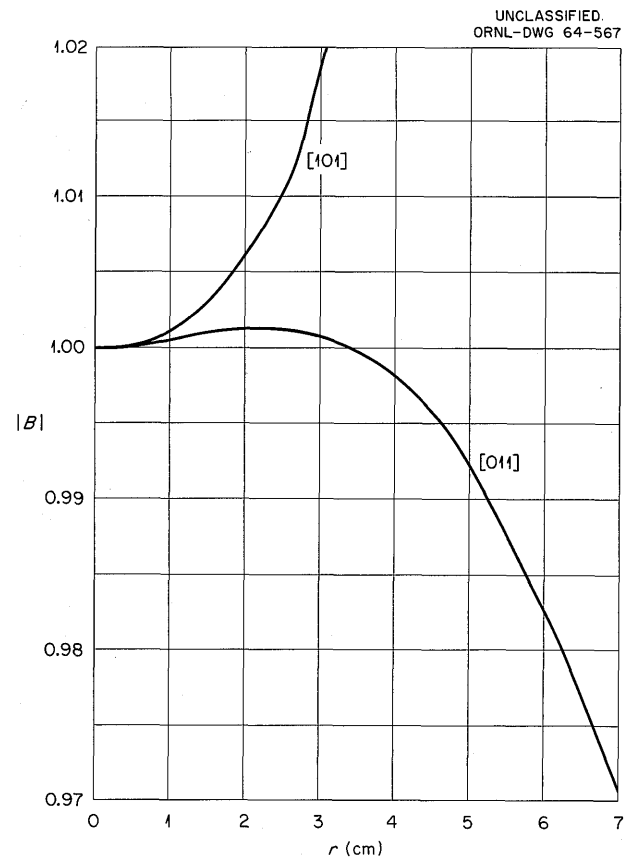

Fig. 9.10. Largest and Smallest Maxima in $|B|$ vs r.

For the rest of our calculations only the case S = 13 cm was considered. In Fig. 9.9 the field as a function of radii in either the [100] or [010] directions (x or y axes) shows a maximum of only 1.002 at about 3.5 cm. For the face diagonal [110], the maximum is bigger (1.004) and at the somewhat larger radius of 4.8 cm. Also in Fig. 9.9 we see that the cube diagonal [111] represents a radius of strong increase, reaching 2% at 4.3 cm.

The directions of maximum and minimum increase are given in Fig. 9.10. The point of 2% increase comes at just beyond 3 cm for the [101] radius (and has grown to 20% by about 7 cm); however, in the [011] the extremely weak maximum of 1.0012 is found only 2.2 cm from the center of the system.

These numerical results are similar to those given by D. A. Baker for finite loops with a length-to-width ratio of 5. As he mentions, the poor mirror ratios could be very much improved by the addition of appropriate homogeneous bucking fields. This means, however, a very great increase of the loss power, if conventional coils were used.

9.2 THE NEW MAGNET LABORATORY

W. F. Gauster D. L. Coffey

The new magnet laboratory is an experimental facility for developing and testing conventional magnet coil designs and for performing experiments with the goal of developing superconducting magnets for thermonuclear research. The costs of building the laboratory were relatively small because the most expensive parts of such a facility – the dc power supply and the water cooling system – were available here for plasma physics experiments.

At this time one magnet coil (designated B_1) and a set of two axially arranged identical coils of the same type (B_2 and B_3) are installed. The first one produces 60 kilogauss when energized with one of the 3-Mw generators (8600 amp, 350 v). The second, operated with two of these generators in series, produces 80 kilogauss.[6] The coils have an inside working diameter of 6.5 in. and generate magnetic fields of very good homogeneity. The field stability with currents of 1000 amp and higher is excellent (±0.05%); for lower currents the regulation needs improvement.

The cooling water is taken from the general closed cooling-water system of the Thermonuclear Division building. It contains 50,000 gal of filtered, demineralized, and deoxidized water, with a circulation rate of 5000 to 12,000 gpm, sufficient for a heat dissipation of 50 Mw.

Figure 9.11 shows a photograph and Fig. 9.12 the floor plan of the magnet laboratory. The coils are marked with B_1 and $B_2 + B_3$, respectively. More space is provided for two additional magnet coils (S_1 and S_2). Generator panel G_1 serves for the operation of one generator and panel G_2 for controlling two additional generators simultaneously. The instrument console C contains monitoring instruments for magnet currents and temperatures. A ballistic galvanometer BG is mainly used for magnetic moment measurements. The two instrument panels E_1 and E_2 house experimental electronic equipment such as microvoltmeters, dc nanovolt amplifiers, x-y recorders, and the control equipment for transistorized current sources, which can be programmed. M_1 and M_2 indicate low-field magnets (up to 1.0 and 10.0 kilogauss, respectively) for experiments with ideal superconductors of first and second kind. A superconducting coil (M_3) with a working diameter of 1 in. allows production of fields up to 50 kilogauss. This coil can be operated with persistent currents for perfect field stability.

It is intended to keep in the magnet laboratory, which is air conditioned, the rather large collection of magnetic measurement instruments which are being used to make field measurements for the various plasma physics experiments – except such instruments as are permanently located at the respective experimental facilities. Rawson

[6] *Thermonuclear Div. Semiann. Progr. Rept. Apr. 30, 1962*, ORNL-3315, p. 74; *Thermonuclear Div. Semiann. Progr. Rept. Oct. 31, 1962*, ORNL-3392, p. 67.

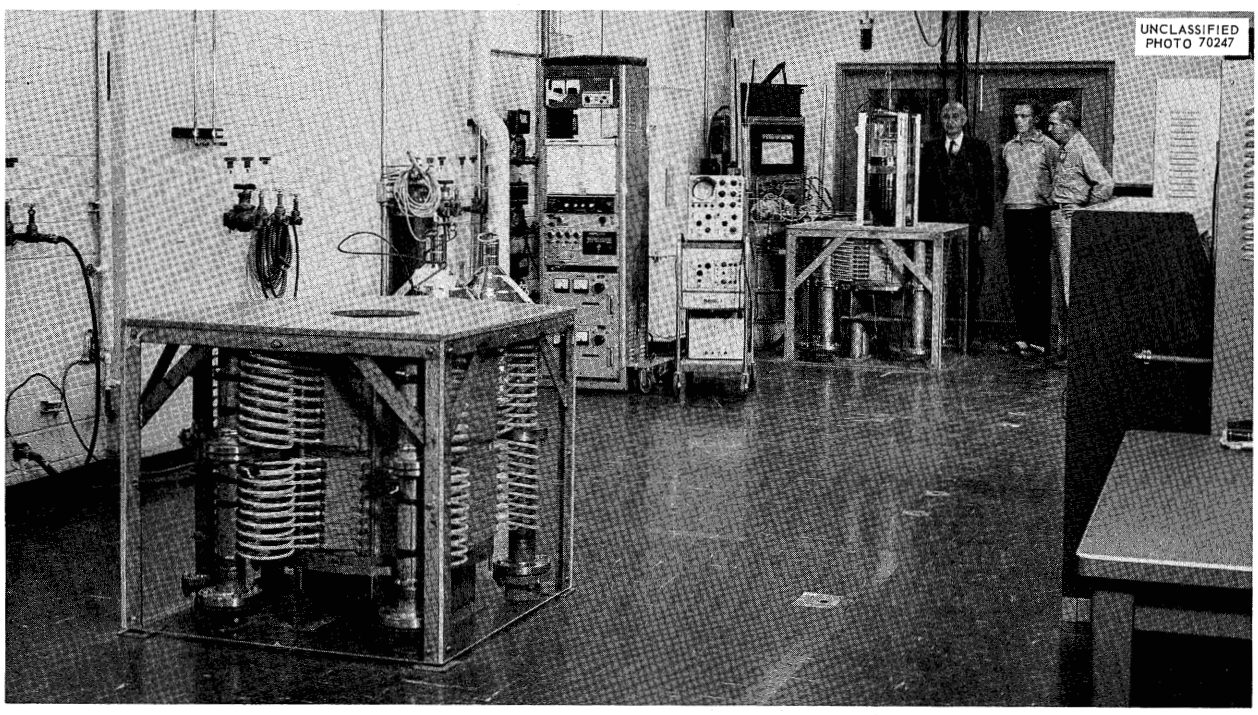

Fig. 9.11. Magnet Laboratory.

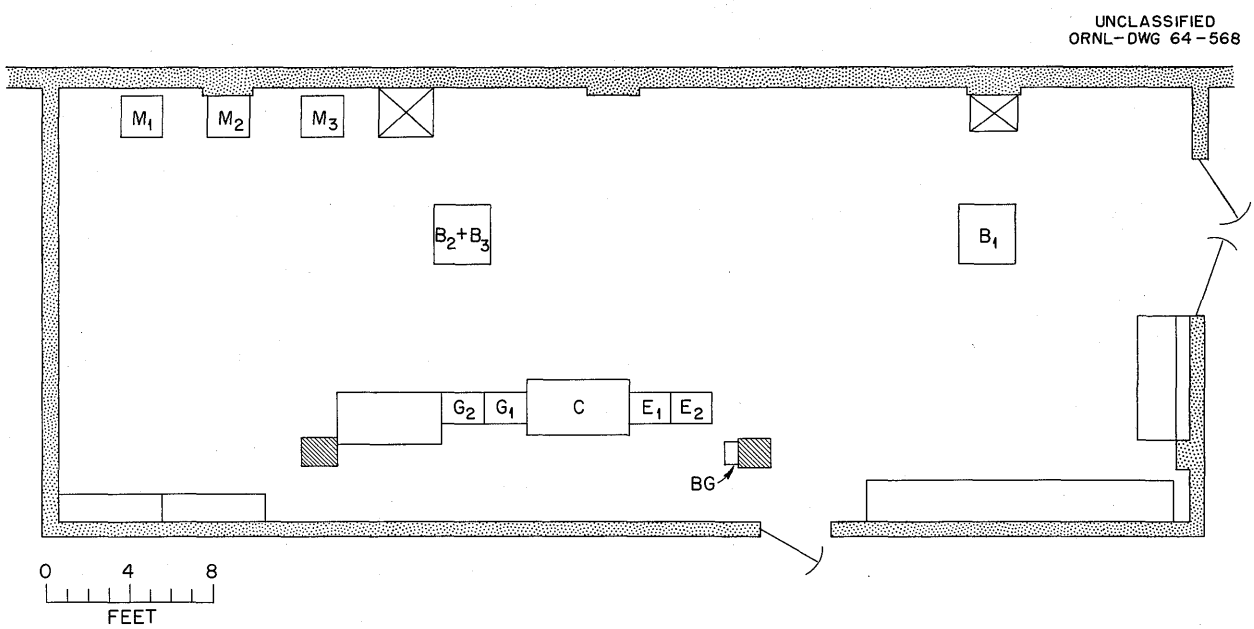

Fig. 9.12. Magnet Laboratory (Floor Plan).

magnetometers (with rotating coils), Hall probe instruments, a ballistic magnetometer, and nuclear magnetic resonance instruments are available. A magnetic coil arrangement with high field homogeneity will be provided for precise calibration of these measurement instruments.

Previous careful tests with the mentioned coils, B_1, B_2, and B_3, gave useful information about mechanical forces, deformation, and stress on the electrical insulation of conventional high-power magnet coils. The axial arrangement of the B_2 and B_3 coils operated with full current produces mechanical forces of approximately 250 tons between the components,[6,7] and the future performance of the coil set should yield valuable experience concerning critical details such as conductor crossover. Careful observations of water temperatures[8] along the water path in the hollow conductors, and tests concerning erosion phenomena in hollow copper conductors[9] are also of great practical importance.

To achieve the goal of developing superconducting magnets with dimensions of interest for thermonuclear research calls for more basic investigations on high-field superconductors. Experiments with larger superconducting coils are very expensive and time consuming, and a more scientific and systematic approach will save effort and money in the long run.

Through the engineering efforts of R. L. Brown, W. L. Wright, R. E. Hill, E. A. Crow, and others, solutions have been found to the many mechanical, electrical, and hydraulic problems which must be solved for successful operation of the laboratory. It is now in full operation.

9.3 A STUDY ON MODELS OF HIGH-FIELD SUPERCONDUCTORS

W. F. Gauster

9.3.1 Introduction

Simple models of high-field superconductors have been proposed by Heinz London,[10] C. P.

[7] *Thermonuclear Div. Semiann. Progr. Rept. Apr. 30, 1962*, ORNL-3315, p. 75; *Thermonuclear Div. Semiann. Progr. Rept. Jan. 31, 1961*, ORNL-3104, p. 113.

[8] *Thermonuclear Div. Semiann. Progr. Rept. Apr. 30, 1963*, ORNL-3472, p. 103.

[9] *Thermonuclear Div. Semiann. Progr. Rept. Apr. 30, 1962*, ORNL-3315, p. 85; *Thermonuclear Div. Semiann. Progr. Rept. Apr. 30, 1963*, ORNL-3472, p. 121.

[10] Heinz London, private communication; see R. A. Kamper, *Phys. Letters* **2**(6), 290 (1962) and C. P. Bean and R. W. Schmitt, *Science* **140**(3562), 26 (1963).

Bean,[11] and Y. B. Kim *et al.*[12,13] They assume that high-field superconductors can carry a critical current density J_c which is either approximately field-independent (London and Bean) or is a function of the local field B (Kim *et al.*). Bean considers also shielding to a field H_c due to soft superconducting material in the interstices of the mesh. Kim *et al.* discuss flux trapping ("tube magnetization") and magnetic moment measurements, consider the general properties which follow from their model when any form of the dependence $J_c(B)$ is assumed, and derive from experiments an empirical relation

$$\frac{\alpha}{|J|} = B_0 + |B| , \qquad (1)$$

which is the starting point of P. W. Anderson's theory of the "flux creep" in hard superconductors.[14] This theory has been further developed and extended to resistive states of hard superconductors by Kim *et al.* in two additional recent publications.[15,16]

The purpose of this study is to give a short, systematic presentation of the flux trapping and magnetic moment performance of hollow (and solid) cylinders of hard superconductors in longitudinal fields which are to be expected when the mentioned three different models are used. The forms derived here are partly more comprehensive than those published by other authors to date. Furthermore, this report deals with measurement methods which can be applied for correlating flux trapping and magnetic moment measurements. Experimental results obtained with bundles of copper-plated Nb-Zr wires and a discussion of the applicability of the model of Kim *et al.* to this special case are presented in the following paper.

[11] C. P. Bean, *Phys. Rev. Letters* 8(6), 250 (1962).

[12] Y. B. Kim, C. F. Hempstead, and A. R. Strnad, *Phys. Rev. Letters* 9(7), 306 (1962).

[13] Y. B. Kim, C. F. Hempstead, and A. R. Strnad, *Phys. Rev.* 129(2), 528 (1963).

[14] P. W. Anderson, *Phys. Rev. Letters* 9(7), 309 (1962).

[15] Y. B. Kim, C. F. Hempstead, and A. R. Strnad, "Resistive States of Hard Superconductors," to be published in the *Physical Review*.

[16] Y. B. Kim, C. F. Hempstead, and A. R. Strnad, *Phys. Rev.* 131(6), 2486 (1963).

9.3.2 Heinz London's model of High-Field Superconductors

It is supposed that the critical current density J_c is approximately constant in the entire range of field strength $0 \leqq H \leqq H_M$. No soft perfect flux exclusion at low fields is assumed. The simplest case of a hollow or solid cylinder cooled in zero field is considered here.

Figure 9.13 shows the current distribution inside the tube wall for six phases of a magnetization

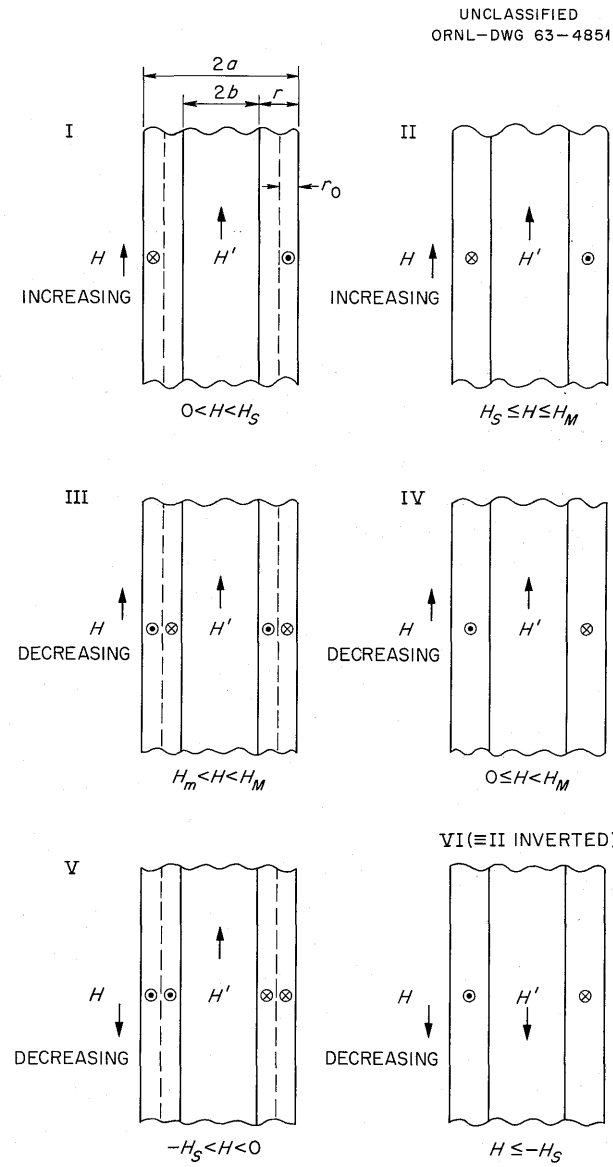

Fig. 9.13. Current Distribution in a High-Field Superconductor Tube for Different States of a Magnetization Cycle.

cycle if a homogeneous external field H parallel to the cylinder axis is applied. The corresponding internal field distribution is represented by Fig. 9.14. When H is raised to a moderate value H_{I}, the field B inside the tube wall decreases linearly (curve I), becomes zero at a distance R_{I} from the outside surface of the tube, and for $R_{I} \leqq R \leqq w$ the field $B = 0$ (curve I′). For $H = H_{II}$, the field penetrates over the entire wall thickness w. If the external field is raised to a maximum H_{M} and then lowered to H_{III}, currents in the opposite direction are supposed to propagate inward from the outer surface to a distance R_{III}. The currents for $R > R_{III}$ remain unchanged and the field distribution III–III′ (Fig. 9.14) results. When H is lowered to H_{IV}, the whole tube wall carries currents in the opposite direction. For $H = H_{V}$ the external field becomes negative; the field H'_{V} inside the tube is still positive. For a still lower value $H = H_{VI}$, the state represented by curve II is inverted.

The flux trapping or tube magnetization curve[12] (i.e., the $H - H'$ diagram) is shown in Fig. 9.15. It must be emphasized, however, that it is very difficult to achieve complete magnetization cycle measurements with high-field superconducting cylinders or tubes, since "flux jumps" might occur.[13]

The field distribution inside the tube for the cases I to VI can be easily calculated. We first consider case II (Figs. 9.13 and 9.14):

$$B = H - \frac{4\pi}{10} J_c R \,. \tag{2}$$

The distance R is measured from the outside surface of the hollow cylinder. Introducing the designations

$$\frac{4\pi}{10} = k, \quad kJ_c w = H^*, \quad \frac{H}{H^*} = h, \quad \frac{B}{H^*} = b, \frac{R}{w} = r \,, \tag{3}$$

UNCLASSIFIED
ORNL-DWG 63-7182R

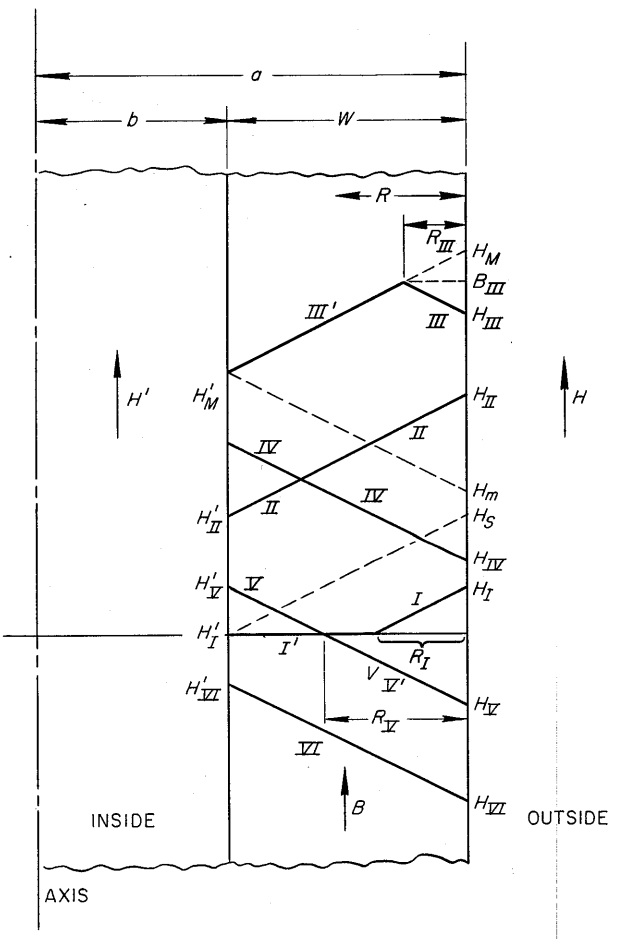

Fig. 9.14. Field Distribution in a High-Field Superconductor Tube for Different States of a Magnetization Cycle.

UNCLASSIFIED
ORNL-DWG 63-6827

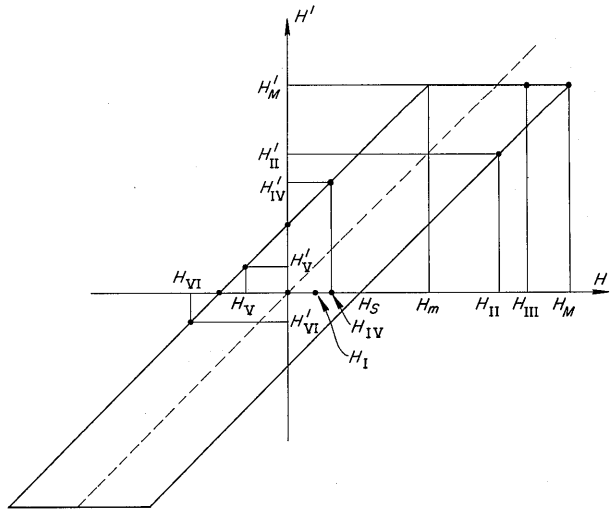

Fig. 9.15. Tube Magnetization Curve for H. London's Model.

we obtain

$$b = h - r\,, \tag{4}$$

and

$$b(r = 0) = h;\quad b(r = 1) = h' = h - 1\,. \tag{5}$$

The corresponding equations for cases I to VI are listed in Table 9.2. Obviously the normalization of the quantities used simplifies the notation very much.

The current and field distribution inside the tube wall is independent of the magnitude of the inside radius $a - w$ of the hollow cylinder. This does not hold, however, for the average magnetic moment per unit volume $\overline{M}$ of the superconducting tube:

$$-4\pi\overline{M} = \frac{1}{\pi[a^2-(a-w)^2]}\int_{R=0}^{w} 2\pi(a-R)(H-B)\,dR\,. \tag{6}$$

In normalized form (with $a = Kw$)

$$-4\pi\overline{m} = -4\pi\,\frac{\overline{M}}{H^*} = \frac{2}{2K-1}\int_{r=0}^{1}(K-r)(h-b)\,dr\,. \tag{7}$$

For a thin-walled tube $K \to \infty$; for a solid cylinder $K = 1$. Another convenient form of Eq. (7) is

$$-4\pi\overline{m} = h - \overline{b}\,,$$

$$\overline{b} = \frac{2}{2K-1}\int_{r=0}^{1}(K-r)b\,dr\,. \tag{7a}$$

Normalized magnetic moment values, based on Heinz London's model, are listed in Table 9.3; moment curves are shown in Fig. 9.16. Here h_M is assumed to be equal to 4.0. The maximum normalized magnetic moment magnitude is $\frac{1}{2}$ for a thin-walled tube (or a slab of hard superconducting material), and $\frac{1}{3}$ for a solid cylinder. Even for very small values of the external field H, the magnetic moment is not reversible. For large external field values the magnetic moment does not decrease.

9.3.3 C. P. Bean's Model[17]

Normalized values are again used [Eq. (3)]. The normalized critical field strength in the interstices

[17] C. P. Bean, *Phys. Rev. Letters* 8(6), 250 (1962).

Table 9.2. Heinz London's Model: Field Distributions

I	h increasing	$0 \leqq h \leqq h_s;\ h_s = 1;\ r_I = h;\ h' = 0$
	$0 \leqq r \leqq r_I$	$b = h - r$
	$r_I \leqq r \leqq 1$	$b = 0$
II	h increasing	$h_s \leqq h \leqq h_M;\ h' = h - 1;\ h'_M = h_M - 1;\ b = h - r$
III	h decreasing	$h_m \leqq h \leqq h_M;\ h_m = h_M - 2;\ h' = h'_M$
		$r_{III} = \frac{1}{2}(h_M - h);\ b_{III} = \frac{1}{2}(h_M + h)$
	$0 \leqq r \leqq r_{III}$	$b = h + r$
	$r_{III} \leqq r \leqq 1$	$b = h_M - r$
IV	h decreasing	$0 \leqq h \leqq h_m$
V	h decreasing	$-h_s \leqq h \leqq 0$ $\quad h' = h + 1;\ b = h + r$
VI	h decreasing	$-h_M \leqq h \leqq -h_s$

Table 9.3. Heinz London's Model: Values for $-4\pi\bar{m}$

Case	Hollow Cylinder	Thin-Wall Tube	Solid Cylinder
I	$h - \frac{K}{2K-1} h^2 + \frac{1}{6K-3} h^3$	$h - \frac{h^2}{2}$	$h - h^2 + \frac{h^3}{3}$
II	$\frac{3K-2}{6K-3}$	$\frac{1}{2}$	$\frac{1}{3}$
III	$\frac{3K-2}{6K-3} - (h_M - h) + \frac{1}{6K-3}\left[\frac{3K}{2}(h_M - h)^2 - \frac{1}{4}(h_M - h)^3\right]$	$\frac{1}{2} - (h_M - h) + \frac{(h_M - h)^2}{4}$	$\frac{1}{3} - (h_M - h) + \frac{(h_M - h)^2}{2} - \frac{(h_M - h)^3}{12}$
IV, V, VI	$-\frac{3K-2}{6K-3}$	$-\frac{1}{2}$	$-\frac{1}{3}$

of the filaments is

$$h_c = \frac{H_c}{H^*} . \tag{8}$$

Field distributions for four characteristic cases are listed in Table 9.4. Cases (c), (*d*), and (*e*) are identical with cases II, III, and IV, respectively, of London's model. No values are shown for h decreasing and $h < h_c$ since in this case an interpretation of Bean's model is not obvious. In Fig. 9.17 magnetic moment curves of solid cylinders and thin-walled tubes are compared for H^* equal to H_c, $3H_c$, and $10H_c$, respectively. The curves for solid cylinders are identical with those shown in Bean's paper[17] (solid lines). The curves for the thin-walled tubes represent cases (*a*), (*b*), and (c) for $K \to \infty$ of Table 9.5 (dashed lines).

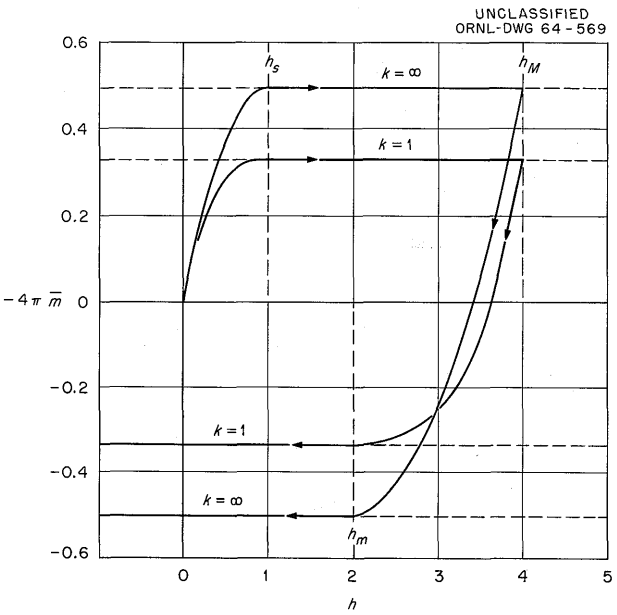

Fig. 9.16. Magnetic Moment Curves for H. London's Model.

9.3.4 Model of Y. B. Kim *et al.*

If the model of Kim *et al.*[18,19] is used, Eq. (1), combined with

$$dB = kJ\, dR , \tag{9}$$

determines the critical current and field distributions in high-field superconductor tubes which are exposed to homogeneous longitudinal external fields. We use normalized designations similar to Eq. (3); however, field values are now divided by

$$H_w = \sqrt{2\alpha k w} \tag{10}$$

[18] Y. B. Kim, C. F. Hempstead, and A. R. Strnad, *Phys. Rev. Letters* **9**(7), 306 (1962).

[19] Y. B. Kim, C. F. Hemstead, and A. R. Strnad, *Phys. Rev.* **129**(2), 528 (1963).

Table 9.4. C. P. Bean's Model: Field Distribution

Case (a)	h increasing	$0 \leqq h < h_c$; $b = h' = 0$
Case (b)	h increasing	$h_c < h < h_c + 1$; $r_b = h - h_c$
	$0 < r < r_b$	$b = h - r$
	$r_b < r < 1$	$b = 0$
Case (c)	h increasing	$h_c + 1 < h \leqq h_M$; $h_M > h_c + 2$
		$b = h - r$; $h' = h - 1$; $h'_M = h_M - 1$
Case (d)	h decreasing	$h_m \leqq h \leqq h_M$; $h_m = h_M - 2$; $h' = h'_M$
		$r_d = \frac{1}{2}(h_M - h)$; $b_d = \frac{1}{2}(h_M + h)$
	$0 \leqq r \leqq r_d$	$b = h + r$
	$r_d \leqq r \leqq 1$	$b = h_M - r$
Case (e)	h decreasing	$h_c \leqq h \leqq h_m$; $b = h + r$; $h' = h + 1$

Table 9.5. C. P. Bean's Model: Values for $-4\pi\bar{m}$

Case	Hollow Cylinder	Thin-Wall Tube	Solid Cylinder
(a)	h	h	h
(b)	$h - \frac{2}{2K-1}\left[Kh(h-h_c) - (K+h)\frac{(h-h_c)^2}{2} + \frac{(h-h_c)^3}{3}\right]$	$h - \frac{h^2 - h_c^2}{2}$	$h - (h-h_c)\left[h_c + h - h(h-h_c) + \frac{2}{3}(h-h_c)^2\right]$
(c)	Table 9.3, Case II		
(d)	Table 9.3, Case III		
(e)	Table 9.3, Case IV		

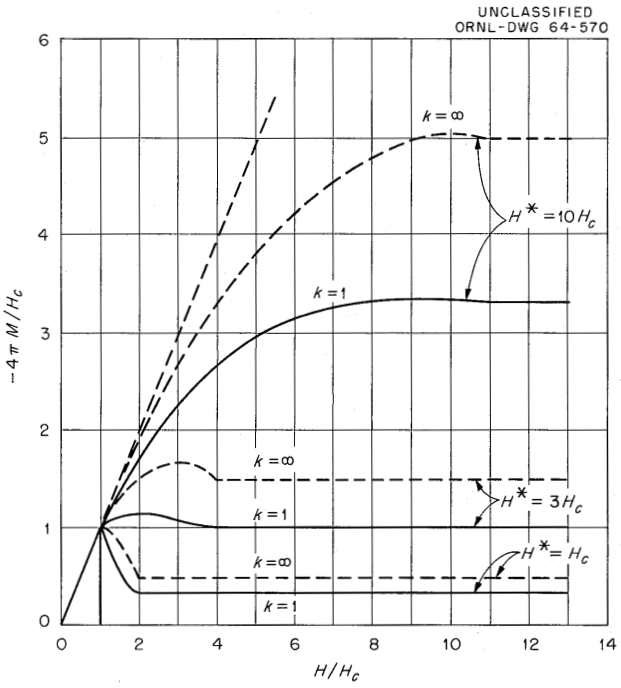

Fig. 9.17. Magnetic Moment Curves for C. P. Bean's Model.

rather than by H^*. Corresponding to the cases I to IV, shown for London's model in Figs. 9.13 and 9.14, field distributions for the model of Kim *et al.* can be easily calculated. They are listed in Table 9.6. The resulting tube magnetization curves for a complete magnetization cycle (no flux jumps considered!) are shown in Fig. 9.18 (compare ref. 18).

Using Eqs. (7) or (7*a*), the magnetic moment values for cases I to VI can be easily computed. A straightforward integration of Eq. (7*a*) with respect to b, using the $r(b)$ values (easily calculated from Table 9.6), yields the $\bar{b}$ values listed in Table 9.7. The equation for case I is very simple, since the higher limit of the integration is $h = 0$. For the other cases, the forms listed in Table 9.7 can be simplified if, instead of b, the variable

$$u = h - b \tag{11}$$

is introduced – which becomes equal to zero at the lower limit of integration. For instance, in case II, r can be written in the form

$$r = (b_0 + h)^2 - (b_0 + b)^2 = u(v - u) \,, \qquad v = 2(b_0 + h) \,. \tag{12}$$

These values introduced in Eq. (7) yield

$$-4\pi\bar{m} = \frac{u_1^2}{2K-1}\left[Kv - \frac{2}{3}(2K + v^2)u_1 + \frac{3v}{2}u_1^2 - \frac{4}{5}u_1^3\right] , \tag{13}$$

$$u_1 = u(b = h') = h - h' .$$

Equations in normalized form are convenient if the quantities B_0 and α have been determined by tube magnetization measurements and magnetic moment curves are to be calculated. For the direct evaluations of magnetic moment measurements nonnormalized equations are preferable. It is easy to rewrite Eq. (13), for instance, in a nonnormalized form. Introducing

$$U_1 = H_w u_1 = H - B \,, \qquad V = H_w v = 2(B_0 + H) \,, \tag{14}$$

we obtain from Eq. (13)

$$-4\pi\bar{M} = \frac{1}{(2K-1)H_w^2}\left[KVH_w^2 - \frac{2}{3}(2KH_w^2 + V^2)U_1 + \frac{3}{2}VU_1^2 - \frac{4}{5}U_1^3\right] . \tag{15}$$

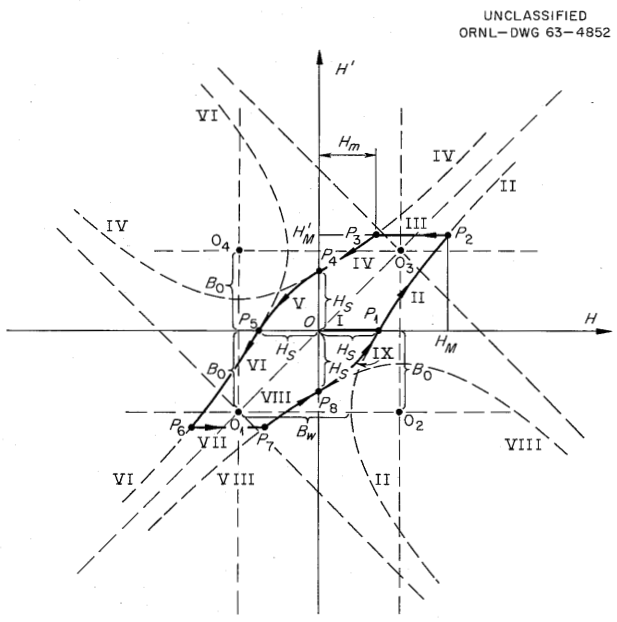

Fig. 9.18. Tube Magnetization Curves for the Model of Y. B. Kim *et al.*

Table 9.6. Model of Y. B. Kim *et al.*: Field Distribution

I	h increasing: $0 \leqq h \leqq h_s$; $h_s = \sqrt{b_0^2 + 1} - b_0$; $r_I = 2\, b_0\ \ h + h^2$; $h' = 0$
	$0 \leqq r \leqq r_I$ $b = \sqrt{(b_0 + h)^2 - r} - b_0$; $r = (b_0 + h)^2 - (b_0 + b)^2$
	$r_I \leqq r \leqq 1$ $b = 0$
II	h increasing: $h_s \leqq h \leqq h_M$; $h' = \sqrt{(b_0 + h)^2 - 1} - b_0$; $h'_M = \sqrt{(b_0 + h_M)^2 - 1} - b_0$
	$b = \sqrt{(b_0 + h)^2 - r} - b_0$; $r = (b_0 + h)^2$
III	h decreasing: $h_m \leqq h \leqq h_M$; $h_m = \sqrt{(b_0 + h_M)^2 - 2} - b_0$; $h' = h'_M$
	$r_{III} = \frac{1}{2}\,[(b_0 + h_M)^2 - (b_0 + h)^2]$; $b_{III} = \sqrt{\frac{1}{2}\,[(b_0 + h_M)^2 + (b_0 + h)^2]} - b_0$
	$0 \leqq r \leqq r_{III}$ $b = \sqrt{(b_0 + h)^2 + r} - b_0$; $r = (b_0 + b)^2 - (b_0 + h)^2$
	$r_{III} \leqq r \leqq 1$ $b = \sqrt{(b_0 + h_M)^2 - r} - b_0$; $r = (b_0 + h_M)^2 - (b_0 + b)^2$
IV	h decreasing: $0 \leqq h \leqq h_M$; $h' = \sqrt{(b_0 + h)^2 + 1} - b_0$
	$b = \sqrt{(b_0 + h)^2 + r} - b_0$; $r = (b_0 + b)^2 - (b_0 + h)^2$
V	h decreasing: $-h_s \leqq h \leqq 0$; $h' = \sqrt{1 + 2\, b_0^2 - (b_0 - h)^2} - b_0$
	$r_V = (b_0 - h)^2 - b_0^2$; $b_V = 0$
	$0 \leqq r \leqq r_V$ $b = b_0 - \sqrt{(b_0 - h)^2 - r}$; $r = (b_0 - h)^2 - (b_0 - b)^2$
	$r_V \leqq r \leqq 1$ $b = \sqrt{(b_0 + h')^2 + r - 1} - b_0$; $r - (b_0 + b)^2 - (b_0 - h)^2 - 2\, b_0^2$
VI	h decreasing: $h_s \leqq -h_s$; $h' = b_0 - \sqrt{(b_0 - h)^2 - 1}$
	$b = b_0 - \sqrt{(b_0 - h)^2 - r}$

Equation (12) can be written as

$$H_w^2 = U_1(V - U_1)\,, \tag{16}$$

and therefore

$$-4\pi\overline{M} = \frac{1}{(2K - 1)(V - U_1)}\left[\left(K - \frac{2}{3}\right)V^2 - \left(\frac{7}{3}K - \frac{3}{2}\right)U_1 V + \left(\frac{4}{3}K - \frac{4}{5}\right)U_1^2\right]. \tag{17}$$

Using the abbreviation

$$\nu = \frac{H' - H}{B_0 + H}\,, \tag{18}$$

we obtain

$$-4\pi\overline{M} = \frac{2}{3}\,\frac{H - H'}{(2K - 1)(2 + \nu)^2}\left[2\left(K - \frac{3}{5}\right)\nu^2 + \left(7K - \frac{9}{2}\right)\nu + 2(3K - 2)\right], \tag{19}$$

and an expression for the magnetic moment in case II for arbitrary values of K. For $K = 1$, Eq. (14) of the paper of Kim *et al.*[19] follows:

$$-4\pi\overline{M} = \frac{H - H'}{15(2 + \nu)^2}\,(8\nu^2 + 25\nu + 20)\,. \tag{20}$$

Table 9.7. Model of Y. B. Kim *et al.*: Values of $(2K - 1)\bar{b}$

$(-4\pi\bar{m} = h - \bar{b})$

I	$h^2[2b_0K + \frac{4}{3}(K - b_0)^2 h - \frac{5}{3} b_0 h^2 - \frac{8}{15} h^3]$
II	$[2b_0(K - 2b_0h - h^2)b^2 + \frac{4}{3}(K + 2b_0^2 - 2b_0h - h^2)b^3 + 3b_0b^4 + \frac{4}{5} b^5]_{b=h'}^{h}$
III	$[2b_0(K + 2b_0h + h^2)b^2 + \frac{4}{3}(K - 2b_0^2 + 2b_0h + h^2)b^3 - 3b_0b^4 - \frac{4}{5} b^5]_{b=h}^{b_m} +$
	$[2b_0(K - 2b_0h_M - h_M^2)b^2 + \frac{4}{3}(K + 2b_0^2 - 2b_0h_M - h_M^2)b^3 + 3b_0b^4 + \frac{4}{5} b^5]_{b=h_M'}^{b_m}$
IV	$[2b_0(K + 2b_0h + h^2)b^2 + \frac{4}{3}(K - 2b_0^2 + 2b_0h + h^2)b^3 - 3b_0b^4 - \frac{4}{5} b^5]_{b=h}^{h'}$
V	$[2b_0(K + 2b_0h - h^2)b^2 - \frac{4}{3}(K + 2b_0^2 + 2b_0h - h^2)b^3 + 3b_0b^4 - \frac{4}{5} b^5]_{b=h}^{0} +$
	$[2b_0(K + 2b_0h' + h'^2 - 1)b^2 + \frac{4}{3}(K - 2b_0^2 + 2b_0 h' + h'^2 - 1)b^3 -$
	$3b_0b^4 - \frac{4}{5} b^5]_{b=0}^{h'}$
VI	$[2b_0(K + 2b_0h - h^2)b^2 - \frac{4}{3}(K + 2b_0^2 + 2b_0h - h^2)b^3 + 3b_0b^4 - \frac{4}{5} b^5]_{b=h}^{h'}$

For a thin-walled tube (or a slab of high-field superconducting material), $K \to \infty$, and Eq. (19) becomes

$$-4\pi\bar{M} = \frac{1}{3}\frac{H - H'}{(2+\nu)^2}(2\nu^2 + 7\nu + 6)\,. \qquad (21)$$

Magnetic moment curves for a complete magnetization cycle (cases I to VI), calculated for $b_0 = 0.7$ and $K = \infty$, 2, and 1, respectively, are shown in Fig. 9.19. Nonnormalized forms for $\bar{M}$, for cases I to V, valid for any ratios of outside to inside tube radii are listed in Table 9.8 of the following paper, which reports on magnetic moment measurements of bundles of copper-plated Nb-Zr wires and discusses the application of the model of Kim *et al.* to the results.

9.3.5 Measurement Methods

Tube magnetization measurements[18] can be made by measuring simultaneously the fields H and H' outside and inside, respectively, of a tube. It must, however, be considered that end effects can influence considerably the measurements. Figure 9.20 shows flux trapping measurements on soft superconducting cylinders.[20] Infinite length of the tube was simulated by means of niobium guard rings, and a tube magnetization curve OAB of almost rectangular shape was obtained. The two other curves, $OA'B'$ and $OA''B''$, represent measurements without guard rings for tube lengths of 5 in. and 1.67 in., respectively. The inside tube diameter was 0.665 in. and the outside diameter 0.750 in. The tube magnetization curves without guard rings are appreciably distorted. The end effects of hard superconducting tubes might be smaller. It is, however, important to consider carefully the possible influence of finite tube lengths, even in this case.[19]

Ballistic magnetic moment measurements in longitudinal fields can be made in different ways.[21] A sample of appropriate shape (demagnetization factor sufficiently small) surrounded

[20] D. L. Coffey, W. F. Gauster, and H. E. Rorschach, Jr., *Appl. Phys. Letters* 3(5), 75 (1963).

[21] D. Shoenberg, *Superconductivity*, p. 53, Cambridge University Press, 1960.

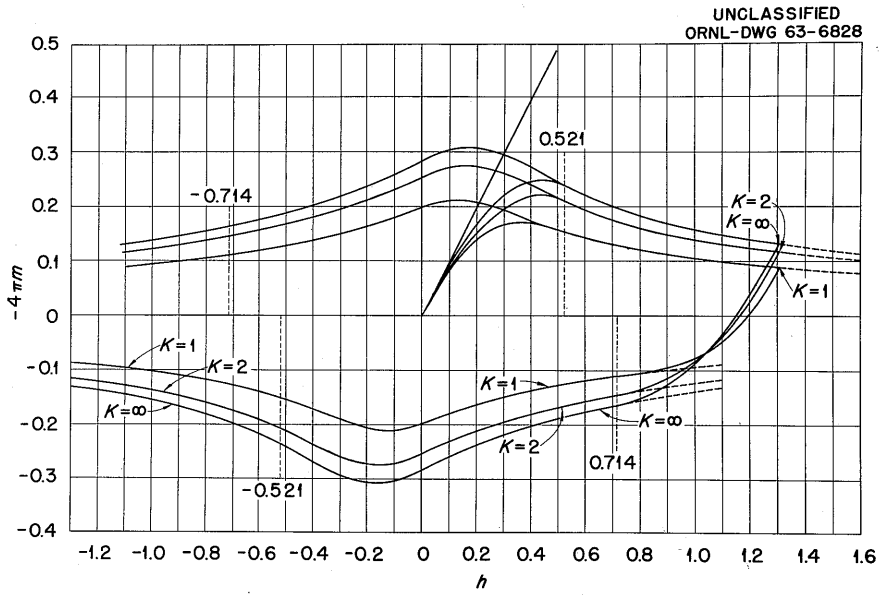

Fig. 9.19. Magnetic Moment Curve for $b_0 = B_0/H^* = 0.7$ (Model of Y. B. Kim *et al.*).

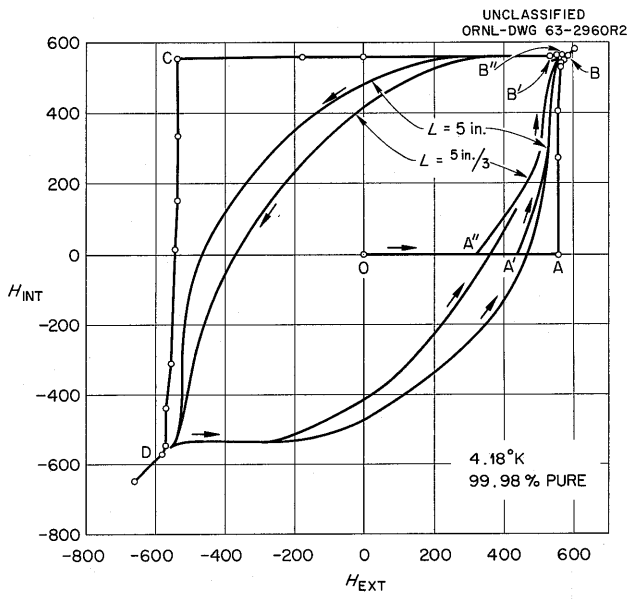

Fig. 9.20. Influence of Finite Length on the Tube Magnetization Curves of a Soft Superconductor.

by a stationary pickup coil is pulled into another coil which is wound in opposite sense. Both coils must be located in the homogeneous zone of the external longitudinal field, and the distance between the coils must be so large that the sample in the initial position does not distort the field in the second coil. Between measurements with different external fields, sufficient time must be allowed so that the sample can reach stationary states. Another method is to keep the sample fixed and to move a pair of symmetrically arranged coils into a field zone where the distortion by the sample can be neglected. This field zone does not have to be homogeneous; only equal fluxes must link both coils in the end positions.

In order to coordinate tube magnetization and magnetic moment measurements with hard superconductor samples, it is very desirable to use the same specimen for both experiments. We suggest the following procedure (Fig. 9.21): Inside a large solenoid which produces the external field, two counterbalanced pickup coils, C_1 and C_2, are arranged in a homogeneous field zone. The superconducting specimen in the form of a tube, with a large ratio of length to diameter, is inside coil C_1. The field is raised to a value H and sufficient time allows the sample to reach equilibrium. The average magnetic moment per unit volume $\overline{M}$ is determined by Eq. (6).

The flux through coil C_1 is

$$\phi_1 = \phi_e + \int_{R=0}^{W} 2\pi(a - R)B\, dR + \pi b^2 H', \quad (22)$$

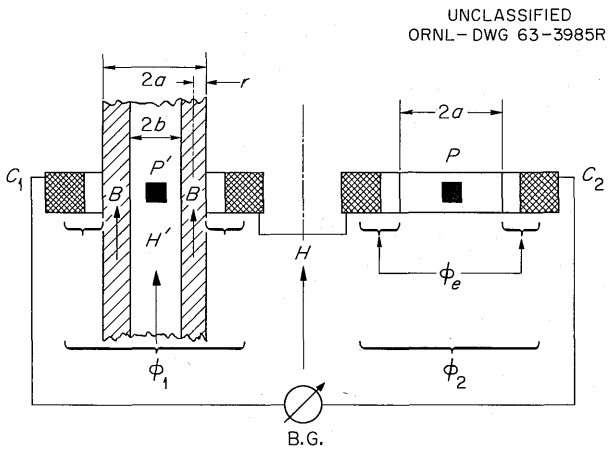

Fig. 9.21. Simultaneous Measurements of Magnetic Moment and Tube Magnetization.

where ϕ_e stands for the flux linked by the coil outside the tube. The flux through coil C_2 is

$$\phi_2 = \phi_e + \pi a^2 H .$$

Therefore,

$$-4\pi\overline{M} = \frac{\phi_2 - \phi_1}{\pi(a^2 - b^2)} - \frac{b^2}{a^2 - b^2}(H - H') . \quad (23)$$

If the coils, C_1 and C_2, are moved simultaneously from the position shown to a field region which is sufficiently distant so that the sample does not influence the field (but not necessarily the same homogeneous zone with field strength H) then the deflection of the ballistic galvanometer is proportional to the term

$$\frac{\phi_2 - \phi_1}{\pi(a^2 - b^2)} .$$

As mentioned previously, it must be only supposed that C_1 and C_2 have been moved into symmetrical field positions – not necessarily a homogeneous field zone. Since H and H' are measured (by conventional probes, for instance, magnetoresistance probes) for finding the tube magnetization curve, the measurements can be used to determine the second term in Eq. (23). In this way a coordination of tube magnetization and magnetic moment measurements can be achieved.

9.3.6 Acknowledgments

The author wishes to acknowledge the most useful discussions with D. C. Hopkins, the invaluable assistance of C. E. Parker, who made the numerical calculations for Fig. 9.20, and the contribution of D. L. Coffey by performing the flux trapping experiments with lead cylinders shown in Fig. 9.21.

9.4 MAGNETIC MOMENT MEASUREMENTS ON NbZr WIRES

D. C. Hopkins[22] W. F. Gauster

9.4.1 Introduction

Several authors published the results of magnetic moment measurements performed with cylindrical samples of high-field superconductors exposed to longitudinal fields. For instance, R. M. Bozorth *et al.*[23] used an Nb_3Sn sample exposed to a longitudinal field raised to a maximum of 85 kilogauss. No field penetration occurred at fields up to 4 to 5 kilogauss. At intermediate fields (5 to 20 kilogauss), irregularities were observed which were considered to be due to changes in domain structure in the mixed state. With decreasing field, flux was frozen in; irregularities were again observed.

F. J. Morin *et al.*[24] published a magnetic moment curve, obtained with a V_3Ga sample in fields up to 87 kilogauss. Again perfect flux exclusion occurred at low fields; irregularities were observed at increasing fields of around 20 kilogauss; the magnetic moment values for decreasing fields, however, were quite regular. Y. B. Kim *et al.*[25] showed that the experimental data of the latter branch of that magnetic moment curve are in good agreement with numerical calculations based on their model. C. P. Bean[26] published magnetic

[22]Summer employee, University of Illinois.

[23]R. M. Bozorth, A. J. Williams, and D. D. Davis, *Phys. Rev. Letters* 5(4), 148 (1960).

[24]F. J. Morin *et al.*, *Phys. Rev. Letters* 8(7), 275 (1962).

[25]Y. B. Kim, C. F. Hempstead, and A. R. Strnad, *Phys. Rev.* 129(2), 528 (1963).

[26]C. P. Bean, *Phys. Rev. Letters* 8(6), 250 (1962).

moment measurements in the range of 0 to 7 kilogauss with two Nb_3Sn samples of different size, which agree well with the calculated data if his model is employed. Finally, a comparison of magnetic moment curves obtained with a V_3Ga sample[27] with numerical values calculated after Heinz London's model should be mentioned as another example of ballistic magnetic moment measurements of high-field superconductors.

Recently Kim *et al.*[28] made voltage drop measurements across a current-carrying Nb–25% Zr wire in a perpendicular field. Applying the theory of flux creep this kind of experiment allows one, in a quite different way, to determine the parameter B_0. A value for α_c can be estimated from their Fig. 8 by letting V approach zero, as it would for the critical state. These values will be compared with our results. Furthermore, we will check the adequacy of their equations for the critical state for describing the shape of our magnetization curves.

9.4.2 Experimental

Experiments described here yielded well-reproducible magnetic moment curves with high-field superconductors when raising the external field from zero to various different maximum values and then lowering the field to zero. It was possible to avoid flux jumps which are the reason for erratic measurement values. The measurement results were compared with calculated values based on the model of Kim *et al.* The experimental arrangement was as follows.

A cross section of the experimental chamber is shown in Fig. 9.22. The chamber was placed in liquid helium at 4.2°K in a vertical magnetic field which at times was raised as high as 60 kilogauss. The pickup coils were connected in series opposition across a ballistic galvanometer (Leeds and Northrup model 2285-D), which was especially rewound for this experiment.

The sample S in this experiment consisted of 25 strands of 10-mil copper-clad Nb–25% Zr wire $1\frac{5}{8}$ in. long. They could be conveniently packed into one of the two $\frac{1}{8}$-in. thin-walled stainless steel tubes ST_1 and ST_2 which acted also as guides for the sensing coils C_1 and C_2.

Measurements were made by jerking the coils upward by a fixed distance (approximately 3 in.) at a reproducible rate by means of a compressed gas cylinder while the sample in its stainless steel tube remained stationary. The resulting deflection – corrected by the small deflection at the same field with the sample in the normal state – is proportional to the average magnetization of the sample.

The corrected deflections were multiplied by a constant factor to reduce the data to absolute

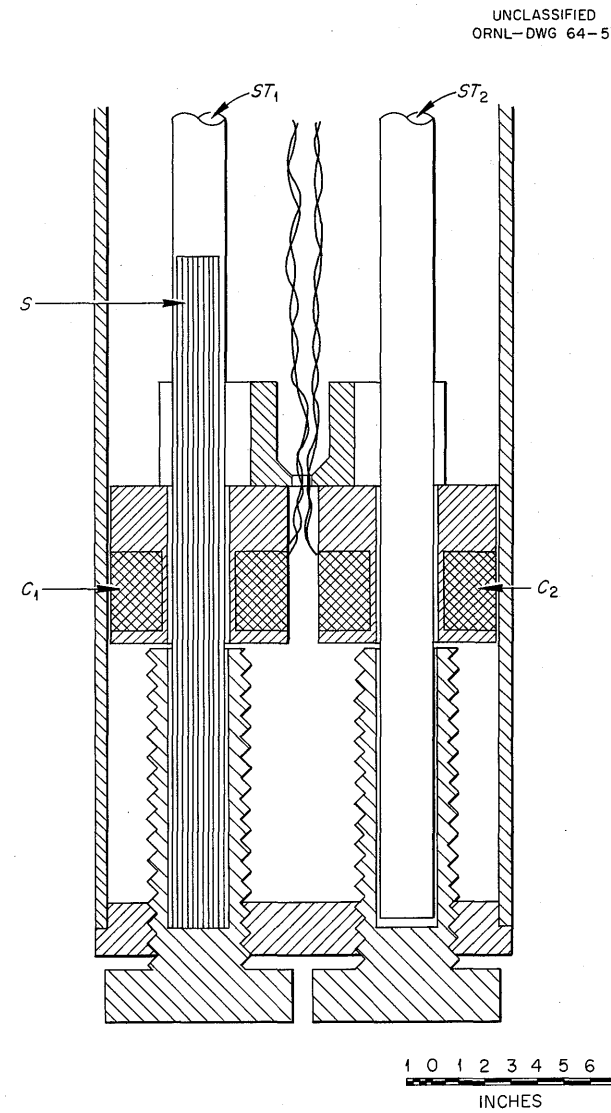

Fig. 9.22. Experimental Chamber for Magnetic Moment Measurements.

[27] C. P. Bean and R. W. Schmidt, *Science* **140**, 26 (1963).

[28] Y. B. Kim, C. F. Hempstead, and A. R. Strnad, *Phys. Rev.* **131**, 2486 (1963).

magnetization units (kilogauss). This factor was determined by assuming a perfect flux exclusion in the sample up to around 1 kilogauss.

The final results are plotted in Fig. 9.23. The open circles represent a cycle from zero applied field and nearly zero magnetization up to 58 kilogauss and then back to zero field again. The open triangles indicate the last half of a similar cycle which goes up to a maximum field of only 10.16 kilogauss. The solid triangles represent the results of increasing the field from the previous end state. The dotted circles show the last half of a cycle starting at zero field but going up only to 20.32 kilogauss.

9.4.3 Results

The measured values represented by the points *a* and *b* in Fig. 9.23 were used to determine the the parameter B_0 and α_c of the model of Kim *et al.* For this purpose a previously calculated set of forms was employed (Table 9.8) which expresses $-4\pi\overline{M}$ in the cases I to V as functions of H (the definition of the cases I to V is given in the preceding paper). In Table 9.8, *a* and *b* are the outer and inner radii, respectively, of a high-field superconductor tube. In the case of a solid cylinder, as considered here, $b = 0$, which simplifies somewhat the general forms. B_1 is defined by

$$B_1 = \frac{8\pi}{10}\alpha a$$

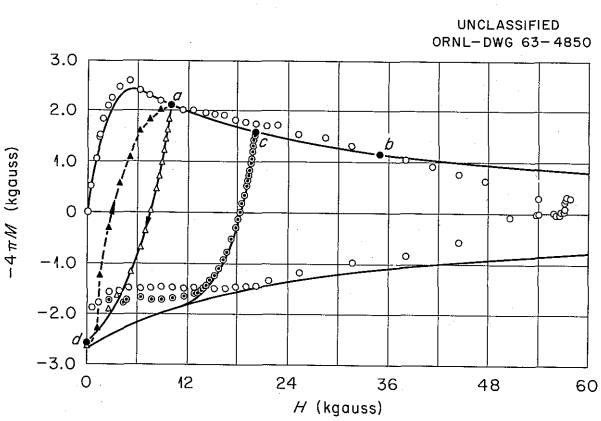

Fig. 9.23. Experimental and Computed Data of Magnetic Moment Measurements.

and H_{II} stands for the maximum field value of the magnetization cycle. Points *a* and *b* belong to the region designated by case II.

After finding B_0 and α_c, H values were calculated for the three magnetization cycles described in Sect. 9.4.2. In Fig. 9.23 they are represented by solid lines.

9.4.4 Discussion

As expected, the fit is not very good at high fields. The behavior upon decreasing the field from either point *a* or *c*, however, is particularly well predicted. The fact that the open circles or circles with dots do not follow the theoretical curve for low applied fields may be due to a greater tendency for the material to go through reversible magnetization states at low fields than at high fields. However, this does not explain the excellent fit of the open triangles even to zero field. This is an experimentally significant effect because the end points of this section of the data (*a* and *d*) could be reproduced with no difficulty. However, when cycling to higher fields it was impossible to reach point *d* no matter how slowly the field was decreased. An explanation for this anomalous behavior has not yet been found.

It is of interest to compare our values of B_0 and α_c with those of Kim, Hempstead, and Strnad:

	Hopkins and Gauster	Kim *et al.*
B_0, kilogauss	22.8	0.5
α_c, kilogauss-amp/cm^2	12.4×10^6	14×10^4

For both parameters our values are roughly two orders of magnitude higher than those of Kim *et al.*

P. W. Anderson[29] explains the meaning of the constant B_0 by the fact that even when the field is near zero, J will have a critical value. The dimensions of one bundle will be determined by the distance, d, between flux pinning sites. If

[29] P. W. Anderson, *Phys. Rev. Letters* **9**, 309 (1962).

Table 9.8. $-4\pi\overline{M}$ Values Based on the Model of Kim *et al.*

I. $$H - \frac{a^2}{(a^2-b^2)B_1^4}\left[2B_0B_1^2H^2 + \frac{4}{3}(B_1^2 - B_0^2)H^3 - \frac{5}{3}B_0H^4 - \frac{8}{15}H^5\right]$$

II. $$(H+B_0) - \frac{a^2}{(a^2-b^2)B_1^4}\left\{\frac{4}{3}B_1^2(B_0+H)^3 - \frac{8}{15}(B_0+H)^5 - \frac{4}{3}B_1^2\left(\frac{b}{a}\right)\left[(B_0+H)^2 - \left(1-\frac{b}{a}\right)B_1^2\right]^{3/2} + \frac{8}{15}\left[(B_0+H)^2 - \left(1-\frac{b}{a}\right)B_1^2\right]^{5/2}\right\}$$

III. $$H - \frac{a^2}{(a^2-b^2)B_1^4}\left\{\frac{4}{3}[2B_1^2 - (B_0+H_{II})^2 + (B_0+H)^2]\left[\frac{(B_0+H)^2+(B_0+H_{II})^2}{2}\right]^{3/2} - \frac{4}{3}B_1^2(B_0+H)^3 - \frac{8}{15}(B_0+H)^5 - \left(1-\frac{b^2}{a^2}\right)B_0B_1^4 - \frac{4}{3}\left(\frac{b}{a}\right)B_1^2\left[(B_0+H_{II})^2 - B_1^2\left(1-\frac{b}{a}\right)\right]^{3/2} + \frac{8}{15}\left[(B_0+H_{II})^2 - B_1^2\left(1-\frac{b}{a}\right)\right]^{5/2}\right\}$$

IV. $$(H+B_0) - \frac{a^2}{(a^2-b^2)B_1^4}\left\{-\frac{4}{3}B_1^2(B_0+H)^3 - \frac{8}{15}(B_0+H)^5 + \frac{4}{3}B_1^2\left(\frac{b}{a}\right)\left[(B_0+H)^2 + \left(1-\frac{b}{a}\right)B_1^2\right]^{3/2} + \frac{8}{15}\left[(B_0+H)^2 + \left(1-\frac{b}{a}\right)B_1^2\right]^{5/2}\right\}$$

V. $$H - \frac{a^2}{(a^2-b^2)B_1^4}\left\{-B_0B_1^4\left(1-\frac{b^2}{a^2}\right) - \frac{4B_0^3B_1^2}{3} - \frac{8}{15}B_0^5 - 4B_0^2\left(B_1^2 + \frac{2}{3}B_0^2\right)H - \frac{8}{3}B_0^3H^2 + \frac{4}{3}(B_1^2+2B_0^2)H^3 + \frac{2}{3}B_0H^4 + \frac{8}{15}H^5 + \frac{4}{3}B_1^2\left(\frac{b}{a}\right)\left[B_0^2 + 2B_0H - H^2 + \left(1-\frac{b}{a}\right)B_1^2\right]^{3/2} + \frac{8}{15}\left[B_0^2 + 2B_0H - H^2 + \left(1-\frac{b}{a}\right)B_1^2\right]^{5/2}\right\}$$

we consider that a flux bundle must not contain less than one flux quantum, B_0 is predicted to be:

$$B_0 \approx \frac{h_c}{2\,ed^2}.$$

In this interpretation, B_0 depends sensitively on d. Our difference from the results of Kim *et al.* could be explained as a difference in d by a factor of about 7.

The difference in α_c could indicate that in our case the free energy barrier resisted more effectively the motion of flux bundles. This is, however, not very possible, since we were supposedly using the same type of material as Kim *et al.* These discrepancies can probably be better explained by the differences in the measuring techniques. Our data are taken with 25 samples and represent an average value over 1 cm length of each sample, whereas the results of Kim *et al.* may be due to the behavior of a "weakest spot" in their long (250 cm) sample. They estimate that this weak spot may be as short as 10^{-3} cm. Thus, it is reasonable that the local values of B_0 and α_c may be appreciably smaller than the average. This explanation would show the great practical importance of producing homogeneous high-field superconductor wires.

The performance of these experiments was effectively supported by R. L. Brown, D. L. Coffey, D. O. Patterson,[30] and W. H. Wagner.

9.5 SCHEMES FOR WINDING COILS FROM TUBULAR CONDUCTORS

J. N. Luton, Jr.

Most of the water-cooled magnet coils of the Thermonuclear Division have been wound of hol-

[30]Summer employee, University of Tennessee.

low tubular conductors.[31] The coolant temperature rise of such a coil is approximately proportional to $l_{wp}^{3/2}$, where l_{wp} is the length of an individual water path; thus, if a coil consumes power in the megawatt range and has a conductor hundreds of feet long, then it must have many parallel water paths.

One scheme for increasing the number of water paths is the parallel-wound, double-layer "pancake" previously described.[32] Several such disks are stacked together to form a rectangular coil. The end connections of all water paths are at the outer cylindrical surface of the coil, leaving the bore and both ends unobstructed. The inner radius of each pancake may be varied at will; thus coils with winding cross sections such as shown in Fig. 9.24 may be built up. In such an arrangement the winding depth for pancakes with an integral number of turns may be varied in steps of $H/2$, where H is the height of an insulated conductor. However, the axial length of each coil section must be an integral multiple of $2W$, where W is the width of the conductor. The schemes described below make it possible to relax these restrictions on coil shape and, for a given conductor, to reduce the size of the minimum increments by which the coil dimensions may be changed.

Figure 9.25, at first glance, looks like the customary two-layer spiral pancake, but it actually contains three layers. Current enters at point 1, spirals down to C_1, where it crosses over to the middle layer, and then spirals out to 1′. The water exits at 1′, but 1′ is electrically connected to 2, and the current sequentially continues through all six water paths, finally emerging at 6′, which could either be connected to the next pancake or serve as a coil terminal. Crossovers C_2, C_4, and C_6 join the middle and bottom layers and are visible from the other side of the model. The crossovers, as well as the conductor ends, are symmetrically spaced. The use of both two- and three-layer pancakes makes it possible to change the coil length, or dimension L of Fig. 9.24, in steps of W instead of $2W$.

Figure 9.26 is the helical pancake, or shell, corresponding to the spiral pancake of Fig. 9.25. Current flows in at 1, down the outer layer to crossover C_1, back the middle layer to 1′, down the inner layer from 2 to C_2, back the middle layer to 2′, up to 3, etc. It may, of course, also be wound as a two-layer shell. In addition, shells of various lengths may be nested to form coils with cross sections as in Fig. 9.27. Coils composed of shells have all electrical and hydraulic terminals at one end, leaving unobstructed surfaces at both the ID and OD of the coil, and therefore complement the spiral-pancake coils.

So far, although dimensions L and D of Figs. 9.24 and 9.27 may be varied in steps of W and H, respectively, they must be at least as large as $2W$ and $2H$, since a single-layer pancake can have no provision for returning the exit end of the tube to the surface containing the entrance ends. In some cases (*e.g.*, in shaping a coil to fit a flux line), it is desirable to make the steps as small as possible. This can be done if it is realized that in a shell or a pancake of three layers, the two classes of crossovers can be independently located. For example, in Fig. 9.26 the inner and middle layers could be extended to the left, moving crossovers C_2, C_4, and C_6 axially an arbitrary amount. Water paths 1, 3, and 5 would be unchanged; 2, 4, and 6 would be lengthened and have a helix which abruptly halved its pitch at the location of the step. The flow paths are shown schematically in Fig. 9.28.

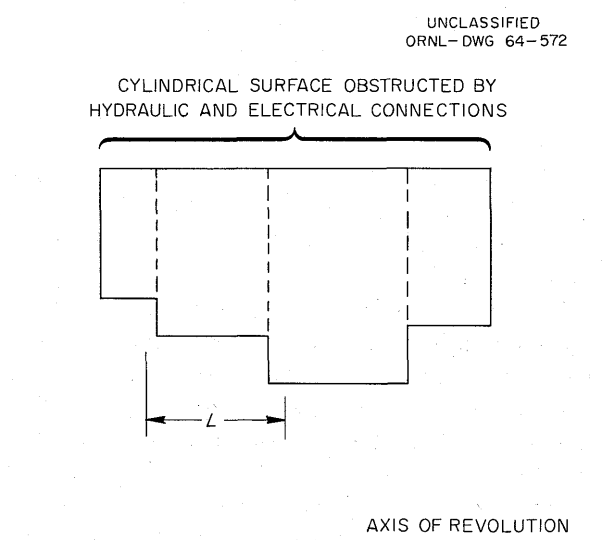

Fig. 9.24. Coil Composed of Stacked Pancakes.

[31] One advantage of this type of coil is that it has no regions where the conductor, insulator, and coolant are in mutual contact.

[32] *Thermonuclear Project Semiann. Progr. Rept. July 31, 1960*, ORNL-3011, pp. 22–23.

If several adjacent one-conductor steps are desired, the shell may be extended to any number of layers, as illustrated in Fig. 9.29. The major restriction is that the section which extends the farthest must be at least two conductors deep. The scheme can equally well be applied to the spiral pancake case, giving axial steps of W in the coil outline.

It thus appears that a coil, with or without steps, may be designed so that its dimensions are all within $\pm W/2$ or $H/2$ of the ideal values, without reducing the reliability and cooling capacity of the coil, and without having conductor ends on more than one coil surface.

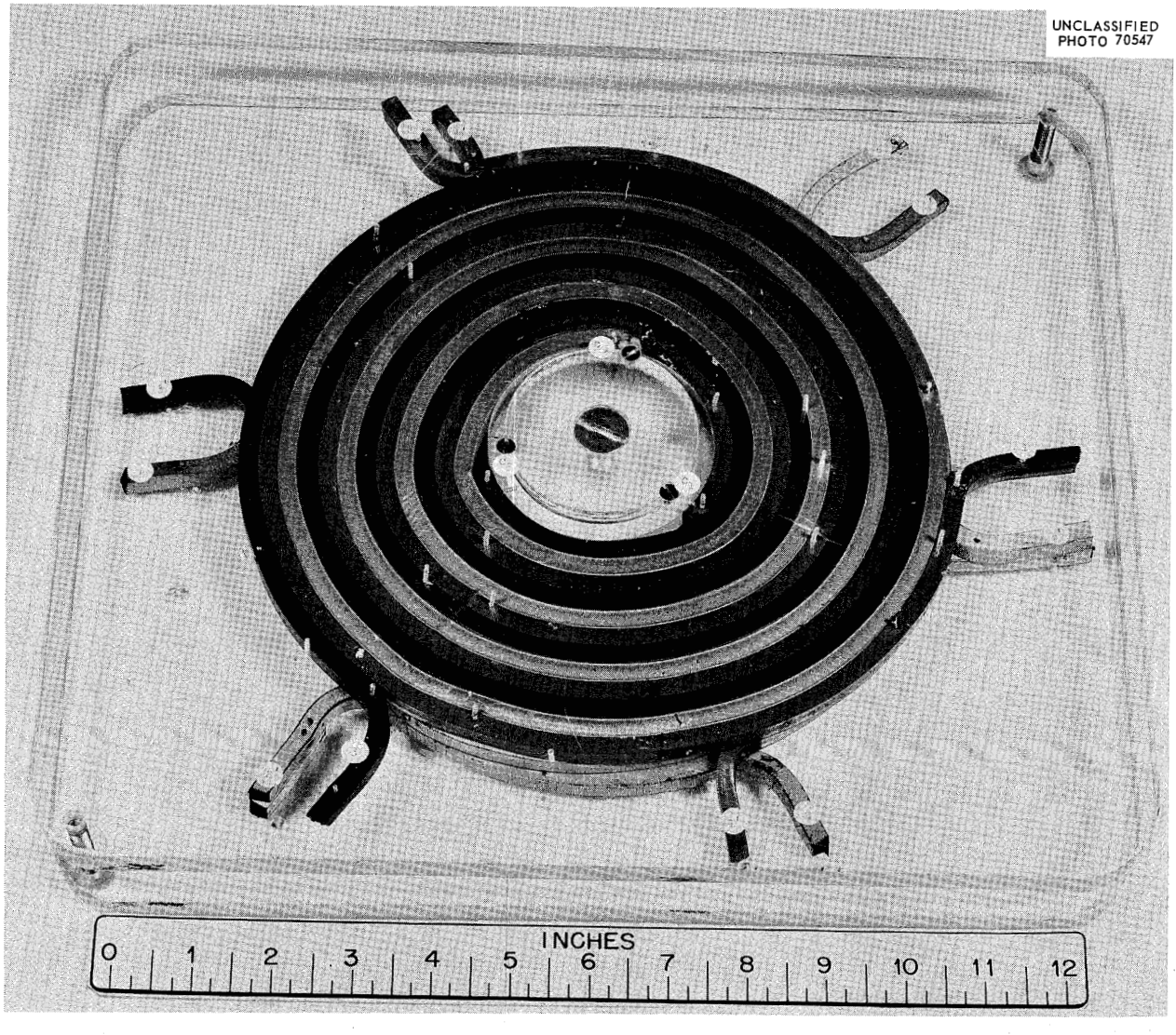

Fig. 9.25. Model of a Three-Layer "Pancake."

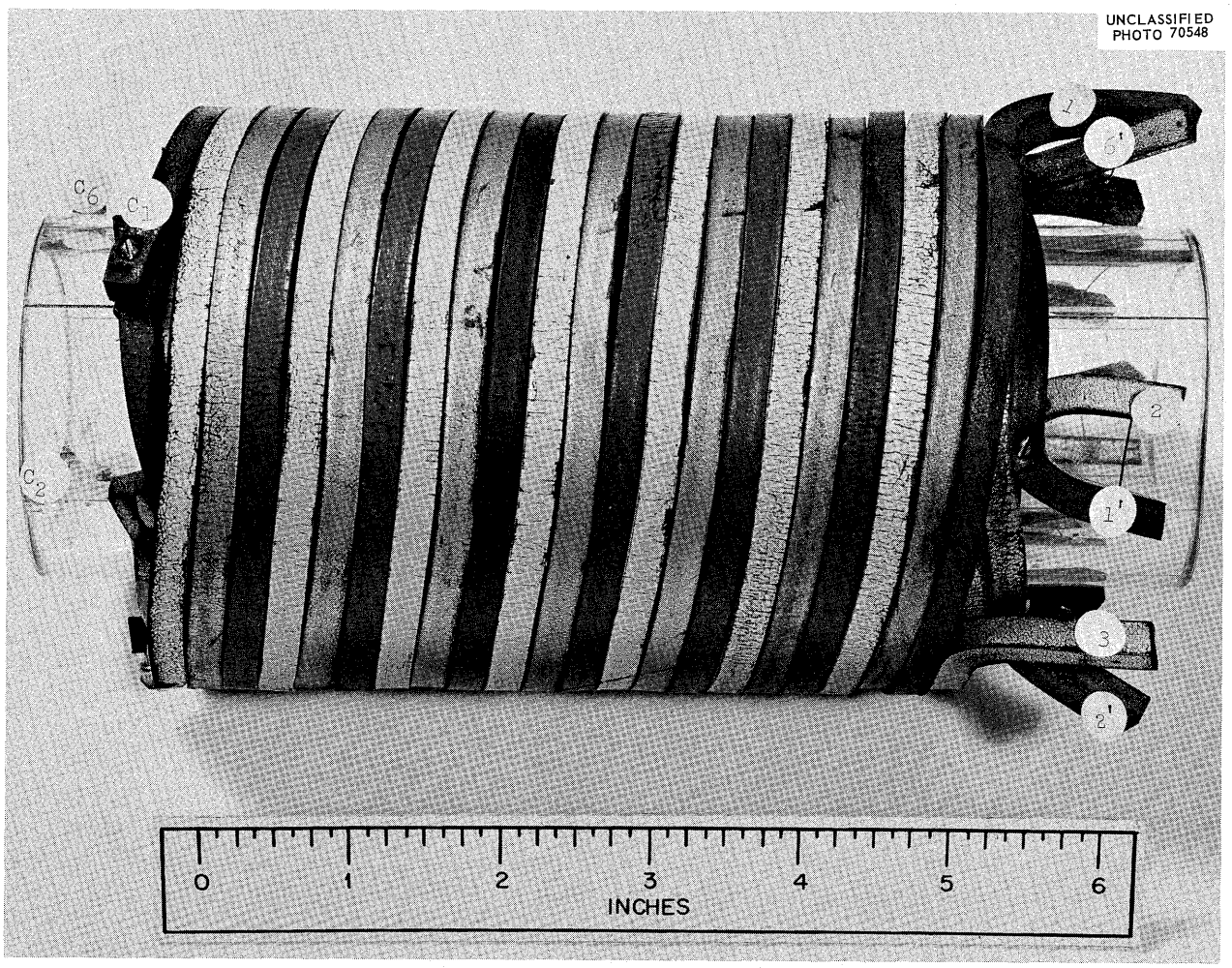

Fig. 9.26. Model of a Three-Layer "Shell."

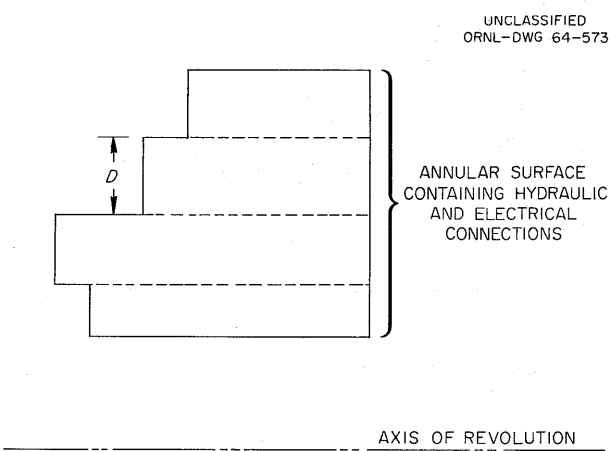

Fig. 9.27. Coil Composed of Nested Shells.

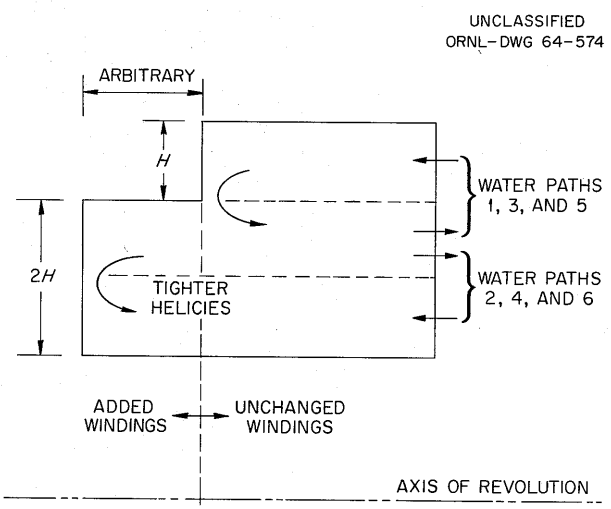

Fig. 9.28. Three-Layer Shell with Step.

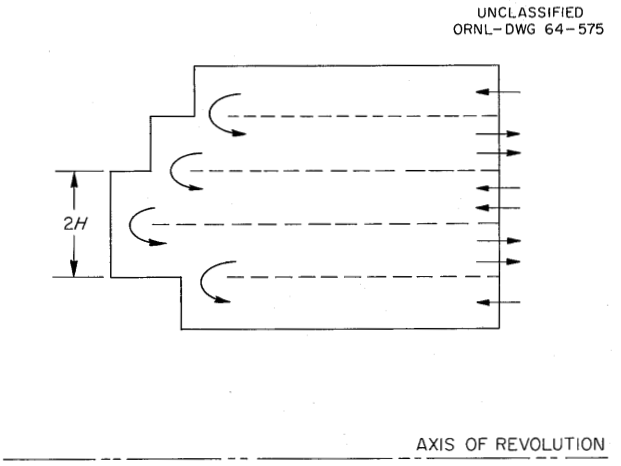

Fig. 9.29. Helical Coil with Adjacent One-Conductor Steps.

10. Vacuum Systems, Techniques, and Material Studies

J. D. Redman[1] D. M. Richardson[1] R. A. Strehlow[1]

10.1 IONIZATION-GAGE CHARACTERISTICS AT VACUUM-SYSTEM BASE PRESSURES

The usual form of the Bayard-Alpert ionization gage has a gage constant (ion current, amperes per emission current, amperes per torr) which is reasonably constant over a wide range of emission currents. Anomalies in gage performance in using vacuum systems have been observed when the gage is being used to monitor base or lowest pressures in a given system, particularly when comparisons with a nude gage in an oil-pumped system are available. A study of gage constant vs emission has been conducted with a modified Veeco RG31A control, or a General Electric 22GC100.

One example of the type of variation in apparent gage constant is shown in Table 10.1. An RG75K tube on an unbaffled oil-pumped system had gage constants which varied as shown in column 2. Adding liquid N_2 to a bottle-type trap gave the results in column 3. The same control circuit (GE) and the same tube were used. As the nitrogen level decreased, the values of K at high emissions decreased toward those of column 2, the untrapped case. Of course, in the trapped case the gage "gassiness" would have been greatly decreased by thorough baking.

It seems that electronic pumping occurs in both cases. The magnitude of this has been found to be 3.5 times the collected ion current at 10 and at 1 ma in a modified B-A gage using a screen instead of a glass envelope. If one makes the assumption that molecules of water when ionized and driven to the wall are neutralized and reemitted rapidly and that oil molecules are deposited without a large probability of being rapidly neutralized and reemitted, the data of Table 10.1 become quite comprehensible. The lack of constancy of the gage constant (sometimes called gage sensitivity) with changes in emission at the base pressure is a measure of gage pumping or gage outgassing. A precise determination of ion collector current as a function of emission will aid in specifying which is the case. Based on this work in which the diffusion pump oil was dioctyl phthalate, an emission current not higher than 0.10 ma is recommended for maximum accuracy at the base pressure unless a determination

Table 10.1. Gage Sensitivity at Various Emission Currents

Log Emission Current (amp)	Gage Factor K (torr^{-1})[a]	
	Untrapped	Trapped
−7	10	10
−6	10.0	10.0
−5	10.0	10.0
−4	10.0	10.0
−3.7	10.0	10.0
−3.3	9.6	
−3.18		14.5
−3	8.0	15.7
−2.4	7.0	26.0
−2	5.5	46.0

[a]Pressure normalized to low emissions in both cases where $I_e \propto I_c$.

[1]Reactor Chemistry Division.

of K vs I_e indicates a satisfactory system and gage cleanliness. Linearity of K with I_e is a sufficient criterion for accuracy only in the gage ionizing region.

These data are consistent with observations by Redhead[2] and Ackley *et al.*[3] on the so-called anomalous residual currents after exposure of a gage to higher pressures of oxygen, etc. Generally this type of study is done on nude-gage geometries in which the pumping-gage constant usually behaves as in Table 10.1, column 2. Higher pressure readings with the nude gage after an exposure to O_2, N_2, etc., represent a higher local pressure in the gage. It has been observed in earlier studies on nude gages in this laboratory that the pressure decay (grid outgassing) can be accelerated by the usual degassing techniques or by running the gage at high emissions (10–20 ma) for 5 min or more.

[2]P. A. Redhead, *Vacuum* 12, 267 (1962).

[3]J. W. Ackley, C. F. Lothrop, and W. R. Wheeler, *Vacuum Symposium Transactions*, ed. by G. H. Bancroft, Macmillan, New York, 1962.

10.2 MASS SPECTROMETRIC STUDIES

A study has been started of fragmentation of organic hydrocarbons which has as its goal the determination of optimum electron energies for characterizing these species in an ultrahigh-vacuum system. Table 10.2 lists the peaks ascribable to the hydrocarbon heptane (C_7H_{14}) at two electron energies as set by the potential of the gating electrode in the source of the Bendix time-of-flight spectrometer.

Table 10.2. Heptane Mass Spectrum

Formula	Mass	Approximate Peak Heights Relative to Mass 100		
		Electron Energy (v)[a]		API Standard Table
		30	70	
CH_2^+	14	0	1.30	
$C_2H_2^+$	26	0	0.04	
$C_2H_3^+$	27	0	0.77	
$C_2H_4^+$, N_2^+, CO^+	28	See text		
$C_2H_5^+$	29	0.34	0.89	
C_2H_6[b]	30	0.07	0.02	
C_3H_3	39		0.46	0.5
$C_3H_5^+$	41	0.66	1.61	2.5
$C_3H_6^+$	42	0.72	0.77	1.4
$C_3H_7^+$	43	3.07	3.07	5.0
$C_4H_7^+$	55	0.17	0.42	0.75
$C_4H_8^+$	56	1.45	1.23	0.85
$C_4H_9^+$	57	1.93	1.81	2.8
$C_5H_{10}^+$	70	1.07	0.92	1.0
$C_5H_{11}^+$	71	2.14	1.81	2.5
$C_6H_{13}^+$	85	0.03	0.04	
$C_7H_{14}^+$	100	1.00	1.00	1.0

[a]Source pressure, $<1 \times 10^{-5}$ torr.

[b]Probably impurity.

Of the listed primary fragments of heptane (masses 85, 71, 57, 43, 29), only mass 29 decreased relative to the parent mass 100 upon reduction of the electron energy. It should be noted that for mass 28, corresponding to $C_2H_4^+$, N_2^+, and CO^+, a large peak was present (even after adjusting the peak height due to nitrogen by using the mass 32 peak) which decreased markedly upon reduction of the voltage. Ethylene and CO as impurities in the sample may therefore be ruled out. The peak height at 70 v was perhaps 5 to 10 relative to mass 100, and at 30 v was perhaps 0.2.

The most dramatic changes in the listed fragment patterns are masses 39, 41, 55, and the small fragments other than 29. The effective removal of several of the secondary fragments (such as 28, 14, 26, 27, and 39) may be followed by a

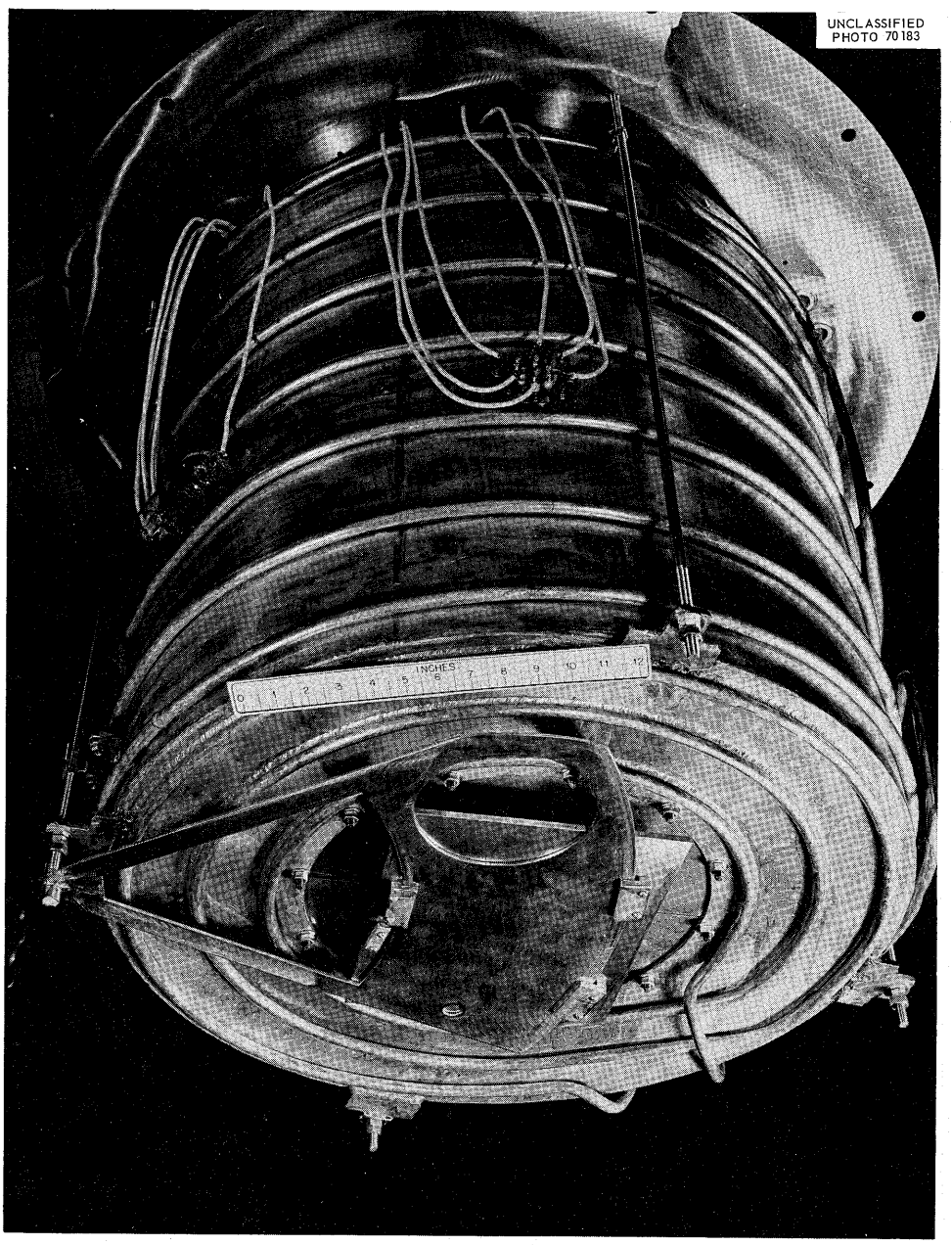

Fig. 10.1. Ultrahigh Vacuum Test Facility Shroud.

further reduction of 41 and 55 at energies nearer the ionizing potential. However, the 1- to 2-v bond strength for organic compounds indicates that little expectation should exist for developing a parent-only source. Decane behaves similarly, as also does dodecane, of course, with larger amounts of masses near those one-half the parent. Toluene, ethyl benzene, and *m*-xylene have also been studied as a consequence of their frequent appearance in mechanical pump oils and forelines of the usual vacuum systems.

10.3 PHYSICAL ADSORPTION AT LIQUID-NITROGEN TEMPERATURES

The 300-liter shrouded ultrahigh-vacuum test facility has been modified to include a pumping speed controllable from <5 to 100 liters/sec. The shroud now has a cooled surface of which 98% is copper (the balance being principally stainless steel), two matched nude ion gages, and a tubulated gage. One of the nude gages is shielded from a new gas-inlet diffuser at the center so that entering gas molecules can be distinguished from those which have interacted one or more times with the wall. A photograph of the shroud (Fig. 10.1) shows the variable conductance as well as two of the shroud gages. A baffle plate located below the shroud was constructed with $^7/_8$-in.-OD copper tubing for nitrogen cooling to achieve the lowest possible temperature for this plate. An auxiliary stable gas-leak system with control capability of 10^{-5} to 10^{-2} torr-liter/sec has been designed, constructed, and tested. This apparatus allows the introduction of gas at a rate as low as 3×10^{10} molecules cm^{-2} sec^{-1} (about 0.1 monolayer/hr).

11. Design and Engineering: Service Report

J. F. Potts, Jr.

The results of the Engineering Services Group are generally reported incidentally with those of the research groups of the Thermonuclear Division. The Group executes or coordinates engineering design, shop fabrication, building operations, and maintenance for the Laboratory.

Design activities for this reporting period are summarized as follows:

Jobs on hand 5-1-63 on which work had not started	14
New jobs received	234
Total jobs	248
Jobs completed	222
Jobs in progress	10
Backlog of jobs 10-31-63	16
Total drawings completed for period (does not include drawings for use in reports, slides, etc.)	333
Overtime (draftsmen, man-days)	0

Shop fabrication for this reporting period is summarized as follows:

Machine Shops	
Completed jobs requiring 16 man-hours or less	195
Completed jobs requiring up to 1200 man-hours	203
Jobs requiring up to 2000 man-hours	1
Completed miscellaneous jobs	58
Completed jobs by outside contractors	8
Number of jobs in progress	48
Average manpower (per week)	28.0
Electromagnet Fabrication	
Completed jobs	7
Number of jobs in progress	3
Average manpower (per week)	3

Publications, Papers, and Traveling Lecture Program

PUBLICATIONS

Author(s)	Title of Article	Journal
Igor Alexeff and R. V. Neidigh	A Plasma Flowmeter: "The Plasma Eater"	*Nucl. Fusion* **3**, 23 (1963)
T. K. Fowler[1]	Lyapunov's Stability Criteria for Plasmas	*J. Math. Phys.* **4**, 559 (1963)
B. S. Chandrasekhar,[2] W. F. Gauster, and J. K. Hulm[2]	Degradation Factor and Diamagnetic Currents in Supermagnets	*Appl. Phys. Letters* **2**, 228 (1963)
D. L. Coffey, W. F. Gauster, and H. E. Rorschach, Jr.[3]	Flux Trapping in Hollow Soft Superconducting Cylinders	*Appl. Phys. Letters* **3**, 75 (1963)
J. R. McNally, Jr., and M. R. Skidmore	Spectroscopic Line Profile Studies of Long, Magnetically Confined, High-Current, Steady-State Vacuum Arcs	*Appl. Opt.* **2**, 699 (1963)
Herman Postma, G. R. Haste, and J. L. Dunlap	Proton Trapping in DCX-1 Resulting from Lorentz Dissociation of H_2^+	*Nucl. Fusion* **3**, 128 (1963)
A. H. Snell	Controlled Fusion Today	*IEEE Trans. Nucl. Sci.* **10**(4), 1 (1963)

[1]Physics Division.

[2]Westinghouse Research Laboratory, Pittsburgh, Pa.

[3]Consultant, the William Marsh Rice University.

PAPERS PRESENTED AT SCIENTIFIC AND TECHNICAL MEETINGS

American Physical Society, Buffalo, N.Y., June 24–26, 1963

Igor Alexeff, R. V. Neidigh, and W. F. Peed, "Plasma Density Measurement by Casting a Shadow in Evaporated Gold."

Sami Cuperman, "Impurity Radiation from Non-Maxwellian Spherical Plasmas."

T. K. Fowler,[1] "Stability Criteria in a Plasma."

J. L. Dunlap, "Plasma Properties of Instabilities in DCX-1."

N. H. Lazar, P. R. Bell, J. E. Francis, R. A. Gibbons, G. G. Kelley, and R. F. Stratton, "Stabilization of the Plasma of a High Energy Injection Mirror Machine by a Vacuum Arc Discharge."

[1]Physics Division.

Society of Nuclear Medicine, Tenth Annual Meeting, Montreal, Canada, June 26–29, 1963

C. C. Harris, P. R. Bell, M. M. Satterfield, and J. C. Jordan, "Further Development in Data Extraction from Scan Records by the Recording Densitometer or 'Rescanner.'"

VIth International Conference Ionization Phenomena in Gases, Paris (Orsay), France, July 8–13, 1963

Igor Alexeff and W. D. Jones, "Direct Measurement of Ionic Sound-Wave Velocity."

W. B. Ard, R. A. Dandl, A. C. England, and R. J. Kerr,[2] "Determination of Electron Density and Energy Distribution in a Very Hot Electron Plasma."

C. F. Barnett, Mozelle Rankin, and J. A. Ray, "Formation of Neutral Atomic Hydrogen Beams."

E. G. Harris,[3] "Ionization-Recombination Instabilities."

Fontenay Study Group on Mirror Configurations, Fontenay-aux-Roses, France, July 15–19, 1963

Igor Alexeff, R. V. Neidigh, and W. F. Peed, "Hot-Electron Plasma by Beam-Plasma Interaction Between Magnetic Mirrors."

W. B. Ard, "Phenomenological Conditions for Stability in Electron Heated Plasma."

P. R. Bell, L. J. Bledsoe, J. S. Culver, R. C. Davis, S. M. DeCamp, J. C. Ezell, R. A. Gibbons, G. G. Kelley, N. H. Lazar, O. B. Morgan, J. D. G. Rather, T. F. Rayburn, R. F. Stratton, J. C. Thompson, C. W. Wright, and A. J. Wyrick, "Stabilization of Instabilities in DCX-2 by Use of a Longitudinal Arc."

J. L. Dunlap, "Plasma Properties of Instabilities in DCX-1."

T. K. Fowler, "Growth Rates of Electrostatic Instabilities in Mirror Configurations."

Third International Conference on the Physics of Electronic and Atomic Collisions, University College, London, July 22–26, 1963

C. F. Barnett and J. A. Ray, "The Dissociation Cross Section of H_2^+ in Hydrogen Gas."

1963 Cryogenic Engineering Conference, Boulder, Colorado, Aug. 20, 1963

W. F. Gauster and D. L. Coffey, "Current-Carrying Capacity and Transition State of Superconducting Solenoids."

Fifth Annual Meeting, Southeastern Chapter, Society of Nuclear Medicine, Miami, Florida, Oct. 17–19, 1963

D. A. Ross, C. C. Harris, M. M. Satterfield, J. C. Jordan, and P. R. Bell, "Scan 'Haziness' with Low-Energy Gamma Rays: Cause and Treatment."

M. M. Satterfield, C. C. Harris, J. C. Jordan, D. A. Ross, and P. R. Bell, "'Counting Rate' Recording in Dynamic Processes: Various Approaches."

---

[2]Deceased.

[3]Consultant, the University of Tennessee.

TRAVELING LECTURE PROGRAM

The Traveling Lecture Program is conducted in cooperation with the Oak Ridge Institute of Nuclear Studies as a part of the AEC's program of disseminating scientific and technical information to universities, particularly those in the South. Lectures delivered by ORNL personnel present unclassified information to university undergraduate and graduate students and members of the faculty. The lectures serve to stimulate interest in research in the university departments and also to assist the teaching staff in expanding the scope of instruction offered under their regular curricula. Through such personal contacts, ORNL staff members are also able to observe departmental activities at the universities. Listed below are members of the Thermonuclear Division who participated in the Traveling Lecture Program during this report period.

P. M. Griffin	A and M College of Texas, May 1, 1963 "Spectroscopy of High Temperature Plasmas"
W. F. Gauster	University of Arkansas, May 14, 1963 "Engineering Aspects of Superconductivity"
W. F. Gauster	William Marsh Rice University, May 16, 1963 "Engineering Aspects of Superconductivity"
Igor Alexeff	Michigan State University, May 20, 1963 "Plasma as a Compressible Fluid"
P. R. Bell	Georgia Institute of Technology, Oct. 17, 1963 "Thermonuclear Experiments at Oak Ridge

ORNL-3564
UC-20 – Controlled Thermonuclear Processes
TID-4500 (26th ed.)

INTERNAL DISTRIBUTION

1. I. Alexeff
2. R. G. Alsmiller
3. W. B. Ard
4. C. F. Barnett
5. C. O. Beasley
6. M. C. Becker
7–12. P. R. Bell
13. D. S. Billington
14. E. P. Blizard
15. C. W. Blue
16. G. E. Boyd
17. R. L. Brown
18. R. E. Clausing
19. D. L. Coffey
20. F. L. Culler
21. J. S. Culver
22. S. Cuperman
23. R. A. Dandl
24. R. C. Davis
25. S. M. DeCamp
26. J. L. Dunlap
27. H. O. Eason, Jr.
28. R. S. Edwards
29. A. C. England
30. J. C. Ezell
31. J. L. Fowler
32. T. K. Fowler
33. J. E. Francis, Jr.
34. J. H. Frye, Jr.
35. W. F. Gauster
36. R. A. Gibbons
37. P. M. Griffin
38. W. R. Grimes
39. G. E. Guest
40. E. Guth
41. G. M. Haas
42. W. Halchin
43. C. C. Harris
44. G. R. Haste
45. R. E. Hill
46. A. S. Householder
47. H. C. Hoy
48. R. P. Jernigan, Jr.
49. W. D. Jones
50. G. G. Kelley
51. M. T. Kelley
52. R. L. Knight
53. J. A. Lane
54. C. E. Larson
55. N. H. Lazar
56. G. F. Leichsenring
57. J. Lewin
58. R. S. Livingston
59. J. N. Luton, Jr.
60. J. R. McNally, Jr.
61. W. D. Manly
62. O. D. Matlock
63. K. Z. Morgan
64. O. B. Morgan
65. R. V. Neidigh
66. M. L. Nelson
67. J. Neufeld
68. C. E. Parker
69. R. B. Parker
70. W. F. Peed
71. H. Postma
72. J. F. Potts
73. M. Rankin
74. J. A. Ray
75. L. H. Reber
76. R. G. Reinhardt
77. D. M. Richardson
78. D. A. Ross
79. P. W. Rueff
80. W. K. Russell
81. H. E. Seagren
82. Y. Shima
83. E. D. Shipley
84. M. R. Skidmore
85. M. J. Skinner
86–96. A. H. Snell
97. W. L. Stirling
98. R. F. Stratton, Jr.
99. R. A. Strehlow
100. J. A. Swartout
101. E. H. Taylor
102. P. A. Thompson
103. H. L. Watts
104. A. M. Weinberg
105. E. R. Wells

106. T. A. Welton
107. W. L. Wright
108. A. J. Wyrick
109. O. C. Yonts
110. Gale Young
111. W. H. Bostick (consultant)
112. J. W. Flowers (consultant)
113. M. W. Garrett (consultant)
114. E. G. Harris (consultant)
115. D. E. Harrison (consultant)
116. W. Heckrotte (consultant)
117. R. Hefferlin (consultant)
118. G. W. Hoffman (consultant)
119. V. W. Hughes (consultant)
120. D. W. Kerst (consultant)
121. E. W. McDaniel (consultant)
122. D. R. Montgomery (consultant)
123. C. E. Nielsen (consultant)
124. W. B. Pardo (consultant)
125. J. M. Reynolds (consultant)
126. F. F. Rieke (consultant)
127. H. S. Robertson (consultant)
128. H. G. Rorschach (consultant)
129. D. J. Rose (consultant)
130. L. P. Smith (consultant)
131. P. M. Stier (consultant)
132. J. D. Tillman (consultant)
133–157. Thermonuclear Division Library
158. Reactor Division Library
159. Biology Division Library
160–162. Central Research Library
163. Laboratory Shift Supervisor
164–238. Laboratory Records Department
239. Laboratory Records, ORNL RC
240–241. ORNL – Y-12 Technical Library Document Reference Section

EXTERNAL DISTRIBUTION

242. S. C. Brown, Massachusetts Institute of Technology
243. M. B. Gottlieb, Princeton University
244. H. Grad, New York University
245. J. M. B. Kellogg, Los Alamos Scientific Laboratory
246. A. C. Kolb, Naval Research Laboratory
247. J. A. Phillips, Los Alamos Scientific Laboratory
248. R. F. Post, University of California, Lawrence Radiation Laboratory
249. A. Simon, General Atomic, San Diego, California
250. L. Spitzer, Princeton University
251. E. Teller, University of California, Lawrence Radiation Laboratory
252. C. M. Van Atta, University of California, Lawrence Radiation Laboratory
253. R. W. McNamee, Union Carbide Corporation
254–255. Research and Development Division, AEC, ORO (1 copy each to H. M. Roth and R. B. Martin)
256–257. Controlled Thermonuclear Research Branch, AEC, Washington (A. E. Ruark)
258. L. D. Smullin, Massachusetts Institute of Technology
259–270. Technical Training and Exchange Branch, Division of International Affairs, AEC, Washington (C. Slesser)
271–902. Given distribution as shown in TID-4500 (26th ed.) under Controlled Thermonuclear Processes category (75 copies – OTS)